Unraveling spin wave dynamics in ferro- and antiferromagnetic materials : a step towards ultrafast magnonics

Aya El Kanj

université PARIS-SACLAY

Unraveling spin wave dynamics in Ferro- and Antiferro- magnetic materials: A step towards ultrafast magnonics

Étude de la dynamique des ondes de spin dans les matériaux Ferro- et Antiferro- magnétiques : une avancée vers la magnonique ultrarapide

Thèse de doctorat de l'université Paris-Saclay

École doctorale n° 564, Physique en Ile-de-France (PIF)
Spécialité de doctorat : Physique
Graduate School : Physique
Référent : Faculté des sciences d'Orsay

Thèse préparée au **laboratoire Albert Fert** (CNRS, Thales, Université Paris-Saclay)
sous la direction de **Abdelmadjid ANANE**, Maître de conférence,
et le co-encadrement de **Romain LEBRUN**, Ingénieur de recherche Thales.

Thèse soutenue à Paris-Saclay, le 15 avril 2024, par

Aya EL KANJ

Composition du Jury

Membres du jury avec voix délibérative

Michel VIRET Directeur de recherche CEA, SPEC, Paris-Saclay	Président
Silvia TACCHI Chercheuse (équiv. HDR), NCR-IOM, University of Perugia	Rapportrice & Examinatrice
Vincent CASTEL Maître de Conférence (HDR), IMT Atlantique, Brest	Rapporteur & Examinateur
Joerg WUNDERLICH Directeur de recherche University of Regensburg	Examinateur

THESE DE DOCTORAT

NNT : 2024UPASP024

université PARIS-SACLAY | ÉCOLE DOCTORALE Physique en l'Île-de-France (PIF)

Titre : Étude de la dynamique des ondes de spin dans les matériaux ferro- et antiferro- magnétiques : une avancée vers la magnonique ultrarapide.

Mots clés : Magnonique, ondes de spin, spintronique, antiferromagnétique, ferromagnétique, radiofréquence

Résumé : Cette thèse porte le sujet de la magnonique, un domaine de recherche étudiant le transport des ondes de spin (SWs) dans les matériaux magnétiques pour les technologies beyond-CMOS. L'objectif de mon travail repose sur la génération, la propagation et la détection des SWs dans les matériaux ferromagnétiques (FM) et antiferromagnétiques (AFM), principalement le Grenat de Fer d'Yttrium ($Y_3Fe_5O_{12}$, connu par YIG) et l'Hématite (α-Fe_2O_3). En conséquence, trois résultats principaux ont été obtenus :

1. **Spectroscopie de temps de vol sur le YIG :** Nous introduisons une méthode d'extraction d'informations temporelles sur les paquets de SWs propagatifs à l'aide d'un Analyseur de Réseau Vectoriel (VNA). L'approche implique la transformée de Fourier inverse des données de domaine fréquentiel, montrant son utilité dans les VNA disponibles commercialement. Nous réalisons donc des mesures sur un film de YIG, ayant un spectre complexe de mode. On arrive alors à identifier les modes ainsi que d'isoler leur contribution afin de pouvoir étudier les propriétés de chaue mode. À partir de ces résultats, nous avons pu mieux comprendre le comportement des SWs dans une ligne de retard de YIG et ainsi adapter la conception des antennes selon l'application souhaitée.

2. **Ondes de spin non dégénérées, non réciproques et ultra-rapides dans l'hématite :** Les ondes de spin dans les AFM sont également étudiés depuis des anées, mais leurs observation en expérimentale font toujours défaut. Les AFM cantés tel que l'hématite avec la présence des interactions Dzyaloshinskii-Moriya et sous l'influence d'un champs magnétique appliqué, permettent un régime d'échange dipolaire de SWs. Nous avons réussi donc à détecter et démontrer la présence de tels SWs ayant un caractère non réciproques ultra-rapides et non dégénérés, en utilisant des moyens de détection inductifs sur l'hématite épais. En utilisant la spectroscopie de temps de vol, nous constatons que les paquets d'ondes de magnons peuvent se propager aussi rapidement que 20 km/s pour les modes de bulk réciproques et jusqu'à 6 km/s pour les ondes de spin de surface se propageant parallèlement au vecteur Néel. Ces résultats peuvent faire avancer le domaine de la magnonique antiferromagnétique et dévoiler la physique riche des SWs cohérents.

3. **Magnon spintronics sur Hematite:** Une technique alternative aux mesures inductives pour détecter les SWs peut être réalisée en utilisant une détection électrique. Cela est accompli en utilisant un transducteur métallique à base de platine via l'effet Hall de spin inverse(ISHE). Nous obtenons une tension de sortie sur l'hématite comparable à celle obtenue dans un FM comme le YIG, marquant une détection électrique efficace des SWs propagatifs à travers ISHE sensible à la surface. Un autre effet a également été obtenu dans cette thèse ; la réalisation de la rectification de diode de spin dans l'hématite. Grace a ces etudes on a pu démontrer que les effets de spin-pumping représentent un outil prometteur pour détecter la dynamique de SW dans les AFM.

Avec ces études, nous visons à contribuer dans l'avancement des applications radiofréquences, ouvrant la voie au développement de la recherche magnonique et magnonique spintronique ultra-rapide pour les futures technologies de l'information.

université PARIS-SACLAY | ÉCOLE DOCTORALE Physique en l'Île-de-France (PIF)

Title : Unraveling spin wave dynamics in Ferro- and Antiferro- magnetic materials: A step towards ultrafast magnonics.

Keywords : Magnonics, spin waves, spintronics, antiferromagnet, ferromagnet, radiofrequency.

Abstract: This thesis holds the subject of magnonics, a research field investigating spin waves (SWs) transport in magnetic materials for potential future beyond CMOS technologies. The aim of my work relies on the generation, propagation, and detection of spin waves in ferromagnetic and antiferromagnetic materials, with a specific focus on Yttrium Iron Garnet ($Y_3Fe_5O_{12}$, known as YIG) and Hematite (α-Fe_2O_3). As a consequence, three main results have been achieved:

1. **Time of flight spectroscopy on YIG:**

We introduce a method for extracting time-domain information on propagating spin-wave packets using a Vector Network Analyzer. The approach involves the inverse Fourier Transform of frequency domain data, showing its utility within the commercially available VNAs. We therefore conduct measurements on a 500 nanometer-thick YIG film, a well-known system in the aim to validate the technique's application. It results in isolating a single SW mode profile from a complex spectrum, enabling the identification of mode origins in addition to conducting individual mode study through time gating. From these results we were able to provide a better understanding of the SWs behavior in a YIG delay line, and therefore tailoring the antennas design according to the needed application.

2. **Non-degenerated, non-reciprocal and ultra-fast spin-waves in Hematite:**

Spin waves in AFM have also been investigated for years, yet experimental observations are still lacking. Canted AFM, such as hematite with the presence of bulk Dzyaloshinskii-Moriya interaction and under applied magnetic fields, allow a dipole exchange regime of AFM spin waves. In this thesis, we were able to detect and demonstrate the presence of ultra-fast nonreciprocal SWs in this regime using inductive means of detection on a bulk Hematite. By using time-of-flight spectroscopy we find that the magnon wave packets can propagate as fast as 20 km/s for reciprocal bulk modes and up to 6 km/s for surface modes propagating parallel to the Néel vector. These findings can push forward the field of antiferromagnetic magnonics, and in unravelling the rich physics of coherent SWs.

3. **Magnon spintronics on Hematite:**

An alternative technique to the inductive measurements to detect the spin waves can be done by using an electrical detection of antiferromagnetic spin-waves. This is achieved by using a platinum-based metallic transducer via the inverse spin hall effect. The response's output voltage on Hematite is comparable to that obtained in ferromagnets like YIG, marking an efficient electrical detection of propagating spin-waves through the surface-sensitive inverse spin-Hall effect with a platinum-based metallic transducer.

Another effect was also achieved in this thesis that is the realization of spin diode rectification in Hematite. In this work we evidence that as expected the Oersted field excitation dominates over spin-torque effects in the case of a single crystal. We also observe the presence of non-linear effects when pumping the system with high powers. To go further, we examine by simultaneously applying both AC and DC currents, the DC dependent characteristics of the system to validate our statements. These mentioned features further demonstrate that spin-pumping effects represent a promising tool to detect the spin-wave dynamics in antiferromagnets, and favorize their integration in magnonic devices.

With these findings, we aim to unlock the potential for future advancements in radiofrequency applications, paving the way for the development of ultrafast magnonic and magnon spintronic based research for future ICT technologies.

ACKNOWLEDGEMENTS

First of all, Madjid, I want to thank you from the bottom of my heart for giving me this amazing opportunity and for taking me on as your intern, even though I had no previous experience. Your constant belief in me has been always motivating me , and you've always encouraged me to trust in my abilities. You always gave me the right push and support whenever I felt down, and I can't thank you enough for helping me to gain the confidence to pursue my journey. I will miss your dark humour and will always remember your advice: "Be more aggressive, less nice!"

Thank you, Romain, for always being there to guide me, teach me, and follow up on my progress. Thanks to you, I have learned all the techniques I used for my Ph.D., especially since I started during the challenging times of COVID. Your extensive knowledge in the field has been my source of information, and I have tried to absorb as much as I can. It was a pleasure working with you, even though we had some rough times (like the Christmas 2023 meetings at 1 a.m. ..hehe :D). Despite those challenges, it was incredibly satisfying when we finally achieved our goals. I deeply appreciate your support and look forward to see your future fruitful work on our dear Hematite.

Isabella, even though we didn't work together very often, you were always there to listen to me, to mentor me, and to help me with your experience, allowing me to believe in myself. I know you sometimes underestimate this, but you are truly an inspiring person and a role model for a strong woman in science. And I am very grateful I met such a person like you and I hope to see you soon on the future girls nights ;) (little Raphael will be so welcomed!)

Ping, Thank you for helping me with experiments and sharing your experience. You have taught me how to push myself to the maximum to achieve my goals, and you have always been inspiring me with your strong motivation. I will always remember all the enjoyable moments we shared at conferences and during our travels, as well as your endless debates with Sougata :D. Additionally, thank you for introducing me to Chinese culture and cuisine; you are an amazing cook, by the way! Now I wish to visit China more than ever!

I will miss my office so much. It was the place where everyone passed by to chat, nag, or take a break (as if it were a second coffee room). I will especially miss my co-bureaus, PauPau and Dianou. I felt so lonely after you left the lab. It was a joy to share this office with you, and thanks to this, we remained friends even after leaving the lab. Thankfully, Amr arrived later on. I will miss our little talks in the office, in Arabic when no one was around, discussing politics, sports, and sometimes science! It was truly a pleasure to meet someone like you, who seemed shy at first but then turned out to be incredibly fun once you get to know them.

Hadi, my dabké dancing partner in crime! Two words for you in Lebanese: hawwena bethoun w nshalla menshufak ahla Dr. w ahla 3aris!

To all the friends that I have made during this PhD, Gaetan, we were the old, tired, grumpy buddies in our fourth year, but we finally made it! I will miss our breaks where we complained

about how we were suffering through writing and not sleeping well, but hopefully, that will never happen again 😊 . I wish you nothing but the best in Grenoble!

Laurette, my Lebanese friend, whenever I needed a break from languages, I just went to chitchat with her! Sarah, we made a great team for social events, and I hope it will continue in the lab with the new leads now!

Diana, Sougata, Srijani, Carole, Sachin, Julian, Dedalo, Vincent H. and so many more (sorry if I missed anyone!) thank you for all the enjoyable moments we had, the social events, and of course, the famous Giens trip!

To all the permanent members in the lab, thank you so much for your efforts in ensuring good cohesion between the teams and the comfort of the working environment. Thank you for creating such positive vibes in the lab while enjoying science!

Yanis, no words can adequately express the amount of support you gave me during the writing time. You have always been the shoulder I leaned on, and I wish nothing but a new journey for us full of adventures (oki not the dangerous ones...) with lots of countries to visit and ice creams to try!

Last but not least, I thought writing this at the beginning of my manuscript is the perfect occasion to share my small story. Ten years ago, nobody, including my medical team, believed that I could live a normal life again. They thought I would be facing a life full of back and forth between illness and hospitals due to the severe Anorexia I had back then. But I guess, reading this manuscript now, proves these people wrong. However, I couldn't have done this alone. It's thanks to the incredible support system I've had during these past 10 years that I keep beating my weaknesses and keep going and going. Thank you Rementi, thank you Talloul, thank you Ammoula, thank you Babi, thank you Mami; I love you more than anything in this world, and without you, I wouldn't be where I am today.

To all ED fighters out there, it's a long journey, it's a chronic issue, and it's okay to break sometimes. Always stay strong, love yourself, and you will heal.

TABLE OF CONTENTS

1 INTRODUCTION

Magnetism is a subject that has been studied for approximately three thousand years. After the discovery of electromagnetic waves and the principles of relativity, rapid progress in this area took place in the last two centuries. With the discovery of the electron spin in 1925 (*1*), and its associated magnetic moment, the exploitation of the magnetic properties of a material gained many interests.

With the growing demand for power-intensive electronic devices in the market, several challenges have emerged in the use of conventional electronics, particularly related to issues like joule heating (*2*). Additionally, constraints within CMOS technology, such as limitations on miniaturization (*3*), contribute to a decline in the applicability of Moore's Law (*4*), which predicts the rate at which the number of transistors increases in circuits. Consequently, there has been a notable shift towards exploring alternatives, beyond-CMOS, that have been gaining significant interest over the past decade aiming to find scalable and high-performance components while overcoming joule heating (*5*).

Magnetic materials have witnessed remarkable global growth over the years which have driven the development of scientific discoveries in this area. The advances in permanent magnetism, magnetic recording, and high-frequency materials are accelerating the progress in computers, telecommunications, and data storage industries, crucial for everyday life.

Spintronics (*6*), firstly discovered in 1936 by Mott, linked the electron spin to its charge. Notably, in magnetic materials the spin orientation can be manipulated by the use of external magnetic fields. The difference in mobility and the population of spin up and spin down electrons in such materials induces a net flow of spin-polarized current. Therefore, this field holds the studies of transferring processing and storing information via the spin of the electron instead of its charge and therefore overcoming the limitations of electronics.

When magnetic moments are spontaneously aligned, the material is called a Ferromagnet, resulting in a finite spontaneous magnetization. This ferromagnetic behavior pertains as long as the temperature is below a critical temperature called the Curie temperature T_c. Thus, the application of low fields can produce a very strong magnetization in such materials. Above T_c, the magnetization vanishes, and the material becomes in a paramagnetic state. Another case can exist, which is when the magnetic moments are aligned anti-parallel the one with respect to the other resulting in a vanished spontaneous magnetization, in this case the material is called an Antiferromagnet, with a critical temperature called, the Néel temperature.

For decades, ferromagnets with high curie temperatures and large magnetization were widely used in the magnetic storage industry, such as magnetic hard drives. In 1988, the discovery of giant magnetoresistance, GMR, by Albert Fert (*7*) and Peter Grünberg (*8*) in alternating ferromagnetic and non-magnetic conductive layers gave rise to a huge fundamental and applied research interest. It quickly promoted the development of a new type of magnetic

sensor, now widely used in the read-head of hard-disk and led for a Nobel prize in Physics in 2007. Soon after the GMR, spin-polarized currents were shown to be used to manipulate magnetic states, via an effect called spin transfer, which is currently implemented in magnetic memories. With these discoveries, spintronics marked a turning point in the development of modern computing three decades ago. Yet, despite its promising application, spin polarized current are generated via electrical currents and therefore do not avoid the building up of losses from joule heating.

When a system of ordered magnetic moments is subjected to a disturbance, causing a deflection from their equilibrium position, these magnetic moments tend to relax towards equilibrium through a damped precessional motion. This localized disturbance results in the propagation of deflected magnetic moments throughout the material, forming a magnetic wave known as a «Spin wave» and was recognized by Bloch in 1929 (*9*). Spin waves possesses wavelengths ranging from the micrometer to the nanometer scale, with velocities reaching a few km/s and frequencies spanning from gigahertz to terahertz. The relationship between their frequency and their wavevector, known by the dispersion relation, is what characterizes these waves and differentiate their wide properties. Such waves can thus propagate in the magnetic medium without interacting with the charge of the electron and thus avoiding heating effects. Thereby the field which studies the spin waves from its excitation, propagation, manipulation, and detection, is called «Magnonics» (*10*), in recognition to the quanta of spinwaves, the magnons. Therefore, owing to their unique characteristics, magnonic nanodevices are perceived as promising candidates for microwave information processing technologies.

The field of magnonics saw significant advances with the introduction of photonic crystals (*11*). The exploration of magnonic crystals commenced with the first introduction in 2001 (*12*), by marking the beginning of widespread research into the concept. From magnonic crystals, extensive investigations into propagating spinwaves, exploiting the rich physics of magnetic materials. This research led to the development of prototype devices for magnonic circuits, including transistors (*13, 14*) magnonic logic gates (*15, 16*), and microwave components like filters , amplifiers, diodes, and circulators (*17*) . To our days, the field is magnonics is now covering a diverse range of cutting-edge subjects all aiming to push the realization of functioning magnonic devices. The topics covered by magnonics are all combined in the latest magnonics roadmap published in 2021 (*18*).

To detect spin-waves, the most commonly used techniques can be electrical techniques such as with inductive antennas or with resonant cavities, optical techniques such as micro-focused Brillouin light scattering spectroscopy (μ-BLS) or time-resolved Magneto-Optical Kerr effect (TR-MOKE), or even X-ray diffraction techniques such as X-ray Magnetic Circular Dichroism (XMCD). In this thesis, we used an all-electrical technique to detect the spinwaves called propagating spinwave spectroscopy, based on the inductive coupling between rf-antennas and the magnetic material. These measurements are carried out using a Vector Network Analyzer (VNA), where two types of measurements can be performed: frequency and time domains. The latter is rarely utilized in magnonics until now. However, in this thesis, we

extensively applied this method to distinguish between the various modes present in a magnonic system, thereby allowing a proficient understanding for the SWs behavior in the material under study and therefore in the enhancement of the RF-antenna designs tailored to the specific application.

When precessing, and due to the presence of magnetic damping in the material, magnetization is subjected to damped oscillations and a limited propagation. For this reason, in magnonic devices, a key challenge is to overcome the magnetic damping in the material to achieve long propagation distances of the spin waves. This necessitates the use of materials with small magnetic damping. Yttrium Iron Garnet (YIG), a ferrimagnetic material, has by far the lowest magnetic damping, allowing the propagation of spin waves to be spread over centimeter distances. However, in the context of micromagnetic approximations, YIG is treated as a ferromagnet. For these reasons, YIG has been considered a reference material for extensive studies on spin-wave dynamics over the years. This has positioned YIG as a promising candidate for developing devices for microwave applications, such as filters and delay lines, as well as magneto-optical devices such as deflectors, thanks to the large Faraday effect in this material. Interestingly, YIG can be grown on various substrates depending on the application. For example, to achieve low damping and a narrow line width, GGG is commonly used. However, promising alternative substrates include the use of silicon or gallium arsenide (*19*), that are especially favored in CMOS applications due to their excellent charge carrier mobility and wide band gap. Therefore, the growth on such substrates opens up the possibility for future magnonic devices integration. Furthermore, YIG remains a main subject of research, in which fundamental physics in magnonics is still under investigation, including Bose-Einstein condensation(*20*, *21*), and exploring the manipulation of spin waves through spin-orbit torques (*22*, *23*, *24*) .

In some applications, the use of ferromagnets fails to meet certain requirements due to some limitation as achieving higher frequencies beyond the GHz region, the presence of stray fields, and the dependence of the spin waves properties on the magnetization. Therefore, it is interesting to explore alternative materials that can fulfill these needs while also uncovering the same physics observed in ferromagnets.

Antiferromagnetic materials can reach resonance frequencies easily in the THz scales (*19*, *20*, *21*), and thereby offering advantages over their counterparts the ferromagnetic materials as they have a vanishing net magnetization and a robustness to exterior fields. However, interest in antiferromagnetic insulators has grown significantly lately due to their potential to reduce Joule heating, and therefore opening the way to transport the spin angular momentum with the propagating spinwave, where the emergence of antiferromagnetic magnonics (*23*).

Extensive theoretical investigations into the dynamics of propagating antiferromagnetic spin-waves, for long and short wavelengths (*30–33*) have been conducted in the past decades. However, due the challenges in both experimental techniques and the integration into magnonic devices, experimental evidence is still lacking in this area.

In certain orthoferrites, magnetostatic effects can arise due to the possible canting of magnetic moments. This is observed in materials, such as $YFeO_3$ (*34*), $TmFeO_3$, $ErFeO_3$ and α-Fe_2O_3. Notably, form works by Boventer et al. , it has been shown theoretically and experimentally that a canted antiferromagnet at room temperature as α-Fe_2O_3 can have two magnon modes, where they were able to access the lower frequency magnon mode (right handed precession) and detect resonances via ISHE and spin pumping, with frequencies lying on the GHz frequency range (30 GHz for a field of 0.5T) (*35*). This hints at the possibility for detecting propagating antiferromagnetic spin-waves in the canted phase of hematite by probing its low-frequency mode. The utilization of an inductive technique such as propagating spin-wave spectroscopy, as detailed in our recently published paper (*36*), provides an experimental proof for observing ultrafast propagating spinwave at few km/s, that is due to the presence of the magnetostatic effects. These results were also backed with theoretical models developed by our collaborators.

In recent years however, substantial progress has been made in the field of antiferromagnetic spintronics (*31*, *32*), particularly with antiferromagnetic insulators (*39*). This research field has focused on manipulating antiferromagnetic order through spin-to-charge mechanisms. Currently, the successful electrical detection using the inverse spin-Hall effect has been limited to the uniform mode (k = 0), resulting in generated voltage amplitudes in the tens of nanovolts range for both colinear (*40*, *41*)and canted antiferromagnets (*29*, *37*). Moreover, works by Lebrun et al. have demonstrated potential for long-distance magnon transport and experimentally validated dissipation-less spin transport in Hematite at room temperature (*44*). Notably, our recent work has provided evidence for the detection of propagating spin-waves via ISHE (*36*). This achievement not only merges spintronics mechanisms with ultrafast propagating spin-waves but also sets the stage for the future integration of magnonic devices with canted antiferromagnets.

In this manuscript, we will investigate spinwave excitation, propagation, and detection in two distinct materials: the ferromagnetic Yttrium Iron Garnet (YIG) and the antiferromagnetic Hematite.

Chapter 2 provides a comprehensive theoretical overview essential for understanding the core concepts explored throughout the thesis. It begins by delineating the major concepts crucial for distinguishing various spin wave modes in ferromagnets. Subsequently, it introduces antiferromagnetic materials, elucidating their energy equations and delving into the specifics of canted antiferromagnets, exemplified by hematite. The chapter concludes by introducing spin transport mechanisms and establishing key concepts that form a crucial link with the subsequent results presented in later chapters.

Chapter 3 is a description of the experimental techniques used throughout the thesis. It contains fabrication methods, characterization, and the detection of spinwaves.

Chapter 4 covers the results of developing an experimental technique through propagating

spin wave spectroscopy. By implementing the time-domain option of the Vector Network Analyzer (VNA), measurements are presented in the time domain after passing an inverse Fourier transformation (*45*), rather than the frequency domain. The chapter highlights a complexity in the YIG spectrum, revealing its multimodal nature and where we conduct a study to distinguish between these intermixed modes.

In **Chapter 5**, the focus shifts to antiferromagnets, specifically the canted phase of hematite. We present an experimental observation of the coherent propagation of spin waves in bulk hematite. These spin waves exhibit non-degenerate mode with velocities of up to 20 km/s as well as possessing a non-reciprocal character. These experimental results are backed by theoretical models developed and provided by our collaborators for the specific case of hematite.

Chapter 6 continues the exploration of hematite, this time integrating magnonic and spintronic phenomena. The investigation of magnon spintronics on hematite involves detecting spin waves using the inverse spin Hall effect, where the excitation is initiated by an inductive antenna and the detection is via a platinum transducer. The chapter goes on to demonstrate a rectification effect based on a spin diode effect in hematite.

Chapter 7 serves as a conclusion and a summary of the presented results throughout the previous chapters. Finally, we conclude the thesis with some perspectives and motivations that can serve to push forward the field of ultrafast magnonics.

1.1 BIBLIOGRAPHY:

1. A. Pais, George Uhlenbeck and the Discovery of Electron Spin. *Physics Today* **42**, 34–40 (1989).
2. E. Pop, Energy dissipation and transport in nanoscale devices. *Nano Res.* **3**, 147–169 (2010).
3. A. Chen, "Emerging research device roadmap and perspectives" in *2014 IEEE International Conference on IC Design & Technology* (IEEE, Austin, TX, USA, 2014; http://ieeexplore.ieee.org/document/6838616/), pp. 1–4.
4. G. E. Moore, Cramming More Components onto Integrated Circuits. *PROCEEDINGS OF THE IEEE* **86** (1998).
5. J. Shalf, The future of computing beyond Moore's Law. *Phil. Trans. R. Soc. A.* **378**, 20190061 (2020).
6. S. A. Wolf, D. D. Awschalom, R. A. Buhrman, J. M. Daughton, S. Von Molnár, M. L. Roukes, A. Y. Chtchelkanova, D. M. Treger, Spintronics: A Spin-Based Electronics Vision for the Future. *Science* **294**, 1488–1495 (2001).
7. M. N. Baibich, J. M. Broto, A. Fert, F. N. Van Dau, F. Petroff, P. Etienne, G. Creuzet, A. Friederich, J. Chazelas, Giant Magnetoresistance of (001)Fe/(001)Cr Magnetic Superlattices. *Phys. Rev. Lett.* **61**, 2472–2475 (1988).
8. G. Binasch, P. Grünberg, F. Saurenbach, W. Zinn, Enhanced magnetoresistance in layered magnetic structures with antiferromagnetic interlayer exchange. *Phys. Rev. B* **39**, 4828–4830 (1989).
9. F. Bloch, Zur Theorie des Austauschproblems und der Remanenzerscheinung der Ferromagnetika. *Zeitschrift für Physik* **74**, 295–335 (1932).
10. V. V. Kruglyak, S. O. Demokritov, D. Grundler, Magnonics. *J. Phys. D: Appl. Phys.* **43**, 264001 (2010).
11. E. Yablonovitch, Inhibited Spontaneous Emission in Solid-State Physics and Electronics. *Phys. Rev. Lett.* **58**, 2059–2062 (1987).
12. S. A. Nikitov, Ph. Tailhades, C. S. Tsai, Spin waves in periodic magnetic structures—magnonic crystals. *Journal of Magnetism and Magnetic Materials* **236**, 320–330 (2001).
13. A. V. Chumak, A. A. Serga, B. Hillebrands, Magnon transistor for all-magnon data processing. *Nat Commun* **5**, 4700 (2014).
14. L. J. Cornelissen, J. Liu, B. J. Van Wees, R. A. Duine, Spin-Current-Controlled Modulation of the Magnon Spin Conductance in a Three-Terminal Magnon Transistor. *Phys. Rev. Lett.* **120**, 097702 (2018).
15. A. Khitun, M. Bao, K. L. Wang, Magnonic logic circuits. *Journal of Physics D: Applied Physics* **43**, 264005 (2010).
16. T. Fischer, M. Kewenig, D. A. Bozhko, A. A. Serga, I. I. Syvorotka, F. Ciubotaru, C. Adelmann, B. Hillebrands, A. V. Chumak, Experimental prototype of a spin-wave majority gate. *Applied Physics Letters* **110**, 152401 (2017).
17. H. Merbouche, M. Collet, M. Evelt, V. E. Demidov, J. L. Prieto, M. Muñoz, J. Ben Youssef, G. de Loubens, O. Klein, S. Xavier, O. D'Allivy Kelly, P. Bortolotti, V. Cros, A. Anane, S. O. Demokritov, Frequency Filtering with a Magnonic Crystal Based on Nanometer-Thick Yttrium Iron Garnet Films. *ACS Appl. Nano Mater.* **4**, 121–128 (2021).
18. A. Barman, G. Gubbiotti, S. Ladak, A. O. Adeyeye, M. Krawczyk, J. Gräfe, C. Adelmann, S. Cotofana, A. Naeemi, V. I. Vasyuchka, B. Hillebrands, S. A. Nikitov, H. Yu, D. Grundler, A. V. Sadovnikov, A. A. Grachev, S. E. Sheshukova, J.-Y. Duquesne, M. Marangolo, G. Csaba, W. Porod, V. E. Demidov, S. Urazhdin, S. O. Demokritov, E. Albisetti, D. Petti, R. Bertacco, H. Schultheiss, V. V. Kruglyak, V. D. Poimanov, S. Sahoo, J. Sinha, H. Yang, M. Münzenberg, T. Moriyama, S. Mizukami, P.

Landeros, R. A. Gallardo, G. Carlotti, J.-V. Kim, R. L. Stamps, R. E. Camley, B. Rana, Y. Otani, W. Yu, T. Yu, G. E. W. Bauer, C. Back, G. S. Uhrig, O. V. Dobrovolskiy, B. Budinska, H. Qin, S. Van Dijken, A. V. Chumak, A. Khitun, D. E. Nikonov, I. A. Young, B. W. Zingsem, M. Winklhofer, The 2021 Magnonics Roadmap. *J. Phys.: Condens. Matter* **33**, 413001 (2021).
19. A. V. Sadovnikov, E. N. Beginin, S. E. Sheshukova, Yu. P. Sharaevskii, A. I. Stognij, N. N. Novitski, V. K. Sakharov, Yu. V. Khivintsev, S. A. Nikitov, Route toward semiconductor magnonics: Light-induced spin-wave nonreciprocity in a YIG/GaAs structure. *Phys. Rev. B* **99**, 054424 (2019).
20. M. Schneider, D. Breitbach, R. O. Serha, Q. Wang, A. A. Serga, A. N. Slavin, V. S. Tiberkevich, B. Heinz, B. Lägel, T. Brächer, C. Dubs, S. Knauer, O. V. Dobrovolskiy, P. Pirro, B. Hillebrands, A. V. Chumak, Control of the Bose-Einstein Condensation of Magnons by the Spin Hall Effect. *Phys. Rev. Lett.* **127**, 237203 (2021).
21. B. Divinskiy, H. Merbouche, V. E. Demidov, K. O. Nikolaev, L. Soumah, D. Gouéré, R. Lebrun, V. Cros, J. B. Youssef, P. Bortolotti, A. Anane, S. O. Demokritov, Evidence for spin current driven Bose-Einstein condensation of magnons. *Nat Commun* **12**, 6541 (2021).
22. M. Collet, X. De Milly, O. d'Allivy Kelly, V. V. Naletov, R. Bernard, P. Bortolotti, J. Ben Youssef, V. E. Demidov, S. O. Demokritov, J. L. Prieto, M. Muñoz, V. Cros, A. Anane, G. De Loubens, O. Klein, Generation of coherent spin-wave modes in yttrium iron garnet microdiscs by spin–orbit torque. *Nat Commun* **7**, 10377 (2016).
23. M. Evelt, V. E. Demidov, V. Bessonov, S. O. Demokritov, J. L. Prieto, M. Muñoz, J. Ben Youssef, V. V. Naletov, G. De Loubens, O. Klein, M. Collet, K. Garcia-Hernandez, P. Bortolotti, V. Cros, A. Anane, High-efficiency control of spin-wave propagation in ultra-thin yttrium iron garnet by the spin-orbit torque. *Applied Physics Letters* **108**, 172406 (2016).
24. H. Merbouche, B. Divinskiy, D. Gouéré, R. Lebrun, A. El-Kanj, V. Cros, P. Bortolotti, A. Anane, S. O. Demokritov, V. E. Demidov, True amplification of spin waves in magnonic nano-waveguides.
25. T. Kampfrath, A. Sell, G. Klatt, A. Pashkin, S. Mährlein, T. Dekorsy, M. Wolf, M. Fiebig, A. Leitenstorfer, R. Huber, Coherent terahertz control of antiferromagnetic spin waves. *Nature Photonics* **5**, 31–34 (2011).
26. J. Li, C. B. Wilson, R. Cheng, M. Lohmann, M. Kavand, W. Yuan, M. Aldosary, N. Agladze, P. Wei, M. S. Sherwin, J. Shi, Spin current from sub-terahertz-generated antiferromagnetic magnons. *Nature* **578**, 70–74 (2020).
27. F. M. Johnson, A. H. Nethercot, Antiferromagnetic Resonance in Mn F 2. *Phys. Rev.* **114**, 705–716 (1959).
28. S. M. Rezende, A. Azevedo, R. L. Rodríguez-Suárez, Introduction to antiferromagnetic magnons. *Journal of Applied Physics* **126**, 151101 (2019).
29. S. M. Rezende, R. L. Rodríguez-Suárez, A. Azevedo, Diffusive magnonic spin transport in antiferromagnetic insulators. *Phys. Rev. B* **93**, 054412 (2016).
30. R. E. Camley, Long-Wavelength Surface Spin Waves on Antiferromagnets. *Phys. Rev. Lett.* **45**, 283–286 (1980).
31. B. Lüthi, D. L. Mills, R. E. Camley, Surface spin waves in antiferromagnets. *Phys. Rev. B* **28**, 1475–1479 (1983).
32. B. Lüthi, R. Hock, Dipolar surface spin waves in antiferromagnets. *Journal of Magnetism and Magnetic Materials* **38**, 264–268 (1983).
33. R. L. Stamps, R. E. Camley, Bulk and surface spin waves in thin-film antiferromagnets. *Journal of Applied Physics* **56**, 3497–3502 (1984).
34. S. Das, A. Ross, X. X. Ma, S. Becker, C. Schmitt, F. Van Duijn, E. F. Galindez-Ruales, F. Fuhrmann, M.-A. Syskaki, U. Ebels, V. Baltz, A.-L. Barra, H. Y. Chen, G. Jakob, S. X. Cao, J. Sinova, O. Gomonay, R. Lebrun, M. Kläui, Anisotropic long-range spin transport in canted antiferromagnetic

orthoferrite YFeO3. *Nat Commun* **13**, 6140 (2022).
35. I. Boventer, H. T. Simensen, A. Anane, M. Kläui, A. Brataas, R. Lebrun, Room-Temperature Antiferromagnetic Resonance and Inverse Spin-Hall Voltage in Canted Antiferromagnets. *Phys. Rev. Lett.* **126**, 187201 (2021).
36. A. E. Kanj, O. Gomonay, I. Boventer, P. Bortolotti, V. Cros, A. Anane, R. Lebrun, Antiferromagnetic magnon spintronic based on nonreciprocal and nondegenerated ultra-fast spin-waves in the canted antiferromagnet α-Fe_2O_3. *Science Advances* **9**, eadh1601 (2023).
37. E. V. Gomonay, V. M. Loktev, Spintronics of antiferromagnetic systems (Review Article). *Low Temperature Physics* **40**, 17–35 (2014).
38. V. Baltz, A. Manchon, M. Tsoi, T. Moriyama, T. Ono, Y. Tserkovnyak, Antiferromagnetic spintronics. *Rev. Mod. Phys.* **90**, 015005 (2018).
39. D. Hou, Z. Qiu, E. Saitoh, Spin transport in antiferromagnetic insulators: progress and challenges. *NPG Asia Mater* **11**, 35 (2019).
40. J. Li, C. B. Wilson, R. Cheng, M. Lohmann, M. Kavand, W. Yuan, M. Aldosary, N. Agladze, P. Wei, M. S. Sherwin, J. Shi, Spin current from sub-terahertz-generated antiferromagnetic magnons. *Nature*, 1–5 (2020).
41. P. Vaidya, S. A. Morley, J. van Tol, Y. Liu, R. Cheng, A. Brataas, D. Lederman, E. del Barco, Subterahertz spin pumping from an insulating antiferromagnet. *Science* **368**, 160–165 (2020).
42. I. Boventer, H. T. Simensen, A. Anane, M. Kläui, A. Brataas, R. Lebrun, Room-Temperature Antiferromagnetic Resonance and Inverse Spin-Hall Voltage in Canted Antiferromagnets. *Phys. Rev. Lett.* **126**, 187201 (2021).
43. H. Wang, Y. Xiao, M. Guo, E. Lee-Wong, G. Q. Yan, R. Cheng, C. R. Du, Spin Pumping of an Easy-Plane Antiferromagnet Enhanced by Dzyaloshinskii--Moriya Interaction. *Phys. Rev. Lett.* **127**, 117202 (2021).
44. R. Lebrun, A. Ross, S. A. Bender, A. Qaiumzadeh, L. Baldrati, J. Cramer, A. Brataas, R. A. Duine, M. Kläui, Tunable long-distance spin transport in a crystalline antiferromagnetic iron oxide. *Nature* **561**, 222–225 (2018).
45. T. Devolder, G. Talmelli, S. M. Ngom, F. Ciubotaru, C. Adelmann, C. Chappert, Measuring the dispersion relations of spin wave bands using time-of-flight spectroscopy. *Phys. Rev. B* **103**, 214431 (2021).

2 CHAPTER 2: THEORY OF FERRO- AND ANTIFERRO- MAGNETS

In this thesis, our exploration focuses on understanding the magnetization dynamics in two distinct types of materials. We begin our investigation with the types of materials most extensively studied in magnonics: Ferromagnets. Having revealed several interesting physical phenomena in ferromagnets, our exploration now extends to investigate other materials, namely, antiferromagnets. Henceforth, this chapter is structured into two parts: ***section 2.1*** *covers the theoretical approaches applied to ferromagnets, while* ***section 2.2*** *is dedicated to Antiferromagnets. To conclude this chapter, we will list the main mechanisms of spin transport in* ***section 2.3****, which have been experimentally investigated in the later chapters.*

2.1 FERROMAGNETISM:

In this first section, we will introduce the essential theoretical tools necessary for studying the dynamics of magnetization in ferromagnetic materials. Our attention will be directed towards solving the equation of motion of the magnetization, starting from the uniform precession case, and progressing towards uncovering the rich dispersion relations that ferromagnets possess. The dispersion of spin wave modes in thin films will be explained and supported by the theory proposed by Kalinikos and Slavin (*1*,*2*) in the dipole exchange regime.

2.1.1 The magnetic state and the Curie-Weiss Law of Ferromagnetism:

Each electron has a spin, for which a magnetic moment is associated. An atom on the other hand, is a collection of electrons, having a total magnetic dipole moment $\boldsymbol{m}$ defined as:

$$\boldsymbol{m} = -\gamma_j \boldsymbol{j}$$

(Eq. 2-1)

where:

- $\boldsymbol{j}$ is the total angular momentum.
- $\gamma_j = \frac{g|e|}{2m_e}$ is the gyromagnetic ratio, with g is the Landé factor, e and m_e are the charge and the mass of an electron respectively.

A material is a collection of atoms, each possessing magnetic moments of varying directions and magnitudes. For this reason, a micromagnetic approach is employed, wherein the material is treated as a continuous medium(*3*). Therefore, the magnetic state of a system is characterized by the magnetization vector $\boldsymbol{H}$ which is a continuous vector field defined as the density of magnetic moments:

$$\boldsymbol{M} = \frac{\sum_V \boldsymbol{m}}{V}$$

(Eq. 2-2)

The response of the magnetization $\boldsymbol{M}$ to an external field $\boldsymbol{H}$, determines the class of the

material. This response can be described by the susceptibility tensor χ defined as(*4*):

$$\boldsymbol{M} = \chi \boldsymbol{H}$$

(Eq. 2-3)

where for diamagnetic materials, χ is a negative scalar and therefore indicating that the magnetization acts in a way opposing to the effect of the magnetic field. On the other hand, for paramagnetic materials, χ is positive, indicating here that the unpaired spins of the electrons within the material align parallel to the external magnetic field $\boldsymbol{H}$, resulting in a net magnetic moment $\boldsymbol{M}$.

Ferromagnets are materials for which $\chi \gg 0$ (in a linear approximation, for isotropic materials) and $\boldsymbol{M}$ depends on the history of $\boldsymbol{H}$. Furthermore, in a ferromagnet a spontaneous magnetization $\boldsymbol{M}$ can exist even in the absence of an external magnetic field $\boldsymbol{H}$ and leading to a long-range magnetic order, yet the relationship of ***(Eq. 2-3)***, remains more complex.

The magnetization of a ferromagnet (without anisotropy terms, described later) is given by the following expression:

$$M = N g \mu_b J B_J(x)$$

(Eq. 2-4)

$B_J(x)$ is the Brillouin function and it describes the dependency of the magnetization on the applied field and on the total angular momentum quantum number J, and x stands for the ratio of the Zeeman energy of the magnetic moments in a medium with an applied magnetic field over the thermal energy and is given by:

$$x = \frac{g \mu_b J}{K_B T} H$$

(Eq. 2-5)

According to Weiss (*5*), one can introduce the concept of internal fields in the material where molecules mutually influence their neighboring moments. Therefore, we can define the molecular field as:

$$\boldsymbol{H}_m = \Lambda \boldsymbol{M}$$

(Eq. 2-6)

where Λ is the molecular field constant. In the presence of an applied field one can write:

$$\boldsymbol{H} = H_{ext} + \Lambda \boldsymbol{M}$$

(Eq. 2-7)

And therefore, the **Weiss-Curie law** gives:

$$\chi = \frac{M}{H} = \frac{C}{T - \theta}$$

(Eq. 2-8)

In this case, we can calculate a critical temperature, called the Curie temperature T_C, above which the ferromagnet behaves as a paramagnetic, and below which the material is in its ferromagnetic state.

In this thesis, the ferromagnetic materials under study are garnets, mainly Yttrium Iron Garnet (*6*), which is in reality, a ferrimagnet. However, on the scales of the micromagnetic description of the studied phenomena, these materials will be treated as ferromagnets.

2.1.2 Magnetic interactions:

The magnetic ordering of a magnetic material arises from the competition between the different energy terms present in the system. In a ferromagnet of finite shape and dimensions, there exist several types of interactions between the spin and its surroundings. In the following we will list the major energies contributing in the expression of the total energy of the system and leading to study the magnetization dynamics.

A. Magnetic anisotropy:

Most magnetic materials are found to be anisotropic, which, by definition, means that their magnetic properties depend on the direction in which they are measured. There are many types of anisotropy, such as magneto-crystalline, magneto-elastic, shape (magnetostatic), and surface anisotropy. The anisotropies mainly discussed in the context of this thesis will focus on magneto-crystalline and magnetostatic anisotropies.

- **Magnetocrystalline anisotropy:**

This magnetocrystalline anisotropy originates from the spin-orbit interaction of electrons. Electron orbitals are linked to the crystallographic structure, and through their interaction with spins, they cause the spins to prefer alignment along well-defined crystallographic directions, known as easy directions or easy axes. Conversely, the non-preferred directions of alignment, for which achieving saturation magnetization costs the most energy, are defined as hard axes. Therefore, the energy cost of this anisotropy can be regarded as the amount required to rotate the spin system far from the easy axis of magnetization, in other words, the energy needed to overcome spin-orbit coupling.

- ***Uniaxial anisotropy***

If there is a unique preferred direction, the anisotropy is uniaxial, and its energy term depends on the angle between the magnetic ordering and the preferred direction. It can be

expressed in even power series of $\sin\theta$ (θ being the angle between the magnetization and the preferred axis) and takes the following form:

$$F_k = K_1 \sin^2\theta + K_2 \sin^4\theta + \cdots$$

(Eq. 2-9)

where, K_1 and K_2 are the first and second-order anisotropy constants, respectively, representing temperature-dependent energy densities that approach zero at the critical temperature for magnetic ordering (*4*).

To express its corresponding effective field, it is more convenient to use directional cosines defined as:

$$\alpha_i = \frac{M_i}{M_s} \; ;$$

$$\alpha_1 = sin\theta cos\varphi \qquad \alpha_2 = sin\theta sin\,\varphi \qquad \alpha_3 = cos\theta$$

(Eq. 2-10)

where M_i is the component of the magnetization $\boldsymbol{M}$ along the i-th axis of the anisotropy coordinate system ($\boldsymbol{u}_1, \boldsymbol{u}_2, \boldsymbol{u}_3$), M_s is the saturation magnetization, θ the angle between $\boldsymbol{M}$ and the preferred axis and φ is the in-plane angle.

Therefore, for an anisotropy along $\boldsymbol{u_3}$ one can express ***(Eq. 2-9)*** as:

$$F_k = K_1\left(1 - \left(\frac{M_3}{M_s}\right)^2\right) + K_2\left(1 - \left(\frac{M_3}{M_s}\right)^2\right)^2 + \cdots$$

(Eq. 2-11)

Therefore, for $\boldsymbol{M}$ // $\boldsymbol{u}_3$ the effective anisotropy field is (*7*):

$$\boldsymbol{H}_u = \frac{2K_1}{\mu_0 M_s}\boldsymbol{u}_3$$

(Eq. 2-12)

- ***Cubic Anisotropy:***

For cubic systems, the energy favors the alignment of magnetization along any of the three orthogonal axis of the cubic referential. The cubic anisotropy has the following general expression:

$$F_{k_c} = K_c(\alpha_1{}^2\alpha_2{}^2 + \alpha_2{}^2\alpha_3{}^2 + \alpha_3{}^2\alpha_1{}^2)$$

(Eq. 2-13)

where K_c is the cubic anisotropy constant.

❖ **The shape anisotropy: Magnetostatic (or dipolar) energy:**

This interaction originates from the interaction of a magnetic moment with the field created by another magnetic moment i.e., the dipolar coupling between magnetic moments, that is a long-range interaction.

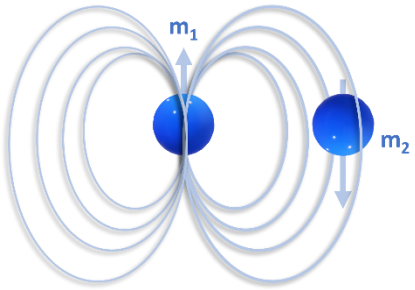

Figure 2-1: Shape anisotropy illustration: *The magnetization of 1 acts as an exterior field felt by 2.*

This interaction, as its name indicates, takes the shape of the studied sample under consideration. Discontinuities in magnetization at the edges of the sample create poles that generate a dipolar field radiating on both sides of the interface. Within the magnetized material, this field opposes the magnetization $\boldsymbol{M}$, which is why it is referred to as the demagnetizing field $\boldsymbol{H_d}$, that is in turn responsible for the existence of magnetic domains.

As a result, the dipolar energy takes the following form:

$$F_d = -\mu_0 \int \boldsymbol{M}.\boldsymbol{H_d}$$

(Eq. 2-14)

B. The exchange interaction:

Exchange energy is the origin of the ferromagnetic ordering, it is the interaction between neighboring spins that tends to align them parallel to each other. Similar to electrostatic energy, there is an energy cost to the system when two charges of the same sign are close to each other, but the effect is opposite when they are apart. Here this energy is called the exchange energy and is defined as:

$$F_{ex} = \frac{A_{ex}}{M_S^2} \int |\nabla \boldsymbol{M}|^2 dV$$

(Eq. 2-15)

where A_{ex} is the exchange constant expressed in J/m, giving the coupling intensity between the interacting spins. It is positive in the case of a ferromagnet, i.e., the spins align parallel to each other. If A_{ex} < 0, the spins will align anti-parallel to each other leading to an

antiferromagnetic ordering. Moreover, this interaction is a short-range interaction, it allows to define a characteristic length scale called the exchange length where the exchange energy dominates the magnetostatic energy.

$$\Lambda = \sqrt{\frac{2A_{ex}}{\mu_0 M_s^2}}$$

(Eq. 2-16)

For a ferrimagnet like YIG, Λ is about 17 nm whereas for a ferromagnet like permalloy NiFe it is about 5 nm.

- ***Superexchange:***

In the context of this thesis, we investigate insulating magnetic oxides, where the magnetic behavior emerges from the interactions between the magnetic moments associated with iron ions. The exchange interaction is of very short range, and in these systems, direct exchange interactions between neighboring magnetic ions are often hindered by the presence of non-magnetic oxygen ions that separate them. Consequently, this interaction is not straightforward and, in a sense, has a longer range, hence the term "super".

The mechanism of superexchange is understood through quantum mechanics, focusing on the hopping processes of electrons through intermediate non-magnetic sites. To illustrate this hopping process (***Figure 2-2***), let's consider a linear chain on which the atoms are aligned. Superexchange is defined as an indirect exchange interaction between magnetic ions that are not neighboring each other. This interaction is facilitated by the hybridization of the 2p orbitals of non-magnetic oxygen atoms with the 3d orbitals of a ferromagnetic 3d transition metal(*8*) . Due to the Pauli exclusion principle, antiferromagnetic ordering is preferred, allowing for the complete delocalization of electrons throughout the entire system. In fact, in the case of an AFM coupling the ground state as shown in ***Figure 2-2.*** **a)** can mix with excited states **b-c)**, meaning that the electron can be delocalized along the Fe-O-Fe chain and therefore lowering the kinetic energy.

In contrast, ferromagnetic ordering would impede electron hopping between the iron atoms as shown in ***Figure 2-2.*** **b-c-d)**, the excited states are states that are not permitted by Pauli principle. However, under specific, yet rare, circumstances and depending on the crystal lattice arrangement, ferromagnetic superexchange may be favored.

The superexchange strength is highly sensitive to the nature of the intermediate non-magnetic atoms and the specific arrangement of the crystal lattice. The energy of the superexchange process depends on the overlap of the electron orbitals involved, the distance between magnetic ions, and the characteristics of the intervening non-magnetic atoms(*8* ,*9*).

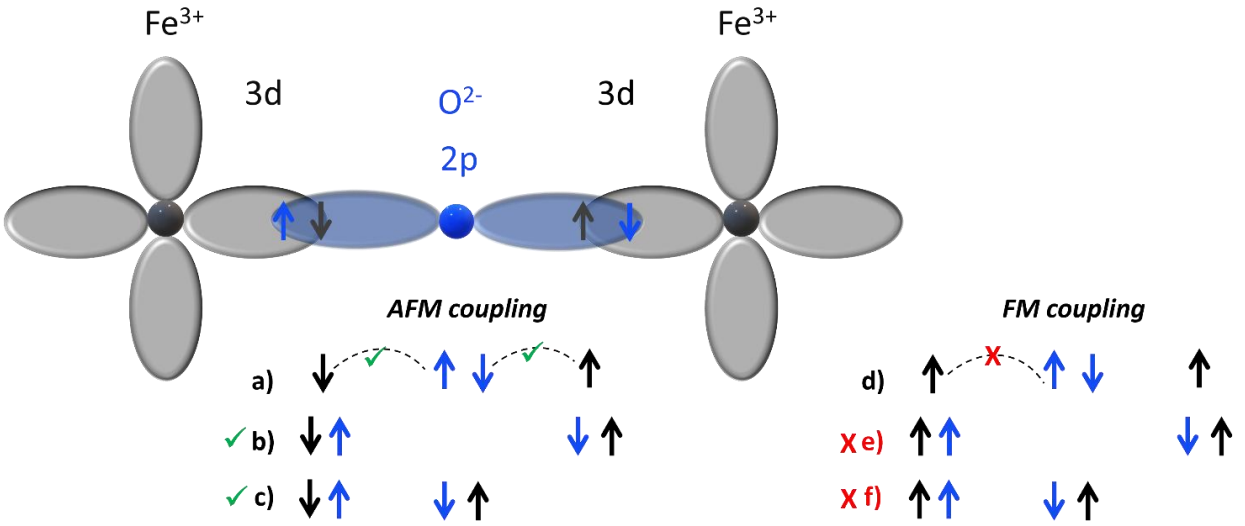

Figure 2-2: Superexchange principle: *Example of superexchange between the 3d and 2p orbitals of Fe and O atoms respectively.* ***a-b-c)*** *represent the case when the magnetic moments of the transition metal are aligned antiparallel (AFM coupling) where* ***a)*** *is the ground state configuration and* ***b-c)*** *are the permitted excited states for which the electrons can be delocalized.* ***d-e-f)*** *represent the case where the magnetic moments are aligned parallel (FM coupling). In this configuration the excited states* ***e-f)*** *are not allowed due to Pauli exclusion principles.*

C. The Zeeman interaction:

When a ferromagnet is subjected to an exterior field $\boldsymbol{H_{ext}}$, its magnetization will tend to align along the direction of this field through the Zeeman energy:

$$F_{Zeeman} = -\mu_0 \int \boldsymbol{M} \cdot \boldsymbol{H_{ext}}\, dV$$

(Eq. 2-17)

where $\mu_0 = 4\pi \times 10^{-7}\, H/m$ is the magnetic permeability and dV is the unit volume.

2.1.3 The equation of motion and the Landau-Lifshitz equation:

Having introduced the interactions present in the system, one can define its total energy:

$$F_{Total} = F_{Zeeman} + F_{ex} + F_d + F_K$$

(Eq. 2-18)

We obtain the equilibrium state by minimizing the total energy. This condition can be re-written in function of an effective magnetic field $\boldsymbol{H_{eff}}$, which considers all the interactions described above at each point of the system such as:

$$\mu_0 \boldsymbol{H_{eff}} = -\nabla_{\boldsymbol{M}} F_{Total}$$

(Eq. 2-19)

The dynamical response of the magnetization can then be described by the following equation given by Landau and Lifshitz in 1935(*10*):

$$\frac{\partial \boldsymbol{M}}{\partial t} = -\gamma \boldsymbol{M} \times \boldsymbol{H_{eff}}$$

(Eq. 2-20)

where this equation means that the magnetization precesses about its local effective field.

One should note that the torque equation conserves the norm of the magnetization vector, and describes its dynamics at a constant energy such as:

$$\frac{d||\boldsymbol{M}||^2}{dt} = 0 \quad and \quad \frac{d(\boldsymbol{M}.\boldsymbol{H_{eff}})}{dt} = 0$$

(Eq. 2-21)

These equations describes a uniform precession of the magnetization which is following a sphere with a radius equal to M_s.

- ***Linearizing the equation of motion:***

To linearize the equation of motion, we will consider several assumptions.

1. The effective field is written as a sum of a static component and a dynamic component. We assume that the static exterior field is parallel to the z-axis and that all the variations in space and time happens in the dynamic components such as:

$$\boldsymbol{H_{eff}}(\boldsymbol{r}, t) = \boldsymbol{H}_{eff_0} + \boldsymbol{h}(t)$$

(Eq. 2-22)

2. Similarly, the magnetization is also decomposed into a static and a dynamic component:

$$\boldsymbol{M}(\boldsymbol{r}, t) = \boldsymbol{M}_0 + \boldsymbol{m}(t)$$

(Eq. 2-23)

3. A further assumption to be made on dynamic components:

$$|\boldsymbol{M}_0| \gg |\boldsymbol{m}(t)| \quad and \quad \boldsymbol{H}_{eff_0} \gg \boldsymbol{h}(t)$$

In such a way, the terms with $\boldsymbol{m} \times \boldsymbol{h}$ will be second order terms, and thus neglected. By replacing the linearized forms in the LL equation, we get:

$$\frac{\partial \boldsymbol{m}}{\partial t} = -\gamma \mu_0 \left[\boldsymbol{M_0} \times \boldsymbol{h} + \boldsymbol{m} \times \boldsymbol{H}_{eff_0}\right]$$

(Eq. 2-24)

To solve this equation, we consider uniform plane wave solutions (k=0) for the dynamic

components:

$$\boldsymbol{m}(t) = \boldsymbol{m}e^{i\omega t} \quad and \quad \boldsymbol{h}(t) = \boldsymbol{h}e^{i\omega t}$$

(Eq. 2-25)

These can be related by the following:

$$\boldsymbol{m}(t) = \chi_p \boldsymbol{h}(t)$$

(Eq. 2-26)

where χ_p is the complex magnetic susceptibility, called the Polder tensor.

We recall the static effective field:

$$\boldsymbol{H}_{eff_0} = \boldsymbol{H}_{ext} + \boldsymbol{H}_d + \boldsymbol{H}_k + \boldsymbol{H}_{ex} + \boldsymbol{H}_{k_c}$$

(Eq. 2-27)

In our case, and for the moment we neglect the exchange field contribution as long as the magnetization is spatially uniform (i.e. single domain structures). Subsequently the demagnetization field can be expressed via a tensor $\bar{N}$ as:

$$\boldsymbol{H_d} = -\bar{N}\boldsymbol{M}$$

(Eq. 2-28)

This tensor depends on the shape of the sample and has a trace that is equal to 1. In the case of an ellipsoid, this tensor becomes diagonal having:

$$\bar{N} = \begin{pmatrix} N_{xx} & 0 & 0 \\ 0 & N_{yy} & 0 \\ 0 & 0 & N_{zz} \end{pmatrix}_{x,y,z}$$

(Eq. 2-29)

If we have a thin film with normal z-axis:

$$N_{xx} = N_{yy} = 0 \;\; and \;\; N_{zz} = 1$$

One can also express the anisotropy field by a tensor, say $\bar{N}_{ani}$ and so the effective field can be re-written (in the magnetization frame) as:

$$\boldsymbol{H}_{eff_0} = \boldsymbol{H}_{ext} - \bar{N}_t^e \boldsymbol{M_0} = \boldsymbol{H}_{ext} - (\bar{N}^{\boldsymbol{e}} + \bar{N}_{ani}^e)\boldsymbol{M_0}$$

(Eq. 2-30)

where $\bar{N}^{\boldsymbol{e}}$ stands for tensor $\bar{N}$, written in the coordinate system of the magnetization $(\boldsymbol{e}_1, \boldsymbol{e}_2, \boldsymbol{e}_3)$ in which $\boldsymbol{M} \,//\, \boldsymbol{e}_3$.

We note that $\bar{N}_{ani}^e$ can be considered as the sum of the cubic anisotropy and uniaxial anisotropy tensors as: $\bar{N}_{ani} = \bar{N}_c + \bar{N}_u$

Regarding cubic anisotropy, its expression in its referential as well as the referential transformation remain complex, and a detailed calculation can be found in refs (*11*) and (*7*).

2.1.4 Ferromagnetic resonance and the Kittel law:

From the third assumption *3* of linearization, one can have that:

$$\boldsymbol{m} \cdot \boldsymbol{M} = 0$$

(Eq. 2-31)

Meaning that $\boldsymbol{m}$ is perpendicular to $\boldsymbol{M}$ in this case (where we recall $\boldsymbol{M}$ is taken to be aligned along $\boldsymbol{e}_3$ in the frame of magnetization).

Therefore, one can derive from ***(Eq. 2-24)*** a system of two equations in the $(\boldsymbol{e}_1, \boldsymbol{e}_2)$ plane:

$$\frac{\partial \boldsymbol{m}_{e1}}{\partial t} = -\omega_M N_{21}^e \, \boldsymbol{m}_{e1} - (\omega_H + \omega_M N_{21}^e)\boldsymbol{m}_{e2}$$

$$\frac{\partial \boldsymbol{m}_{e2}}{\partial t} = (\omega_H + \omega_M N_{11}^e \,)\boldsymbol{m}_{e1} + \omega_M N_{12}^e)\boldsymbol{m}_{e2}$$

(Eq. 2-32)

where,

$$\omega_H = \gamma(H_{ext} - N_{33}^e M_s) \quad and \quad \omega_M = \gamma M_s$$

(Eq. 2-33)

To solve such a system, we apply assumption 2, assuming a plane wave solution. The existence of such a solution is governed by a condition on ω, known as the **Kittel law** (*12*):

$$\omega = (\omega_H + N_{22}^e \omega_M)\,(\omega_H + N_{11}^e \omega_M) - \omega_M^2 N_{12}^e N_{21}^e$$

(Eq. 2-34)

The Kittel law expresses the ferromagnetic resonance frequency as a function of the external field as well as in the magnetic properties of the studied sample.

In the following, we will derive the form of the resonance frequency for two cases:

1) *No anisotropy; Isotropic thin film with a normal axis along z*

In this case:

$$\bar{N} = \begin{pmatrix} 0 & 0 & 0 \\ 0 & 0 & 0 \\ 0 & 0 & N_{zz} = 1 \end{pmatrix}_{x,y,z}$$

To get $\bar{N}^e$, one should do a coordinate transformation from $(\boldsymbol{x}, \boldsymbol{y}, \boldsymbol{z})$ to $(\boldsymbol{e}_1, \boldsymbol{e}_2, \boldsymbol{e}_3)$, the calculations can be found in *(7)*.

This results in:

$$\bar{N}_t^e = \begin{pmatrix} \sin^2\theta & 0 & -\sin\theta\cos\theta \\ 0 & 0 & 0 \\ -\sin\theta\cos\theta & 0 & \cos^2\theta \end{pmatrix}_{\boldsymbol{e}_1\boldsymbol{e}_2\boldsymbol{e}_3}$$

(Eq. 2-35)

Therefore, the resonance frequency is given by:

$$\omega = \omega_H \left(\omega_H + \omega_M \sin^2\theta\right)$$

(Eq. 2-36)

2) *Anisotropic thin film with a normal along z-axis and a uniaxial perpendicular anisotropy (along $\boldsymbol{e}_3$).*

In this case:

$$\bar{N}_t^e = (1 - \frac{H_u}{M_s}) \begin{pmatrix} \sin^2\theta & 0 & -\sin\theta\cos\theta \\ 0 & 0 & 0 \\ -\sin\theta\cos\theta & 0 & \cos^2\theta \end{pmatrix}_{\boldsymbol{e}_1\boldsymbol{e}_2\boldsymbol{e}_3}$$

(Eq. 2-37)

One can define the effective magnetization as:

$$M_{eff} = M_s - H_u$$

(Eq. 2-38)

The resonance then takes the same form as ***(Eq. 2-36)***, by replacing ω_M with $\omega_{M_{eff}}$:

$$\omega = \omega_H \left(\omega_H + \omega_{M_{eff}} \sin^2\theta\right)$$

(Eq. 2-39)

with: $\omega_{M_{eff}} = \gamma M_{eff}$

An important note is that, for this special case of anisotropy, equilibrium conditions on the equations of motion *(7)* lead to the conclusion that for a negative value of the effective magnetization the stable configuration of the magnetization is a an out of plane orientation from the sample of the thin film ($\theta = \frac{\pi}{2}$), for small magnetic fields. This means that the anisotropy in this case is strong enough to overcome the shape (in-plane) anisotropy of the thin film.

2.1.5 Spin waves: FM thin films in the dipole-exchange regime

Ferromagnetic resonance, as we described in the previous section, applies to a wavevector $\boldsymbol{k} = \boldsymbol{0}$. A wave of a precessing magnetization at a frequency ω and a wave vector $\boldsymbol{k}$ is called a **spin wave**. It can be pictured as a chain of non-uniform oscillations of spins at the same

frequency f, but with a dephasing the one between to the other, and hence creating a wave, propagating in the material with group velocities much lower than the speed of light. In this sense, the wave is now described by a propagating ($\boldsymbol{k} \neq \boldsymbol{0}$) plane wave solution:

$$\boldsymbol{m}(\boldsymbol{r}, t) = \boldsymbol{m}_0(\boldsymbol{r}) e^{(\boldsymbol{K}\cdot\boldsymbol{r} - i\omega t)}$$

(Eq. 2-40)

When the wavelengths are relatively larger than the exchange length, dipolar interactions dominate in the system and taking into account magnetostatic approximations is required to determine the dispersion relation of the spin wave.

However, this approximation loses its validity when the wavelength becomes relatively comparable to the exchange length. Therefore, the effect of exchange interaction in the system should be considered. This consideration is accompanied by including boundary conditions governed by spin pinning on the surface of the magnetic film. Kalinikos and Slavin conducted extensive calculations, determining solutions for both isotropic ferromagnets in 1986 (*1*) and later extending the theory for anisotropic ferromagnets in 1990 (*2*).

Here, we will focus in our study on a film with a thickness t in the xy-plane with a width w. Both the magnetic field $\boldsymbol{H}$ and magnetization $\boldsymbol{M}$ are aligned parallel to each other and within the plane of the film. We recall the angle φ is the in-plane angle of the rotation of the magnetization frame with respect to the frame (x, y, z).

Therefore, the wavevector $\boldsymbol{k}$ have an in-plane component K_p and an out-of-plane component κ_m. The out-of-plane component is quantized owing to the finite thickness of the film and the wavevector is therefore written as:

$$k^2 = {K_p}^2 + {\kappa_m}^2$$

(Eq. 2-41)

where κ_m is the wavevector of the m-th thickness mode.

For the in-plane component, if we were in a case where $w >> t$, we can consider the width of the film as infinite and therefore:

$$\boldsymbol{K}_p = k_x^2 + k_y^2$$

(Eq. 2-42)

However, when considering a defined width, the k-vector gets confined as well along the width, if we consider the direction of the width is along y, and the width confinement order n, one can therefore write:

$$\boldsymbol{K}_p = k_x^2 + k_{y,n}^2$$

(Eq. 2-43)

Therefore, the quantization conditions on the wavevector $\boldsymbol{k}$ reads:

$$k_{y,n} = \frac{n\pi}{w} \; ; \; n = 1,2,3 \ldots \text{ and } \; \kappa_m = \frac{m\pi}{t} \; ; m = 0,1,2 \ldots$$

The dispersion relation in this case is written as:

$$\omega = \sqrt{(\omega_H + \Lambda^2 \omega_M k^2)(\omega_H + \Lambda^2 \omega_M k^2 + \omega_M F_{mm})}$$

(Eq. 2-44)

where:

- Λ is the exchange length.
- $F_{mm} \propto (P_{mm} sin^2 \varphi_p)$ with P_{mm} being the matrix elements related to the dipolar field with the prefix m indicating the thickness mode order, and φ_p ,the angle in the plane between $\boldsymbol{M}$ and $\boldsymbol{K}_p$; $\varphi_p = \varphi - \varphi_k$
  With $\varphi_k = arcos(\frac{k_x}{k_x^2 + k_y^2})$, the angle of $\boldsymbol{k}$ in (x, y, z).

  These matrix elements are defined as:

$$F_{mm} = P_{mm} + \sin^2\theta \left[1 - P_{mm}\left(1 - \cos^2\varphi_p\right) \frac{\omega_M P_{mm}(1 - P_{mm})\sin^2\varphi_p}{\omega_H + \Lambda^2 \omega_M k^2}\right]$$

(Eq. 2-45)

$$P_{mm} = \frac{K_p^2}{k^2}\left(1 - \frac{K_p^2}{k^2}\frac{2}{1 + \delta_{0m}}\frac{1 - (-1)^m e^{-K_p t}}{K_p t}\right)$$

(Eq. 2-46)

We recall that θ is the angle at which the magnetization is oriented, and for a film that is magnetized in-plane we have $\theta = 90°$.

- ***Note on thickness modes:***

In an unbound ferromagnet, the wave vector can take any value. However, for the case of thin films with a thickness *t*, the wavevector component along the confined axis (z-axis) becomes discretized. In such cases, the presence of spin-wave thickness modes is observed.

When the width of the structure is much larger than its thickness ($t << w$), no thickness modes can be formed, therefore $m = 0$. This implies that $K_p t << 1$ and thus:

$$P_{00} = P \approx \frac{1 - e^{K_p t}}{K_p t} \approx 1 - \frac{K_p t}{2}$$

(Eq. 2-47)

2.1.6 Damped oscillations and relaxation processes:

Until now, we have been considering a ferromagnet in its ideal state, where the magnetization

can precess without encountering any magnetic losses. However, this is not true for real systems. Therefore, it is necessary to account for energy dissipation, referred as the damping, in the system. Magnetic damping enables the magnetization to relax towards a saturated state. Thus, the equation of motion can be fully described by the Landau-Lifshitz-Gilbert equation(*13*,*14*), which phenomenologically includes a relaxation parameter called the Gilbert damping coefficient α:

$$\frac{\partial \boldsymbol{M}}{\partial t} = -\gamma \boldsymbol{M} \times \boldsymbol{H_{eff}} + \frac{\alpha}{M_s} \boldsymbol{M} \times \frac{d\boldsymbol{M}}{dt}$$

(Eq. 2-48)

and by using the plane wave solution**:**

$$i\omega m = -\gamma[\boldsymbol{M} \times \boldsymbol{h} + \boldsymbol{m} \times \boldsymbol{H}] + \boldsymbol{i}\omega \frac{\alpha}{M_s} \boldsymbol{M} \times \boldsymbol{m}$$

(Eq. 2-49)

Consequently, this additional torque results in a damped precessional motion of the magnetization around the effective field.

To find an analytical solution for the Landau-Lifshitz-Gilbert equation, we need to linearize the equation as done previously for the LL equation. This will yield in replacing $\omega_H \rightarrow \omega_H + i\alpha\omega$. Therefore ***(Eq. 2-32)*** is modified as:

$$0 = i\omega - \omega_M N_{21}^e \boldsymbol{m}_{e1} - (\omega_H + i\alpha\omega + \omega_M N_{21}^e)\boldsymbol{m}_{e2}$$

$$0 = (\omega_H + i\alpha\omega + \omega_M N_{11}^e)\boldsymbol{m}_{e1} + (i\omega + \omega_M) N_{12}^e \boldsymbol{m}_{e2}$$

(Eq. 2-50)

If we go back to ***(Eq. 2-26)***, the Polder tensor is defined by the following matrix:

$$\chi_p = \begin{bmatrix} \chi & i\chi_a & 0 \\ -i\chi_a & \chi & 0 \\ 0 & 0 & 0 \end{bmatrix}$$

where, χ and χ_a are the symmetric and antisymmetric elements and defined as:

$$\chi = \frac{\omega_M \omega_H}{\omega_H^2 - \omega^2}$$

$$\chi_a = \frac{\omega_M \omega}{\omega_H^2 - \omega^2}$$

(Eq. 2-51)

with $\omega_M = \gamma \mu_0 M_S$ and $\omega_H = \gamma \mu_0 H_0$.

Again, by considering $\omega_H \rightarrow \omega_H + i\alpha\omega$, the components of the of the susceptibility matrix will be complex, the calculations are found in (*11*) and (*7*) :

$$\chi(\omega) = \chi' + i\chi''$$

(Eq. 2-52)

$$\chi' = \frac{(\omega_H - \omega)\omega_M}{(\omega_H - \omega)^2 + (\alpha\omega)^2}$$

$$\chi'' = \frac{-\alpha\omega\omega_M}{(\omega_H - \omega)^2 + (\alpha\omega)^2}$$

(Eq. 2-53)

From these expressions, that are plotted in ***Figure 2-3***, one can notice that the imaginary part has a Lorentzian shape, with a maximum occurring at $\omega = \omega_H$, i.e. the FMR condition. On the other hand, the real part at this particular frequency is found to be zero, with a change in sign occurring as we move from values before to after the resonance point. In practice, the magnetic field is often swept at a fixed frequency, therefore one can determine the full width at half maximum of the resonance peak:

$$\Delta H = \frac{2\alpha\omega}{\gamma\mu_0}$$

(Eq. 2-54)

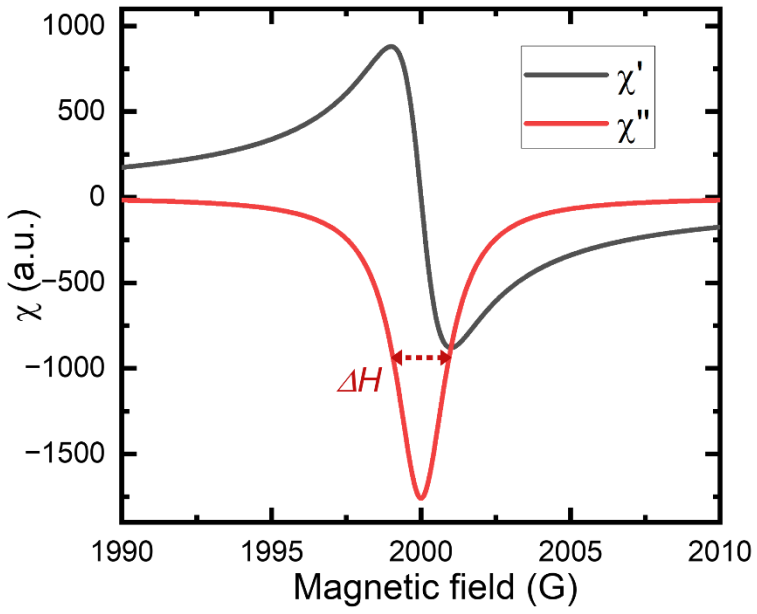

Figure 2-3: Magnetic susceptibility:*The susceptibility dependance on the swept magnetic field in presence of damping, representing the real (in black) and imaginary parts (in red), where a resonance peaks is shown at 2000 G, the parameters used are as for YIG with* $\alpha = 10^{-4}$, $M_s = 1750\ G$, $\frac{\gamma}{2\pi} = 28\ GHz/T$.

2.2 ANTIFERROMAGNETISM:

As we have seen so far, for a material to exhibit ferromagnetic behavior, the exchange constant J that characterizes the exchange interaction between two neighboring spins, with their magnetic moments aligned in the same direction, must be positive. Conversely, when J is negative, it signifies that the spins of adjacent atoms are antiparallel, resulting in a vanished net magnetization.

More specifically, for oxides, the negative J results from the super-exchange process mediated by ligand ions positioned between the magnetic ions. Henceforth, the material is called ***antiferromagnet*** (AFM) and was first discussed by Louis Néel *(18*).

In fact, in this class of materials, there exists a critical temperature called the Néel temperature (T_N), below of which antiferromagnetic materials exhibit ordered magnetic behavior (ordered phase). Above this temperature, the thermal energy disrupts the ordered arrangement of magnetic moments within the material, thus making this material a paramagnet. Below T_N, the magnetic moments of neighboring spins align antiparallel to each other, resulting in an absence of net macroscopic magnetization, and makes these materials resilient under exterior magnetic fields.

Despite extensive theoretical studies on antiferromagnets, their practical application initially seemed unpromising. A first turnaround in this concept was the discovery of the Giant Magnetoresistance Effect (GMR) by Albert Fert and Peter Grünberg in 1988, marking the birth of the field of spintronics. In GMR, the antiferromagnets role is hidden as they act as a passive layer to pin the direction of a ferromagnetic layer through the effect of exchange bias. In contrast, their counterparts ferromagnets play the main active role in the development of spintronic devices such as hard disk read-head, TMR sensors or more recently MRAM memories. However, antiferromagnets have intrinsically interesting properties that cannot be found ferromagnets. Notably, antiferromagnets are highly insensitive to external magnetic fields, they possess ultrafast dynamics enabling to operate within the THz frequency range and able to produce large magneto-transport effects (*19*). About 10 years ago, theory works (*23*,*24*) predicted that most of the spintronic phenomena could be adapted or extended to the different cases of antiferromagnetic systems. In 2016, a demonstration of electrical switching of antiferromagnetic CuMnA- devices (*23*) using Néel spin-orbit torque opened up the way for spintronic applications for AFMs and together with the advancements in experimental techniques pushed to the emergence and advances in antiferromagnetic spintronics.

In the following, we will introduce basic concepts regarding antiferromagnets and discuss the various interactions present in these materials, which are used to derive equations describing AF-resonance. Subsequently, we will focus on the specific case of canted antiferromagnets, specifically, Hematite. We will introduce the material and explore the modifications in the equations describing the spin dynamics in such systems.

2.2.1 Antiferromagnetic susceptibility:

Magnetic susceptibility is a measure of how much a magnetic field can control the magnetization of a material. It describes the response of the spins within the material in aligning themselves along the direction of an applied magnetic field, where this responsiveness depends on the temperature.

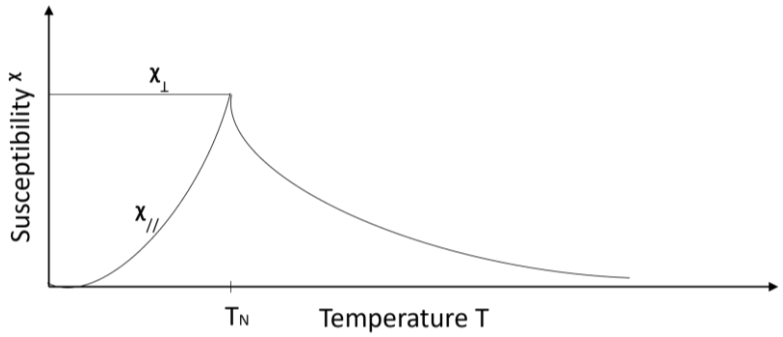

Figure 2-4: Illustration for the susceptibility variation with the temperature.

For AFMs, one needs to differentiate between two types of magnetic susceptibilities: the parallel susceptibility and the perpendicular susceptibility(*24*):

1. Parallel Magnetic Susceptibility, $\chi_{//}$: It describes the case when the external magnetic field is applied parallel to the easy axis of the AFM. The magnitude is small yet not negligible and is dependent about how strong the magnetic ordering is:

$$\chi_{//} = \frac{|M|}{H}$$

2. Perpendicular Magnetic Susceptibility, $\chi_{\perp}$: It describes the case when the external magnetic field is applied in a direction perpendicular to the easy axis. Its magnitude is usually greater than $\chi_{//}$. In this case the magnetic moments start to cant in the direction of the magnetic field by a small angle.

The temperature dependence of the susceptibility of an antiferromagnetic material can be represented by the Curie-Weiss law for the perpendicular susceptibility:

$$\chi_{\perp} = \frac{C}{T - \theta}$$

(Eq. 2-55)

where, C is the curie constant, T is the temperature and θ is the Weiss constant, and for antiferromagnets is negative.

2.2.2 Types of antiferromagnets:

Antiferromagnets, in contrast to ferromagnets, are more abundant in nature and can be found exhibiting various electric properties, such as insulators, semiconductors, metals, semimetals, or superconductors.

In metallic systems, energy losses and Joule heating effects arise from the motion of electrons and collisions, that are involved in spin transport mechanisms. This can be avoided in magnetic insulators, where electrons can be considered fixed in their atomic positions. An example of such materials is YIG, in which magnons can travel up to centimeter distances(*6*) without interacting with electrons. As shown by Kajiwara et al.(*25*), the possibility of spin transport via magnons positions magnetic insulators as promising candidates for realizing energy-saving information carrier devices with long propagation distances.

They are ordered magnetic materials where, in the absence of external fields, the spontaneous magnetization is either vanished or nearly equal to zero. In the latter case, the material can be considered a weak ferromagnet while maintaining antiferromagnetic ordering.

This ordering is linked to the exchange interactions of spins, which for antiferromagnets, are of important values, to push their antiparallel alignment. Due to these factors, magnetic moments within the crystal lattice can be arranged in different configurations, resulting in a net magnetization that tends towards zero. Therefore, based on their magnetic structures and their spin orientations several types of antiferromagnets exist where we can list them into two categories:

A. Collinear antiferromagnets:

In collinear antiferromagnets, neighboring magnetic moments are aligning antiparallel to one another along a certain crystallographic axis (***Figure 2-5***). The magnetic ordering can therefore be represented by a Néel vector **n** in collinear AFMs, and they can be classified in three types according to their alignment direction in the crystallographic structure:

- **A-type:** The magnetic moments within a specific spin plane are coupled ferromagnetically, meaning they tend to align in the same direction within that plane. Whereas, between neighboring spin planes, the magnetic moments are coupled antiferromagnetically, meaning they point in opposite directions in adjacent planes.

- **C-type:** Oppositely to the A-type, here, adjacent magnetic moment, within a given plane are coupled antiferromagnetically. Whereas, the coupling between planes is ferromagnetic, with neighboring planes exhibiting parallel magnetic moments.

- **G-type:** this type is the combination of both A- and C- types. In this case, both the coupling within each plane and between neighboring planes are antiferromagnetic. The magnetic moments are antiparallel both within a plane and between planes.

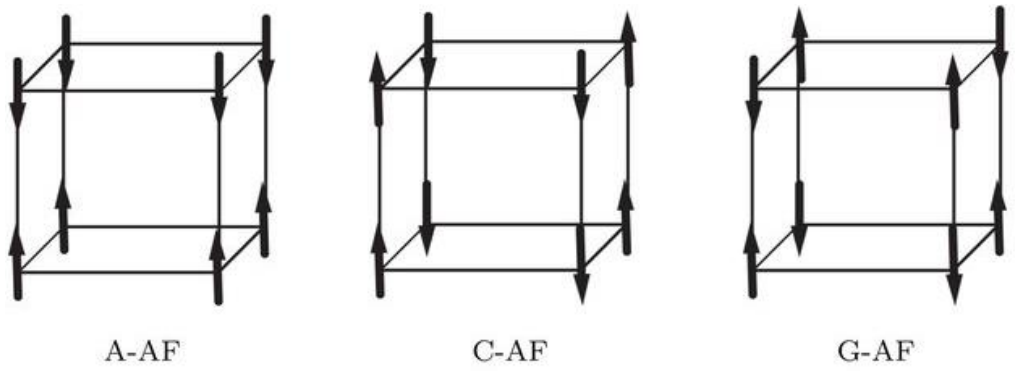

Figure 2-5: Types of collinear AFMs: *Figure from ref. (26), showing the arrangement of the magnetic moments and spin orientation in the three types of AFM.*

In presence of magnetic anisotropy such as the magneto-crystalline anisotorpy, the Néel vector can have a preferred direction resulting in two main families of collinear antiferromagnets, namely: ***Easy-axis*** and ***Easy-plane*** AFMs. In the first case, the magnetic moments tend to align preferably along the direction of a specific axis while for the easy-plane case, the magnetic moments tend to align preferentially within a plane.

B. Non-collinear antiferromagnets:

Unlike collinear antiferromagnets, there exists another type where the magnetic moments in this case do not align along a specific axis. In certain scenarios, there may be a deviation in the alignment of spins, causing the angle between neighboring spins to slightly differ from π. This misalignment leads to a canting of the magnetic moments, resulting in a small spontaneous magnetization and giving weak ferromagnetic behavior to the material, the reason why these types of materials are referred as «*weak ferromagnets*». This type of AFMs, the spin texture is more complicated than in the collinear case as we can find materials with spiral magnetic ordering such as $BiFeO_3$ (*28*), or antiferromagnetic skyrmions(*29, 30*). These emerges as hot topics in AFM spintronics by having the potential to serve as information carriers for advancing beyond CMOS technology and neuromorphic applications. However, and within the scope of this thesis, as a first step in this field, we aim to demonstrate proof of concepts of spin wave propagation in a simple antiferromagnetic case. For this reason, our focus will be on the case of Hematite (α-Fe_2O_3) above the Morin transition (described later), so that the measurements can be performed at room temperature in its easy-plane canted phase (***Figure 2-6.*** **a)**).

More complex non-collinear antiferromagnets exist, as for the case for some cubic and hexagonal - Mn_3X types or some antiperovskite (represented by Mn_3AN). An example for this, is given in ***Figure 2-6.*** **b)** of a cubic Mn_3Sn is shown, with a long range triangular antiferromagnetic order.

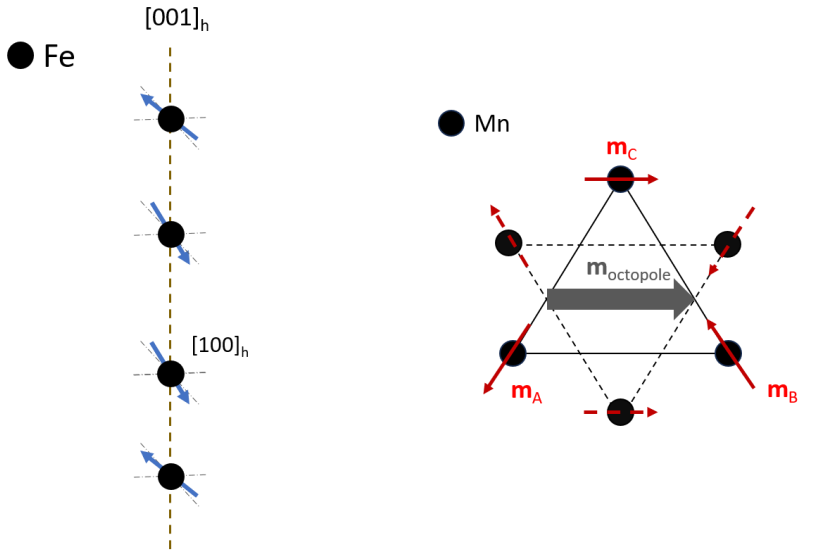

a) *α-Fe_2O_3 : canted easy-plane phase*

b) *Mn_3Sn with triangular magnetic ordering*

Figure 2-6: Magnetic moments orientation non-collinear AFM: *a) Hematite in the canted easy plane phase, the magnetic moments lie in the basal plane [100] perpendicular to the [001] , b) illustration of a triangular magnetic ordering in Mn_3Sn.*

In this type of AFMs, studies represent the magnetic ordering in this type of AFM using multipole moments (*31*) rather than the Neel ordering as in collinear AFM. Therefore, we can find many properties rising from their band structure topologies, as those found in FM, particularly due to the time-reversal symmetry breaking. Among these effects are as the ones found in FM; the large anomalous Hall effect (*32*), anomalous Nernst effect (*33*), the magneto-optical Kerr effect (*34*), all of which are crucial for providing information on the AFM state.

2.2.3 Weiss-like model of Antiferromagnetism:

Now for an antiferromagnetic system, Néel developed the Weiss model to cover antiferromagnets. To proceed, it suffices to represent the system as two interpenetrating sublattices, labeled as 1 and 2. Each sublattice possesses a total magnetization denoted as $\boldsymbol{M_1}$ and $\boldsymbol{M_2}$, respectively, such as: $\boldsymbol{M} = \boldsymbol{M_1} + \boldsymbol{M_2}$, with $\boldsymbol{M_1} = -\boldsymbol{M_2} = |\boldsymbol{M}|$. The closest neighboring magnetic moments (as in ***Figure 2-7***) are located on the opposite sublattice.

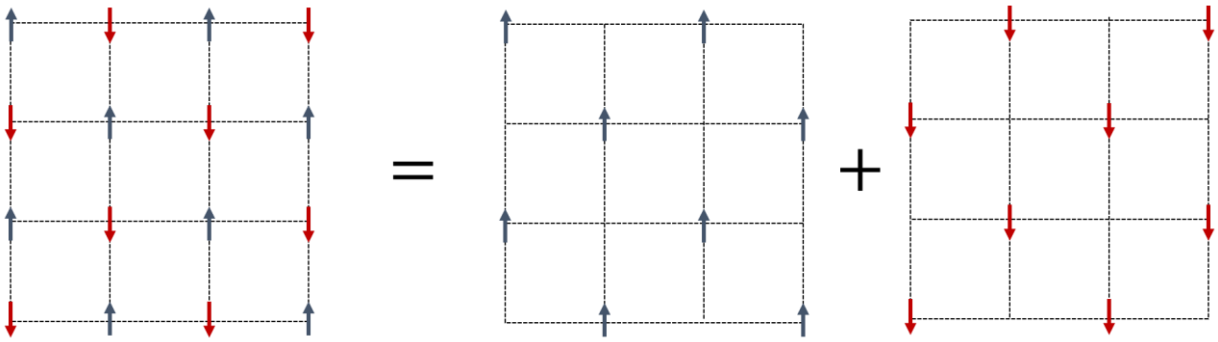

Figure 2-7: Antiferromagnet can be considered as two interpenetrating sublattices.

We will assume that the molecular field acting on one sublattice is directly proportional to the magnetization of the other sublattice. Therefore, we can define the molecular field over N sublattices as:

$$H_{m_j} = \sum_{i=1}^{N} \Lambda_{ji} M_i$$

(Eq. 2-56)

So, for sublattice 1 and 2:

$$\mathbf{H}_{m_1} = \Lambda_{11}\boldsymbol{M}_1 + \Lambda_{12}\boldsymbol{M}_2$$

$$\mathbf{H}_{m_2} = \Lambda_{21}\boldsymbol{M}_1 + \Lambda_{22}\boldsymbol{M}_2$$

(Eq. 2-57)

In presence of an exterior field one can write:

$$\mathbf{H}_1 = \mathbf{H}_{ext} + \mathbf{H}_{m_1}$$

$$\mathbf{H}_2 = \mathbf{H}_{ext} + \mathbf{H}_{m_2}$$

(Eq. 2-58)

By utilizing the two equations mentioned earlier and applying the first order terms approximation of $B_J(x)$, one can derive linear equations in terms of $\boldsymbol{M}_1$ and $\boldsymbol{M}_2$. For antiferromagnets, there exists a temperature, called the Néel temperature T_N, at which the sublattice magnetization approaches zero due to thermal fluctuations. Above this temperature, the material exhibits paramagnetic behavior. Consequently, the application of a small magnetic field induces a small magnetic moment aligned along that field. Therefore, for $T > T_N$, the induced moment $\boldsymbol{M}$ can be written as:

$$\boldsymbol{M} = \frac{N g^2 \mu_B^2 J(J+1)}{6 K_B T}[2\boldsymbol{H} + (\Lambda_{11} + \Lambda_{12})\boldsymbol{M}]$$

(Eq. 2-59)

Hence, we can find, from the Curie-Weiss law *(**section 2.1.1**)*, the paramagnetic temperature of an antiferromagnet θ as:

$$\theta = -C(\Lambda_{11} - \Lambda_{12})$$

(Eq. 2-60)

In absence of external magnetic field, one can therefore similarly calculate the identical sublattice magnetization at the Neel temperature, and we find:

$$T_N = C(\Lambda_{11} - \Lambda_{12})$$

(Eq. 2-61)

Below the Néel temperature, each of the sublattices have a spontaneous magnetization $\boldsymbol{M_1}$ and $\boldsymbol{M_2}$, that vary with the temperature, as for a ferromagnet. However, for all temperature the total magnetization ($\boldsymbol{M} = \boldsymbol{M_1} + \boldsymbol{M_2}$) is always vanishing due to the opposite orientations. As consequence, a parameter called the staggered magnetization, defined as the difference between the magnetizations on each sublattice $\boldsymbol{M_1} - \boldsymbol{M_2}$, becomes non-zero at temperatures below T_N. This staggered magnetization serves as an order parameter for antiferromagnets and is known as the Neel vector, $\boldsymbol{n}$.

2.2.4 Origin of weak ferromagnetism:

As previously mentioned, a specific type of antiferromagnets exists wherein the net magnetization does not fully vanish and therefore classifying the material as a weak ferromagnet while retaining its antiferromagnetic properties. This is mainly the case of antiferromagnetic crystals like α-Fe_2O_3 and in manganese (Mn) and cobalt (Co) carbonates. The origin of such behavior remained not entirely understood and initial explanation for this weak antiferromagnetism was attributed by Néel to impurity effects (*35*) and later on to antiferromagnetic domains walls magnetization (*36*). Thereafter, Dzyaloshinskii (*37*) developed a phenomenological argument based on a thermodynamic theory, using Landau's second-order phase transitions. He concluded that in the absence of an applied magnetic field, when $\boldsymbol{M_1}$ and $\boldsymbol{M_2}$ lie along the [111] axis, there would be no ferromagnetism (State I). On the other hand, when $\boldsymbol{M_1}$ and $\boldsymbol{M_2}$ lie in the (111) plane, the basal plane, the magnetic moments would be rotated from π by a small angle of about 10^{-4} rad (State II), proportional to D/H_E, and therefore the system will choose the state at which the energy is the lowest at a given temperature. In this context, the Dzyaloshinskii canting energy is expressed in the mean field approximation as:

$$F_{DMI} = -\boldsymbol{D}.\boldsymbol{M_1} \times \boldsymbol{M_2}$$

(Eq. 2-62)

However, this argument of Dzyaloshinskii, did not address the origins of this interaction nor provide a method for calculating the parameter D. This was due to the fact that previous theories did not consider the anisotropic superexchange. In 1960, Moriya developed a theory covering the microscopic origin of the canting of moments(*38*), by using the formalism developed by Anderson in 1959 of the superexchange interactions (*8*). He explained that this interaction originates from spin-orbit coupling of two magnetic ions mediated by a nonmagnetic atom, which is the definition of the antisymmetric exchange interaction (superexchange). He eventually showed that D has the form of:

$$D \sim \left(\frac{\Delta g}{g}\right) J$$

(Eq. 2-63)

where $\Delta g (= g - 2)$ is the contribution of the orbital moment to the g-factor (*8*).

Moreover in ***(Eq. 2-62)***, $\boldsymbol{D}$ is a vector lying along a high symmetry axis. This interaction is

therefore called the Dzyaloshinskii-Moriya interaction, and it exists in materials where the ions are coupled via superexchange with a broken inversion of symmetry within the unit cell of the material. As a result, in cases where the magnetic moments are perpendicular to $\boldsymbol{D}$, this interaction causes the magnetic moments to cant with a small angle between them, leading to the rise of a small net magnetic moment. In cases where the magnetic moments $\boldsymbol{M}_1$ and $\boldsymbol{M}_2$ are parallel to $\boldsymbol{D}$, the Dzyaloshinskii-Moriya field has no effect on them, and therefore, no canting of the moment takes place.

Another aspect to note is that in materials with no breaking of the inversion symmetry, no DMI exists. For example, in Cr_2O_3, which has the same $R\bar{3}c$ crystal structure as Fe_2O_3 but with an inversion of symmetry with respect to the center between the two Cr ions, there is no Dzyaloshinskii-Moriya interaction.

2.2.5 The equations of motion: Adapted LLG equation for Antiferromagnets.

When dealing with ferromagnets, we introduced the equation of motion that describes magnetization dynamics using the Landau-Lifshitz-Gilbert equation. This equation can be adapted analogously for antiferromagnets, which involve a two-sublattice system represented by the index *j*. Therefore, one can write:

$$\frac{\partial \boldsymbol{M}_j}{\partial t} = \gamma_j \boldsymbol{M}_j \times \boldsymbol{H}_{eff,j} + G_j$$

(Eq. 2-64)

where, G_j is the Gilbert damping term:

$$G_j = \frac{\alpha_j}{M} \boldsymbol{M}_j \times \frac{\partial \boldsymbol{M}_j}{\partial t}$$

(Eq. 2-65)

and γ_j is the magneto-mechanical ratio, different in general for different sublattices. On the other hand, the damping factor α_j can be considered similar for all the sublattices as $\alpha_j = \alpha$

To linearize these equations, we express the magnetizations and effective fields as the sum of steady and ac components, similar to what was done for ferromagnets (***section 2.1.3***). We then substitute the linearized forms of $\boldsymbol{H}_{eff,j}$ and $\boldsymbol{M}_j$ into ***(Eq. 2-64)***. A note to take into account is that the ac components of the magnetization $\boldsymbol{m}_j$ are a linear function of the ac exterior field and are linked via a susceptibility tensor $\vec{\vec{\chi}}$, therefore the total ac magnetization can be written as:

$$\boldsymbol{m} = \sum_{j=1}^{N} \boldsymbol{m}_j = \vec{\vec{\chi}} \boldsymbol{h}$$

(Eq. 2-66)

Assuming that the ac component is small compared to the steady components, we obtain, in

a zero approximation, the steady-state condition given by:

$$\boldsymbol{M}_j \times \boldsymbol{H}_{eff,j} = 0$$

(Eq. 2-67)

while in the first approximation, the system of 2 linear equations for the complex amplitudes given as (*11*):

$$i\omega \boldsymbol{m}_j + \gamma_j \boldsymbol{m}_j \times \boldsymbol{H}_{eff,j} + \gamma_j \boldsymbol{M}_j \times \boldsymbol{h}_{eff,j} + \frac{i\alpha_j \omega}{\boldsymbol{M}_j} \boldsymbol{m}_j \times \boldsymbol{M}_j = -\gamma_j \boldsymbol{M}_j \times \boldsymbol{h}$$

(Eq. 2-68)

with h being the ac amplitude of the external field.

2.2.6 Antiferromagnetic resonance:

The theory of antiferromagnetic resonance was independently developed by Kittel(*39*) and Nagamiya (*40*) at the beginning of the 1950's and it was further extended by Keffer and Kittel in 1952 (*41*). In this section we will solve the equation of motion to find the resonance frequencies in an AFM. First let us list the energy terms taken into account in the effective field expression which in turn is given by:

$$H_{eff} = -\frac{\partial F}{\partial \boldsymbol{M}}$$

(Eq. 2-69)

where the total free energy F is the sum of the following terms:

$$F = Exchange + Zeeman + Anisotropy$$

(Eq. 2-70)

- **The exchange energy:**

$$F_E = -J_{Exc} \boldsymbol{M}_1 . \boldsymbol{M}_2$$

(Eq. 2-71)

where J_{Exc} is the exchange coupling strength.

- **The Zeeman energy:**

When an external field is applied, it adds up an important interaction with the magnetization, that is the Zeeman interaction given by:

$$F_H = -\boldsymbol{H} . (\boldsymbol{M}_1 + \boldsymbol{M}_2)$$

(Eq. 2-72)

- **The anisotropy:**

The energy term associated to the magnetocrystalline anisotropy is expressed as in (***Eq. 2-9***),

but adapted here for the two sublattice model. If we take the case of a hexagonal structure with the z-axis being the axis of anisotropy (c-axis) we can therefore write:

$$F_k = K_1 (\sin^2 \theta_1 + \sin^2 \theta_2) + K_2(\sin^4 \theta_1 + \sin^4 \theta_2)$$

(Eq. 2-73)

with $K_2 \ll K_1$, and θ_1 and θ_2 are the angles that $\boldsymbol{M}_1$ and $\boldsymbol{M}_2$ make with the preferred axis, respectively.

By energy minimization, the uniaxial anisotropy is mainly determined according to the sign and values of K_1 and K_2 .The most commonly possible configurations for AFM are associated with easy-axis (K_1>0) or easy-plane anisotropies (K_1<0).

An additional contribution from the basal plane crystalline anisotropy can come into play in ***(Eq. 2-73)*** This is achieved by considering a higher-order term in K, denoted as K_3. For hexagonal structures, it is expressed as a sixth-order term, and thus, the magnetocrystalline energy becomes:

$$F_k = K_1 (\sin^2 \theta_1 + \sin^2 \theta_2) + K_2(\sin^4 \theta_1 + \sin^4 \theta_2) + K_3(\sin^6 \theta_1 \cos 6\varphi_1 + \sin^6 \theta_2 \cos 6\varphi_2)$$

(Eq. 2-74)

where φ_1 and φ_2 are the angles from some crystallographic axis in the basal plane, and it is considered that $K_3 << K_2 << K_1$.

A specific case arises when magnetic moments are canted, due to the presence of DMI, and we will specifically focus on the canted easy-plane case. Note that as discussed in ***section 2.1.2A*** for ferromagnets, anisotropy terms in antiferromagnets can take various forms. In our case we can limit ourselves to the major contribution of the magnetocrystalline anisotropy solely.

Finally, the total energy can be written as:

$$F_k = -J_{Exc}\boldsymbol{M_1}.\boldsymbol{M_2} - \boldsymbol{H}_{ext}.(\boldsymbol{M_1} + \boldsymbol{M_2}) + K_1 (\sin^2 \theta_1 + \sin^2 \theta_2) + K_2(\sin^4 \theta_1 + \sin^4 \theta_2) + K_3(\sin^6 \theta_1 \cos 6\varphi_1 + \sin^6 \theta_2 \cos 6\varphi_2)$$

(Eq. 2-75)

Since $K_2 << K_1$, we will only limit ourselves to the second order term of the anisotropy ($K = K_1$.), to describe the key features of the easy-axis and easy-plane cases. We also neglect the basal plane anisotropy.

Consequently, the effective field:

$$H_{eff} = -J_{Exc}\boldsymbol{M}_{2,1} + \boldsymbol{H}_{ext} + \frac{K}{M^2} M_{1,2_Z}\boldsymbol{z}$$

(Eq. 2-76)

where $\boldsymbol{M}$ is the net magnetization.

For the sake of simplicity, we will use in the following the mean field representation for each term as:

$$H_E = -J_{exc}M \qquad H_A = \frac{K}{M}$$

(Eq. 2-77)

A. Easy-axis antiferromagnets:

For an easy-axis AFM, $K > 0$, and the preferred axis is the c-axis. Now we need to find the angles at which we have a minimal energy, in other words, the derivative of the total energy ***(Eq. 2-75)*** with respect to θ_1 and θ_2 is equal to zero. One therefore gets the following equation (*11*):

$$-J_{Exc}\mathrm{M}^2 \sin(\theta_{1,2} - \theta_{2,1}) + -H_{ext}\mathrm{M}\sin(\theta_H - \theta_{2,1}) + K \sin\theta_{1,2}\cos\theta_{1,2} = 0$$

(Eq. 2-78)

where $M = |\boldsymbol{M}_1| = |\boldsymbol{M}_2|$ and θ_H is the angle that the magnetic field makes with the easy axis.

Two cases of the applied field can be considered:

1. The field is applied parallel to the easy-axis, therefore from energy minimization one gets a condition on the angles as:

$$\cos\theta_{//} = \frac{H_{ext}}{2H_E - H_A}$$

(Eq. 2-79)

with, $\theta_2 = \theta_1 = \theta_{//}$.

2. The magnetic field is applied in plane, perpendicular to the easy axis, we get from ***(Eq. 2-78)***:

$$\sin\theta_{\perp} = \frac{H_{ext}}{2H_E + H_A}$$

(Eq. 2-80)

with, $\theta_2 = \theta_1 = \theta_{\perp}$.

In the both cases, this means that the angle between the two antiferromagnetic sublattices decreases with an increasing applied field until it reaches a moment where both are parallel. This happens when the external field energy (Zeeman energy) has completely overpassed the exchange energy keeping the sublattices antiparallel to one to the other. This transition is therefore called the «*spin flip*».

Now to find the resonance frequency equations, we project the linearized equation of motion onto the coordinate axes, and we take into account the effective field equation. In order to

find the eigenfrequencies, the determinant of the obtained system of equations is set to zero, and for α =0 we get two eigenfrequencies ω_1 and ω_2.

In ***Figure 2-8***, we illustrate the transitions for the case of an easy axis AFM. In case 1, we consider the magnetic moments, starting from an antiparallel state, aligned on the easy- axis at a low applied field H_{ext} illustrated by $H_{//}$ as shown in (a). For this state, the resonance frequencies are found to be (*11*) :

$$\omega_{1,2} = \gamma(H_c \pm H_{ext})$$

(Eq. 2-81)

where for most antiferromagnets, it can be assumed that $H_E >> H_A$, and therefore H_C is given by:

$$H_C = \sqrt{2H_E H_A}$$

(Eq. 2-82)

From these resonance equations, one can notice that at zero applied field, the resonance in an easy-axis AFM exists and can have relatively high values. For example, a resonance of 135 GHz for Cr_2O_3 (*42*) can be obtained. Or even up to 1 THz as observed in NiO with an easy plane anisotropy (*43*, *44*). This is in contrast, for a ferromagnet like YIG, for which a resonance frequency 30 GHz would require an applied field of 1 T.

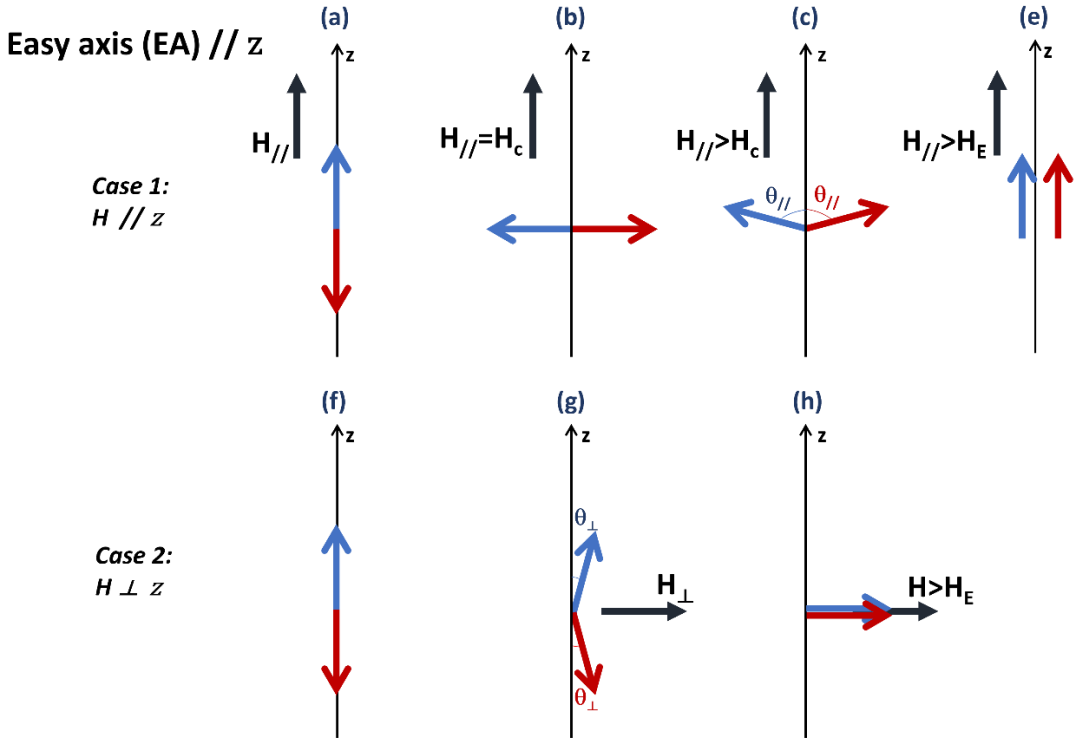

Figure 2-8: Spin flop and spin flip in the case of an easy axis antiferromagnet.

Upon increasing the magnetic field, the angle between the magnetizations $\boldsymbol{M}_1$ and $\boldsymbol{M}_2$ decreases. At some value of the field, $H_{//} = H_c$, and before the spin flip, the angle between

the magnetic moments and the applied field reaches 90° (shown in (b)). This phase transition is a first order transition and is called «*spin flop*» (*45*). In this case the, $\omega_2 = 0$. By surpassing H_c, the angle $\theta_{//}$ keeps decreasing (as in (c)). The eigenfrequencies of the excited magnons are therefore:

$$\omega_1 = \gamma\sqrt{H_{ext}^2 - H_c^2}$$

(Eq. 2-83)

$$\omega_2 = 0$$

(Eq. 2-84)

As $\theta_{//}$ reaches 0, the magnetic moments align parallel to each other and parallel to the applied field (shown in (e)) ; this is the spin flip transition and it happens as $H_{ext} \approx H_E$(*11*).

The magnon dispersion for the case of an easy-axis antiferromagnet is therefore below and above the spin slip field H_c is therefore presented in ***Figure 2-9***.

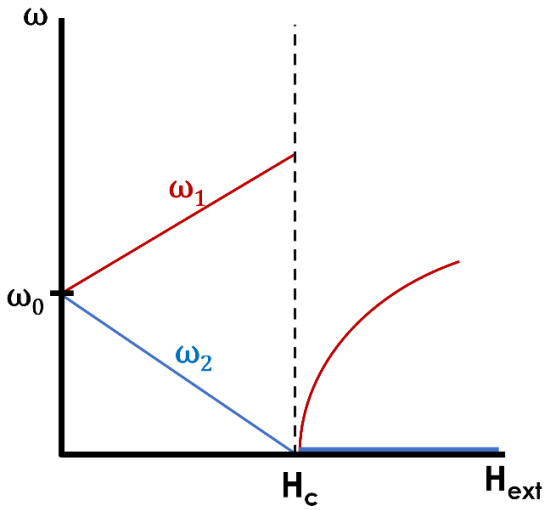

Figure 2-9:Magnon dispersion for an easy axis AFM.

Another scenario happens, shown in ***Figure 2-10*** in case 2, when the applied magnetic field is applied in plane, perpendicular to the antiparallel magnetic moments that are aligned along the easy axis. In this case the angle between $\boldsymbol{M}_1$ and $\boldsymbol{M}_2$ decreases gradually with growing applied field (as shown in (g)), therefore the resonant frequencies are given by (*11*):

$$\omega_1 = \gamma\sqrt{H_c^2 + H_{ext}^2}$$

(Eq. 2-85)

$$\omega_2 = \gamma\sqrt{H_c^2 - \frac{H_A}{H_E}H_{ext}^2}$$

(Eq. 2-86)

Henceforth at $H_\perp \approx H_E$ the magnetic moments are aligned parallel and towards H_{ext}(as in (h)).

B. Easy-plane antiferromagnets:

For K<0, the sublattices magnetization $\boldsymbol{M}_1$ and $\boldsymbol{M}_2$ now lie within the basal plane. Here H_A is negative, therefore with $|H_A| << H_E$, we can approximate ***(Eq. 2-75)*** to:

$$\sin\theta_\perp = \frac{H_{ext}}{2H_E}$$

(Eq. 2-87)

Here, for the calculation of the eigenfrequencies, the in-plane anisotropy is considered very weak in front of the out of plane and therefore neglected.

When H_{ext} is directed out of the easy plane, the results of this case of AFM, are similar to the easy axis AFM above the spin flop, as presented in ***Figure 2-10***, case 1.

However, when the field is applied in plane, a new case rises where the magnetic moments cant toward the in-plane field until that they reach the spin flip and align parallel to H_{ext} as shown in case 2 of ***Figure 2-10*** (where H_{ext} is denoted by ***H***).

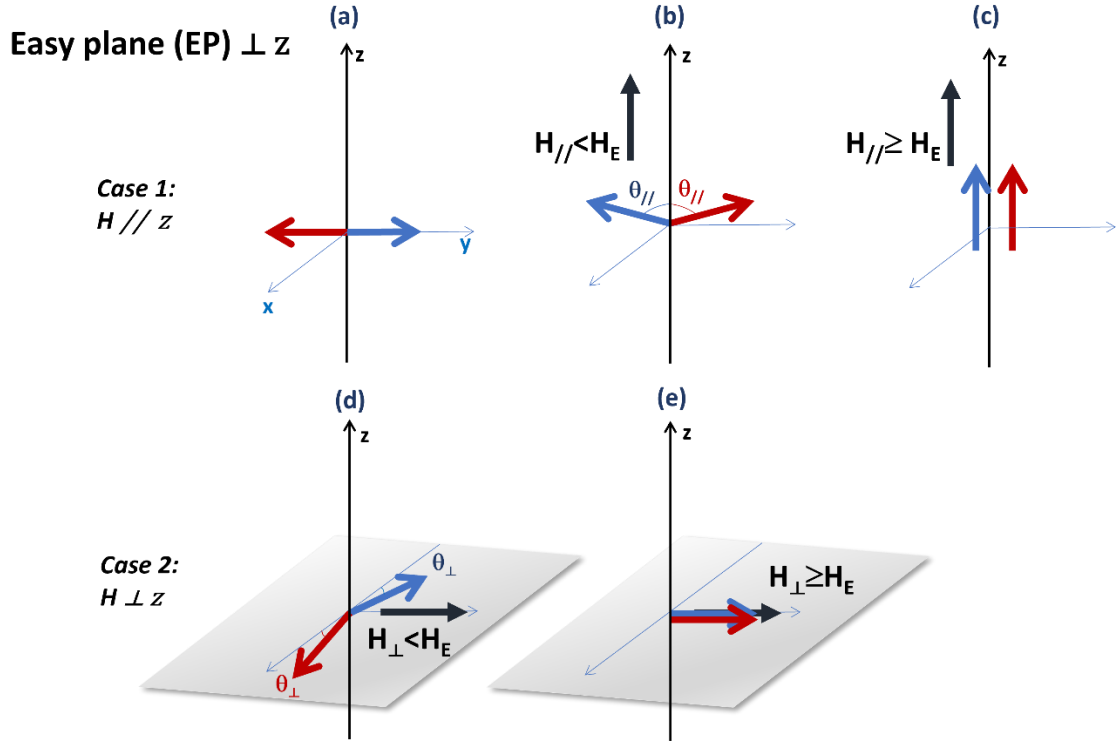

Figure 2-10: Spin flip and spin flop in an easy plane antiferromagnet.

Thereby, with the same approach used in the previous section we can proceed to find the solution of the equation of motion. At fields lower than the spin flip as in **case 2-(d)** of ***Figure***

2-10, one gets two resonance frequencies given by (*11*) :

$$\omega_1 = \gamma H_{ext}\sqrt{1+\frac{|H_A|}{2H_E}}$$

$$\omega_2 = \gamma\sqrt{2H_E\,H_A - \frac{|H_A|}{2H_E}\,H_{ext}^2}$$

(Eq. 2-88)

One can notice that the expression for ω_1 becomes zero in the absence of an applied field. However, this not true in reality, as the calculations neglect the term related to in-plane anisotropy. Moreover, this mode is excited by the transverse component of ac magnetic field (with respect to $\boldsymbol{H_{ext}}$, which is directed along the y-axis). While ω_2 is excited by a longitudinal part of the ac magnetic field (parallel to $\boldsymbol{H_{ext}}$)

C. Canted antiferromagnets:

Consider now that in our antiferromagnet there exists a DMI field that induces a weak moment. Therefore, the energy from DMI ***(Eq. 2-62)*** should be added to the total free energy. In this case, by replacing H_{ext} by $(H_{DMI}+H_{ext})$ and by considering $H_{DMI}^2 + H_{ext}H_{DMI} \sim H_{DMI}^2$, the low frequency mode can be written as:

$$\omega_1 = \gamma\sqrt{H_{ext}(H_{DMI}+H_{ext})}$$

(Eq. 2-89)

However, in order to derive a more general expression that incorporates basal plane anisotropy, magnetostriction, and second-order anisotropy, the total free energy can be generalized for both the canted easy-plane and canted easy-axis phases. In this sense, and for the sake of simplicity, if one do not take the hexagonal terms of the anisotropy but only the bi-axial terms, anisotropies (within the easy-plane) can be defined by two types:

1. An easy-plane anisotropy, which occurs in the basal plane (the sixth order term with K_3 in ***(Eq. 2-75)***) and is aligned along the y-axis, described by a field $H_{aniso-in}$.

2. A hard-axis anisotropy aligned along the c-axis (i.e., z-axis) and described by a field $H_{aniso-out}$ (terms with K_1 and K_2 in ***(Eq. 2-75)***)

   Therefore, the total free energy now writes:

$$F_T = M[H_E(\boldsymbol{m_1}\cdot\boldsymbol{m_2}) - \boldsymbol{H_{DMI}}\cdot(\boldsymbol{m_1}\times\boldsymbol{m_2}) + \frac{H_{aniso-out}}{2}\left(m_{1_z}^2 + m_{2_z}^2\right) - \frac{H_{aniso-in}}{2}\left(m_{1_y}^2 + m_{2_y}^2\right) - \boldsymbol{H}\cdot(\boldsymbol{m_1}+\boldsymbol{m_2})]$$

(Eq. 2-90)

This equation can be generalized for both phases. It has been developed in the letter from *I*.

Boventer et al. (*46*) by considering the two phases where; below the Morin temperature (canted easy-axis antiferromagnet with $H_{aniso-out}$ = 0) as well as above the Morin temperature (canted easy-plane antiferromagnet with $H_{aniso-out} >> H_{aniso-in}$).

By solving the LLG equation as in the reference (*11*), it turns out that two resonance frequencies exist (*46*):

A circularly polarized low frequency mode, for which the ac magnetic field is perpendicular to the magnetization direction:

$$\omega_{10} = \gamma\sqrt{H_E H_{aniso-in} + H(H_{DMI} + H_{ext})}$$

(Eq. 2-91)

and a linearly polarized high frequency mode, for which the ac magnetic field aligns with the magnetization direction:

$$\omega_{20} = \gamma\sqrt{H_E(H_{aniso-out} + H_{aniso-in}) + H_{DMI}(H_{DMI} + H_{ext})}$$

(Eq. 2-92)

with γ is gyromagnetic ratio.

Therefore, the in-plane anisotropy consideration here, shows non-vanishing resonance frequencies in the absence of an applied field. We notice that, in this case, the low frequency mode energy gap depends on the in-plane anisotropy $H_{aniso-in}$ and the exchange field H_E , while the higher frequency mode gap depends on the exchange, the DMI, the in-plane and the out of plane anisotropy. This explains the high frequency values of resonance for such mode.

D. Summarizing on the different magnon modes:

In the easy-axis AFM, as discussed, the magnetic field breaks the magnon mode degeneracy when applied along the easy axis (and below the spin flop). In this situation, magnetic moments of the two sublattices, can exhibit either left or right-handed circular precession (*41*) , as depicted in ***Figure 2-11. a)***.

In the case of the easy-plane AFM, we observed that even without an applied field, two non-degenerate magnon modes can exist. For the low-frequency mode, magnetic moments undergo highly elliptical motion within the basal plane, while for the high-frequency mode, the precession axis is out of plane (*47*,*48*). This implies that the Néel vector exhibits a linear precession, carrying vanishing spins on average as the magnetic moments precess with opposite chiralities (*49*). Both mode precessions are illustrated in ***Figure 2-11. b)***.

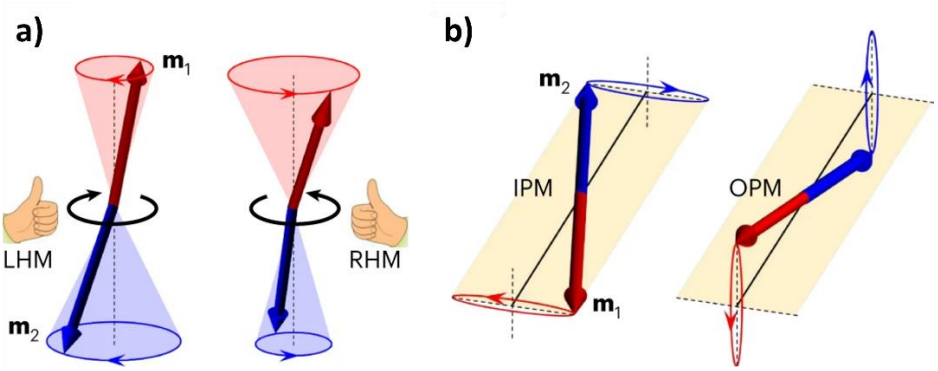

Figure 2-11: Magnon modes precession modes: *a) The sublattice magnetization m1 and m2 in an easy axis AFM undergo an circular precession in left or right handed chirality. b) m1 and m2 undergo linear precession in an easy-plane AFMand showing the in plane precession mode and the out of plane mode. Figure is extracted from ref (*50*)*

Finally, for the canted easy-plane phase, the low-frequency magnon mode undergoes circularly polarized precession, while the high-frequency mode undergoes linearly polarized precession as depicted in ***Figure 2-12***:

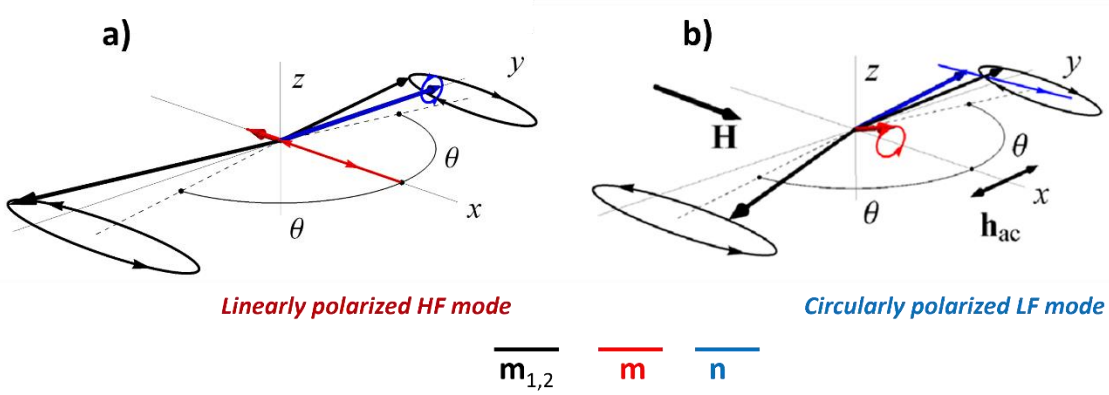

Figure 2-12: Precession modes in a canted easy plane AFM : *a) the low-frequency modes. b) the high-frequency modes. The sublattice magnetizations are indicated by black arrows, while the normalized magnetization and Néel parameter are represented by red and blue arrows, respectively. Figure adapted from ref (46).*

2.2.7 Spin waves in antiferromagnets:

Theoretical exploration of antiferromagnetic spin-wave dynamics, including both long and short wavelengths (including dipole-exchange modes), was extensively studied in the last decades(*51*) due to the emerging interests in antiferromagnetic materials. However, in normal antiferromagnets the frequency range of the spin-waves lies within the THz and sub-THz region (*52*,*53*) which complicate their detection as well as the difficulty integrating them in magnonic devices.

In canted antiferromagnets, as shown in **(*Eq. 2-91*)**, and upon application of a magnetic field,

two magnon modes exist . Moreover, dipolar effects can potentially induce a change in the dispersion relation and give rise to non-degenerate magnon modes for some direction of propagating spin-waves. This gives the possibility to detect them by electrical means as we will show in **Chapter 5**, where we focus on the specific case of Hematite. For this aim, interests are shifted towards canted antiferromagnets with dipolar interactions, where many theoretical works developed models for magnetostatic spinwaves in antiferromagnets with dipolar interactions(*54*, *55*) .

In neglection to dipolar effects, to determine the spinwaves dispersion, always in the two-sublattice model, to determine the spin waves dynamics in the case where the propagation vector $\boldsymbol{k} \neq \mathbf{0}$, in a similar fashion of what have been done in ferromagnets, one can substitute the magnetization in the LLG equation by a plane wave solution. The spinwaves dispersion relation can be generalized as (*51*):

$$\omega_1 = \sqrt{\omega_{10}^2 + c^2 k^2} \qquad and \qquad \omega_2 = \sqrt{\omega_{20}^2 + c^2 k^2}$$

(Eq. 2-93)

where $\omega_{10,20}$ are the AFMR frequencies and c is the phase velocity whose value does not depend on propagation direction.

2.2.8 Magneto-static spin-wave in canted antiferromagnets:

This section is developed by Prof. Olena Gomonay from Johannes Gutenberg University of Mainz.

In presence of dipolar effects as for the case of canted antiferromagnets, the following modifications of spin wave modes are possible (*56*, *57*).

First, the oscillations of the Néel vector induce a nonzero magnetization in the material which leads to a lift of the degeneracy of the bulk spin-wave modes (see **section A**). When this dynamic magnetization is oriented perpendicular to the sample surface, surface modes might also appear (see **section B**). When this happens, the origin of the surface mode is the magnetostatic dipolar field where it should vanish outside the film and penetrate into the sample until a finite length. In case of the canted antiferromagnets, additional contributions into the spectra can appear due to oscillations of the nonzero magnetic moments.

A. Bulk magnon spectra :

Here we focus on calculating the bulk magnon spectra of easy-plane canted antiferromagnets. The external magnetic field $\boldsymbol{H}_{ext}$ is applied parallel to the easy plane, perpendicular to equilibrium orientation of the Néel vector $\mathbf{n}_0$ ($\boldsymbol{H}_{ext} \perp \boldsymbol{n}_0$). We consider the DMI field $\boldsymbol{H}_{DMI}$ aligned along z-axis of unit vector $\boldsymbol{z}$.

When dipolar effects are not considered one can write the magnetization as:

$$\boldsymbol{m_0} = \frac{H_{DMI}\boldsymbol{z} \times \boldsymbol{n}_0 + \boldsymbol{H}_{ext}}{H_E}$$

(Eq. 2-94)

Now, to include magnetostatic effects, we need to calculate magnon spectra by solving coupled equations for fluctuations of the Néel vector and the potential of dipole field ψ (*56*, *58*). Here, we will focus on the dipolar effects that modify magnon spectra compared to ***(Eq. 2-93)***. In canted antiferromagnets, the dipolar effects appear due to nonzero magnetization originating from:

1) Canting of the magnetic sublattices that is due to DMI field and external magnetic field :

$$\boldsymbol{m}_{can} = \frac{H_{DMI}\boldsymbol{z} \times \boldsymbol{n} + \boldsymbol{H}_{ext}}{H_E}$$

(Eq. 2-95)

2) Dynamic magnetization due to oscillations of the Neel vector:

$$\boldsymbol{m}_{dyn} = \boldsymbol{n} \times \dot{\boldsymbol{n}}/(\gamma H_E)$$

(Eq. 2-96)

Following a similar development as the ones performed for ferromagnets(*59*), we can determine the effects of dipolar effects on the spin-wave spectra of canted antiferromagnets.

The Néel vector can oscillate in plane or out of plane of the sample. In the former case, this leads to an out of plane magnetization $\boldsymbol{m}_{dyn}$, therefore upon propagation perpendicular to the magnetic field, $\boldsymbol{m}_{dyn}$can create surface charges leading to surface waves. This is a mode that we have experimentally measured and will be shown and discussed in detail in Chapter 4. One should notice that out-of-plane mode dynamic magnetization oscillates in the easy-plane, and thus in the sample plane for a c-plane crystal as studied later, and thus contributes only into the bulk mode for $\boldsymbol{k} \perp \boldsymbol{n}_0$ ($\boldsymbol{H}_{ext}//\boldsymbol{k}$). Contrary to ferromagnets, we can distinguish two orientations of the exterior magnetic field with respect to k by:

1. **Case of $\boldsymbol{k}//\boldsymbol{n}$, ($\boldsymbol{H}_{ext} \perp \boldsymbol{k}$):**

In this configuration, we have a contribution of the dipolar field into the gap for the bulk modes as:

$$f_{\boldsymbol{k}||\boldsymbol{n}_0} = \sqrt{f_{10}^2 + \left(\frac{1}{2\pi}\right)^2 \left[\frac{4\pi M_s}{H_E}\gamma^2(H_{ext} + H_{DMI})^2 + c^2k^2\right]}$$

(Eq. 2-97)

In this case magnetostatic (dipolar) contribution into the energy gap is proportional to oscillations of the canted magnetization (terms with DMI and magnetic field), but it is diminished (compared to ferromagnets) due to the small factor $\frac{4\pi M_s}{H_E}$

2. Case of $\boldsymbol{k \perp n_0}$, $(\boldsymbol{H_{ext}}//\boldsymbol{k})$:

In this configuration, the dynamic dipolar field can couple with both the in-plane and out-of-plane modes in presence of a non-zero k_z. We thus provide a more general expression of the bulk spin-wave dispersion for $\boldsymbol{H_{ext}}//\boldsymbol{k}$:

$$f^2_{\boldsymbol{k}\perp\boldsymbol{n}_0} = \frac{1}{2}\left(f_1^2 + f_2^2 + \frac{4\pi M_s}{H_E}(f_1^2 \sin^2\theta \ + f_2^2 \cos^2\theta)\right) - \frac{1}{2}\sqrt{\left[f_1^2 + f_2^2 + \frac{4\pi M_s}{H_E}(f_1^2 \sin^2\theta \ + f_2^2 \cos^2\theta)\right]^2 - 4\left(1 + \frac{4\pi M_s}{H_E}\right) f_1^2 f_2^2}$$

(Eq. 2-98)

where θ is the angle between the k-vector and the z-axis.

Due to the non-uniform radiofrequency magnetic field generated by the excitation rf-antenna over the sample thickness, a transverse component of k can exist. However, by considering a uniform thickness mode meaning, k_z=0 ,i.e., $\theta = \frac{\pi}{2}$, the expression of ***(Eq. 2-98)*** for the bulk mode with $\boldsymbol{k} \perp \boldsymbol{n}_0$ is then reduced to:

$$f_{\boldsymbol{k}\perp\boldsymbol{n}_0} = \left(1 + \frac{4\pi M_s}{H_E}\right)\sqrt{f_{10}^2 + \left(\frac{ck}{2\pi}\right)^2}$$

(Eq. 2-99)

This equation therefore shows a positive dispersion and is close to f_{10} at **k** = 0 Due to smallness of $\xi = \frac{4\pi M_s}{H_E} \ll 1$.

One should notice in ***(Eq. 2.99)*** that dipolar fields contribute to the energy gap and also support an inhomogeneous distribution of magnetization for non-zero k_z. This results in a softer dependence on f(k) and can lead to a negative group velocity at small k-values when k_z is nonzero (i.e., $\theta \neq \pi/2$). However, at larger k-values, dipolar fields are balanced by exchange interactions, favoring homogeneous ordering, and the dependence of $f(k)$ always shows a positive group velocity. In ***Figure2-13***, we present a graph representing non-zero k-values in the z-direction. In a bulk single crystal, numerous thickness modes can respond to an external excitation and they can also hybridize which can complexify the mode identification.

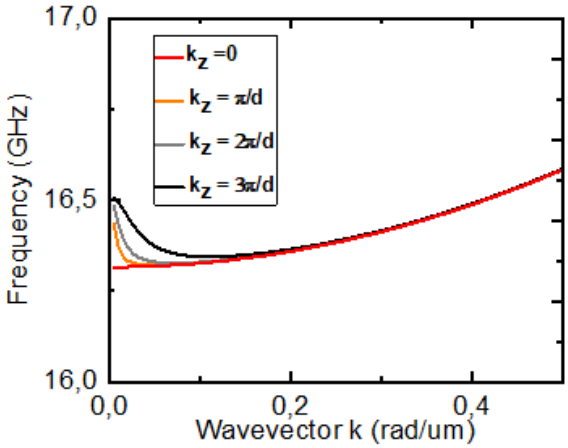

Figure2-13: *Frequency dispersion of $\boldsymbol{k} \perp \boldsymbol{n_0}$ modes with non-zero k_z = 0, indicating a non-uniform profile of the spin-wave mode within the bulk of the sample. The material parameters to compute these curves are for those of Hematite.*

- **Group velocity:**

In the limit of **k** vector within the center of the Brillouin zone, we determine the following group velocity for the **bulk** spin-wave modes:

$$v_g = \frac{c^2 k}{2\pi f(k;H)}$$

(Eq. 2-100)

where the frequency $f(k;H)$ of the spin-wave is given by the both configurations of ***(Eq. 2-97, 2-99)*** and depends on the magnetic field. For a fixed value of the **k**-vector, $f(k;H)$ increases with the field and hence the group velocity decreases.

B. Surface magnon spectra :

The presence of a dipolar field can also lead to the emergence of surface modes. In this scenario, an out-of-plane component of magnetization is required, which, in the case of c-plane crystal, arises from the dynamic magnetization arising from the cross product: $\boldsymbol{n} \times \dot{\boldsymbol{n}}$.

Although the oscillations of DMI-induced canted magnetization are consistently in-plane for this crystal orientation, they still contribute to the formation of the surface mode. Additionally, the stabilization of surface spin-waves necessitates a negative permeability within the bulk to prevent the penetration of magnetization oscillations into the sample's interior, which occurs due to the presence of a canted moment.

As such, surface in-plane modes are allowed, for any orientation of propagation vector within the plane. To model the system, we still follow the approach from Refs. (*56*, *58*) and use magnetostatic boundary conditions at one of the sample surfaces, while assuming that the sample is thick enough and that the influence of the other surface can be neglected. We then

obtain the following formula for the frequency of the surface mode for **k** // **n**:

$$f_{sur} = \frac{f_{10}^2 + \left(\frac{ck}{2\pi}\right)^2}{\frac{\gamma(H_{ext} + H_{DMI})}{\pi}} + \frac{\gamma}{4\pi}\left(1 + \frac{4\pi M_s}{H_E}\right)(H_{ext} + H_{DMI})$$

(Eq. 2-101)

where here, the z-component of vector $\boldsymbol{k}$ is imaginary.

- **Group velocity:**

In the limit of k vector within the center of the Brillouin zone, we determine the following group velocity for the bulk spin-wave modes, we can also determine the group velocity of the surface spin-wave modes:

$$v_g = \frac{c^2 k}{2\pi f_D + \gamma H}$$

(Eq. 2-102)

with, $f_D = \frac{\gamma H_{DMI}}{2\pi}$.

One can notice from this expression also that the surface spin-wave group velocities decrease as a function of the applied magnetic field.

2.2.9 Hematite: The case of a canted easy-plane antiferromagnet

Hematite is an insulating antiferromagnet and is composed solely of oxygen ions O^{2-} and trivalent iron atoms Fe^{3+}. It crystallizes in the corundum structure (α-Al_2O_3), which can be described as a hexagonal crystal structure, with lattice constants of a = 504 pm and c = 1375 pm. In this structure, oxygen ions are arranged in a hexagonal close-packed assembly, while two thirds of the octahedral sites are occupied by trivalent iron ions. The stacking sequence can thus be described in terms of alternating iron and oxygen layers stacked along the c-axis [001] as a –(Fe–O_3–Fe)– stack.

According to Néel (*60*), below a T_N = 963 K, α-Fe_2O_3 is antiferromagnetic with weak ferromagnetism. The high-spin d^5 Fe^{3+} cations within one bilayer in the (0001) planes (i.e., the basal plane) are ferromagnetically coupled to each other while antiferromagnetically coupled to the adjacent Fe bilayers (along the c-axis). The magnetic moment is determined to be 4.6 μ_B per atom.

At temperatures below T_N, the magnetic moments lie within the basal plane (easy plane phase) and possess a small canting, resulting from the presence of an antisymmetric exchange interaction (bulk Dzyaloshinskii-Moriya interaction. This canting causes a net magnetic moment that is perpendicular to the antiferromagnetic order, the Néel vector, **n**.

However, below the Néel temperature, there exists a critical temperature known as the Morin

temperature, which was reported by Morin in 1950(*61*). This temperature marks the onset of a first-order spin reorientation transition, referred to as the Morin transition and is about 253K for bulk hematite. When the temperature falls below T_M, the magnetic moments lying within the basal plane spontaneously reorient themselves from their easy plane phase to align precisely with the c-axis, that is their easy-axis phase. This transition is a unique phase transition only existing for hematite and some other orthoferrites like DyFeO3.

The theoretical explanation for the Morin transition has been provided by J. O. Artman, J. C. Murphy, and S. Foner (*62*). The authors suggest that this phenomenon is due to the competition between two types of anisotropies: single ion anisotropy and magnetic dipole anisotropy, each with distinct temperature dependencies. To accurately determine the Morin transition, precise information regarding the crystal lattice constants is essential. In ***Figure 2-14***, we show the orientation of the magnetic moments of the sublattices 1 and 2 in the case where the temperature is above the morin temperature (i.e. in the canted phase of Hematite) , the DMI field aligned along the c-axis, with the canted moment ***M*** and the Néel vector **n**.

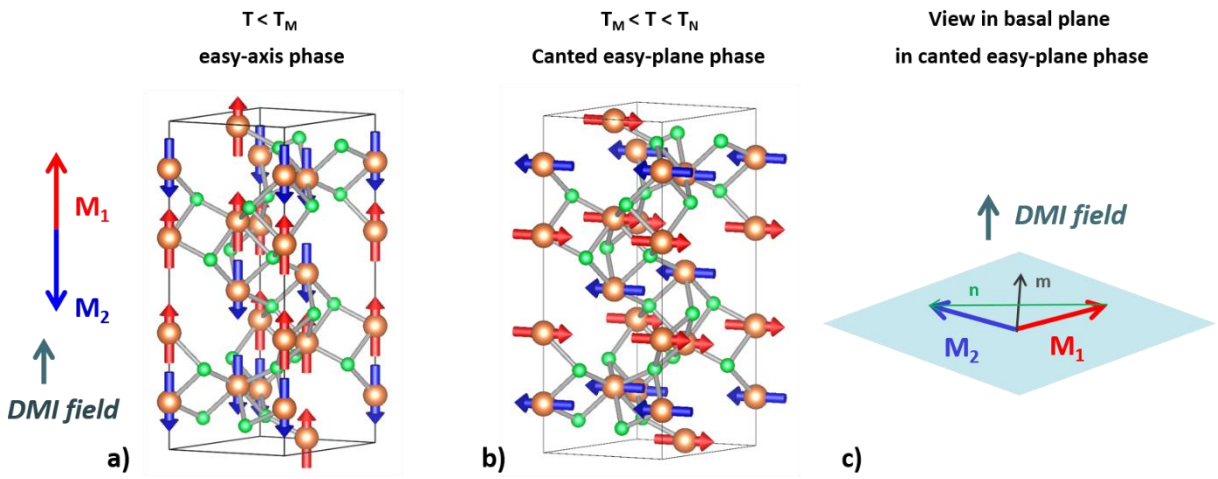

Figure 2-14: Hematite transition phases: *a) The hexagonal unit cell of hematite, red spheres represent iron atoms, and green spheres represent oxygen atoms. This representation is in the canted easy plane phase occurring above the Morin temperature but below the Neel temperature. The spins of the Fe atoms are aligned in the basal plane of hematite. b) Orientation of magnetic moments,* $\boldsymbol{M}_1$ *and* $\boldsymbol{M}_2$*, in the basal plane of hematite, resulting in a canted magnetic moment (*$\boldsymbol{M} = \boldsymbol{M}_1 + \boldsymbol{M}_2$*) due to the presence of bulk DMI aligned along the c-axis. m is perpendicular to the antiferromagnetic ordering direction, and δ represents the angle of canting between* $\boldsymbol{M}_1$ *and* $\boldsymbol{M}_2$*, as depicted in the figure. The figures are taken from (*63*).*

Previously we have introduced the different magnetic interactions in an AFM, here we will consider the specific case of Hematite. Concerning the anisotropies, we can also add to what we have discussed before, an anisotropic exchange term, referred to as F_{KE} that can also be included. Here, its corresponding field can be incorporated in that of the crystalline H_{K_1} (Morrison, 1973). The total free energy is therefore as ***(Eq. 2-90)***.

By deriving the total free energy, the morin transition point can be uncovered. Given that K_2 shows weak temperature dependence above the Morin temperature the phase transition is dictated by the temperature dependence of K_1 ***(Eq. 2-75)***. And where the anisotropy along the c-axis has to change signs to promote either an easy axis or easy plane antiferromagnet.

Below the Morin temperature, the equations of the easy axis phase of AFM discussed in ***section 2.2.6A*** can be applied. Yet the critical field H_c is modified by the DMI field. These modes have been observed on ranges of few hundred of GHz as reported in (*64*) and (*65*) . Above the Morin temperature, in the canted easy plane phase, as discussed in ***section 2.2.6C***, we have the existence of two magnon modes due to the canting. These modes have been reported experimentally(*66*) where it is important to mention that in the absence of an applied field, the gap of the low frequency mode depends on the exchange field and the in-plane anisotropy $H_{aniso-in}$. This latter is of a considerable small value in Hematite (about $6 \cdot 10^{-5}\ mT$ (*67*)) and therefore is the main cause why the low frequency mode in hematite lie within the GHz range as observed in (*68*).

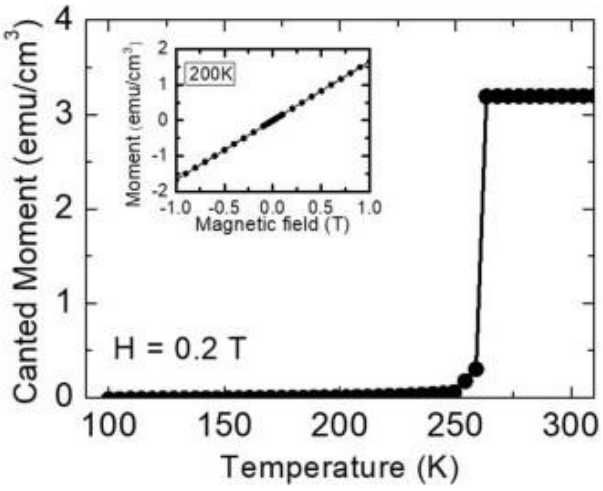

Figure 2-15:Morin transition temperature for hematite: *The temperature dependence of magnetization in the single crystal is measured using a SQUID. The weak ferromagnetic moment is suppressed below the Morin temperature of 260 K. In the inset, at 200 K (below the Morin temperature), there is a complete absence of a ferromagnetic moment. Measurement result extracted from Ref.*(*69*).

This considerably low range of the low frequency mode of Hematite (often called the ferromagnetic mode) opens up the possibility to detect the spinwaves by our experimental setup which relies on commercially available Vector Network analyzers and via the propagating spinwave spectroscopy method(cf. **Chapter 3**). Thereby, in this thesis we focus on the case of a bulk Hematite in the canted easy-plane phase, where the magnon dispersion relations discussed in ***section 2.2.8*** will serve us to validate our experimental observations that will be further discussed in detail in **Chapter 5**.

2.3 SPIN TRANSPORT AND SPIN CURRENTS

Spin electronics, or spintronics, is the field in which the ability to manipulate and enhance currents with different spin types is made possible. The field relies on using the different mobilities of spin-up and spin-down electrons for data storage and transfer via the interactions of the magnetic moments with its surroundings. Specifically, insulating ferromagnets have gained significant interest due to the absence of heat dissipation, therefore opening up the possibility to lossless spin transport, for which numerous advancements have been achieved in this domain.

Works by Kajiwara et.al in 2010 (*25*) demonstrated that injecting an electric current into an heavy metal in proximity with a ferromagnetic insulator film (YIG, in their case) could generate a torque on the magnetization and excite propagating spin-waves. More precisely, when a non-magnetic metal with high spin-orbit coupling, such as platinum, is placed on top of a magnetic insulator, an electric current injected through the metal undergoes conversion into a pure spin current, via the Spin Hall Effect (SHE) (*70*, *71*). This pure spin current can then diffuse in the magnetic insulator, generating a torque to its magnetization, namely the Spin-Transfer Torque (STT) (*72*, *73*) . This mechanism of obtaining a torque from a pure spin current, that is by turn acquired through the spin-orbit interaction of a heavy metal, is termed spin-orbit torque (SOT) (*74*).

In the following, we will explain further these mechanisms, starting with a definition of spin currents, serving to understand the basics the spin Hall effect, spin pumping, and spin torques.

2.3.1 Defining a spin current:

A spin current represents the flow of spin angular momentum within a material. Unlike electrical currents, which involve the movement of electric charge, spin currents describe the transportation of electron spin orientations. Therefore, we can define this spin current (*75*)as the following tensor:

$$\overline{J_s} = \begin{bmatrix} j_{s,x}^{x} & j_{s,y}^{x} & j_{s,z}^{x} \\ j_{s,x}^{y} & j_{s,y}^{y} & j_{s,z}^{y} \\ j_{s,x}^{z} & j_{s,y}^{z} & j_{s,z}^{z} \end{bmatrix}$$

(Eq. 2-103)

where $J_{s,j}^{i}$ designates the polarized spin current density, propagating along the direction of i with a polarization oriented along the direction of j.

For materials with preferential direction of the magnetization, the spin, have two possible polarizations (eigenvalue) along the preferential direction namely the spin up and spin down of value $\pm\frac{\hbar}{2}$. The difference between the spin up and spin down charge currents $\boldsymbol{j}_{\uparrow}$ and $\boldsymbol{j}_{\downarrow}$, respectively, is called a spin current:

$$\boldsymbol{j}_s = \begin{pmatrix} j_{s,y}^x \\ j_{s,y}^y \\ j_{s,y}^z \end{pmatrix} = -\frac{\hbar}{2e}(\boldsymbol{j}_\uparrow - \boldsymbol{j}_\downarrow)$$

(Eq. 2-104)

where the total charge current is:

$$\boldsymbol{j}_c = \boldsymbol{j}_\uparrow + \boldsymbol{j}_\downarrow = \frac{1}{e}(\sigma_\uparrow \nabla\mu_\uparrow + \sigma_\downarrow \nabla\mu_\uparrow)$$

(Eq. 2-105)

with σ are the conductivity of the spin up and spin down, and μ is the electrochemical potential. This means that, to have a spin currents, one would have a difference in the conductivity of the both polarization of spins (polarized spin currents), or a difference in their chemical potential, i.e. in their fermi energy level, which leads to creation of pure spin currents.

For the first case of **spin polarized currents**, we note that a spin polarized current happens for transition metals (such as Fe, Co and Ni and permalloy) having the same energy level i.e. $\nabla\mu_\uparrow$=$\nabla\mu_\uparrow$=$\nabla\mu$. Therefore, one can write:

$$\boldsymbol{j}_c = \frac{1}{e}(\sigma_\uparrow + \sigma_\downarrow)\nabla\mu$$

(Eq. 2-106)

Whereas for the latter case, for **pure spin currents**, the conductivity is the same, while the electrochemical potential is different, therefore, resulting in vanishing charge current, which explains the term 'pure' for pure spin current. This occurs in normal metals and where the difference in the density of states of the two population of spins at the equilibrium is referred to as spin accumulation (of the excess spin population) and is expressed by:

$$\boldsymbol{\mu}_s = \boldsymbol{\mu}_\uparrow - \boldsymbol{\mu}_\downarrow$$

(Eq. 2-107)

whose orientation is defined by the direction of the accumulated spins.

The pure spin current is given by:

$$\boldsymbol{j}_s = -\frac{\hbar}{2e}\,\sigma\nabla\boldsymbol{\mu}_s$$

(Eq. 2-108)

2.3.2 Spin Hall Effect:

By injecting an electric current, $\boldsymbol{I}$, with a current density $\boldsymbol{j}$ through a material with a strong spin-orbit coupling, such as 4d and 5d transition metals (heavy metals as Platinum, Tantalum (*76*) or Tungsten(*77*) for example), a spin dependent scattering of electrons causes the formation of a pure spin current I_s, with a spin current density $\boldsymbol{j}_s$ perpendicular to the charge current $\boldsymbol{j}$. This leads to a spin accumulation with opposite spin polarity (up or down) on the

opposite borders of the heavy metal: This mechanism is called the **Spin Hall Effect.** This coupling between the charge current to the spin current was fully described by Dyakonov and Perel (*78*) and can be studied through drift current diffusion and continuity equations(*79*,*80*). As a result, the efficiency of the conversion is phenomenologically described by a parameter, called the spin hall angle, θ_{SHE} ,given by:

$$\boldsymbol{j}_s = -\frac{\hbar}{2e}\,\theta_{SHE}(\boldsymbol{e}_p \times \boldsymbol{j}_c)$$

(Eq. 2-109)

with $\boldsymbol{e}_p$ is the unit vector of the polarization direction.

The SHE factor is expressed as a percentage, which is strongly material dependent (*71*). A collection of different θ_{SHE} for different metals can be found in (*81*). In this thesis, we have used Platinum, where the value of the spin hall angle can fluctuate from 0.3% (*82*) to 11% (*76*)

A reciprocal effect is associated to this effect, which is called the inverse spin hall effect (*73*). It is described as the conversion of pure spin currents to a charge current via the spin orbit coupling in the nonmagnetic layer, this mechanism is a very interesting tool to measure spin currents (*83*) and in this case relation above becomes:

$$\boldsymbol{j}_c = -\frac{2e}{\hbar}\,\theta_{SHE}(\boldsymbol{e}_p \times \boldsymbol{j}_s)$$

(Eq. 2-110)

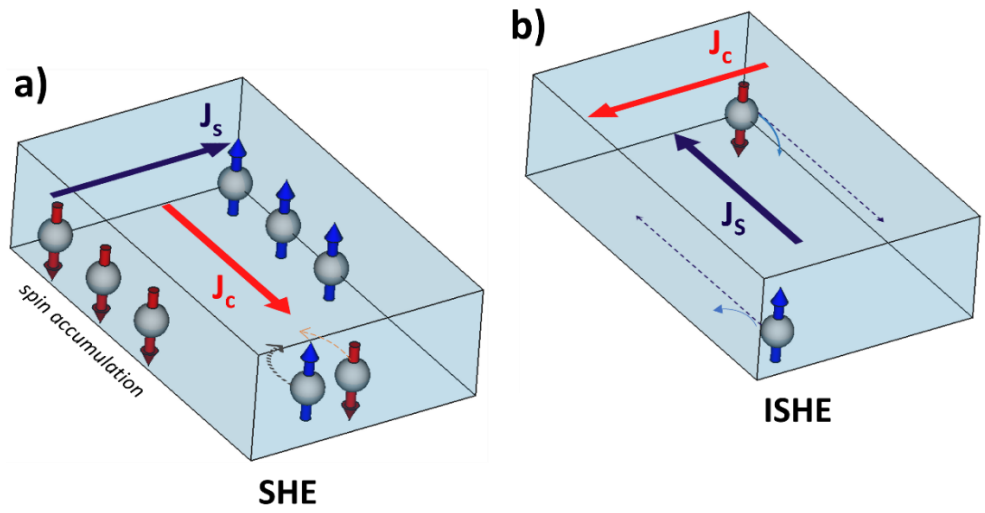

Figure 2-16: Spin Hall Inverse Spin Hall effects illustrations: *a) Upon injection of a charge current, a spin current is generated due to the separation of opposing electron's spins b) The inverse mechanism, a spin polarized current, generate a charge current in the transverse direction.*

This mechanism, therefore, remains a useful tool to generate or detect pure spin currents. In our case, we will utilize it to exploit the coupling between this effect and the magnetization dynamics of a magnetic material placed underneath as in (*25*) and (*84*).

To complete the picture of spin transport mechanisms from the non-magnetic metal to the

FM or AFM, we will cover spin pumping and spin transfer torque mechanisms in the following.

2.3.3 Spin Pumping and Spin Transfer Torques.

A. Spin pumping:

When a magnetic material (MM) of thickness t_{MM} with magnetization $\boldsymbol{M}$ is in contact with a heavy metal (NM) of thickness t_{NM}, as described above, a transmission of a part of the angular momentum of the magnetic material towards the heavy metal is possible. This phenomenon is known as spin pumping.

Spin pumping is a mechanism that can be detected in ferromagnetic (or antiferromagnetic) resonance measurements. When the magnetic material is subjected to an external magnetic field or any other perturbation, its magnetic moments will precess. As a result of its contact with the non-magnetic material, an additional relaxation channel is opened up (indicated by the decrease of the cone of precession for the magnetic moments) leads to the transfer of a portion of the angular momentum across the interface from the MM to the NM. This leads to an increase of the magnetic damping of the magnetic material.

From the perspective of the heavy metal, the received angular momentum can induce a pure spin current flowing perpendicular to the MM|NM interface given by (*85*) :

$$j_s^{MM\to NM} = \begin{pmatrix} j_{s,y}^{x} \\ j_{s,y}^{y} \\ j_{s,y}^{z} \end{pmatrix} = -\frac{\hbar}{4\pi M_s}\, g^{\uparrow\downarrow}(\boldsymbol{M} \times \frac{d\boldsymbol{M}}{dt})$$

(Eq. 2-111)

where $g^{\uparrow\downarrow}$ is the spin mixing conductance, expressed in m^{-2}, it describes the efficiency of the spin transfer between MM and the NM at the interface and depends on the quality of the used materials.

Many scenarios are possible for the pumped spin current; It can be either totally absorbed by the NM, partially absorbed, or totally reflected back into the magnetic material. The latter case can happen when the thickness of the NM is below the spin diffusion length, and therefore, the back-reflected current to the ferromagnetic material, i.e., $j_s^{back} = j_s^{MM\to NM}$ (*86*). In our case, where Platinum is used, with considerably low spin diffusion lengths we can consider that $j_s^{back} = 0$ and therefore, in this case, the Platinum layer can be referred as a 'spin sink'. Henceforth, its effect on the magnetization can be described by an additional damping torque on the LLG equation as:

$$T_{SP} = -\frac{\gamma}{t_{MM}} j_s^{MM\to NM}$$

(Eq. 2-112)

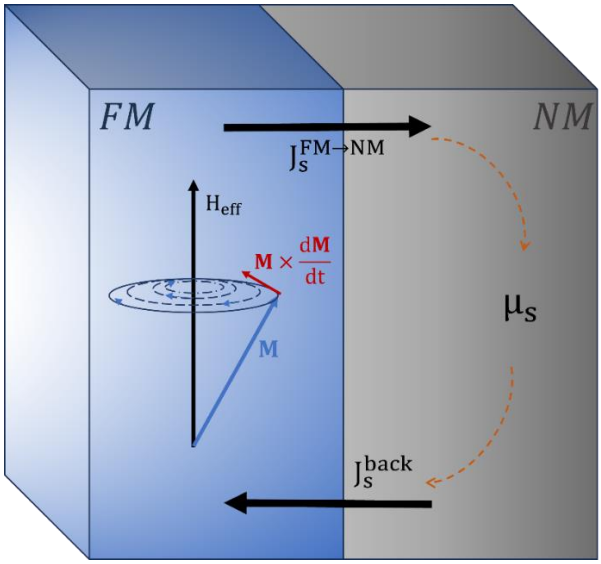

Figure 2-17: Spin pumping principle in a FM|NM interface: *The magnetization precession around H_{eff} drives a spin current $J_s^{FM\rightarrow NM}$ across the interface leading to an additional damping to the magnetization precession proportional to $\boldsymbol{M} \times \frac{d\boldsymbol{M}}{dt}$ as represented in the expression of the torque T_{sp}.*

- ***Case of Antiferromagnets:***

In antiferromagnets , it was shown that the spin mixing conductance at the interface of a non-magnetic layer (metal or insulator) is as large as in FM/NM (*87*). This has encouraged the exploration of high-frequency spintronics at AFM/NM interfaces. It was believed that the spin pumping can not take place in compensated AFMs due to the vanishing magnetization. However, it was then demonstrated in (*87*) that the spin pumping in such AFMs from the magnetization sublattices adds up rather than canceling out.

In the following, we present expressions for spin pumping in an applicable model, considering as well more complex AFM systems (as systems with bi-axial anisotropy for example.). Additionally, this model also takes into account the spin accumulation in the normal metal.

Following the system described previously for a FM, in ***Figure 2-17***, let's now place an antiferromagnet instead of the ferromagnet. Therefore, in addition to the magnetization, the dynamics are also described by the Néel vector, denoted as $\boldsymbol{n}$, with a dynamic term $\boldsymbol{n}(t)$.

The dynamic Landau-Lifshitz-Gilbert (LLG) equation describing the precession of $\boldsymbol{n}$ and $\boldsymbol{m}$ is given by ref. (*88*):

$$\frac{d\boldsymbol{n}}{dt} = (\omega_n \times \boldsymbol{n} + \omega_n \times \boldsymbol{m}) + \boldsymbol{\tau}_{\boldsymbol{n}}$$

$$\frac{d\boldsymbol{m}}{dt} = (\omega_n \times \boldsymbol{n} + \omega_n \times \boldsymbol{m}) + \boldsymbol{\tau}_{\boldsymbol{m}}$$

(Eq. 2-113)

where $\omega_{n,m}$ and $\boldsymbol{\tau}_{\boldsymbol{n,m}}$are the resonance frequencies and the spin pumping torques of $\boldsymbol{n}$ and $\boldsymbol{m}$. The frequencies are derived from the total free energy expression with respect to each vector.

The spin pumping torques are given by (*87*):

$$\boldsymbol{\tau}_{\boldsymbol{n}} = \alpha(\boldsymbol{n} \times \frac{d\boldsymbol{m}}{dt} + \boldsymbol{m} \times \frac{d\boldsymbol{n}}{dt})$$

$$\boldsymbol{\tau}_{\boldsymbol{m}} = \alpha(\boldsymbol{n} \times \frac{d\boldsymbol{n}}{dt} + \boldsymbol{m} \times \frac{d\boldsymbol{m}}{dt})$$

(Eq. 2-114)

where α is the sum of the intrinsic damping α_0 of the material and the spin pumping damping α_{SP} (that depends on the spin mixing conductance and the thickness of the AFM).

The spin current from spin pumping from the antiferromagnetic precessions into the normal metal is therefore given by:

$$\boldsymbol{I}_S^p = \frac{\hbar}{2\pi} g_\perp (\boldsymbol{n} \times \frac{d\boldsymbol{n}}{dt} + \boldsymbol{m} \times \frac{d\boldsymbol{m}}{dt})$$

(Eq. 2-115)

with $g_\perp$, is the transverse spin mixing conductance (*87*).

The accumulation of spins at the interface of the normal metal leads in turn to a back-flow current:

$$\boldsymbol{I}_S^b = \frac{1}{2\pi} g_\perp (\boldsymbol{n} \times (\boldsymbol{\mu}_s \times \boldsymbol{m}) + \boldsymbol{m} \times (\boldsymbol{\mu}_s \times \boldsymbol{m})$$

(Eq. 2-116)

Now that the spin current is pumped into the metal, ISHE can take place leading to the generation of a charge current that is perpendicular to the spin current and the polarization direction. Therefore the ***(Eq. 2-110)*** can still be applied and we re-write is as:

$$\boldsymbol{j}_c = -\frac{2e}{A\hbar}\, \theta_{SHE} (\boldsymbol{e}_p \times (\boldsymbol{I}_S^p + \boldsymbol{I}_S^b)$$

(Eq. 2-117)

where A is the surface area of the AFM/NM interface.

B. Spin Transfer Torque:

Spin transfer torque is the transfer of angular momentum between spins and the magnetization of a magnetic material where it involves the manipulation and control of the orientation of the magnetization in a magnetic layer using spin-polarized currents.

When a spin-polarized current (that is a flow of electrons with aligned spins) is injected into the MM, it can exert a torque on the magnetic moments of the material. This torque can cause the magnetization to precess or even switch its direction. This torque is given by:

$$\boldsymbol{T}_{ST} = \frac{\beta}{M_s}\boldsymbol{M} \times (\boldsymbol{M} \times \boldsymbol{\sigma})$$

(Eq. 2-118)

with $\beta = \frac{\gamma}{t_{MM}} j_S^{NM \to MM}$.

To study the effect of the STT on the magnetic system, we add to the LLG equation a Slonczewski-like torque (also called damping like or non-adiabatic torque):

$$\frac{\partial \boldsymbol{M}}{\partial t} = -\gamma \boldsymbol{M} \times \boldsymbol{H}_{eff} + \underbrace{\frac{\alpha}{M_s}\boldsymbol{M} \times \frac{d\boldsymbol{M}}{dt}}_{\boldsymbol{Damping\ torque\ term}} - \underbrace{\frac{\beta}{M_s}\boldsymbol{M} \times (\boldsymbol{M} \times \boldsymbol{\sigma})}_{\boldsymbol{Spin\ Transfer\ Torque}}$$

(Slonczewski)

(Eq. 2-119)

Depending on the sign of $\boldsymbol{M} \times \boldsymbol{\sigma}$, the spin transfer torque can be either parallel or antiparallel to the damping torque.

In the first case this leads to an amplification of the system's damping, followed by a suppression of the magnetization precession. Whereas in the second case, compensation of the damping will take place.

For current densities larger than a given threshold (determined by the system parameters), the damping can be fully compensated, and the system enters a switching or auto-oscillation regime.

Therefore, when placing Platinum on top of a magnetic film, it is crucial to consider the direction of the generated spin current and its spin polarization $\boldsymbol{\sigma}$, ensuring it is perpendicular to the interface towards the magnetic layer. To generate an non-zero torque, this polarization needs to be parallel to magnetization of the magnetic materials (*89*).

- ***Case of Antiferromagnets:***

If we take now the case of an antiferromagnet, the spin transfer torques that will add up to the LLG equation of ***(Eq. 2-113)*** are given by (*90*):

$$T_{STT}^{n} = \frac{\gamma}{4\pi AL} g_{\perp}(\boldsymbol{n} \times (\boldsymbol{\mu}_s \times \boldsymbol{m}) + \boldsymbol{m} \times (\boldsymbol{m} \times \boldsymbol{\mu}_s)$$

$$T_{STT}^{m} = \frac{\gamma}{4\pi AL} g_{\perp}(\boldsymbol{n} \times (\boldsymbol{\mu}_s \times \boldsymbol{m}) + \boldsymbol{m} \times (\boldsymbol{\mu}_s \times \boldsymbol{m})$$

(Eq. 2-120)

where L is the saturation magnetization for each sublattice and can be defined by :

$$L\boldsymbol{m} = \frac{\boldsymbol{M}_1 + \boldsymbol{M}_2}{2}$$

(Eq. 2-121)

From the equations of ***(Eq. 2-120)*** one can notice from the spin mixing conductance factor (that also can be described by α_{SP}). This means that the STT is linked to SP, so that the existence of one is linked to the existence to the other. This will be further discussed in **Chapter 6** on ST-FMR measurements on Hematite.

2.4 BIBLIOGRAPHY:

1. B. A. Kalinikos, A. N. Slavin, Theory of dipole-exchange spin wave spectrum for ferromagnetic films with mixed exchange boundary conditions. *J. Phys. C Solid State Phys.* **19**, 7013–7033 (1986).
2. B. A. Kalinikos, M. P. Kostylev, N. V. Kozhus, A. N. Slavin, The dipole-exchange spin wave spectrum for anisotropic ferromagnetic films with mixed exchange boundary conditions. *J. Phys. Condens. Matter* **2**, 9861–9877 (1990).
3. W. F. Brown, Domains, micromagnetics, and beyond: Reminiscences and assessments. *J. Appl. Phys.* **49**, 1937–1942 (1978).
4. S. Blundell, *Magnetism in Condensed Matter* (Oxford University Press, Oxford ; New York, 2001)*Oxford master series in condensed matter physics*.
5. Weiss, Pierre, L'hypothèse du champ moléculaire et la propriété ferromagnétique. *J Phys Theor Appl* **6**, 661–690 (1907).
6. A. A. Serga, A. V. Chumak, B. Hillebrands, YIG magnonics. *J. Phys. Appl. Phys.* **43**, 264002 (2010).
7. A. Prabhakar and D. Stancil, *Spin Waves: Theory and Applications* (Springer US, Boston, MA, 2009).
8. P. W. Anderson, New Approach to the Theory of Superexchange Interactions. *Phys. Rev.* **115**, 2–13 (1959).
9. L. Shekhtman, O. Entin-Wohlman, A. Aharony, Moriya's anisotropic superexchange interaction, frustration, and Dzyaloshinsky's weak ferromagnetism. *Phys. Rev. Lett.* **69**, 836–839 (1992).
10. L. Landau, E. Lifshits, ON THE THEORY OF THE DISPERSION OF MAGNETIC PERMEABILITY IN FERROMAGNETIC BODIES. **53**.
11. A. G. Gurevich, G. A. Melkov, Magnetization Oscillations and Waves (1996).
12. C. Kittel, On the Theory of Ferromagnetic Resonance Absorption. *Phys. Rev.* **73**, 155–161 (1948).
13. T. L. Gilbert, Classics in Magnetics A Phenomenological Theory of Damping in Ferromagnetic Materials. *IEEE Trans. Magn.* **40**, 3443–3449 (2004).
14. Anonymous, Abstracts of Papers to be Presented at the 1955 Thanksgiving Meeting at the University of Chicago, Chicago, Illinois, November 25 and 26, 1955. *Phys. Rev.* **100**, 1235–1235 (1955).
16. L. Néel, Théorie du paramagnétisme constant. Application au manganèse.
18. L. Néel, Propriétés magnétiques de l'état métallique et énergie d'interaction entre atomes magnétiques. *Ann. Phys.* **11**, 232–279 (1936).
19. I. Fina, X. Marti, D. Yi, J. Liu, J. H. Chu, C. Rayan-Serrao, S. Suresha, A. B. Shick, J. Železný, T. Jungwirth, J. Fontcuberta, R. Ramesh, Anisotropic magnetoresistance in an antiferromagnetic semiconductor. *Nat. Commun.* **5**, 4671 (2014).
20. E. V. Gomonay, V. M. Loktev, Spintronics of antiferromagnetic systems (Review Article). *Low Temp. Phys.* **40**, 17–35 (2014).
21. A. H. MacDonald, M. Tsoi, Antiferromagnetic metal spintronics. *Philos. Trans. R. Soc. Math. Phys. Eng. Sci.* **369**, 3098–3114 (2011).
22. J. Železný, H. Gao, K. Výborný, J. Zemen, J. Mašek, A. Manchon, J. Wunderlich, J. Sinova, T. Jungwirth, Relativistic Néel-Order Fields Induced by Electrical Current in Antiferromagnets. *Phys. Rev. Lett.* **113**, 157201 (2014).
23. P. Wadley, B. Howells, J. Železný, C. Andrews, V. Hills, R. P. Campion, V. Novák, K. Olejník, F. Maccherozzi, S. S. Dhesi, S. Y. Martin, T. Wagner, J. Wunderlich, F. Freimuth, Y. Mokrousov, J. Kuneš, J.

S. Chauhan, M. J. Grzybowski, A. W. Rushforth, K. W. Edmonds, B. L. Gallagher, T. Jungwirth, Electrical switching of an antiferromagnet. *Science* **351**, 587–590 (2016).
24. J. M. D. Coey, Magnetism and Magnetic Materials.
25. Y. Kajiwara, K. Harii, S. Takahashi, J. Ohe, K. Uchida, M. Mizuguchi, H. Umezawa, H. Kawai, K. Ando, K. Takanashi, S. Maekawa, E. Saitoh, Transmission of electrical signals by spin-wave interconversion in a magnetic insulator. *Nature* **464**, 262–266 (2010).
26. W. Hai-Ping, D. Kai-Ming, T. Wei-Shi, X. Chuan-Yun, H. Feng-Lan, L. Qun-Xiang, The structural, electronic, and magnetic properties of $SrFeO_n$ (n = 2 and 2.5): a GGA+ U study. *Chin. Phys. B* **18**, 5008–5014 (2009).
27. A. Haykal, J. Fischer, W. Akhtar, J.-Y. Chauleau, D. Sando, A. Finco, F. Godel, Y. A. Birkhölzer, C. Carrétéro, N. Jaouen, M. Bibes, M. Viret, S. Fusil, V. Jacques, V. Garcia, Antiferromagnetic textures in BiFeO3 controlled by strain and electric field. *Nat. Commun.* **11**, 1704 (2020).
28. I. Sosnowska, T. P. Neumaier, E. Steichele, Spiral magnetic ordering in bismuth ferrite. *J. Phys. C Solid State Phys.* **15**, 4835–4846 (1982).
29. A. N. Bogdanov, U. K. Rößler, M. Wolf, K.-H. Müller, Magnetic structures and reorientation transitions in noncentrosymmetric uniaxial antiferromagnets. *Phys. Rev. B* **66**, 214410 (2002).
30. H. Jani, J.-C. Lin, J. Chen, J. Harrison, F. Maccherozzi, J. Schad, S. Prakash, C.-B. Eom, A. Ariando, T. Venkatesan, P. G. Radaelli, Antiferromagnetic half-skyrmions and bimerons at room temperature. *Nature* **590**, 74–79 (2021).
31. T. Nomoto, R. Arita, Cluster multipole dynamics in noncollinear antiferromagnets. *Phys. Rev. Res.* **2**, 012045 (2020).
32. S. Nakatsuji, N. Kiyohara, T. Higo, Large anomalous Hall effect in a non-collinear antiferromagnet at room temperature. *Nature* **527**, 212–215 (2015).
33. M. Ikhlas, T. Tomita, T. Koretsune, M.-T. Suzuki, D. Nishio-Hamane, R. Arita, Y. Otani, S. Nakatsuji, Large anomalous Nernst effect at room temperature in a chiral antiferromagnet. *Nat. Phys.* **13**, 1085–1090 (2017).
34. T. Uchimura, J.-Y. Yoon, Y. Sato, Y. Takeuchi, S. Kanai, R. Takechi, K. Kishi, Y. Yamane, S. DuttaGupta, J. Ieda, H. Ohno, S. Fukami, Observation of domain structure in non-collinear antiferromagnetic Mn3Sn thin films by magneto-optical Kerr effect. *Appl. Phys. Lett.* **120**, 172405 (2022).
35. L. Néel, Preuves expérimentales du ferromagnétisme et de l'antiferromagnétisme. *Ann. Inst. Fourier* **1**, 163–183 (1949).
36. Y.-Y. Li, Domain Walls in Antiferromagnets and the Weak Ferromagnetism of α - Fe 2 O 3. *Phys. Rev.* **101**, 1450–1454 (1956).
37. I. Dzyaloshinsky, A thermodynamic theory of "weak" ferromagnetism of antiferromagnetics. *J. Phys. Chem. Solids* **4**, 241–255 (1958).
38. T. Moriya, Anisotropic Superexchange Interaction and Weak Ferromagnetism. *Phys. Rev.* **120**, 91–98 (1960).
39. C. Kittel, Theory of Antiferromagnetic Resonance. *Phys. Rev.* **82**, 565–565 (1951).
40. T. Nagamiya, Theory of Antiferromagnetism and Antiferromagnetic Resonance Absorption, II. *Prog. Theor. Phys.* **6**, 350–355 (1951).
41. F. Keffer, C. Kittel, Theory of Antiferromagnetic Resonance. *Phys. Rev.* **85**, 329–337 (1952).
42. S. Foner, High-Field Antiferromagnetic Resonance in Cr 2 O 3. *Phys. Rev.* **130**, 183–197 (1963).
43. Y. Shoji, E. Ohmichi, H. Takahashi, H. Ohta, "Antiferromagnetic Resonance Spectroscopy of NiO in the Terahertz Region" in *2022 47th International Conference on Infrared, Millimeter and Terahertz Waves (IRMMW-THz)* (IEEE, Delft, Netherlands, 2022).

https://ieeexplore.ieee.org/document/9895753/), pp. 1–2.
44. Z. Wang, S. Kovalev, N. Awari, N. Awari, M. Chen, S. Germanskiy, B. Green, J.-C. Deinert, T. Kampfrath, J. Milano, J. Milano, M. Gensch, Magnetic field dependence of antiferromagnetic resonance in NiO. *Appl. Phys. Lett.* (2018).
45. N. J. Poulis, J. Van Den Handel, J. Ubbink, J. A. Poulis, C. J. Gorter, On Antiferromagnetism in a Single Crystal. *Phys. Rev.* **82**, 552–552 (1951).
46. I. Boventer, H. T. Simensen, A. Anane, M. Kläui, A. Brataas, R. Lebrun, Room-Temperature Antiferromagnetic Resonance and Inverse Spin-Hall Voltage in Canted Antiferromagnets. *Phys. Rev. Lett.* **126**, 187201 (2021).
47. S. J. Williamson, S. Foner, Antiferromagnetic Resonance in Systems with Dzyaloshinsky-Moriya Coupling; Orientation Dependence in α Fe 2 O 3. *Phys. Rev.* **136**, A1102–A1106 (1964).
48. A. J. Sievers, M. Tinkham, Far Infrared Antiferromagnetic Resonance in MnO and NiO. *Phys. Rev.* **129**, 1566–1571 (1963).
49. O. Gomonay, V. Baltz, A. Brataas, Y. Tserkovnyak, Antiferromagnetic spin textures and dynamics. *Nat. Phys.* **14**, 213–216 (2018).
50. J. Han, R. Cheng, L. Liu, H. Ohno, S. Fukami, Coherent antiferromagnetic spintronics. *Nat. Mater.* **22**, 684–695 (2023).
51. V. G. Bar'yakhtar, B. A. Ivanov, M. V. Chetkin, Dynamics of domain walls in weak ferromagnets. (1985).
52. T. Kampfrath, A. Sell, G. Klatt, A. Pashkin, S. Mährlein, T. Dekorsy, M. Wolf, M. Fiebig, A. Leitenstorfer, R. Huber, Coherent terahertz control of antiferromagnetic spin waves. *Nat. Photonics* **5**, 31–34 (2011).
53. J. Li, C. B. Wilson, R. Cheng, M. Lohmann, M. Kavand, W. Yuan, M. Aldosary, N. Agladze, P. Wei, M. S. Sherwin, J. Shi, Spin current from sub-terahertz-generated antiferromagnetic magnons. *Nature* **578**, 70–74 (2020).
54. R. E. Camley, Long-Wavelength Surface Spin Waves on Antiferromagnets. *Phys. Rev. Lett.* **45**, 283–286 (1980).
55. B. Lüthi, R. Hock, Dipolar surface spin waves in antiferromagnets. *J. Magn. Magn. Mater.* **38**, 264–268 (1983).
56. B. Lüthi, D. L. Mills, R. E. Camley, Surface spin waves in antiferromagnets. *Phys. Rev. B* **28**, 1475–1479 (1983).
57. V. I. Ozhogin, Nonlinear dynamics of antiferromagnets with anisotropy of easy-plane type, *JETP Letters* (1965).
58. V. V. Tarasenko, V. D. Kharitonov, Surface magnetostatic waves in uniaxial antiferromagnets. *JETP Lett.* **33** (1971).
59. J. R. Eshbach, R. W. Damon, Surface Magnetostatic Modes and Surface Spin Waves. *Phys. Rev.* **118**, 1208–1210 (1960).
60. L. Néel, R. Pauthenet, Etude thermomagnétique d'un monocristal de Fe2O3-alpha.
61. F. J. Morin, Magnetic Susceptibility of α Fe 2 O 3 and α Fe 2 O 3 with Added Titanium. *Phys. Rev.* **78**, 819–820 (1950).
62. J. O. Artman, J. C. Murphy, S. Foner, Magnetic Anisotropy in Antiferromagnetic Corundum-Type Sesquioxides. *Phys. Rev.* **138**, A912–A917 (1965).
63. Andrew Ross, Ph.D. thesis, *Probing Magnetostatic and Magnetotransport Properties of the Antiferromagnetic Iron Oxide Hematite, Johannes Gutenberg-Universität Mainz* (2018).

64. L. J. Cornelissen, J. Liu, R. A. Duine, J. B. Youssef, B. J. Van Wees, Long-distance transport of magnon spin information in a magnetic insulator at room temperature. *Nat. Phys.* **11**, 1022–1026

(2015).
65. S. Foner, S. J. Williamson, Low-Temperature Antiferromagnetic Resonance in α-Fe2O3. *J. Appl. Phys.* **36**, 1154–1156 (1965).
66. P. W. Anderson, F. R. Merritt, J. P. Remeika, W. A. Yager, Magnetic Resonance in α-Fe $_2$ O $_3$.. *Phys Rev* **93**, 717–718 (1954).
67. A. H. Morrish, *Canted Antiferromagnetism: Hematite* (WORLD SCIENTIFIC, 1995; https://www.worldscientific.com/doi/abs/10.1142/2518).
68. E. J. Samuelsen, G. Shirane, Inelastic neutron scattering investigation of spin waves and magnetic interactions in α-Fe $_2$ O $_3$. *Phys. Status Solidi B* **42**, 241–256 (1970).
69. R. Lebrun, A. Ross, S. A. Bender, A. Qaiumzadeh, L. Baldrati, J. Cramer, A. Brataas, R. A. Duine, M. Kläui, Tunable long-distance spin transport in a crystalline antiferromagnetic iron oxide. *Nature* **561**, 222–225 (2018).
70. S. O. Valenzuela, M. Tinkham, Direct electronic measurement of the spin Hall effect. *Nature* **442**, 176–179 (2006).
71. J. Sinova, S. O. Valenzuela, J. Wunderlich, C. H. Back, T. Jungwirth, Spin Hall effects. *Rev. Mod. Phys.* **87**, 1213–1260 (2015).
72. A. Azevedo, L. H. Vilela Leão, R. L. Rodriguez-Suarez, A. B. Oliveira, S. M. Rezende, dc effect in ferromagnetic resonance: Evidence of the spin-pumping effect? *J. Appl. Phys.* **97**, 10C715 (2005).
73. E. Saitoh, M. Ueda, H. Miyajima, G. Tatara, Conversion of spin current into charge current at room temperature: Inverse spin-Hall effect. *Appl. Phys. Lett.* **88**, 182509 (2006).
74. A. Manchon, S. Zhang, Theory of spin torque due to spin-orbit coupling. *Phys. Rev. B* **79**, 094422 (2009).
75. S. Maekawa, S. O. Valenzuela, E. Saitoh, T. Kimura, *Spin Current* (Oxford University Press, 2012;.
76. C. Hahn, G. De Loubens, O. Klein, M. Viret, V. V. Naletov, J. Ben Youssef, Comparative measurements of inverse spin Hall effects and magnetoresistance in YIG/Pt and YIG/Ta. *Phys. Rev. B* **87**, 174417 (2013).
77. C.-F. Pai, L. Liu, Y. Li, H. W. Tseng, D. C. Ralph, R. A. Buhrman, Spin transfer torque devices utilizing the giant spin Hall effect of tungsten. *Appl. Phys. Lett.* **101**, 122404 (2012).
78. V. I. Perel', SPIN ORIENTATION OF ELECTRONS ASSOCIATED WITH THE INTERBAND ABSORPTION OF LIGHT IN SEMICONDUCTORS.
79. M. I. Dyakonov, Ed., *Spin Physics in Semiconductors* (Springer, Berlin, 2008)*Springer series in solid-state sciences*.
80. M. I. Dyakonov, Magnetoresistance due to Edge Spin Accumulation. *Phys. Rev. Lett.* **99**, 126601 (2007).
81. J.-C. Rojas-Sánchez, N. Reyren, P. Laczkowski, W. Savero, J.-P. Attané, C. Deranlot, S. Gambarelli, M. Jamet, J.-M. George, L. Vila, H. Jaffrès, "Spin pumping and inverse spin Hall effect in platinum and other 5 *d* metals: the essential role of spin-memory loss and spin-current discontinuities at interfaces" H.-J. Drouhin, J.-E. Wegrowe, M. Razeghi, Eds. (San Diego, California, United States, 2014; p. 916729.
82. T. Kimura, Y. Otani, T. Sato, S. Takahashi, S. Maekawa, Room-Temperature Reversible Spin Hall Effect. *Phys. Rev. Lett.* **98**, 156601 (2007).
83. O. d'Allivy Kelly, A. Anane, R. Bernard, J. Ben Youssef, C. Hahn, A. H. Molpeceres, C. Carrétéro, E. Jacquet, C. Deranlot, P. Bortolotti, R. Lebourgeois, J.-C. Mage, G. de Loubens, O. Klein, V. Cros, A. Fert, Inverse spin Hall effect in nanometer-thick yttrium iron garnet/Pt system. *Appl. Phys. Lett.* **103**, 082408 (2013).
84. M. Evelt, V. E. Demidov, V. Bessonov, S. O. Demokritov, J. L. Prieto, M. Muñoz, J. Ben Youssef,

V. V. Naletov, G. de Loubens, O. Klein, M. Collet, K. Garcia-Hernandez, P. Bortolotti, V. Cros, A. Anane, High-efficiency control of spin-wave propagation in ultra-thin yttrium iron garnet by the spin-orbit torque. *Appl. Phys. Lett.* **108**, 172406 (2016).
85. C.-F. Pai, Y. Ou, L. H. Vilela-Leão, D. C. Ralph, R. A. Buhrman, Dependence of the efficiency of spin Hall torque on the transparency of Pt/ferromagnetic layer interfaces. *Phys. Rev. B* **92**, 064426 (2015).
86. A. Brataas, Yu. V. Nazarov, G. E. W. Bauer, Finite-Element Theory of Transport in Ferromagnet–Normal Metal Systems. *Phys. Rev. Lett.* **84**, 2481–2484 (2000).
87. R. Cheng, J. Xiao, Q. Niu, A. Brataas, Spin Pumping and Spin-Transfer Torques in Antiferromagnets. *Phys. Rev. Lett.* **113**, 057601 (2014).
88. Ø. Johansen, A. Brataas, Spin pumping and inverse spin Hall voltages from dynamical antiferromagnets. *Phys Rev B* **95**, 220408 (2017).
89. T. Kimura, Y. Otani, T. Sato, S. Takahashi, S. Maekawa, Room-Temperature Reversible Spin Hall Effect. *Phys. Rev. Lett.* **98**, 156601 (2007).
90. Ø. Johansen, H. Skarsvåg, A. Brataas, Spin-transfer antiferromagnetic resonance. *Phys. Rev. B* **97**, 054423 (2018)

3 CHAPTER 3: EXPERIMENTAL TECHNIQUES

During the course of this thesis, we were interested in exploring the spin waves dynamics in thin films of garnets including in plane magnetized nm-thick YIG. Interestingly, our exploration extended to antiferromagnets, specifically, hematite. This was in the aim of developing devices for radiofrequency applications for information transfer technologies.

We employed a variety of techniques, including both device fabrication and measurements. For device fabrication, we executed many lithography steps, including optical and electron beam lithography, ion beam etching, metal deposition, and chemical procedures.

For performing the measurements, one way is to use RF-currents and fields, which is the basis of the PSWS technique. We, as well, carried on non-local electrical measurements on α-Fe_2O_3, where these measurements will be detailed further in chapter 6 dedicated to inverse spin Hall measurements on Hematite.

In the following, we will show and list the devices that were studied, detail about the nanofabrication and explain the PSWS technique.

3.1 DEVICE FABRICATION

3.1.1 An overview of the devices:

In this manuscript, we will investigate several types of devices, each designed to explore specific magnonics and spintronics aspects in different materials.

Starting with **Chapter 4**, we focus on a magnonic delay line applied to an in-plane magnetized YIG thin film deposited on a GGG substrate. The primary goal is to show how to realize a time-domain study using the PSWS technique, that serves to study the multiple mode profile of spin waves arriving at nearly same frequencies but with different group velocities. The device is constituted of an etched YIG waveguide, on which two gold antennas are deposited as shown in ***Figure 3-1***. ***a)***. The antennae used throughout this thesis including this device and others, are of GSG type.

Continuing to **Chapter 5**, we shift our interest to exploit SWs in antiferromagnets. The device under study consists of two RF antennas deposited on a full film of a bulk hematite as shown in as shown in ***Figure 3-1. b)***. Different sizes and separation distances of these antennas were fabricated in order to unravel coherent propagating SWs in the canted antiferromagnet, α-Fe_2O_3.

Lastly, in **Chapter 6** we study of spintronic applications in Hematite. It involves the fabrication of devices with platinum. This part covers two significant aspects: firstly, the exploration of the inverse spin Hall effect (ISHE) (***Figure 3-1. c)***) as a mean to detect these propagating SWs using a non-local method. The device is constituted of one RF-antenna to excite the SWs ,

and a detector constituted of a platinum stripe placed few micrometers away from the injection antenna. Secondly, the realization and the investigation of a spin diode effect, as depicted in ***Figure 3-1. d)*** , where here the platinum stripe is placed in a way connected to the signal line of the antenna, serving to conduct ST-FMR measurements.

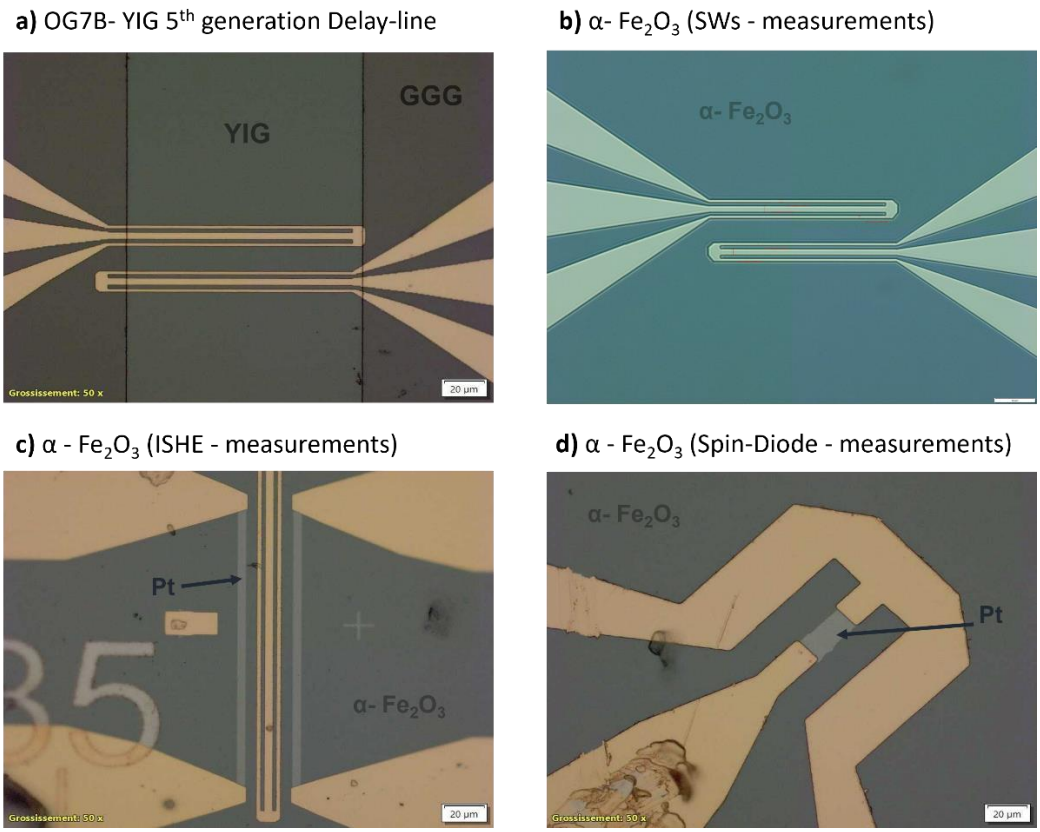

Figure 3-1: Optical images of the used devices thourghout the manuscript.

3.1.2 Fabrication techniques:

An important part of my thesis was dedicated for fabricating the devices listed above. In the following section, I will briefly describe the protocol followed for the fabrication, that was done using both optical and electron lithography (*1–3*).

It's worth mentioning that either of the two lithography techniques share the same operating principle ; however, they differ in resolution. For fine resolution, e-beam offers a high resolution of less than a few tens of nanometers, as well as a precise alignment, which is crucial for devices containing many components. On the other hand, optical lithography provides a resolution of about 1 µm. The latter is considered a more convenient solution due to its speed and efficiency for larger structures.

Firstly, cleaning the samples is a crucial step in nanofabrication to ensure that the surfaces are free from contaminants, dust, and other impurities. All of the samples used (including YIG, and α-Fe_2O_3) can be cleaned by immersing the sample in an acetone bath, then rinsing with propanol, and blow-drying with a stream of N_2. Oxygen plasma can also be used if acetone

doesn't work to remove residues of resist or stubborn dust particles.

Secondly, one needs to coat the sample with an appropriate resist. A resist is an organic material (a polymer) that is sensitive to light (photolithography) or electrons (electron-beam lithography) exposition. When this happens, chemical changes occur to the resist and thus one can create a pattern on the coated substrate by selectively exposing and then developing the resist. The selection of the resist depends on the criteria of the wanted pattern to fabricate as well as on the thickness and uniformity desired. For our devices, we have primarily used positive resists:

- SPR700.1 for photolithography, providing a thickness of 1 μm.
- PMMA-A4 and PMMA-A6 with thicknesses of 200 nm and 400 nm, respectively, for electron beam lithography.

When using e-beam lithography, and since our samples are insulators, one need to have an additional resist coating on top of the PMMA to prevent electron charging on the sample's surface. This additional coating is achieved using an agent called E-spacer 300Z. The use of this agent, is rather easy and practical since it can be easily removed with water. Then the sample is ready for the lithography step.

After exposure to UV or electron beam, the resist chemical decomposition changes, and subsequently, by utilizing a developing agent (base), the resist is removed in the locations where it was exposed (in the case of a positive resist or retained in the case of a negative resist).

Once the development is over, and the patterned structures are successfully done, one needs to fill the uncovered area with a metal. The metal deposition can be done either with sputtering or PVD physical vapor deposition with a soft pre-etch step prior the deposition. This step is followed by a lift-off process. Finally, the lift-off process involves placing the sample, which now has patterns with resist areas and a thin layer of metal on top, into an acetone bath. The acetone will dissolve the resist and thus the metal on top is lifted, while leaving the metal on the patterns intact.

In some of the devices (as with YIG), where we have waveguides, an additional etching step is required to remove the magnetic layer outside of the patterned waveguides. To achieve this, we use ion beam etching (IBE). Therefore, after the waveguide patterning and development step, the sample is metallized with a hard mask composed of 10 nm Au, 40 nm Al, 30 nm Ti, and lastly of 5 nm Pt for capping the Al from oxidizing. This is followed by a lift-off process that will leave the hard mask on the waveguides as a protection prior the etching.

3.2 FERROMAGNETIC RESONANCE FMR:

To characterize the magnetic films, FMR measurements (*4*) were conducted before nanofabrication. This allows to extract magnetic properties such as damping and effective magnetization which is helpful to anticipate the expected dispersion and spin wave properties prior to the experiment.

To start, the film is placed onto an rf-coplanar waveguide, that is placed between two magnetic coils that can provide an external field, to saturate the sample, up to 8000 Oe. Then to excite the magnetic film, we inject rf-field, with which the precession occurs at a direction perpendicular to the external field. This rf-field is generated by an rf-source with a frequency range spanning from 1 to 30 GHz. In a typical measurement, the frequency remains fixed while the external field strength is varied. The resulting signal travels back and forth along the open-end coplanar waveguide and is detected by a reflection diode (as a voltage), where changes in this reflected signal are used to indicate the resonance.

Since the signal detected from the magnetic material is often weak and noisy, the signal is sent from the reflection diode to a lock-in amplifier to extract the precession frequency from the noise. For this a small part of the static magnetic field is modulated at a low frequency (f_0=73 Hz). The power absorbed at the reflected diode is thus composed of two contributions; The first contribution originates from the background and is independent of the modulation, while the second is due to the precession and is field modulation-dependent. By measuring the derivative of the absorbed power, the background contribution can be eliminated. The derivative of the absorbed power has an anti-Lorentzian shape and can be fitted using Kittel's law (as described in **Chapter 2**).

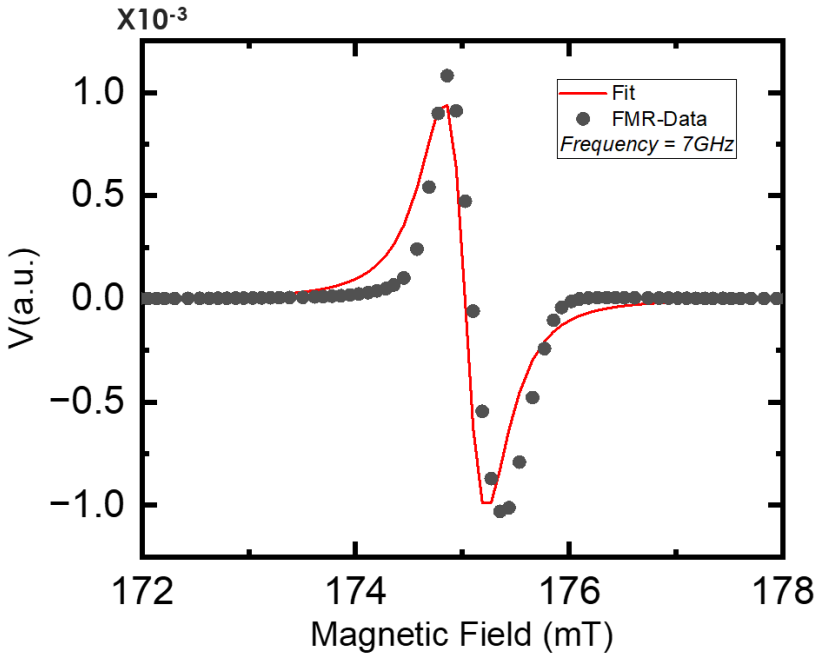

Figure 3-2: Typical FMR measurement on a 280-nm thick YIG film*: Anti-lorentzian shape of FMR peak at a magnetic field of 175 mT at a fixed frequency of 7 GHz, the points represent the collected data*

points from the experiment, while the red curve is the theoretical fit.

3.3 PROPAGATING SPIN WAVES SPECTROSCOPY PSWS

3.3.1 Principle and set-up

The principle of this type of measurement relies on inductive coupling between the metallic antennas and the magnetic material underneath. The principle consists of two inductive antennas through which we excite (emitter) with one and we detect (receiver) with the other.

Firstly, the lithographed sample is placed on a thin plexiglass plate (not shown in the figure) that is installed on top of an electromagnet (GMW). The electromagnet movement is controlled by a motor whereas the magnetic field is controlled by a DC power supply (KEPCO). To connect the device to the VNA, two microwave probes (40 GHz from Formfactor) are connected to the VNA ports, (port 1 and port 2) via rf-coaxial cables. The setup is mounted with a microscope, a camera and a screen, which enables the visualization of both the sample and the probes. This allows a precise positioning of the probes on the larger pads of the rf-antennas on the device. The set-up and its components are shown in ***Figure 3-3***.

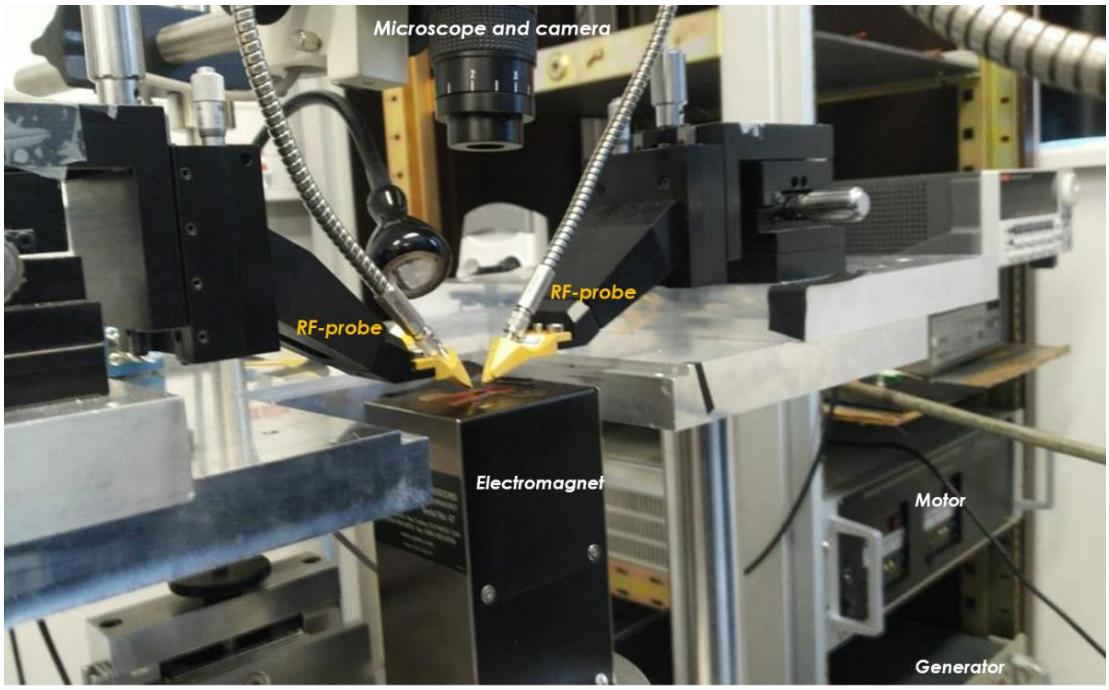

Figure 3-3: The experimental set-up of the Propagating spin wave spectroscopy (PSWS).

To detail the mechanism, as shown in ***Figure 3-4***, from the VNA port, we inject a microwave current $I_{rf}(\omega)$ into the emitter antenna. As a result, a local dynamic magnetic field $h_{rf}(\omega)$ is created in its vicinity. This alternating field couple with the underlying magnetic film (of thickness t) and transfer its energy to the magnetic moments in the film. Therefore, the magnetization $\boldsymbol{m}(\omega, k)$ undergoes a non-uniform precession, leading to the excitation of spinwaves.

These spinwaves can propagate in a direction perpendicular to the antenna, and in both direction (to the left and right of the emitter) with k-vectors that are imposed by the antenna excitation spectrum. Therefore, these spinwaves will propagate and reach the second antenna, where they generate a varying flux translated by an rf-voltage $V(\omega)$.

It's worth to mention that, when conducting the measurement with the VNA, it sweeps two times. In the first, antenna 1 act as an emitter while antenna 2 as a detector, and vice versa for the second sweep.

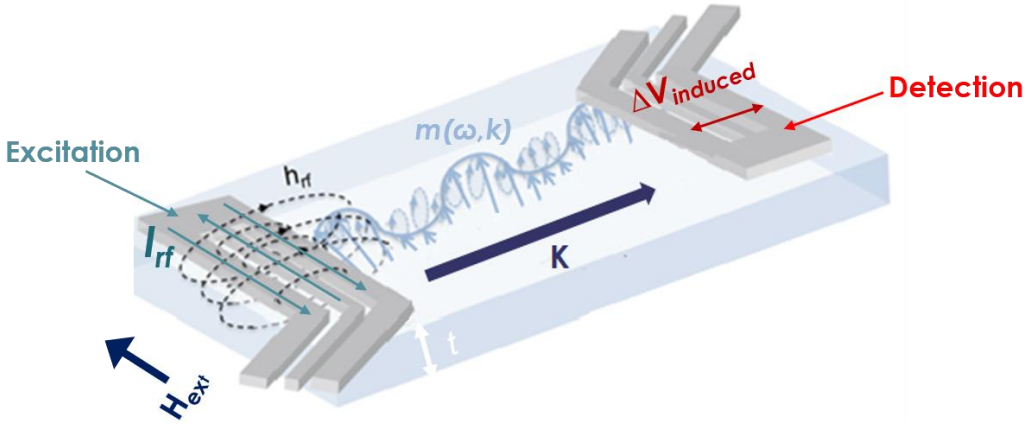

Figure 3-4: Scheme of the experimental set-up highlighting the principle of propagating SW spectroscopy: *The spinwaves are excited with an rf-current injected in the antenna, this will generate an rf-field that will couple with the magnetic layer. The spinwaves are thus excited and propagate with a wavevector k towards the second antenna where, they are detected through voltage variation ΔV.*

3.3.2 About the antenna's excitation spectrum

The k-selectivity of the antenna is determined by its excitation spectrum, that is influenced by several factors as the shape, size, and material composition. This spectrum of the antenna(in the k-space) is given by the Fourier transformation of the linear microwave current density . This quantity when normalized by the total current I which is proportional to the SWs inductance (*5*).

We consider that our problem is an infinitely long strip line of width w, thus the current spatial current density distribution is given by the following crenel function:

$$J(x) = \frac{I}{w}$$

(Eq. 3-1)

where x is the region from 0 to w.

The Fourier transform of the current density in a signal line of width w_s is given by the following expression:

$$\left|\frac{\tilde{J}(k_x)}{I}\right| = sinc(\frac{k_x w_s}{2})$$

(Eq. 3-2)

In the case of many lines, as for the Ground-Signal-Ground antenna that we used for most of our experiments. One can use the linearity of the Fourier transform and so we can up each line contribution provided the correct phase is used and that the current distribution is identical to each line:

$$\left|\frac{\tilde{J}(k_x)}{I}\right| = sinc\left(\frac{k_x w_g}{2}\right)e^{jk_x\left(\frac{w_g}{2}\right)} + sinc\left(\frac{k_x w_s}{2}\right)e^{jk_x\left(w_{gap}+\frac{w_s}{2}+\frac{w_{groumd}}{2}\right)} + sinc\left(\frac{k_x w_g}{2}\right)e^{jk_x\left(2w_{gap}+\frac{w_s}{2}+wg\right)}$$

(Eq. 3-3)

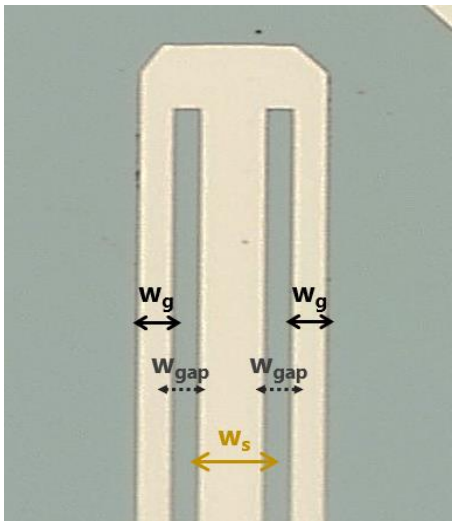

Figure 3-5: Optical image of a Ti/Au G-S-G antenna patterned by e-beam lithography: *A representation of the widths definitions as used in the manuscript.*

3.3.3 Measuring with Vector Network Analyzers (VNA):

A Vector Network Analyzer is an instrument that helps to measure the amplitude and the phase of a signal.

The specificity of this instrument is that it contains both the source and the receiver. The source is to provide a stimulus signal while the receiver is to collect this signal after passing through the device under test (DUT). Therefore, the VNA measures the received signal, that can be, a transmitted signal between one injection port to another, or also the signal that is reflected to the same injection port.

The receivers of the VNA compare it with the injected where we can have the results on either the VNA itself (internally) or externally via a computer. In the following, the results obtained from PSWS are done via a 4-port VNA (**R&S®ZVA67**), where only two ports were used.

A. The S-parameters:

The data collected by the VNA are represented by parameters called Scattering Parameters (S-parameters), which are represented in a 2x2-matrix. The S-parameters are complex values (with a real and an imaginary part) that fully characterize the behavior of the device under test in frequency domain (by giving access to the amplitude and phase)

$$S(\omega) = \begin{pmatrix} S_{ii} & S_{ij} \\ S_{ji} & S_{jj} \end{pmatrix}$$

(Eq. 3-4)

where,

$S_{ii} = \frac{Wave\ reflected\ from\ port\ i}{Wave\ incident\ at\ port\ i}$, are the reflected S-parameters

$S_{ij} = \frac{Wave\ transmitted\ at\ port\ i}{Wave\ incident\ at\ port\ j}$, are the transmitted S-parameters

From the S-parameters we can extract the rf-voltage $V(\omega)$, where ω stands for the excitation frequency of the VNA. If a signal is injected in port 1 with a signal V^+ one part of this signal is reflect at the same port with the same amplitude V^-. Yet other part from the signal is transmitted with V_2^-that is detectable at port 2, and vice versa for the second antenna. This leads to the following matrix giving the relationship between the injected (V^+) and the transmitted or reflected voltages (V^-):

$$\begin{pmatrix} V_1^- \\ V_2^- \end{pmatrix} = \begin{pmatrix} S_{ii} & S_{ij} \\ S_{ji} & S_{jj} \end{pmatrix} \begin{pmatrix} V_1^+ \\ V_2^+ \end{pmatrix}$$

(Eq.2-3-5)

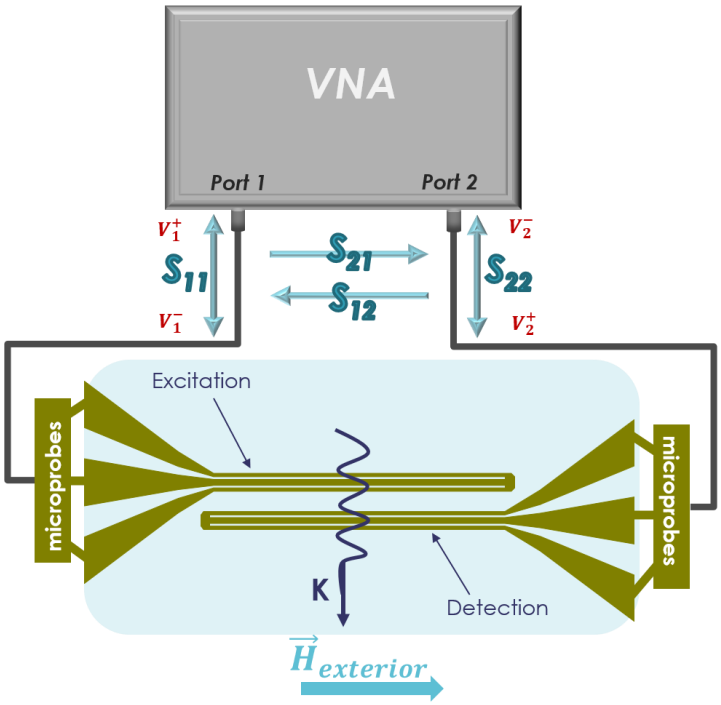

Figure 3-6: Schematic of the PSWS experiment with the VNA-parameters.

Since our measurement are by the use of gold antennae, the coupling between the antennae and the insulating YIG is purely inductive. Therefore, to give a physical insight to our measurements, it is important to convert the S-parameters into Inductance parameters. This is done by the following mathematical transformation:

$$Z(\omega) = \frac{V(\omega)}{I(\omega)} = j\omega\, L(\omega)$$

(Eq. 3-6)

Leading to,

$$L(\omega) = \frac{Z_0}{j\omega}(I_2 - S(\omega))^{-1}(I_2 + S(\omega))$$

(Eq. 3-7)

where,

$L(\omega) = \begin{pmatrix} L_{ii} & L_{ij} \\ L_{ji} & L_{jj} \end{pmatrix}$, $I_2 = \begin{pmatrix} 1 & 0 \\ 0 & 1 \end{pmatrix}$ and, Z_0 = *the impedance of the VNA ports (5 ohms)*

B. Calibration of the VNA:

Despite the high efficiency of Vector Network Analyzer (VNA) measurements, various losses can occur due to errors in the VNA internal circuit, associated cabling, and the 40 GHz Z probes from Formfactor. These losses can affect the measurements by introducing some noise and deformation to the signal. To fix this issue, a calibration process is performed to remove these losses and eliminate any parasitic signals.

One commonly used calibration technique is the Short-Open-Load-Thru (SOLT) calibration method. For this, a calibration substrate provided by FormFactor is used, on which we can find elements with known standards that are LOAD (match), OPEN, SHORT (reflection standards) and THRU (transmission standards). To do the SOLT calibration we connect the VNA to the calibration substrate by the microprobes and we perform measurements of the Short, Open, Load, and Thru (50 ohms) the one after the other.

The Short standard is a short-circuited termination with negligible physical length. it is modeled as a transmission line length and a frequency-dependent inductance L. When connected to the VNA, it establishes a reference for zero electrical length. The VNA measures the reflection coefficient of the Short, and this value is used to subtract delays or phase shifts in the measurement.

The Open standard works as a reference for infinite electrical length. It is modeled as a transmission line length and a frequency-dependent capacitance C. It compensates reflections and impedance mismatches at the end of the transmission line. During calibration, the VNA measures the reflection coefficient of the Open to correct these effects in next measurements.

The Load calibration standard, set at 50 ohms impedance, acts as a reference for a matched termination, enabling more accurate measurements for reflection coefficients. It is modeled as a transmission line length, a shunt capacitance, a resistance, and a series inductance.

The Thru calibration standard ensures precise measurements for transmission coefficients. It is modeled as a transmission line length with some frequency dependent loss, given by:

$$Loss(f) = Loss(f_0)\sqrt{\frac{f}{f_0}}$$

(Eq. 3-8).

Thus, it counts for the losses that are caused by phase shifts or any contribution external or internal components of the VNA such as connectors, cables, the ports etc.

After the calibration is done, the VNA has collected all the data needed so that it can compare it with the S-parameters files of the 'ideal' standards. Thus, it will create a baseline reference, that can compensate the systems losses and imperfections when measuring the DUT.

C. The measurement parameters.

To minimize the noise level, some parameters in the VNA can be set before starting a measurement such as the bandwidth of the processed signal, the averaging over data points and the number of points.

- ***The bandwidth (IFBW)***

The VNA transforms the signal from its source into a lower intermediate frequency (IF). This bandwidth is adjustable and can be set down to 10Hz (in the ZVA). To get rid of parasitic noise in a signal, one needs to reduce the BW. However, this will lead to an increase in the sweep time, as a tenfold decrease in the IF bandwidth results in a 10 dB reduction of noise.

- ***Averaging factor***

In the VNA one can set the number of consecutive sweeps to be averaged. An average over several sweeps reduces random effects on the signal and thereby enhance its shape. As in the case of IFBW, increasing the average factor will require an increase in the sweep time.

- ***The power level:***

The Power level is the strength of the RF signal that is injected into the material under study. The more power we inject, the stronger the excitation of SWs, thus the less signal to noise ratio. However, heating effects can affect the measurements in this case, as well as that excessive power in garnets for example leads to non-linear excitation of SWs which alter the SWs behavior. As a precaution, conducting a power sweep prior to measurement can be advantageous. This sweep helps to identify the power threshold beyond which the system enters the non-linear regime.

In addition to these parameters that aim to reduce the noise level, other parameters can be set to conduct the measurement such as the frequency sweep range, the number of points (i.e., the frequency step) that are also crucial to define the resolution of the signal.

D. Time domain option:

Throughout my Ph.D., we utilized the time domain option available in our vector network analyzers. The importance of this technique lies in visualizing the data from the PSWS in function of time. With this, one can eliminate noises, fluctuations and eventually differentiate between the different modes arriving with different time delays but with close resonance frequencies. In **Chapter 4** we provide a full description and explanation of this technique.

3.4 BIBLIOGRAPHY:

1. W. Fahrner, *Nanotechnology and Nanoelectronics: Materials, Devices, Measurement Techniques* (Springer Berlin Heidelberg, 2005; https://books.google.fr/books?id=Y-g2FL8Qv2kC)*EngineeringPro collection*.

2. E. Sharma, R. Rathi, J. Misharwal, B. Sinhmar, S. Kumari, J. Dalal, A. Kumar, Evolution in Lithography Techniques: Microlithography to Nanolithography. *Nanomaterials* **12** (2022).

3. C. Vieu, F. Carcenac, A. Pépin, Y. Chen, M. Mejias, A. Lebib, L. Manin-Ferlazzo, L. Couraud, H. Launois, Electron beam lithography: resolution limits and applications. *Applied Surface Science* **164**, 111–117 (2000).

4. Y. Zhang, J. Um, B. Stadler, R. Franklin, Permeability and Ferromagnetic Resonance Study for Magnetic Nanowires Substrate With Copper Layer. *IEEE Microw. Wireless Compon. Lett.* **30**, 1065–1068 (2020).

5. V. Vlaminck, M. Bailleul, Spin-wave transduction at the submicrometer scale: Experiment and modeling. *Phys. Rev. B* **81**, 014425 (2010).

4 CHAPTER 4: TIME DOMAIN USING VECTOR NETWORK ANALYZERS

In this chapter, we will present how to extract time-domain information about propagating spin-wave packets using a standard Vector Network Analyzer (VNA). This approach, based on the inverse Fourier Transform of the frequency domain data acquired by the VNA, has recently been introduced and mathematically described by Devolder et al. (1). Here, we will explain the main principle behind this approach and demonstrate that it can be achieved using the commercially available time-domain option of most VNAs. To do this, we will conduct measurements on a well-known spin wave material, namely, nanometer-thick Yttrium Iron Garnet (YIG).

The motivation behind performing VNA measurements in the time domain rises from the ability to visualize multiple modes propagating at nearby frequencies, each with different group velocities. This will allow us to recognize the origin of these modes and study the spectrum of individual isolated modes using time gating. Thus, having all the advantages from the VNA, we can now measure propagating spin-waves by using all-electrical means, with an enhanced measurement quality, enabling us into to extract more information from the rich signal of the measured SWs.

However, it should be noted that this approach, based on continuous wave (CW) excitation, cannot provide information about the transient regime of spin waves. To access the transient regime of spin waves, one would need to perform pulsed VNA measurements, which are beyond the scope of this study.

To understand this technique, we will focus on the propagation of spin waves in a nanometer-thick YIG waveguide in both the Damon Eshbach and the backward volume wave configurations (2-4). These spin waves will be excited by radio-frequency (RF) gold antennas of the Ground-Signal-Ground (G-S-G) type.

This chapter is divided into three parts, where in the beginning, we will discuss the properties of the YIG material, and the structure of the device under study, as well as the antenna design. In the second part, we will explore the expected dispersion relation of spin waves from the Kalinikos and Slavin spin wave dispersion model. The model used is for the case with a material having an in-plane magnetization and within the dipole-exchange regime (cf. Chapter 2).

Thereafter, in the last part we present the measurements performed in the time domain and explain all the needed parameters to take into consideration. We will further investigate the different spinwave modes and their properties, analyze the obtained data and compare with the measurements conducted in the frequency domain.

4.1 DESCRIPTION OF THE MATERIAL AND THE PATTERNED DEVICE:

The material under study consists of a 500 nm-thick Yttrium Iron Garnet (YIG) grown over a GGG substrate (500 µm). It consists of an etched 120 µm wide and 450 µm long YIG waveguide. To excite the spinwaves, we fabricate, by optical lithography, two G-S-G antennas placed on top of the YIG, made from a 20 nm Titanium (Ti) over a 280 nm layer of Gold (Au). The distance between the two antennae is of 15 µm (measured from edge-to-edge)

The antenna design, excitation spectrum and nanofabrication processes of the whole device have been explained in detail in **Chapter 3**.

As discussed, the excitation spectrum of a given antenna depends on its design. This spectrum, obtained from the Fourier transformation of the current density distribution (given by a cardinal sine function) in the antenna, is depicted in ***Figure 4-1*. b)** by the blue curve and corresponds to the spectra associated with the utilized GSG antenna. The signal line of the antenna has a width $\mathbf{w_s}$ of 4 µm, while the ground lines are $\mathbf{w_g}$ of 2 µm wide, with a separation distance **s** of 2 µm between them (see ***Figure 4-1*. a)**).

From the spectrum, one can notice that the highest amplitude is achieved at a wavevector of k= K_1 = 0.6 rad/µm. This wavevector corresponds to the most efficiently excited spin wave by the RF antenna. Following this peak at K_1, there are two additional peaks of lower amplitude K_2 , K_3 and K_4 and the presence of their corresponding excited SWs will be discussed later in this chapter.

The dispersion relation for the in-plane YIG waveguide, for the Backward Volume Waves (BW, in full black line) and the Damon Eschbach (DE, in dashed black line) configuration, are presented in ***Figure 4-1***. **b)**. As shown, it presents the relationship between frequency and wavevector **k** for a given external field of 100 mT.

We emphasize that the propagation direction of the spin waves is perpendicular to the antenna, i.e., in this case, in the x-direction (k_x), while the applied external field ($\boldsymbol{H_{ext}}$) lies in the plane parallel to k, i.e. $\boldsymbol{H_{ext}} \,//\, \boldsymbol{k}$ for BW and perpendicular to k, i.e. $\boldsymbol{H_{ext}} \perp \boldsymbol{k}$ for DE configurations.

In the BW configuration, the excitation by inductive antennae is solely influenced by the out-of-plane component of the dynamic field. This is due to the fact that the x-component aligns parallel to the equilibrium magnetization. On the contrary, in the DE configuration, the excitation is affected by both the z-component and x-component. Consequently, the BW configuration is less efficiently excited by inductive antennae than the DE modes.

We conducted this study in both configurations to highlight the importance of the time domain measurements in investigating the different SWs modes properties.

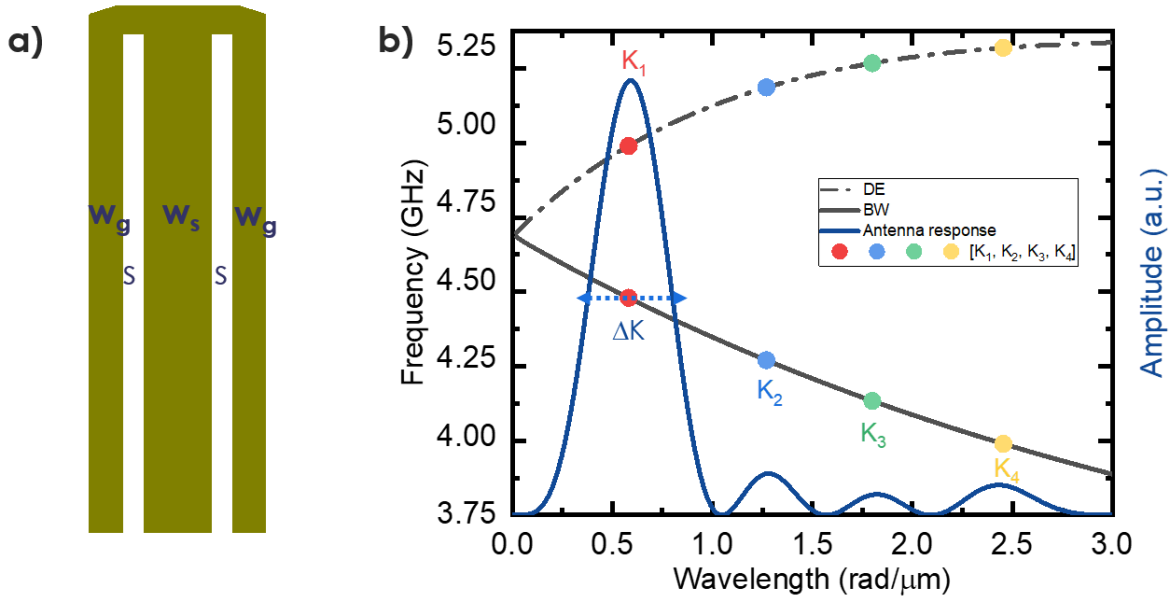

Figure 4-1: Antenna design and excitation spectrum: *a) G-S-G antenna design with w_g, w_s, and s being the ground width, signal width and their separation distance respectively. b) the excitation spectra of the antenna in a) obtained by Fourier transform of the current density distribution (blue line), showing maximum k-vector at a value of K_1= 0.6 rad/μm. The full and dashed lines represent the BW and DE dispersion relations with an external field of 100 mT, respectively.*

Moreover in ***Figure 4-1***. **b)**, the red points correspond to the peaks related to the antenna spectrum, indicating the resonance frequencies associated with their corresponding value of wavevectors. Thus, we can get resonance frequencies of ~ 4.1, 3.9 and 3.75 GHz for wavevectors at values of k= K_1, K_2 , K_3 and K_4 respectively at a field of 100 mT.

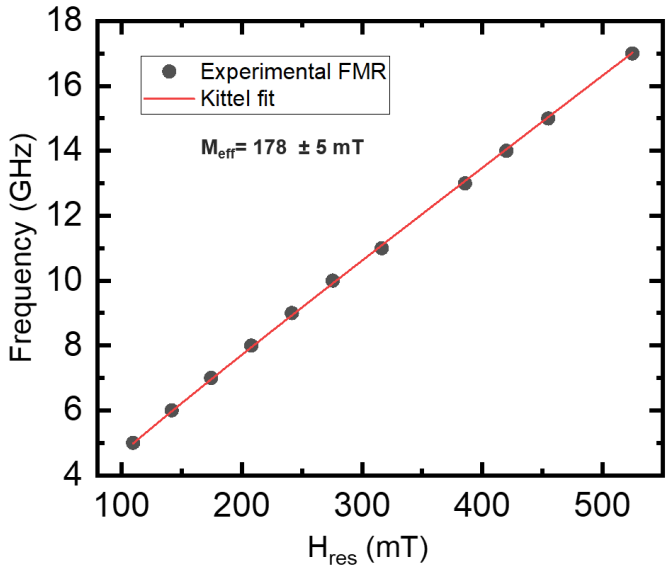

Figure 4-2: FMR experiment: *Plot showing the frequency with respect to the resonance fields extracted from the FMR measurements (black points). The red line represents a fit using the Kittel formula, resulting in a M_{eff}= 1780 G*

To determine the magnetic properties of the material under study, we conducted FMR

measurements. We fix the frequency while sweeping the external magnetic field and thus we can recognize at which field the resonance occurs for the given frequency. The measurements were taken at a power level of 10 dBm (without being in the nonlinear regime).

This measurement was repeated at different frequencies, enabling us to generate the plot shown in ***Figure 4-2***. These data points were subsequently fitted to the Kittel formula, resulting in the extraction of an effective magnetization value of 1780 G.

4.2 MEASUREMENTS IN FREQUENCY DOMAIN:

4.2.1 Reflection and Transmission spectra

A. Calibration of the VNA

Despite the high efficiency of Vector Network Analyzer (VNA) measurements, various losses can occur due to errors in the VNA internal circuit, associated cabling, and the 40 GHz Z probes from FormFactor. These losses can affect the measurements by introducing some noise and deformation to the signal. To fix this issue, a calibration process is performed to remove these losses and eliminate any parasitic signals.

One commonly used calibration technique is the Short-Open-Load-Thru (SOLT) calibration method. For this, a calibration substrate provided by FormFactor is used, on which we can find elements with known standards that are LOAD (match), OPEN, SHORT (reflection standards) and THRU/LINE (transmission standards). To do the SOLT calibration we connect the VNA to the calibration substrate by the microprobes and we perform measurements of the Short, Open, Load, and Thru (50 ohms) the one after the other.

B. Parameters of the measurements:

In the presented measurements, we used a 500-nm-thick YIG sample. The frequency domain sweeps were conducted from 2 GHz to 8 GHz with a step of 1 MHz, which is a total of 6001 data points. We applied an averaging factor of 2 to enhance the signal quality. The excitation power was set at -20 dBm throughout the measurements. To achieve the BVW configuration of spin waves, the frequency sweeps were performed by varying the exterior field values in a direction parallel to the antennae, while in a perpendicular direction to achieve DE configuration.

4.2.2 Reflection and Transmission spectra

In the following section, we performed Propagating Spin Wave Spectroscopy (cf. **Chapter 3**). We present an analysis of a frequency sweep ranging from 2 to 8 GHz, along with a swept external field applied in the plane of the film and perpendicular to the antenna direction, as illustrated in the ***Figure 4-3***. **b)**. To excite these spin waves, we connected two of the VNA ports, each to a microprobe in which an RF current is injected. The microprobe, now in contact with the gold pads of the antennas, injects the RF currents, thereby generating RF-magnetic fields. These fields interact with the magnetization of the YIG, and as a result, we can effectively detect these excitations through the S-parameters collected by the VNA.

Given that our measurement technique is inductive, we are interested in understanding the signal's inductance. For this reason, it is convenient to transform the S-parameters (in dB) into L-parameters (in Henry) (cf. **Chapter 3**).

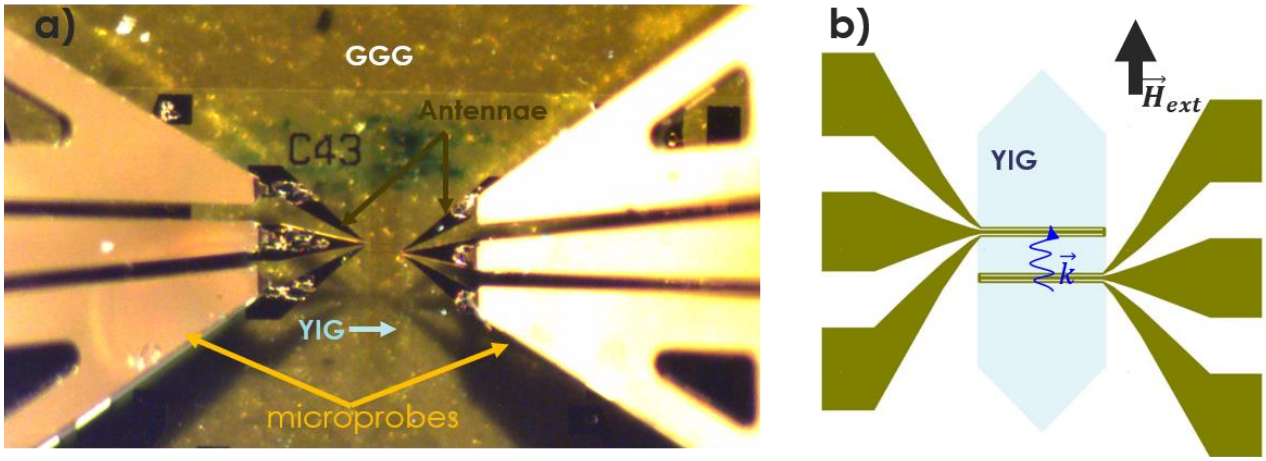

Figure 4-3: The connected device. *a) Optical image of the device under study, named C43, showing a YIG waveguide surrounded by the GGG substrate, and two gold antennae that are connected to the VNA via the RF-microprobes. b) Sketch of the design: it shows the direction of propagation direction of the excited SWs by the RF-antennae in the YIG waveguide, given by the wavevector* $\vec{k}$*. The external field* $\vec{H}_{ext}$ *is applied parallel to* $\vec{k}$ *resulting in the Backward volume wave configuration.*

A. Transmission Spectra:

Firstly, we will focus on the transmission signal of the spin waves. The excited spin waves, excited by the RF-field of the antenna, propagate in the waveguide and reach the second antenna. There, they generate a varying flux, thereby inducing an RF-voltage across the antenna. This, in turn, leads to the detection of the transmitted S-parameters and thus of the induced inductance of these propagating spin waves.

The transmission spectrum is constituted of two primary components: the direct electromagnetic interaction linking the antennae, namely the cross-talk, and the magnonic interactions leading to the propagation of spin waves.

Two important information are encoded within this signal; the propagation losses from the amplitude and the phase from the imaginary part. From the former, we could extract the spin-diffusion by comparing the signal amplitudes from devices separated by two different distances d. From the latter, we can extract the group velocity, which will be described in detail in the next sections.

In ***Figure 4-4***. **a,c)**, we present the transmitted inductance parameters $|L_{21}|$ as function of the applied magnetic field parallel to the k-vector (BW configuration). As seen, the spectrum consists of several branches: one broad main branch that is followed by less intense peaks at lower frequencies. To understand the signal's shape, we took a cross-section of the colormap in ***Figure 4-4. b,d)*** at a given field of $\mu_0 H_{ext} = 100\, mT$, where we plot the transmitted inductance in function of the frequency. The spectrum consists of one main lobe (the absolute value) containing the associated oscillations (the imaginary part) preceded by a secondary lobe with its corresponding oscillations.

When focusing on the main resonance, it becomes evident that in both the absolute value

and more importantly the imaginary part hosts some ripples. This implies that we have a mixture of propagating modes hindered within our spectrum. These modes propagate at similar or very nearby frequencies but each at a different group velocity, i.e., different propagation time. Thus, the presence of these ripples adds complexity to the extraction of the group velocity from the signal measured in frequency domain. To differentiate between these modes, we need to access their propagation time, which is done later in *section 4.3* by performing time domain measurements.

In our case it is still feasible since here we are dealing with a significantly thick YIG waveguide, thus the noise to signal ratio is quite low, however in other systems where the inductive response is low, the group velocity extraction becomes impossible. Again, this is where a time domain-VNA measurement is needed.

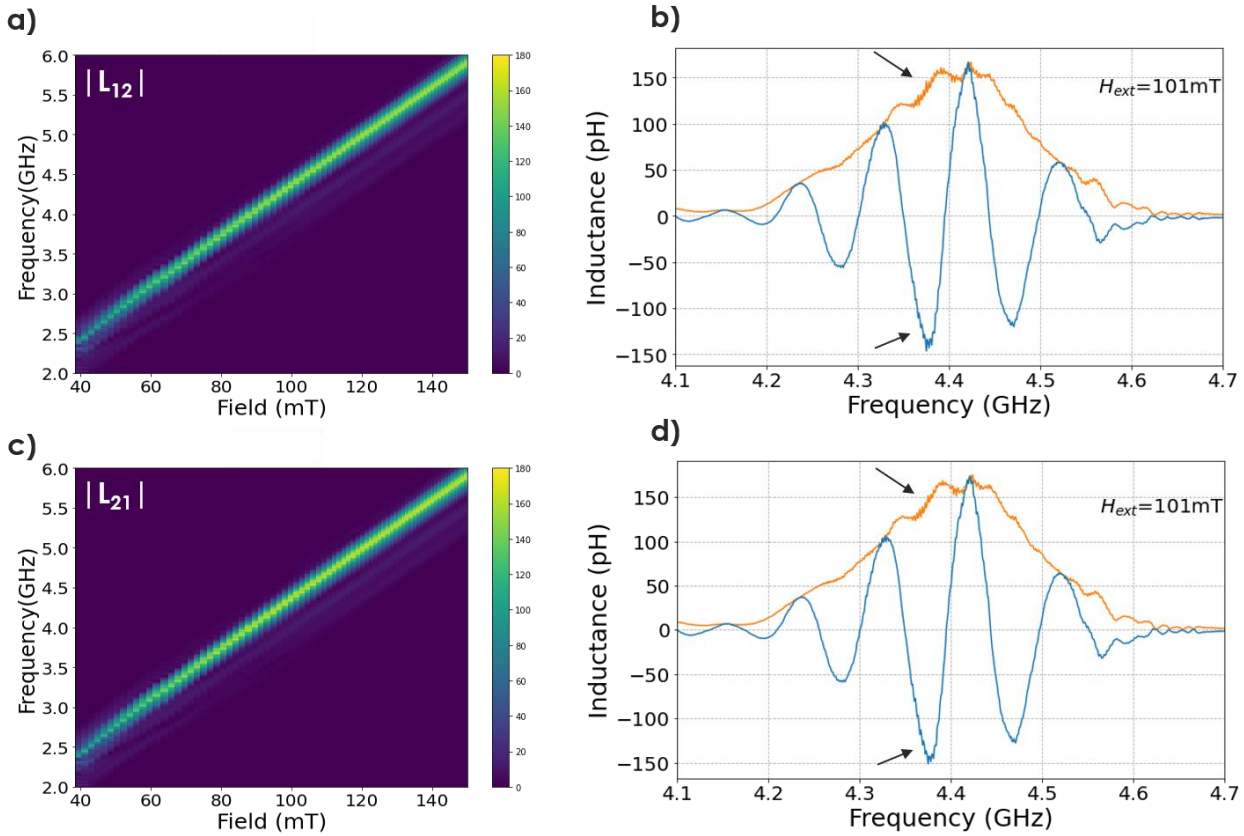

Figure 4-4: Transmission Spectra: *a) and c): colormap showing the absolute value of the inductance parameter L_{12} and L_{21} respectively in function of the swept fields and frequencies. b) and d) shows the shape of the resonance peaks in function of the frequencies at an applied fields $\mu_0 H_{ext}$=101mT, the orange line is the absolute value while the blue oscillations are the imaginary part.*

B. Reflection Spectra:

The reflection spectrum of spin waves measured by the VNA is the signal reflected from one antenna and then reflected back to itself. At each applied field, the VNA sweeps along the given frequency range, and when the detected reflected signal peaks at some given values of the frequency, this is the resonance. Thus, it provides us with information about spin waves

that are excited underneath the antenna ($k = 0$, non-propagating SW) as well as the signal from the reflected SWs after traveling the waveguide ($k > 0$). These non-propagating SWs are described by the Kittel formula and therefore one can extract information about the magnetic properties within the material, such as the effective magnetization, anisotropies, and the damping.

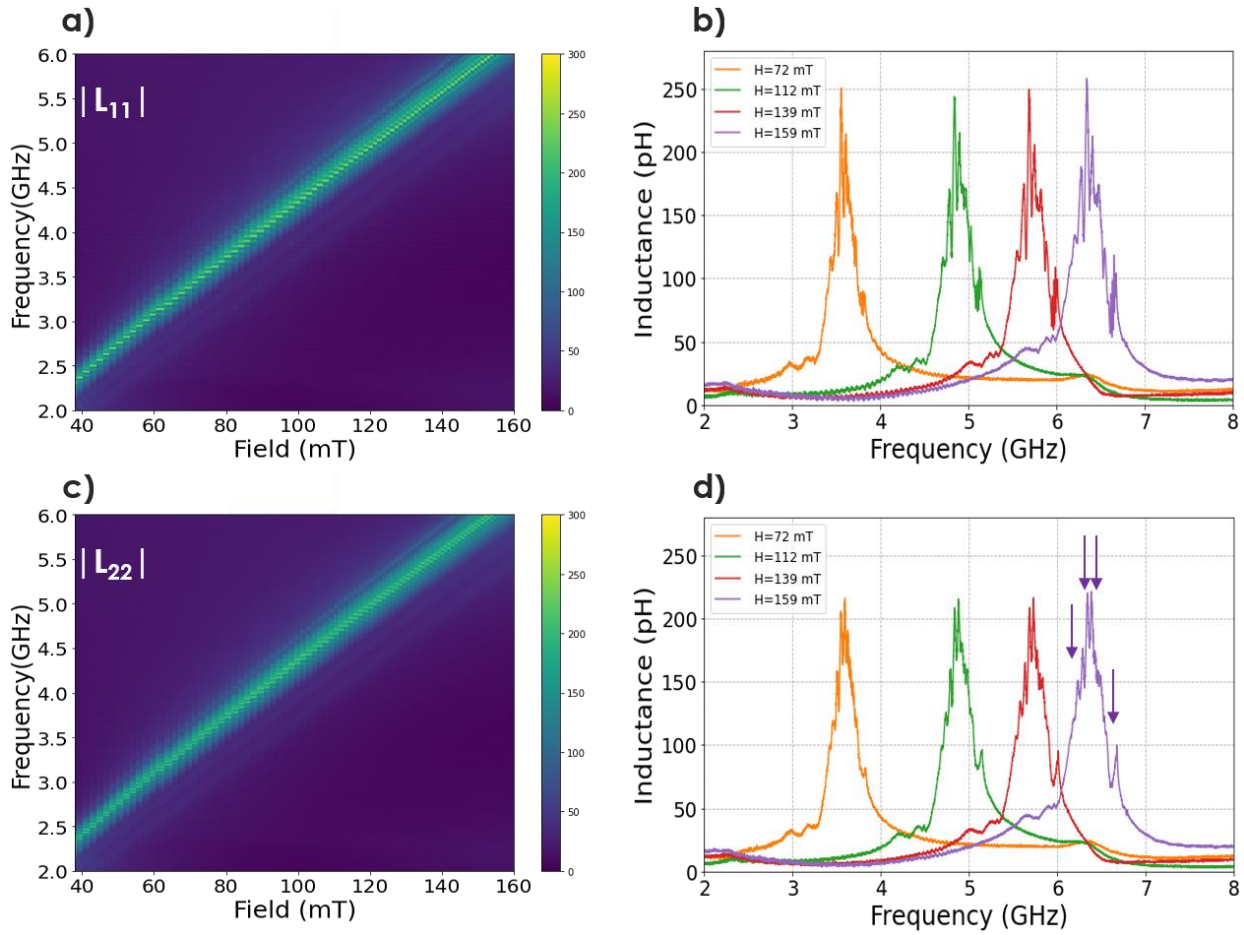

Figure 4-5: Reflection Spectra: *a) and c): colormap showing the absolute value of the inductance parameter L_{11} and L_{22} respectively in function of the swept fields and frequencies. b) and d) shows the shape of the resonance peaks in function of the frequencies at several applied fields: $\mu_0 H_{ext}$= 39.37, 76.8, 110.58, 134.82 and 153.84 mT*

In ***Figure 4-5***. **a), c)** we show the colormap constructed by taking the absolute values of the reflected inductance parameters collected from port 1 and port 2 of the VNA (L_{11} and L_{22}, respectively) as functions of the swept fields and frequencies.

As seen, the spectrum consists of several branches: one main intense branch that is followed by less intense peaks at lower frequencies, as well as a narrow branch at slightly higher frequencies than the main one. This is a result of the shape of the resonance peak, which as shown from the figures ***Figure 4-5***. **b), d)**, is constituted of multi-peaks (see arrows).

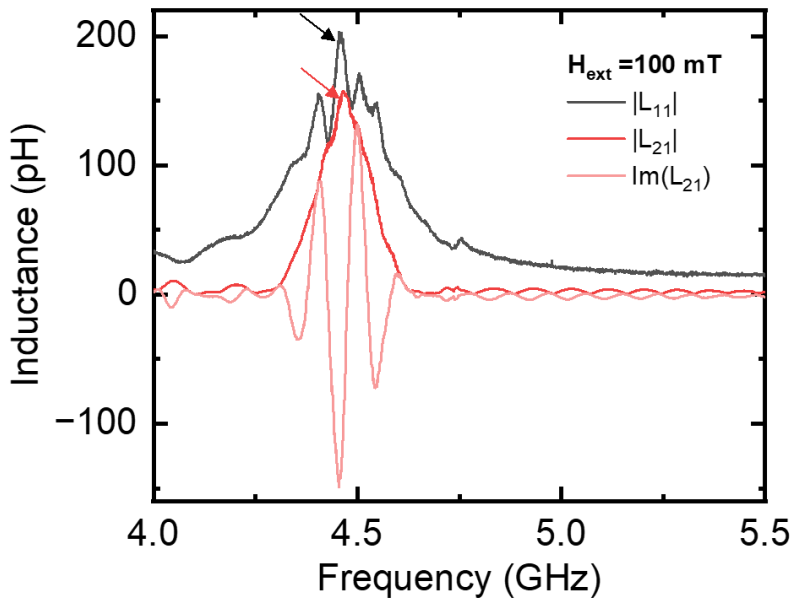

***Figure 4-6: Comparing transmission and reflection**: $|L_{11}|$, $|L_{21}|$ and $im(L_{21})$ at $\mu_0 H_{ext}$ = 100 mT. $|L_{11}|$ has a multipeak shape due to reflections in the YIG waveguide while $|L_{21}|$ peaks around one frequency (~ 4.45 GHz). The overlap between L_{21} and L_{11} indicates that the main resonance peak in $|L_{11}|$ is due to a k>0.*

Now to recognize whether the main peak is an FMR peak, one need to compare the reflection and transmission signals. If both represents a resonance at the same frequency at the same field, then this is mainly due to the excitation of a spinwave at $k > 0$, on the contrary if the resonant frequency is shifted then, the one in the reflection spectrum is due to $k = 0$ (FMR) and thus can be fitted with Kittel model.

Therefore we represent this in ***Figure 4-6***, where the highest amplitude peak of the L_{11} curve (in black) and the peak present in the signal of L_{21} (in red) overlap at the same frequency (around 4.5 GHz), indicating by so, that the highest excited mode represented in the reflection spectrum corresponds to a non vanish wave-vector.

In ***Figure 4-7*** we plot the theoretical curve of the resonance frequency with respect to the applied magnetic field at $k = 0$ (black line) and $k = K_1$ (red line), with the M_{eff} found with the FMR measurements on the film ($M_{eff} = M_s$ = 1750 G) . Then, we extract the frequencies of the peaks represented in L_{11} spectra. We find that the last peak of the spectrum matches well with the curve of $k = 0$, while the most intense peak corresponds to the $k = K_1$ (the one overlapping with L_{21}).

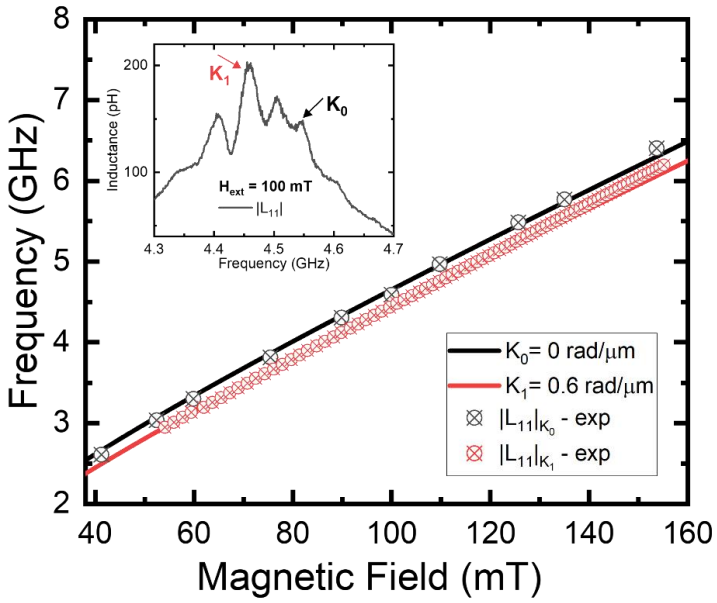

Figure 4-7: Experimental versus theoretical: *Full lines (black and red) represent the theoretical curves of the resonance frequency versus the applied field for k=0 and k=0.6 rad/µm. The points are resonance frequencies extracted from the L_{11} experimental spectra. Inset show $|L_{11}|$ in function of frequency at a field of 100 mT.*

- ***Discussion***

In addition to what has been discussed above, one can notice that the reflection spectrum hosts several peaks around the maximum. This issue has been addressed in chapter 6 in the thesis of Hugo Merbouche, where a complete study of the delay line was conducted.

The difference here is that we are dealing with a relatively thick film. Therefore, the multiple peaks are most likely related to the non-propagative excited modes underneath the antenna, which can also be explained by the transmission peak shape representing only one peak (as in ***Figure 4-6***)

4.2.3 Group velocity extraction

In the following we will explain how to extract the group velocity, first we will show what is expected from theory, then we will explain how to extract them from the experimental data from the PSWS experiment.

A. The expected group velocity (from theory):

By differentiating the frequency with respect to wavevector ($\frac{\partial f}{\partial k}$) using the equation derived from the Kalinikos-Slavin formulation (*5*) (cf. **Chapter 2**), for magnetostatic spin waves with no anisotropies, we can determine their group velocity. This helps us to construct the curve depicted in ***Figure 4-8*** which presents the group velocity as a function of wavevector ***k***.

Specifically, we can extract the expected group velocity for each spinwave mode of the antenna. The corresponding group velocities for an external field of 100 mT are gathered in ***Table 4-1*** in both DE and BW modes.

k (rad/µm)	v_g in DE (km/s)	v_g in BW (km/s)
K_1 = 0.6	2.22	-2
K_2= 1.27	1.19	-1.65
K_3= 1.8	0.67	-1.45
K_4= 2.45	0.3	-1.21

Table 4-1: Calculated group velocities for DE and BW modes:*The group velocities associated to each mode of the antenna in both DE and BW configurations. The values are calculated for an external field of 100 mT.*

By such, we can directly access the propagation characteristics of different spin-waves modes in the system, which is crucial for optimizing the performance of the antenna depending on the application we need.

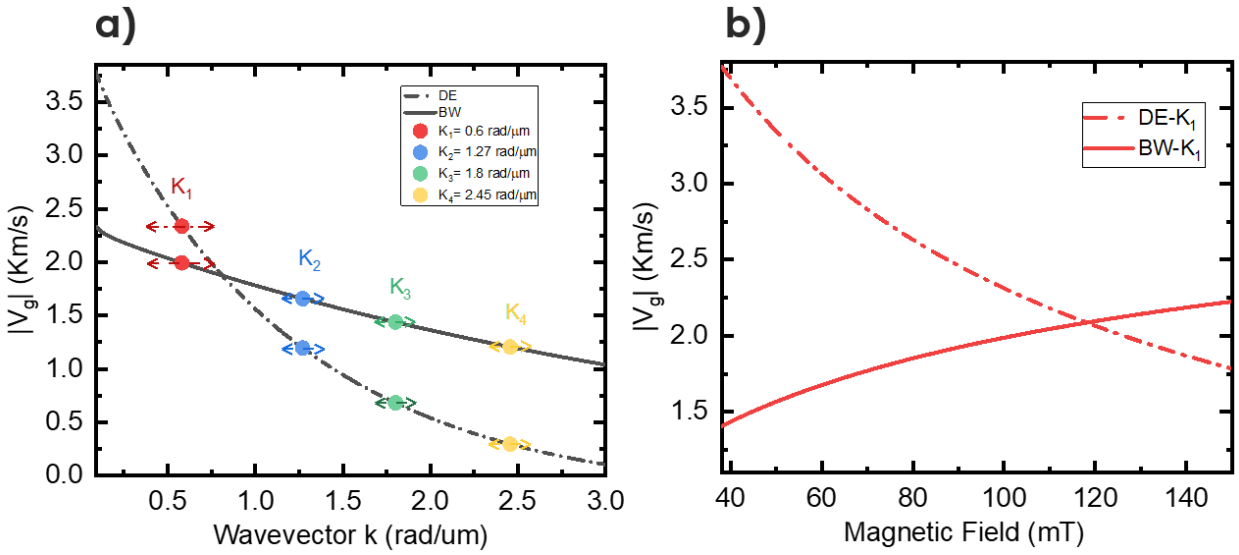

Figure 4-8: *Analytical Group velocity adapted from Kalinikos and Slavin: a)The absolute group velocity in the 300-µm wide YIG conduit extracted from the derivative of the frequency w.r.t to k, for the MsBVW (BW, full line) and MsSW (DE ,dashed line), on each of the lines we represent the k-values excited by the antenna (k_1,k_2, k_3 and k_4). b) The absolute group velocity in function of the applied field at one given $k=K_1$ for BW full lines and DE modes (dashed lines).*

B. The extracted group velocity (from experimental data):

The VNA is phase-sensitive, meaning that the collected S-parameters are complex quantities with real and imaginary parts (as explained in **Chapter 3**), where the phase is accessed from the imaginary part. From ***(Eq. 2-40)***, which describes the SW as a propagating wave, the phase can be written as:

$$\varphi = kd - \omega t + \varphi_0$$

(Eq. 4-1)

Here, 'd ' represents the distance propagated by the wave. Thus, the derivative of the phase with respect to the wave vector is:

$$\frac{d\varphi}{dk} = d$$

(Eq. 4-2)

which is equivalent to:

$$\Delta\varphi = \Delta k \cdot d$$

(Eq. 4-3)

Now, the VNA measures the accumulated phase delay at its ports. When the phase delay at one port is equal to one period of oscillations (2π), it means that the spinwave has propagated the distance *s,* that is the separation between the antennae. In other words:

$$2\pi = \Delta k \cdot s$$

(Eq. 4-4)

Thus, we can, from the imaginary part, extract the group velocity by the following formula:

$$v_g = \frac{d\omega}{dk} \approx \frac{\Delta\omega}{\Delta k} = \frac{2\pi\Delta f}{\Delta k} = \Delta f \cdot s$$

(Eq. 4-5)

As illustrated in ***Figure 4-9***, Δf corresponds to the frequency difference between peak-to-peak oscillations in the imaginary part of the transmitted signal, during a phase delay of 2π. This allows us to estimate the group velocity of the spinwave modes from the S-parameters, and it provides valuable information into the wave propagation characteristics in the system.

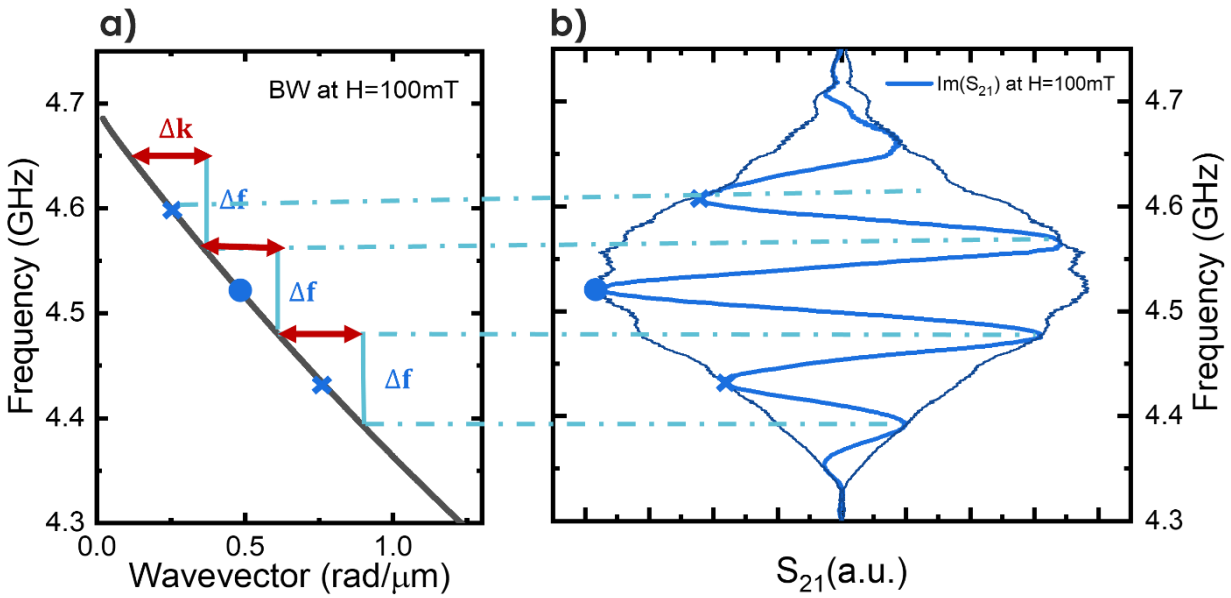

Figure 4-9: Indirect method to extract group velocity: *a) Analytical dispersion equation showing the frequency versus the k vector (BW mode). c) Im(S_{21}) (blue) in function of frequency, showing the frequency difference Δf in a phase difference Δφ of 2π , that is the frequency taken from peak-to-peak oscillation. The main peak is presented as the blue dot on the curve of a) along with the secondary peaks as the crosses. The distance between the cross and the point is 2π.*

- ***Applying the extraction method to the frequency domain measurements:***

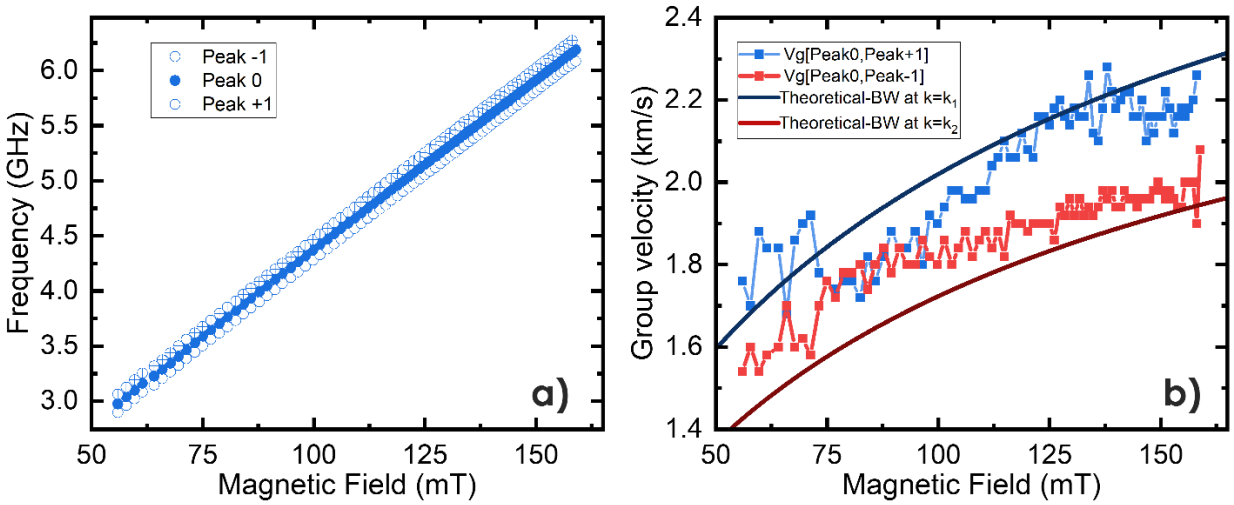

Figure 4-10: Group velocity extraction from frequency domain measurements: *a) Extraction of the oscillation's peaks from the imaginary part of L_{21} in function of frequency and field, central peaks data points(named Peak 0) are represented by the full blue dots, the lower frequency peak (Peak -1) by the crossed dots, and the higher peak (Peak -1) by the empty dot. b) The group velocity calculated from peak-peak oscillations by taking the difference between Peak 0 and Peak +1(blue square) and the difference between Peak 0 and Peak -1 (red squares). The calculated group velocities from theory of the BW modes are shown at $k=k_1$ (dark blue line) and $k=k_2$ (dark red line)*

❖ **Discussion:**

As it is evident from ***Figure 4-10***, from the oscillations of the wave-packet (panel **a)**), we were able to extract two group velocities (blue and red squares) that are in general agreement with the velocities corresponding to the modes $k=K_1$ and $k=K_2$, respectively (panel **b)**). However, the modes possess distinct phases, providing an explanation for the fluctuations in the group velocity extraction in some regions of the field, especially the low field region, below 100 mT, where the experimental data can't provide information on the differentiation between the modes and therefore the inability to capture the whole physics of our system.

This limitation is indeed linked to the richness of our spectrum that hosts multiple spinwave modes. These spinwaves are close in frequency, thereby broadening the spinwaves resonance peak. Nevertheless, they have different group velocities and, consequently, different delays. This therefore require a measurement in the time domain to isolate the contribution of each of these modes and investigate its origin solely.

One of the possible reasons to comprehend the richness of modes in our system is to consider the thickness modes. Given that our YIG has a thickness of 500 nm, thickness modes may contribute. Consequently, further investigation is needed and can be done through accessing the propagation times of the spinwaves.

Nevertheless, the presence of antenna modes, is also a major reason to be considered. As observed from the figure depicting the antenna excitation spectrum, the most efficient k vector is 0.6. However, this will not exclude that the excitation of secondary k- values (at 1.27, 1.8 and 2.45 rad/µm) can also contribute in the signal ***Figure 4-1*****. b)**.

In the following section, we will explain the measurements on the same system, but this time conducted in the time domain by using the VNA, where the origin of the different SWs will be discussed.

4.3 MEASUREMENTS IN TIME DOMAIN

4.3.1 Understanding Time Domains in Vector Network Analyzers: How it works?

- *Some history*

Time domain reflectometry (*6*) is a technique that was introduced in 1960s, to get the response of a device in time domain. It consists of sending an electrical pulse, that can be a step or an impulse along a device (transmission line) and observing the reflections of this pulse as it encounters impedance changes or discontinuities along the line.

The measurements can be observed on an oscilloscope (*7*), where the x-axis represents time, and the y-axis represents voltage. The reflected signals appear as voltage spikes on the oscilloscope display. The time delay between the transmitted pulse and these voltage spikes corresponds to the distance between the source and the impedance variation causing the reflection.

However, with TDR we encounter some limitations such as resolution issues, complexities of comprehending the measured signal, lack of information on the frequency as well as its capacity allowing only reflection measurements.

Then in 1970's, it was shown that is possible to convert the measurements in frequency domain to time domain by using the means of Inverse Fourier Transform (IFT).

Therefore, from both TDR and VNA we can have frequency-time domains information; however, they operate differently. A TDR analyzes the reflected signal with a wideband oscilloscope where the result is in time domain. However, a VNA sweeps first in frequency, then uses mathematical transformations to the time domain to obtain TDR like response. This is achieved by utilizing a narrowband receiver, which employs down-conversion and filtering prior to the transformation. This significantly reduces system noise, resulting in an improved signal-to-noise ratio and a superior dynamic range compared to TDR. This advantage is particularly crucial in applications where high-speed SWs signals in GHz region with low crosstalk levels, need to be measured accurately.

As a result, we can make use of the high performance and fast measurements of the VNA for measuring signals in time domain. Therefore, allowing to add up on the TDR measurements, the ability on measuring the transmission signals, having frequency information and advanced measurements such as time gating.

- *Some theory*

Here, we will detail how the VNA operates and provide a simplified explanation of how it acquires time domain data.

The relationship between the frequency and time domains is established through FT:

$$H(f) = \int_{-\infty}^{+\infty} h(t)\, e^{-j(2\pi f)t} dt$$

(Eq. 4-6)

where $H(f)$ is the frequency domain transfer function and, $h(t)$ is the converted the time transfer function (impulse function).

What the VNA does is the other way around, it measures the data in frequency domain and then transform them into time domain via IFT:

$$h(t) = \int_{-\infty}^{+\infty} H(f)\, e^{+j(2\pi f)t} df$$

(Eq. 4-7)

Since the measurements with VNAs consist of a discrete set of data points, then the discrete form of IFT should be used (IDFT). Here, the analyzer uses an extension to this transformation, that is the inverse chirp Z transformation (*8*, *9*).

$$CZT[h(t)] = \sum_{0}^{N-1} h(t).\, z_k^{-n}$$

(Eq 4-8)

with z = A. W^{-k} and k=0,1, ...,N-1.

This transformation imposes an additional condition for the analyzer that is that the time domain response is repeated after a time interval which is equal to $\Delta t = \frac{1}{\Delta f}$, where Δf is the frequency spacing between two points of a VNA sweep.

Consequently, chirp-z usage comes in handy when dealing with non-uniformly distributed data points or when the input and output samplings are not required to be identical, as it allows to zoom in and out in the time axis, which is not possible while using the IFT. In addition to this flexibility on data points, the chirp-z offers more accuracy as well on the transformation especially when the data has complex frequency responses with rapidly varying phase information. This accuracy arises from the ability to choose appropriate windowing functions to control sidelobes and artifacts (*10*).

To note that, prior to the transformations, the data acquired in the frequency domain undergoes a filtering step that can be performed via two modes: either a bandpass or a lowpass mode. By selecting the appropriate filtering mode, we can select the right parameters matching the properties of our expected signal, thus avoiding unwanted noises and aliasing issues when obtaining the time transformed data.

In the following, we will provide further details about these modes and the necessary parameters for conducting the measurements (*10*). We will then validate the accuracy of the measured data by comparing the obtained time domain parameters with manually

transformed frequency domain parameters using means of IFT. Lastly, we will show another advantage of this type of measurement, that are measurement in the frequency domain but with a time gate.

A. Principles of Time domain and Gating

As we have discussed so far, the vector network analyzer permits measuring the scattering parameters (amplitude and phase) in the frequency domain. However, measuring in the time domain is an option that we can add and is available in most of the VNAs such as **R&S®ZVA67** 4-port **VNA** (*11*) used for this study. This type of measurement is based on the means of IFT of the S-parameters in the frequency domain (via lowpass impulse / or bandpass transformation types). Thus, this technique allows localizing the time at which the response host noise, or equivalently different signals propagating at different speeds at similar frequencies, by so, we can determine a *"gate"* in time, allowing to avoid the noise region and focus on the region of interest. This comes beneficial in PSWS measurement for systems having a low signal to noise ratio as well as for systems hosting many SWs modes.

Gating essentially functions as a time-domain filter. It operates by selecting a gate window, defined by setting a starting and ending gate time, represented as [T_{start}: T_{stop}]. Indeed, we fix this window ourselves, depending on the information we need to extract from the signal and thus the S-parameters only within this pre-determined time window undergo a Fourier Transformation back into the frequency domain (via bandpass impulse transformation type), as depicted in ***Figure 4-11.***

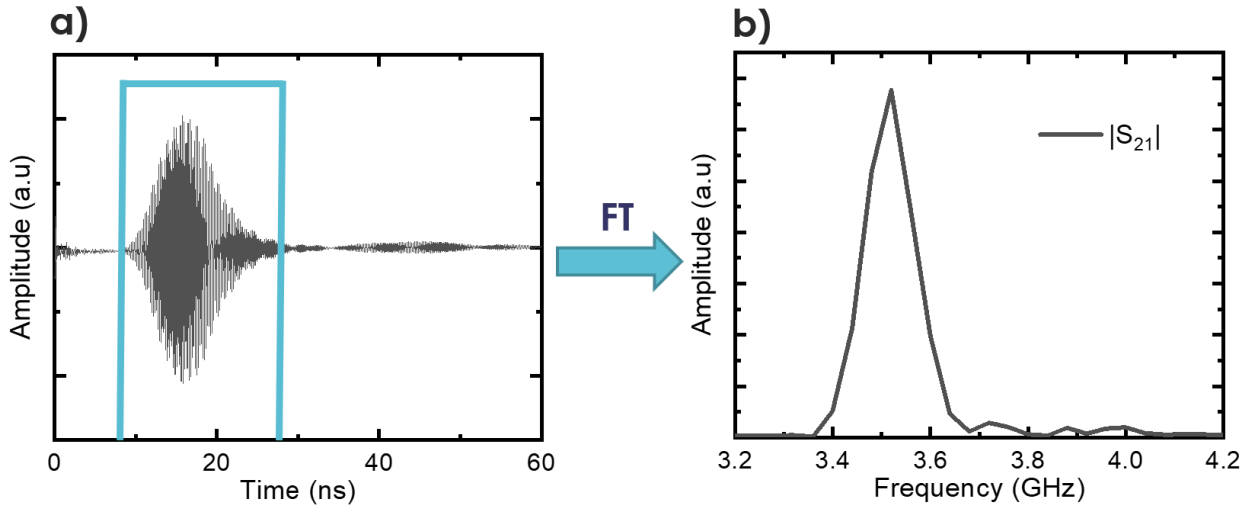

Figure 4-11: *Principle of time domain spectroscopy and gating: (a) Exemplary spectra taken for a YIG film of 500 nm, to enhance the signal amplitude in this example, for H = 100 mT, with an applied gate of boundaries T_{start}=8 ns and T_{end} =30 ns. (b) Fourier transform of the spectra in (a) showing a resonance frequency at 3.5 GHz.*

As a summary, here's how the VNA operates in steps when measuring in the time domain:

1. The VNA measures the S-parameters in the frequency domain.

2. The acquired data undergoes a processing step aimed at filtering out-of-band frequency components and noise, which is essential for obtaining a meaningful time-domain spectrum.

3. After filtering, the data is transformed into the time domain using the chirp-z transformation.

Now, let's focus on step 2; this can be done via two modes: the bandpass and the lowpass modes.

The VNA imitate the TDR measurements that are either due to a step or impulse response. Thus, from eq (***Eq. 4-7***), the response function form depends on the filtering mode that is used and can be chosen by the user.

B. A remark on the response function $h(t)$ and the measurement response resolution:

The response function (***Eq. 4-7***) can be either a step or an impulse function, and the choice of function is made prior to the transformation according to the chosen transformation mode. In the Bandpass mode, since the transformation does not include the DC point (zero frequency), the impulse response is obtained. However, in the Lowpass mode, both the step and impulse responses are available. The impulse function is derived from the step function and provides direct access to the frequency domain through FT, which is not the case with the step function.

Additionally, the impulse function allows us to mimic the system's response to a pulse of energy over time, making it valuable for studying the propagation of signals in a linear regime. In contrast, the step function allows us to analyze how a signal varies over time by continuously applying a continuous pulse to the system and observing its response.

In our case, the Lowpass mode with the impulse response is particularly useful because it provides direct access to the frequency domain when transformed back via FT. This feature makes it more suitable for our specific analysis needs.

The measurement response resolution defines the precision between two closely spaced responses. It is therefore determined by the frequency span and the used mode.

- ***Bandpass impulse***:

In this type, the results are obtained with no restrictions on the sweep range, it can take place from any start to any stop frequency, with equidistant sweep points.

In we depict how the points will be taken for the transformation. Only the measured points from F_L to F_H are taken while the zero-point frequency (DC point) is not included in the calculation.

The transformation bandpass window is thus centered between the start and stop frequencies. The IFT is applied from minus one-half of the frequency span to plus one-half of the span that is given by ($BW = F_H - F_L$).

This yields in complex valued data points where the information on the phase is lost. For this reason, this type of measurement is used essentially for measuring the magnitude of the signal (in our case the magnitude of the inductive signal from SWs).

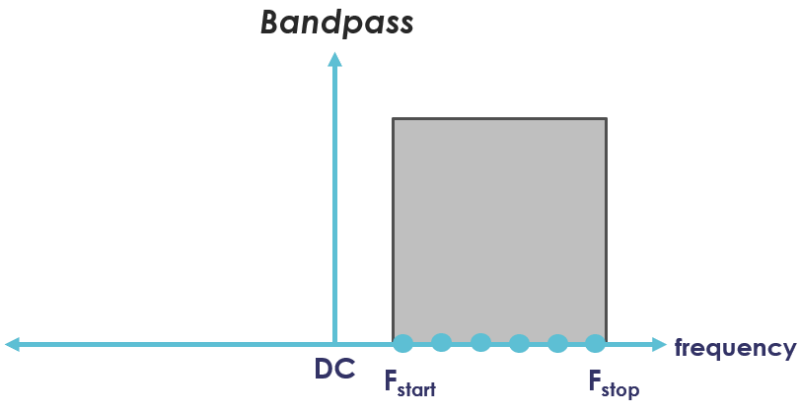

Figure 4-12: Bandpass impulse transformation scheme

- ***Lowpass impulse:***

Further requirements are necessary when selecting this type for the transformation. First the measurement results in frequency domain are continued to the DC value (f=0) and mirrored to negative frequencies meaning that the frequency sweep range is doubled. This means that the resolution of the response is twice the resolution of the bandpass mode.

Second, with this type of sweep points taken on the positive frequency range must be equidistant and harmonically related to the DC point. These considerations impose that the frequency points need to be distributed on a harmonic grid. Add to this, since now the transformation includes the DC points, this value should be extrapolated.

By mirroring the positive data points to the negative region, we assume that the response is Hermitian, that is the negative points are the conjugate of the positive data points. This result that, in the lowpass impulse type, the response is real-valued, and the phase information is covered.

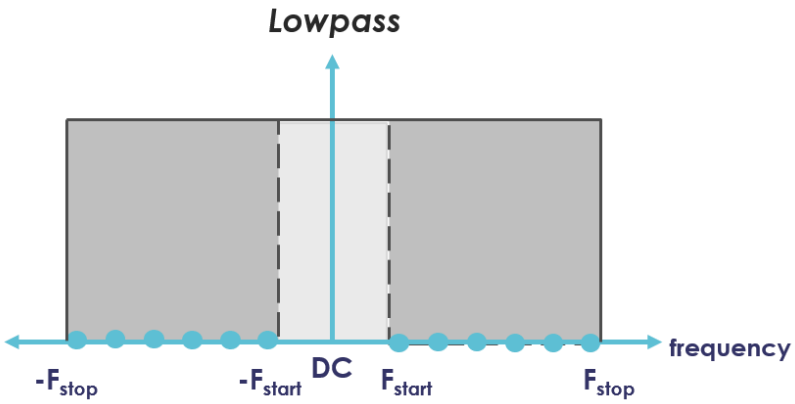

Figure 4-13: Lowpass transformation scheme.

C. Parameters of measurements (low pass impulse):

In the following, we will introduce two requirements to consider when taking the data in the lowpass mode. Then we will explain how to set-up the various parameters for obtaining the correct data when using this processing mode.

- ***The DC Value:***

As explained previously for the low pass mode, since the FT includes effects of the DC value on the frequency response and VNA's do not measure the DC response, the DC value must be extrapolated.

To establish the measurement result at the zero point, (specifically when f = 0), there are two potential methods of extrapolation:

- Continuous Extrapolation: In this approach, the DC value is extrapolated continually after each sweep based on the results of the sweep.

- Manual Entry of DC Value: Alternatively, the DC value can be manually entered. In this scenario, the DC value is extrapolated using a one-time extrapolation from the currently available measurement values.

In our case, we avoid continuous extrapolation as it will change after each sweep thus offsetting the measurement, thus resulting in artifacts in the measured signals.

- ***The harmonic grid:***

For a lowpass transformation, the frequency sweep points should lie in a harmonic grid. This means, the data points should be harmonically related to the DC point by the frequency step Δf. For this, the VNA provides three possible algorithms to calculate the harmonic grid:

1. Stop Frequency and number of points.
2. Frequency gap and number of points
3. Stop frequency and approximate frequency gap.

The user can choose either of these algorithms, which yield the same results but depend on the user's preferences for data analysis.

In our measurements we chose to keep the stop frequency and number of points. With this approach, the VNA calculates a harmonic grid based on the chosen stop frequency and number of points (N_f). The sweep points are then evenly distributed across the frequency range (span, S_f) that is, between a minimum frequency f_{min} (the minimal frequency of the analyzer) and the fixed stop frequency f_{stop}(set by the user). Thus, this can lead to a frequency gap increase in the grid if the f_{min} is lower than the f_{start} (as in our case).

The analyzer must calculate the DC point and the additional points that are between the DC and the first measured point. This is done by linear interpolation of the magnitude and phase done by the analyzer between the first measured point and the DC. Then this DC value and the points between DC and the f_{min} should be extrapolated.

To note that the user thus can select one of these algorithms depending on the measurement sweep points where each has its advantages and drawbacks on sweep time, time domain resolution and unambiguity of the range.

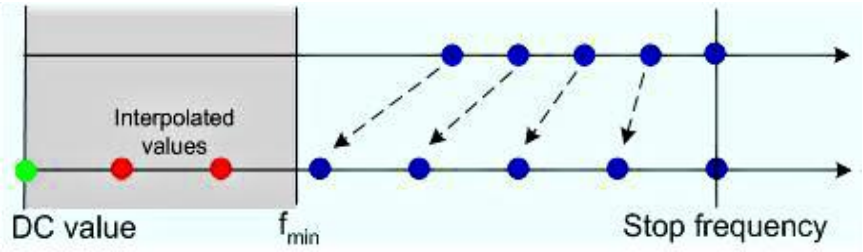

Figure 4-14: Harmonic grid representation: with a fixed stop frequency and number of points: *The sweep points distributed evenly in a harmonic grid, leading to an increase in the frequency gap between two consecutive points.*

- ***How to set in Practice?***

The concept relies on that we are using FT, and so we need to maximize as far as we can the number of points in frequency. This is why the starting frequency point should be low enough; f_{start} as close as possible to f_{min} , while, at the same time, considering a reasonable sweeping time. Then the end point f_{end} remains within the desired measurement range.

In the low pass mode that includes the DC point, the closest the f_{start} to the DC point the better resolution we can get. As a rule of thumb, the f_{start} should be away from f=0 by $m \cdot \Delta f$, where m is the number of points between the DC and f_{start} and should not be more than 20% of the total number of points.

Then, one should choose a Δf that is the frequency step between equidistant points. Consequently, this allows to determine a total number of sweep points,

$$N_f = \frac{S_f}{\Delta f}$$

(Eq. 4-9)

with S_f is the span over the frequency range ($S_f = F_{Stop} - F_{start}$).

When converting to the time domain, with the impulse response, the chirp-z transformation imposes an unambiguous time range that is defined by:

$$T = \frac{1}{frequency\ step} = \frac{1}{\Delta f}$$

(Eq. 4-10)

This value represents the maximum time interval before the measurement starts to repeat itself within the specified frequency range.

4.3.2 Experimental Results: The Transmission Spectra in time domain

In the following we will focus on the transmission spectrum obtained by measuring the same system measured in ***section 4.2***, this time in the time domain.

A. Parameters of the measurement:

In order to acquire our data correctly, it is necessary to follow the logic explained in ***section 4.3.1***

For this measurement we performed a field sweep ranging from 0 to 215 mT. The corresponding signal thus spans from a frequency of 2 GHz to 7 GHz. Here, we will extend our measurement range from 10 MHz up to 25 GHz, with a frequency step Δf of 1MHz.

To ensure accuracy, it's essential to set our starting frequency as close as possible to the DC point. For instance, if we select a starting frequency of 10 MHz, the number of points is then determined by:

$$N_f = \frac{S_f}{\Delta f} + 1 = \frac{f_{end} - f_{start}}{\Delta f} + 1 = 24990 + 1 = 24991\ total\ number\ of\ points.$$

The +1 is to ensure that both the end and start frequencies are included in the measurement.

Now, to set up the time domain the necessary parameters are:

Time Range: The maximal time range in which we recover the proper signal within this frequency spectrum, and before the response starts to repeat itself is given by the frequency step Δf:

$$Time\ Range < \frac{1}{\Delta f} = 1000\ ns$$

Time Range Resolution: Time domain range resolution is the ability to locate a single response in time. It is determined by the digital resolution of the display, calculated as the time domain range divided by the number of points.

A time range of 1 μs , will give a time resolution of 8 ps, to decrease it we will sweep on a time of 500 ns and thus a resolution of:

$$\Delta t\ = \frac{Time\ Range}{N_f} = 4\ ps$$

N.B: Improving time range resolution improves the display resolution, but not measurement resolution.

Concerning the DC value, we set its value manually at 0.0, and thus it is not extrapolated continuously.

Therefore, by carefully considering both frequency and time domain parameters, we optimize the S-parameters acquisition in the time domain.

B. Experimental Results: S-parameters in Time Domain:

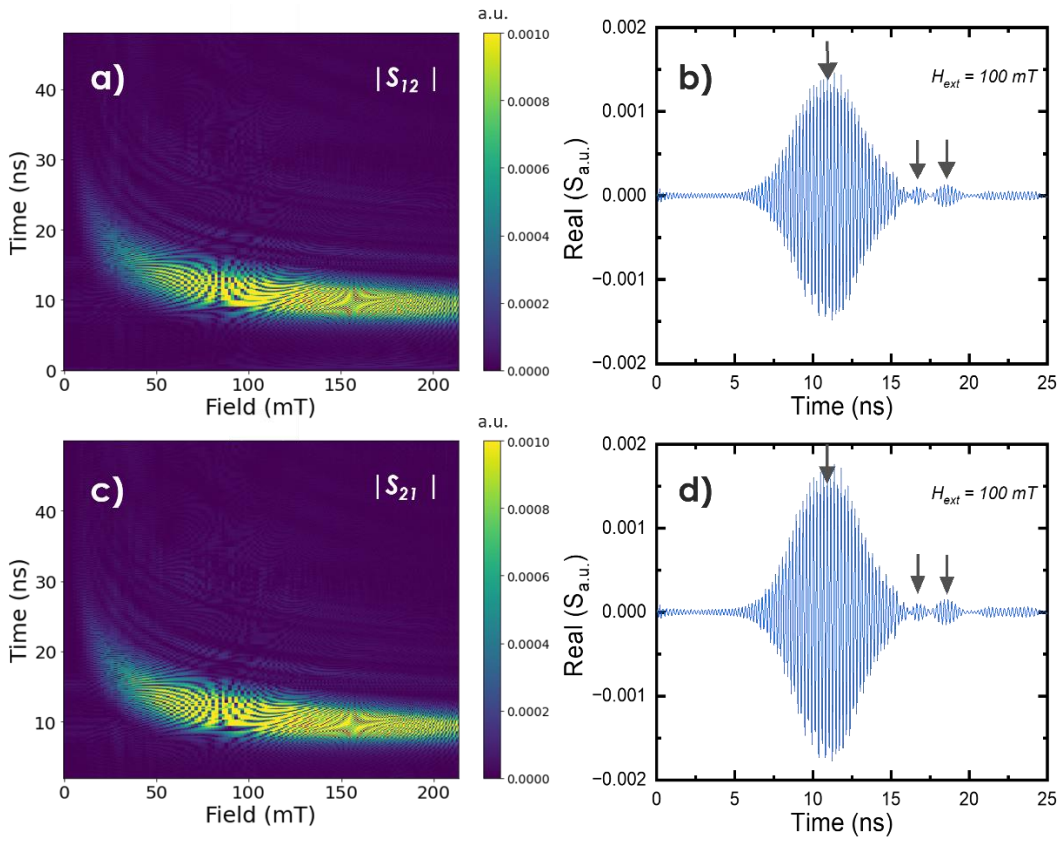

Figure 4-15: Transmitted S-parameters in function of time in BW configuration. *a), c) colormaps of the $|S_{12}|$and $|S_{21}|$respectively, in function of time and swept field. b), d) the real value of the S(t) at H=100mT, the arrows show the different lobes in the spectrum well-separated in time.*

By setting the appropriate parameters, the VNA saves the S-parameters in function of the time sweep. In this measurement type (lowpass impulse), the S-parameters are real-valued. In ***Figure 4-15*** *and* ***Figure 4-16*** panels ***a)*** and ***c)*** show the real value of the transmitted S-parameters (S_{12} and S_{21} respectively) with respect to the swept time and the field in BW and DE configuration, respectively.

First, in the BW configuration ***(Figure 4-15)***, as clearly shown, the signal is composed of one prominent main mode (indicated by the wide and intense branch). This mode is followed in time by two secondary branches that arrive later. In panels **b)** and **d)**, we present a cut of this spectrum at a specific field ($\mu_0 H_{ext} = 100\, mT$). Here, we can define the propagation time associated with the different modes. The oscillations corresponding to these modes are highlighted by the black arrows, and as observed, they oscillate over a specific 'traveling duration' which we will discuss later. Thus, we can estimate propagation times of approximately 10 ns, 16 ns, and 19 ns ± 3 ns for the main mode, the intermediate mode, and the last mode, respectively.

Second, in the DE configuration ***(Figure 4-16)***, again, our spectrum is composed of one prominent intense mode. This propagates on the durations ranging from 0 to few tens of ns. In this configuration the spectrum is much complex and richer in modes. In panels **b)** and **d)**,

we present S(t) at $\mu_0 H_{ext} = 150\, mT$. The difference of amplitude between S_{12} and S_{21} due of non-reciprocity of the DE configuration is reestablished which is also a sign of the reliability of these measurements.

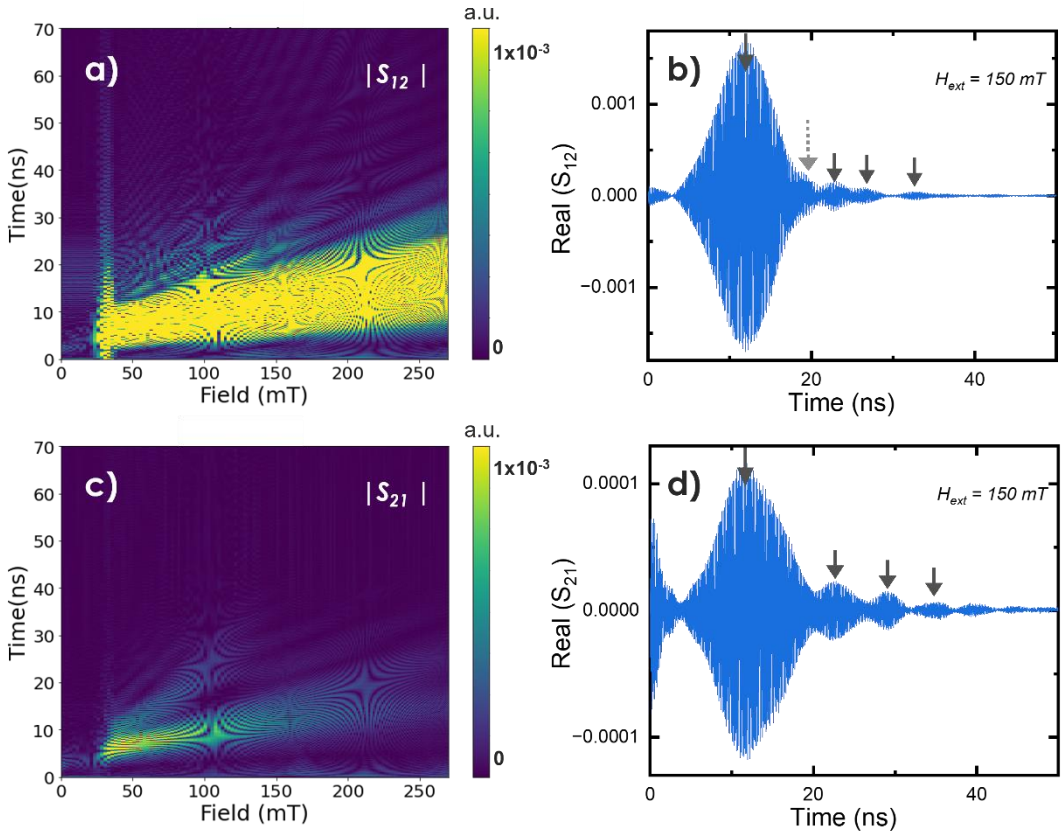

Figure 4-16: Transmitted S-parameters in function of time in DE configuration. *a) and c) colormaps of the absolute value of the S_{12} and S_{21} respectively, in function of time and swept field. b) and d) the real value of the S-parameter in function time at $\mu_0 H = 150$ mT, the arrows show the different lobes corresponding to the different modes available in the spectrum.*

- ***Note on cross-talk***

To amplify small signals and to facilitate the analysis, a logarithmic scale is employed. We take the logarithm of the absolute value of the S-parameters, as depicted in ***Figure 4-17***. In panel **a)** we notice, a signal that emerges from 0 to 2 ns (enclosed in red). This signal can be attributed to cross-talk. To ascertain whether this cross-talk impacts the entire measurement range, we replicate the same measurement but now from 2 ns to 501.6 ns. In ***Figure 4-17. b)*** remarkably, the signals from both measurements are indistinguishable. This is confirmed by taking the difference between the data acquired from 0 ns and the ones after 2 ns (red dots) which indicates that the cross-talk is significantly distant and has no influence on our signal. However, we can notice a slight enhancement of noise.

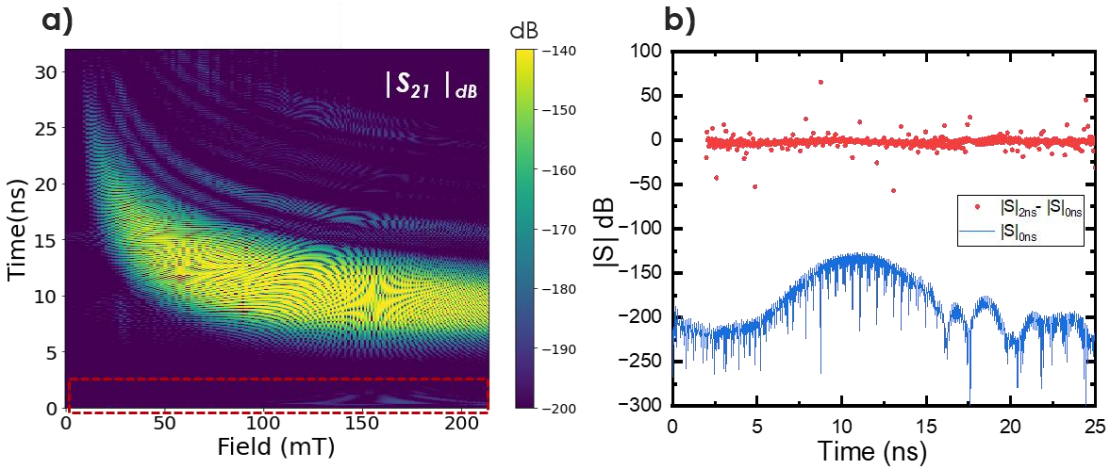

Figure 4-17: Magnitude representation of S-parameters in dB: *a) Colormap of S_{21} in the logarithmic scale, displaying an amplified signal that enables the detection of a signal emerging from 0 to 2 ns (cross-talk). b) Representation of logarithmic S, featuring a measurement starting at 0 ns (blue line). The red points illustrate the difference between data measurements taken after 2 ns and the ones at 0 ns, which is fluctuates around zero implying that the cross-talk does not interact with the overall transmission spectrum.*

4.3.3 Validation of time domain measurements and recovery of modes origins:

To validate the reliability of the measurements, one way is to convert the time domain data back to the frequency domain so that we can compare it with the initially measured frequency domain data. Once validated, one can isolate the response of each mode by applying the Fast Fourier Transform (FFT) over the time intervals in which the branches exist. For this purpose, we will use the BW configuration to demonstrate and explain the method utilized to recover the modes. Finally, we will present the results using the DE configuration.

A. Gating with Fourier Transform:

To validate the accuracy of the acquired data, we employ Fast Fourier Transform (FFT) on the S-parameters in the time domain, to convert them back to the frequency domain. This allows us to make a direct comparison with the data points collected in the frequency domain, and thus ensures the correctness of our measurements. In the following sections, we will provide a detailed analysis of the BW configuration data. Subsequently, we will present the obtained results following a similar analysis of the DE configuration.

Firstly, the result of the Fourier Transform is shown in ***Figure 4-18.*** **a)**. It results in a matching signal in a comparison with what we obtained of the S-parameters measured in the frequency domain (***Figure 4-18.*** **b)**). Moreover, if we take a closer look at a cross-section from both spectra (***Figure 4-18.*** **c)**), we see that both signals are nearly indistinguishable. Therefore, this confirms the reliability and validity of the time domain measurements.

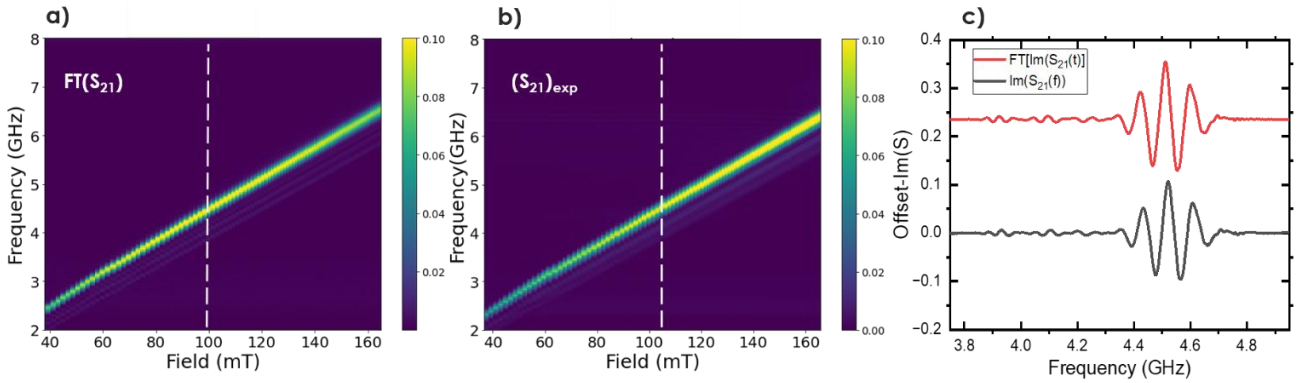

Figure 4-18: Validity of Time Domain*: a) Colormap of Fourier Transfer of the impulse response S(t) function of the field and the obtained frequency. b) Colormap the of the S-parameters obtained from frequency domain measurements. c) Comparison of the imaginary part from the S-parameters from a) (represented in red), and from b), (represented in black).*

Thanks to this, it is thus possible to isolate the signal from each mode individually. In other words, one can choose a specific time interval when this mode propagates and apply the FFT. This will result in obtaining the result in the frequency domain with the proper spectral information associated to this isolated mode.

C. Origin of modes:

As discussed in **Chapter 2**, in a thin film or a waveguide, as in our case, the confinement of spinwaves can also occur along the thickness direction. This confinement leads to the quantization of the wavevector component perpendicular to the surface and as a result the emergence of distinct thickness modes each at specific frequencies. However, if the width of the waveguide is much larger than the thickness, the confinement effect might be not strong enough and thus the quantization of such modes is not possible. In our case the width-to-thickness ratio is of a factor of 200, meaning that the contribution of the thickness SWs is indeed much lower than the ones of the uniform ones imposed by the antenna's k-values.

❖ *Results in Backward Volume Waves configuration:*

One can verify this statement, by calculating the expected delays of the different modes depicted in ***Figure 4-19*** for the BW configuration. By comparing panels, **a)** to **b)** (the experimental colormap of $S_{21}(t, H)$), one can deduce that for propagation times below 40 ns, the primary contributions come from the uniform modes with wavelengths corresponding to the antenna's k-values. In this range, the branch with the highest intensity, extended from 5 to 15 ns is associated with the maximal antenna efficiency at $k=K_1$, while the subsequent narrower branches correspond to K_2, K_3, and K_4, extended over 15 to 25 ns . However, for longer propagation times, the signal, though of reduced intensity, originates from the potentially available thickness modes with n=1, corresponding to $k=K_1$ and $k=K_2$. This should be confirmed by transforming the different wave packets back into the frequency domain to verify whether they have similar frequencies as the main spin-wave packets (lobes of the antenna) or different ones (thickness modes) for a given magnetic field value.

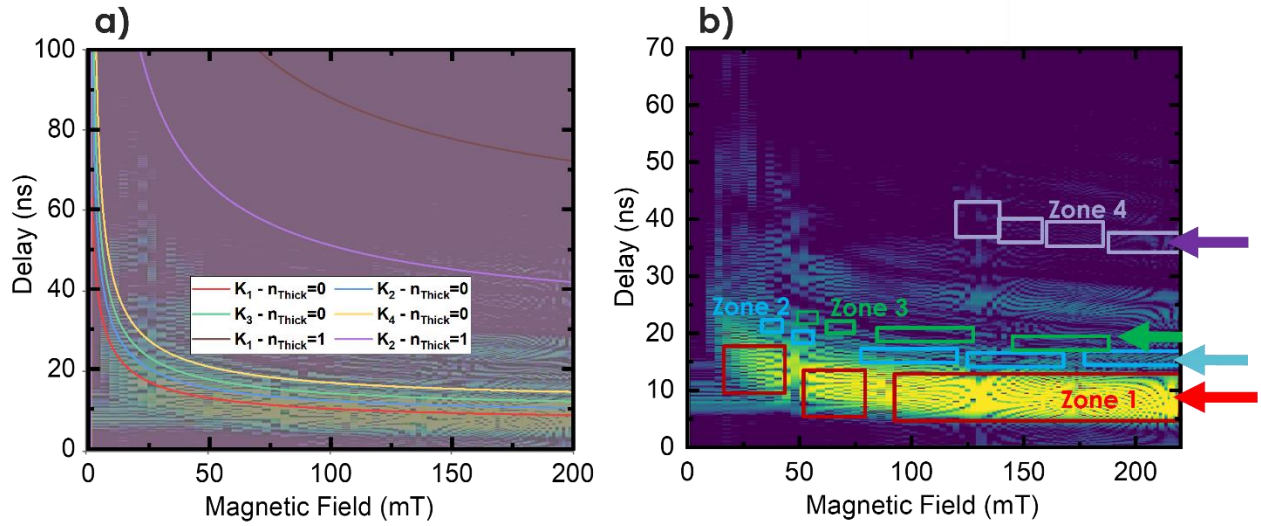

***Figure 4-19: BW-Zones for FT**: a) The expected delay from the potentially available modes in the system. b) Colormap showing the decomposition of the time domain spectrum into zones over which the FT is performed.*

As shown on the maps, the time delay for a given mode isn't constant across all fields. It decreases as the applied field increases. Therefore, we need to split the mode's signal into zones where the delay remains roughly the same as the field varies. For example, zone 1 (in red) corresponding to the main branch is decomposed into three regions, [10:15 ns], [6:12 ns] and [5:11 ns].

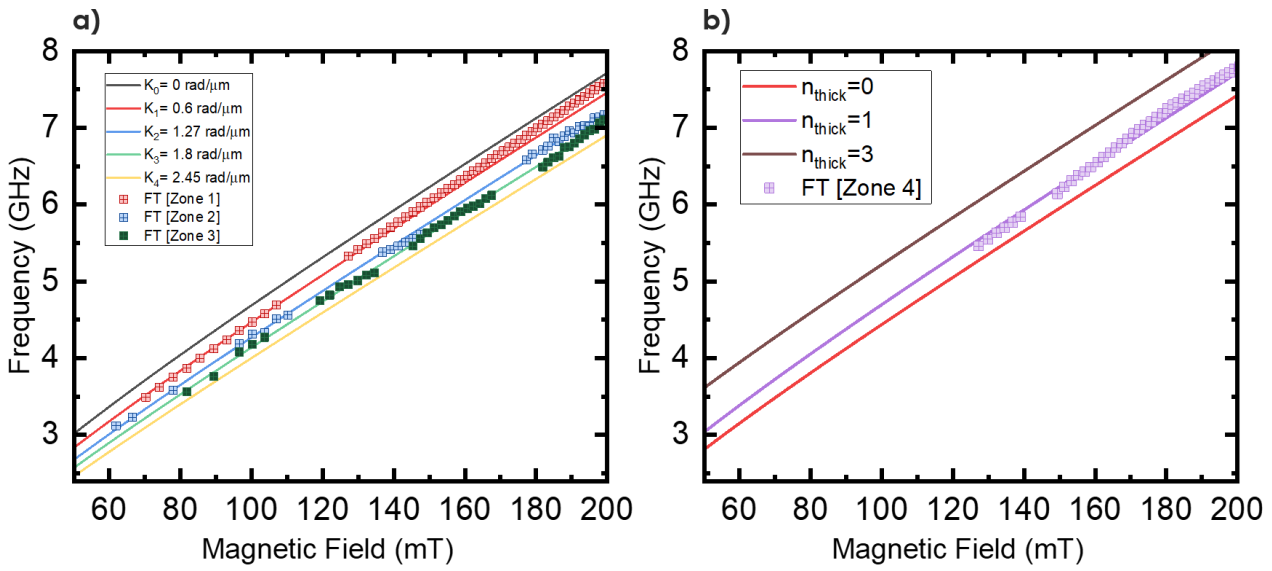

***Figure 4-20: BW- Theory versus Experiment:** a) Antenna modes: The expected modes from theory (full lines) versus the result from the FT of zones in **Figure 4-19**. The FT over zone 1 enclosing the most intense branch in the spectrum (red dots) matches the theoretical curve (red line) for $k=K_1$. The same result is obtained for the slower narrow branches; zone 2 in blue and zone 3 in green matching the theoretical curves of $k=K_2$ and $k=K_3$, blue and green curves, respectively. b) Thickness modes: the expected dispersion relation of the thickness modes with $k=K_1$ in the system, with $n_{thick}=0$ representing the same curve $k=K_1$ in panel a). The FT of the zone 4 for the slowest branch in the spectra overlapping with the first thickness mode with $k=K_1$.*

The results are presented in ***Figure 4-20***. In panel **a)** The points represent the results obtained from the Fourier Transform applied to various zones, while the solid lines correspond to the expected frequencies for the first-order width modes with K_1, K_2, K_3, and K_4.

For Zone 1, which holds the most intense part of the spectrum, the FT points (red dots) align closely with the frequencies at $k = k_1$. Then, the FT of Zone 2 (blue dots) matches the blue line corresponding to $k = K_2$, while zone 3 aligns with the green line ($k = K_3$). This indicates that the first three lobes indeed correspond to the modes originating from the unform modes of the antenna's k-values, as observed in Figure 20 from the delay.

Now, for the slower modes (occurring later than 30 ns) within Zone 4, when we perform the FT, we observe that these correspond to the first-order thickness mode expected for our waveguide at $k = K_1$ (panel **b)**).

However, upon closer examination of this region (for delays t > 40 ns), we notice the presence, even though at low intensity, of several modes. By referring to the expected delays in the spectrum, these modes should correspond to the thickness modes at the different wavevectors of the antenna. To delve deeper into this region, we conduct FFT analysis across different zones, as represented in ***Figure 4-21***. This analysis clearly reveals that, for these three zones; [40:50 ns], [50:100 ns], [70:100 ns] and where the signal seems to be repeated, we recover two branches that are very close in frequency, matching the frequencies of the first-order (n=1) thickness modes at $k = K_1$ and $k = K_2$.

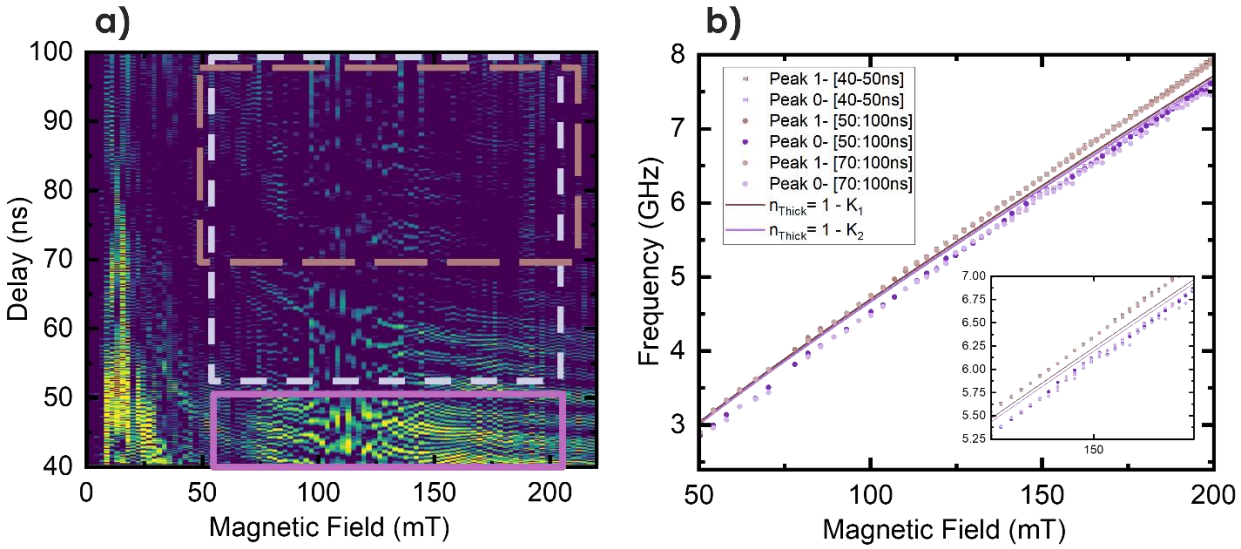

Figure 4-21: Thickness modes for delays > 40 ns: *a) Zone 4 decomposition into three regions; [40,50ns], [50,100], [70,100ns] where we notice a repetition of the pattern observed on [40:50ns]. b) Result of the FT (points) reveals the exitance of two branches in the treated zones matching the first order thickness modes for $k=K_1$ and $k=K_2$.*

To note that the branches lying between zones 3 and zone 4 are nothing than a repetition of the signals from zone 1 to 3 where their FT fit correspondingly to the theoretical lines as in the case of zone 1 to 3 and may be potentially due to the reflection of the signal, i.e., the backward propagation of the spin waves (SWs), as these signals occur at delay times that are

higher than twice the duration of the initial propagating modes describes in ***Figure 4-19*** and ***Figure 4-20***.

- ***Results in Damon Eshbach configuration:***

Continuing our exploration, we move to the DE configuration where, in this case, the spectrum becomes considerably more complex and richer in modes. As illustrated in ***Figure 4-22.* a)** we expect the presence of multiple modes extending on the range of 100 ns within the range of the swept fields. However, due to the antenna's k-selectivity at each lobe, the dispersion curve is supposedly broader than the lines representing individual modes. This results in mode mixing, making the isolation of a single mode a challenging task.

Nevertheless, it is possible to identify certain field ranges where the modes are slightly separated. By pinpointing these distinct zones, one can then apply the FT. When we perform FT on the highlighted zones in panel a), we observe that the points in zone 1 correspond to the uniform mode (n_{thick}=0) for k=K_1, while the points in zone 2 correspond to (n_{thick}=0) k=K_2. It is possible that within the frequency ranges of these modes, thickness modes may exist. To investigate this, we plot in ***Figure 4-22.* a)** the expected theoretical values of the delay for thickness modes (for the first thickness mode n_{thick}=1 at k=K_1 (purple) and k=K_2 (brown). The delay for such modes is larger than those in zones 1 and 2, and therefore we can disregard their contribution to the signal in these zones. This is confirmed by panel b), where we observe that the FT of zone 1 and 2 align with n_{thick} =0 at k=K_1 (red) and k=K_2 (blue), respectively.

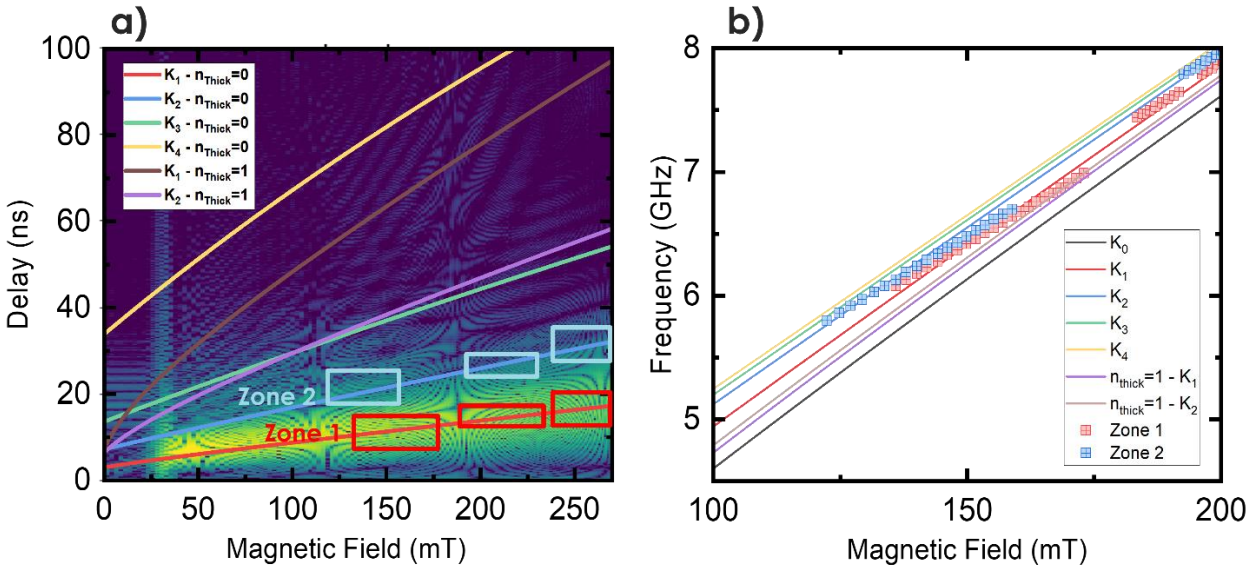

Figure 4-22: DE- Theory versus Experiment: *a) The experimental colormap of S and the expected delay from the antenna and thickness modes from theory (full lines). We specify the zones over which we perform the FT: zone 1 and zone 2, where the signal is the least mixing. b) The frequencies of the theoretical antenna and thickness modes in function of the applied field (full lines). The FT of zone 1 and zone 2 (red and blue dots) match well the expected modes at k=K_1 and k=K_2 represented by red and blue lines respectively.*

The Group velocity extraction:

Intuitively, we can think of extracting the group velocity associated to each branch simply from the time range axis and the distance d between the antennas:

$$v_g\,(km/s) = \frac{d\ (\mu m)}{Time\ Range\ (ns)}$$

The distance between the antennas is taken to be from center to center and taken as $d = 18\ \mu m$. By applying this to the time range axis in ***Figure 4-15,*** we find the group velocity values associated to each mode (***Figure 4-23.* a)**). This allows us to extract the following information; The main mode propagates on the orders of 1.7 to 2.2 km/s, followed the lower three modes on the orders of 1 km/s , 0.5 km/s and around 0.2 km/s for the last one.

In fact, when the impulse response of a wave, S(t), is spread over time, it indicates that its phase velocity depends on the frequency. This is a characteristic of a non-dispersive wave. This is translated by the fact that the antenna has a bandwidth delta k, which allows to excite modes with slightly different frequencies and, consequently, slightly different delays.

This behavior is clear in our spectrum, particularly in the impulse response of the first arriving mode, where the signal spreads over approximately 5 ns. As shown in ***Figure 4-23.* b)** this results in a group velocity of the main mode that falls within a range, from 1.5 to 2.5 km/s at $\mu_0 H_{ext} = 100\ mT$.

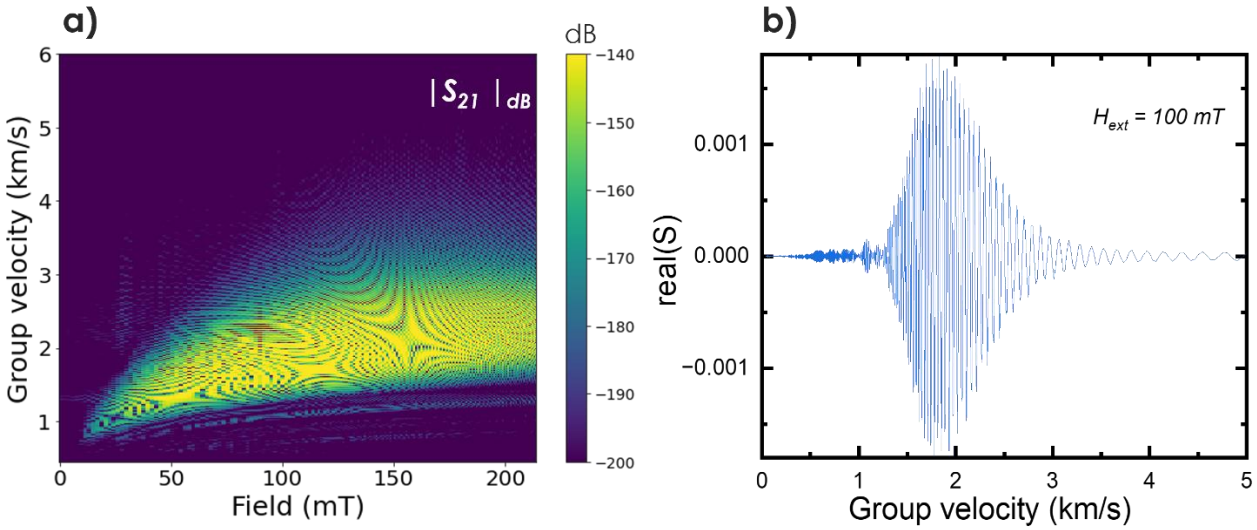

Figure 4-23: BW- Group velocity from time domain data: *a) colormap showing $|S_{21}|$ in log scale in function of the group velocity values and the swept field. The group velocity is obtained directly from the time axis and the distance between antennas. b) A cut at $\mu_0 H_{ext}$ = 100 mT showing real(S_{21}) in function of the group velocity showing the maximum signal arrives with a group velocity of 1.8 km/s, that is the propagation velocity of the main branch.*

However, for the slower modes, these have a narrower duration, hence a less dispersive character, as they are less efficiently excited by the antenna.

For this reason, a simple multiplication of the time domain axis won't let us conclude the exact values of the group velocity. This is why one should think of isolating the signal of one mode in the frequency domain as shown in the previous section.

Nonetheless, it's important to recall that we are using a Fourier Transform of measurement that has a certain number of data points N and where the transformed data to frequency domain is halved (since it yields results from $-f_{stop}$ to $+f_{stop}$). This will lead to poor resolution for concluding about signal properties when integrating over small intervals of time. For instance, if one wants to isolate the main mode, an integration over [6:12 ns], which corresponds to 1500 points in time domain and thus 750 points in the transformed frequency domain that spans over 25 GHz which leads into a reduced resolution. While this approach can provide an estimate of the velocity range within the integrated zone, it does not yield precise information about the oscillations. To achieve this, another way would be to perform measurements in frequency with a time gate.

4.3.4 Frequency with time gate:

The single mode profile can be achieved in two ways; either by conducting a Fourier transform on the specific time interval in which the mode is present within the time domain data, as done in ***section 4.3.3***, or by directly calculating it using the VNA through frequency domain measurements with a *time gate*.

Therefore, this measurement method remains useful for eliminating any noise contributed by connection delays and serves as an effective technique to remove the crosstalk between the inductive antennae. In the figure, we present a comparison between the non-gated S-parameters in dB and the gated S-parameters.

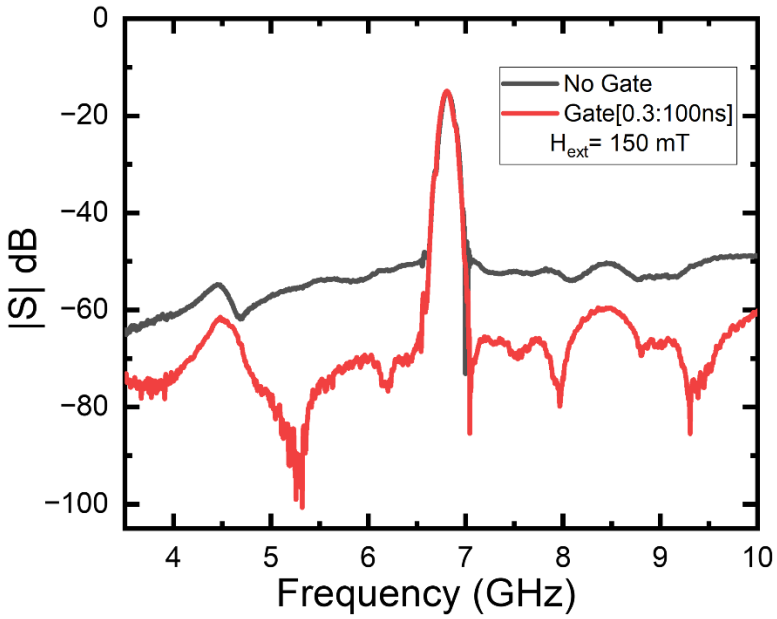

Figure 4-24: $|S_{12}|$ in dB: *non-gated data (black) and gated data from 0.3 to 100 ns (red) at $\mu_0 H_{ext}$=150 mT in DE configuration.*

In ***Figure 4-24***, we show the transmission $|S_{12}|$ measured at a magnetic field of 150 mT (DE configuration) and present them in two different scenarios. In the first measurement, there is no applied gate, i.e., the measurement starts from 0 until 100 ns as represented in black color. In the second measurement, we repeat the experiment, but this time the measurement starts from 0.3 ns and ends at 100 ns (red color). From the figure, it becomes evident that the baseline is slightly decreased in the second case. Therefore, this indicates that using a gating in the frequency domain measurements helps in the elimination of potential cross-talk and noise from the measured signal.

Thus, with this type of measurement, one can have a precise information within the frequency domain of these modes. By applying a gate within the time range over which the spin wave modes propagate, we can thus measure the signal coming mainly from a given mode. Yet, depending on the shape of the response, one can have, as in our case, a variation of the delay with respect the applied field, meaning that the isolation can only occur over a small range of fields for a given gating.

In the following we will be studying measurements using the frequency with time gate option, over frequencies ranging from 2 to 8 GHz with a step of 1 MHz (6001 data points) in the BW configuration.

In a first case, we apply a gate of 5 to 20 ns, which corresponds to the period during which all present modes propagate. The result, shown in ***Figure 4-25.*** **a)**, retrieve the presence of modes once again. However, in this case, the ripples that were encountered when no gating was performed, are nearly vanished. This improvement in the signal can be attributed to the elimination of the various losses through gating.

In a second case, we seek to isolate the main mode. Based on the time domain measurements, we established that this mode's duration spans from 5 to 14 ns. By applying a gate corresponding to this time interval, we obtain a spectrum with the transmitted signal of the main mode, as shown in***Figure 4-25.*** **b)**. Over this time range and over some fields, modes from $k=K_1$ and $k=K_2$ can co-exist, which explain the frequency of the measured mode lying in between the frequencies expected from both modes (full lines). Add to this, from the inset, we can confirm the absence of the lower frequency modes.

Then in panel **c)**, we present the measurement with the gate, spanning from 15 to 25 ns. In this time range, mode 1 intensity is reduced, and the lower frequency modes now take place. The inset highlights the deformation of the main mode and the mixed oscillations from the low-frequency modes. At low fields, the presence of the first mode is still observable, indicating the possible hybridization of modes. Conversely, at high fields, the modes are distinctively separated which explains the frequency range of the modes observed within this time range when compared to the ones expected from theory.

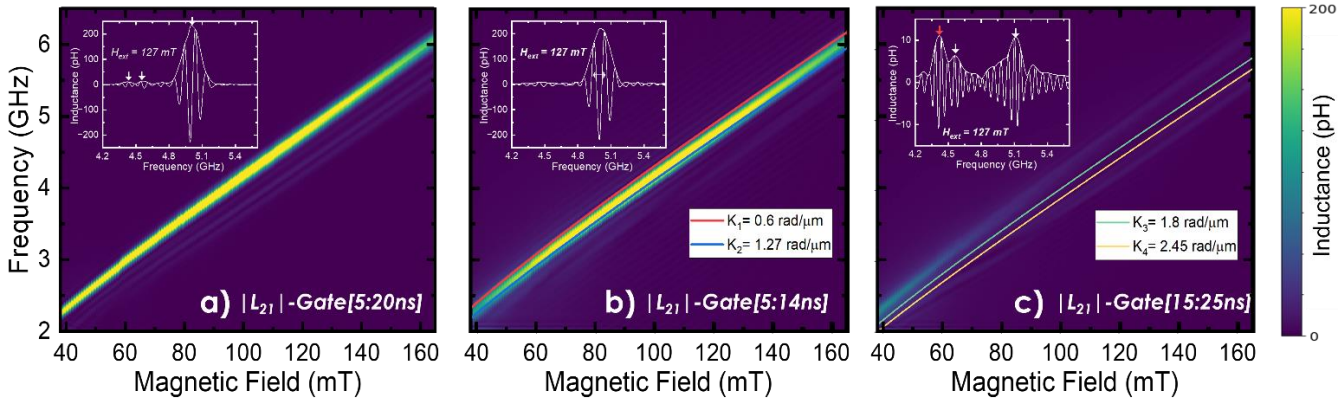

Figure 4-25 : Transmission spectra for different gates: *a) The colormap of $|L_{21}|$with a gate of [5:20 ns] showing the retrieved profile of the three modes. The inset illustrates a net signal profile with ripples eliminated. b) The colormap of $|L_{21}|$, using a gate of [5:14 ns], results in the isolation of the main mode and the elimination of the signal originating from the other low-frequency modes. c) L_{21} with a [15:25 ns] gate, the two low-frequency modes are isolated, while the signal from the first main mode is diminished. The inset shows the imaginary part at 127 mT.*

To conclude this study, let's return to the calculation of group velocity. By using the oscillations of the gated main mode, we take the peak-to-peak difference (horizontal arrow in the inset of ***Figure 4-25. b)*** multiplied by the distance between the antennae. This result in values that evolve from 1.5 to 2 km/s over the range of 40 to 160 mT (***Figure 4-26. a)***). These results exhibit less fluctuations and thus more reliable, in comparison to what is obtained without any applied gating (***Figure 4-10***).

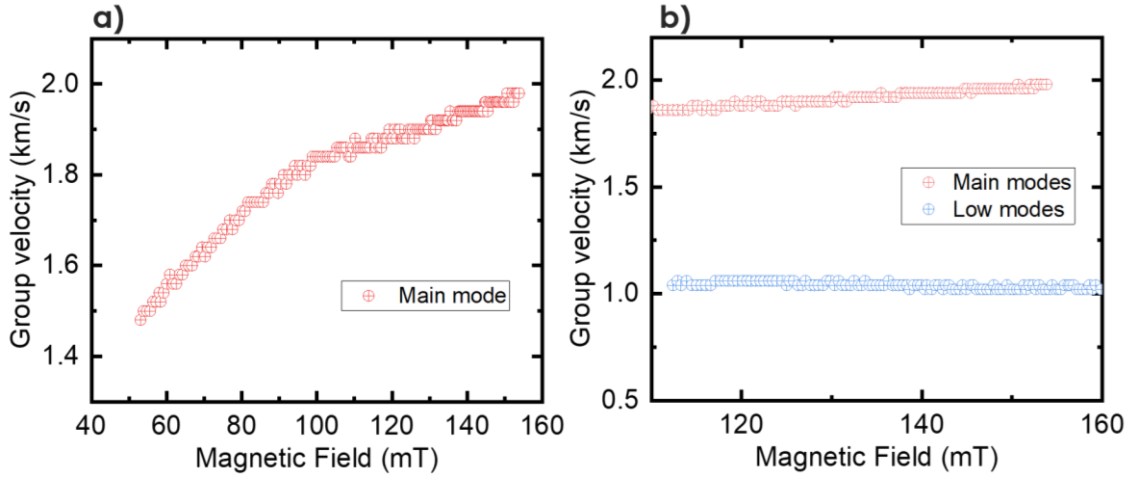

Figure 4-26: Group velocity extraction in the case of time gating: *a) The calculated group velocity in the case of [5:14 ns] gate. b) The calculated group velocity from the data with a gate of [15:25 ns]. The low frequency mode has a velocity of 1 km/s while we retrieve back the same velocity for the main mode. The extractions are only done at higher fields where hybridization of modes is weak.*

Furthermore, in panel **b)**, the extracted group velocity here is with using the oscillations from the gated S-parameters of the low frequency modes (see inset of ***Figure 4-25. c)***). The results show a velocity extracted at magnetic fields starting at 110 mT since this is where we have less hybridization of modes and thus, we can separate from the oscillations coming from

mode K_3 and the main one, as depicted in the inset ***Figure 4-25. c)***. Again, we can get a main mode propagating on the range of 2 km/s within a field ranging from 110 to 160 mT, and another slower low frequency mode propagating at 1 km/s. These values fall in the range of the expected group velocities for the YIG waveguide in BW configuration.

4.4 BIBLIOGRPHY:

1. T. Devolder, G. Talmelli, S. M. Ngom, F. Ciubotaru, C. Adelmann, C. Chappert, Measuring the dispersion relations of spin wave bands using time-of-flight spectroscopy. *Phys. Rev. B* **103**, 214431 (2021).

2. J. R. Eshbach, R. W. Damon, Surface Magnetostatic Modes and Surface Spin Waves. *Phys Rev* **118**, 1208–1210 (1960).

3. U. K. Bhaskar, G. Talmelli, F. Ciubotaru, C. Adelmann, T. Devolder, Backward volume vs Damon–Eshbach: A traveling spin wave spectroscopy comparison. *J. Appl. Phys.* **127**, 033902 (2020).

4. M. Sushruth, M. Grassi, K. Ait-Oukaci, D. Stoeffler, Y. Henry, D. Lacour, M. Hehn, U. Bhaskar, M. Bailleul, T. Devolder, J.-P. Adam, Electrical spectroscopy of forward volume spin waves in perpendicularly magnetized materials. *Phys. Rev. Res.* **2**, 043203 (2020).

5. Kalinikos and Slavin - 1986 - Theory of dipole-exchange spin wave spectrum for f.pdf. https://iopscience.iop.org/article/10.1088/0022-3719/19/35/014/pdf.

6. J. A. Strickland, "Time-domain reflectometry measurements" (1970; https://api.semanticscholar.org/CorpusID:137337743).

7. I. Hickman, *Oscilloscopes* (Elsevier Science, 2001; https://books.google.fr/books?id=O2oj04vbQqgC)*Electronics & Electrical*.

8. A. V. Oppenheim, R. W. Schafer, R. W. Schafer, *Discrete-Time Signal Processing* (Pearson, Harlow, Third edition, Pearson new international edition., 2014)*Always learning*.

9. L. R. Rabiner, R. W. Schafer, C. M. Rader, The Chirp z-Transform Algorithm and Its Application. *Bell Syst. Tech. J.* **48**, 1249–1292 (1969).

10. ZVA_ZVB_ZVT_OperatingManual_en_33.pdf.

11. ZVA. https://www.rohde-schwarz.com/us/products/test-and-measurement/network-analyzers_64043.html.

5 CHAPTER 5: UNRAVELING SPIN-WAVES IN HEMATITE

Antiferromagnetic materials are promising candidates for magnonic devices operating on the sub-THz frequencies. In these materials, spinwaves can reach a high group velocity exceeding a few tens of km/s. This potential is due to the strong exchange field and quadratic spin-wave dispersion found in antiferromagnets (1,2). For these reasons, researchers have extensively studied antiferromagnetic spin waves, including dipole-exchange modes, in both the long and short wavelength limits over the past few decades (3,4). However, up to now, there are no experimental observations of propagating properties of spin waves in AFMs, both in direct and reciprocal space.

In contrast to their counterparts, ferromagnetic materials, as in the case shown in Chapter 4, detecting spin wave dynamics in these materials is relatively straightforward due to the presence of large stray fields. These stray fields enable the inductive detection of spin waves. However, in antiferromagnetic materials, dipolar fields are either entirely absent or of small values that they have a negligeable impact, making it significantly more challenging to detect and study spin wave dynamics by inductive means.

Canted antiferromagnets, are antiferromagnetic materials with presence of a bulk Dzyaloshinskii-Moriya interaction (5, 6) . The DMI is responsible for the canting of the magnetic moments resulting in small non compensated dipolar fields which makes spinwaves detection possible. Thanks to this, canted-antiferromagnets are anticipated to present more pronounced dipole-exchange spin-wave modes in the small wave vector k region (< 6 rad/µm) (7–10) as required to facilitate their observations using standard inductive detection.

Recently, many of these canted antiferromagnet materials, such as Hematite and orthoferrites, have also been identified as altermagnet (11, 12), a new class of magnetic materials with opposite spin-sub-lattices, a nearly vanishing compensated magnetic order but at the same time a broken T-symmetry leading to spin-splitting in the momentum space. Such a lifted degeneracy of the electronic spin and magnon band structures shall enable to open to antiferromagnets, the same rich physics of spin current transport and spin wave dynamics (13) than in ferromagnets (14).

In this sense, insulating canted antiferromagnets such as Hematite (introduced in Chapter 2) or orthoferrites, possessing resonance frequencies ranging from 10 to 600 GHz (15–17), DMI fields from 1 to 20 T (18), and low magnetic damping (16, 19, 20), are thus prime candidates to develop the field of antiferromagnetic and alter-magnonics.

In the following, we will represent the magnetic characterization of our Hematite sample. Then we will explain the experimental scheme and the different orientations to take into account for this study on propagative SWs in Hematite. Thereby, we will show the results of our observations of propagating spin waves using PSWS on a bulk slab of Hematite. The measurements are conducted at room temperature, that is the temperature above the Morin transition and at

which Hematite is in a canted easy plane phase (21). Depending on the orientation of the applied magnetic field $\boldsymbol{H}$ *, we will be particularly interested in two configurations: one in which the propagation vector* $\boldsymbol{k}$ *is perpendicular to the antiferromagnetic order* $\boldsymbol{n}$*, and another where* $\boldsymbol{k}$ *is parallel to the antiferromagnetic order. Subsequently, we will use time-of-flight SW spectroscopy to examine the group velocity and non-reciprocity of these observed propagating spin waves.*

5.1 MAGNETO-STATIC SPIN-WAVE IN ANTIFERROMAGNETS

Since dipolar interactions are absent for normal antiferromagnets, spin waves modes are degenerate and can propagate within the material's bulk with a standard quadratic dispersion in their wavevector $\boldsymbol{k}$.

In **Chapter 2**, we have seen the derivation of total free energy in Hematite. From this, we were then able to show the magnon dispersion relation for $k = 0$ and build on the basic model that neglects the dipolar effects. In this context, the magnon spectra splits into two branches; one low frequency and one high frequency mode. As our measurements are conducted with a VNA, our frequency range is restricted to the region where only the low frequency mode is accessible. Therefore, further calculations were then carried on to include the dipolar effects for this case, where we can distinguish between two magnon modes; bulk and surface. In each of these modes, according to the orientation of the applied field, and due to presence of the dipolar effects, two configurations are possible for the Néel vector with respect to the propagation direction of the spinwaves excited by the antennas. In the following we will summarize the equations that are going to be used as a basis to validate our experimental observations. The details and explanation of the derivation of the equations can all be found in **Chapter 2** and (*22*).

5.1.1 Dispersion relation of Bulk magnons

1. **Case of** $\boldsymbol{k}//\boldsymbol{n}$ **,** $(\boldsymbol{H} \perp \boldsymbol{k})$**:**

In this configuration, we recall the dispersion relation with a contribution of the dipolar field into the gap for the bulk modes as (*3*):

$$f_{\boldsymbol{k}||\boldsymbol{n}_0} = \sqrt{f_{10}^2 + \left(\frac{1}{2\pi}\right)^2 \left[\frac{4\pi M_s}{H_E}\gamma^2(H + H_{DMI})^2 + c^2k^2\right]}$$

(Eq. 5-1)

With:

- $\boldsymbol{f_{10}} = \boldsymbol{f_{low,k=0}} = \left(\frac{\gamma}{2\pi}\right)\sqrt{\boldsymbol{H_E}\boldsymbol{H_{aniso-in}} + \boldsymbol{H}(\boldsymbol{H_{DMI}} + \boldsymbol{H})}$
- γ is gyromagnetic ratio.
- H_E is exchange field that keeps sublattice magnetizations antiparallel.

- H_{DMI} is DMI field that induces canting of magnetic sublattices.

- $H_{aniso-in}$ and $H_{aniso-out}$ are the in-plane and out-of-plane anisotropy.

2. Case of $\boldsymbol{k} \perp \boldsymbol{n_0}$, $(\boldsymbol{H}//\boldsymbol{k})$:

In the absence of z-component of the wave vector (k_z=0), the bulk mode with $\boldsymbol{k} \perp \boldsymbol{n_0}$ is reduced to the following expression:

$$f_{k\perp n_0} = \left(1 + \frac{4\pi M_s}{H_E}\right)\sqrt{f_{10}^2 + \left(\frac{ck}{2\pi}\right)^2}$$

(Eq. 5-2)

5.1.2 Dispersion relation of Surface magnons :

We recall the following formula for the frequency of the surface mode for $\boldsymbol{k}\,//\,\boldsymbol{n}$, $(\boldsymbol{H} \perp \boldsymbol{k})$ adapted from (*9*, *10*, *12*):

$$f_{sur} = \frac{f_{10}^2 + \left(\frac{ck}{2\pi}\right)^2}{\frac{\gamma(H + H_{DMI})}{\pi}} + \frac{\gamma}{4\pi}\left(1 + \frac{4\pi M_s}{H_E}\right)(H + H_{DMI})$$

(Eq. 5-3)

5.2 MAGNETIC CHARACTERIZATION OF HEMATITE:

The studied sample is a c-plane 500 µm thick single crystal of the antiferromagnet α-Fe_2O_3 in its canted phase (at room temperature) (purchased from the company Surface Net). The magnetic properties of the crystal are similar to the ones detailed in Ref.*(33)* and summarized in ***Table 5-1***. These are used as initial parameters for the theoretical expressions and fits.

	H_E (T)	H_A (T)	H_a (T)	H_D (T)
α-Fe_2O_3	1000	2×10^{-3}	6×10^{-5}	2.26

Table 5-1: Material parameters of the α-Fe_2O_3 used for this study.

Therefore, we characterized the amplitude of the canted moment at room temperature in the studied single crystals using a standard vibrating sample magnetometer (VSM). In ***Figure 5-1***, the measurements are done with a magnetic field applied directed in-plane with respect to the sample. The extracted total magnetic moment is about 25 memu for the canted moment of a single crystal with a size of 5 x 5 x 0.5 mm^3. This leads to a canted moment of about 2 emu/cm^3 in line with previous reports in single crystals (*23*, *24*).

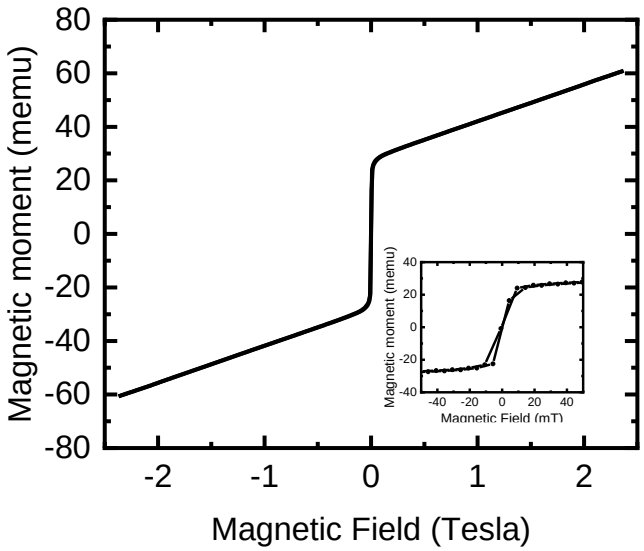

Figure 5-1: VSM with in-plane magnetic field: *Magnetic moment of the sample when applying a magnetic field within the sample plane (c-plane, easy-plane of hematite). Inset corresponds to a zoom at low magnetic fields to show the hysteresis loop associated with switching of the canted moment.*

We also performed VSM for a magnetic field applied in a direction perpendicular to the sample plane in order to check the orientation of the small canted moment. As shown in ***Figure 5-2***, we observe the absence of switching of the canted moment, which verifies the fact that the c-axis is a hard axis in the canted easy-plane phase of Hematite. At an applied magnetic field of up to 2.5 T, the measured net moment is approximately 30 memu, which remains considerably lower than the net moment of 60 memu, obtained when applying a magnetic field oriented parallel to the sample's plane. This indicates that a magnetic field of

2.5 T is not strong enough to align the canted moment along the applied magnetic field. Therefore, one cannot investigate the possibility to stabilize surface spin-waves with an out-of-plane canted moment with this orientation of single crystals, as explained in (*25–27*).

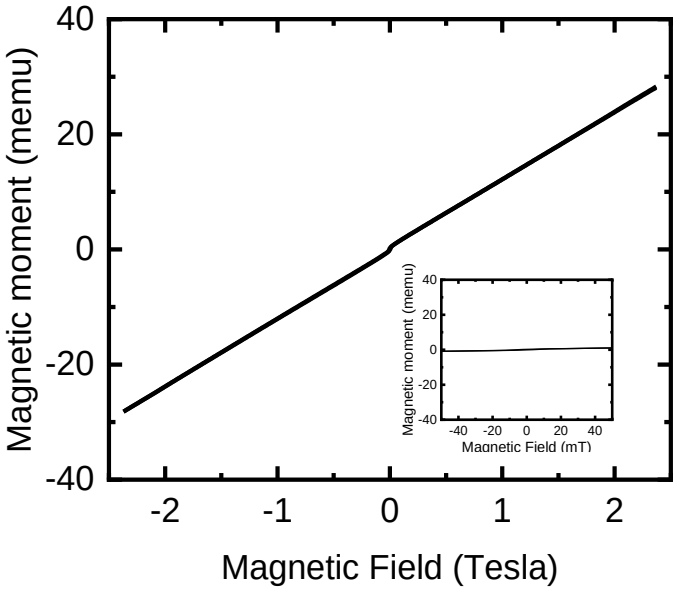

Figure 5-2: VSM with out-of-plane magnetic field: *Magnetic moment of the sample when applying a magnetic field perpendicular the sample plane (c-plane, easy-plane of hematite). Inset corresponds to a zoom at low magnetic fields and show the absence of switching of the canted moment.*

5.3 THE EXPERIMENTAL DESCRIPTION:

5.3.1 Antenna design and k-selectivity:

For our study, we use radio-frequency antennas of ground-signal-ground (GSG) type separated by a distance *d*. When an rf-current is injected, the antenna generates a dynamic magnetic field that excite the SWs. Thus, the antennae's shape defines the wave vector of the excited SW. The antenna excitation spectrum is predicted from calculating the Fourier transform of the spatial current distribution in the antennas (*28*).

In this work, we have used only one geometry of antenna with 3 different ground-signal lines widths in order to select different k-vectors.

The widths and the k-values are represented in ***Table 5-2***, where w_g and w_s are the widths for the ground and signal lines respectively. These two are separated by a distance *s*, the separation distance.

Device Name	***w_g (µm)***	***w_s (µm)***	***s (µm)***	***k (rad/µm)***
Design 1	2	4	2	0.6
Design 2	1	2	1	1.1
Design 3	0.5	1	0.5	2.3

Table 5-2: The designs description:*Table showing the ground-signal-ground widths w_g and w_s and the separation distance s from a ground line to a signal line, for three devices, resulting in three different characteristic k-vector associated for each antenna.*

For the devices with the largest dimensions (Design 1, dimensions listed in the table), we employed SMART PRINT-UV optical lithography to pattern the GSG antenna onto the sample. On the other hand, for the smaller devices (Designs 2 and 3), we utilized electron beam lithography for patterning. Following the patterning process, we deposited a bilayer consisting of 20 nm of Ti and 280 nm of Au onto the structured areas with evaporation. Thereafter, the sample was immersed in acetone to lift off the resist, resulting in the holding of the metallic GSG antennae on top of the sample.

The current density profiles of the 3 different designs in k-space are shown in ***Figure 5-3***.

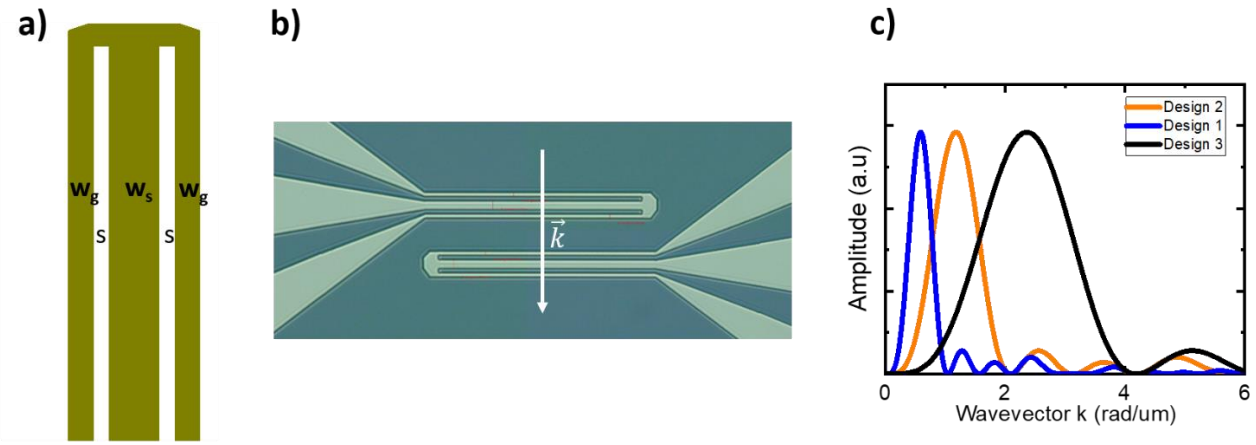

Figure 5-3: G-S-G antenna design*: a) Schematic: the ground lines of width w_g are separated by a distance s from the central signal line of width w_s, b) Optical microscope image for one design showing the direction of propagation of the spin-waves $\vec{\boldsymbol{k}}$, c) Current density profile of three different sizes of GSG antenna in function of the wavevector* ***k*** *and showing the maximum k-value i.e. the value at which the spin-wave is excited ; Each curve corresponds to one antenna in one design ; Blue for design 1, orange for design 2 and black for design 3.*

5.3.2 The experimental scheme:

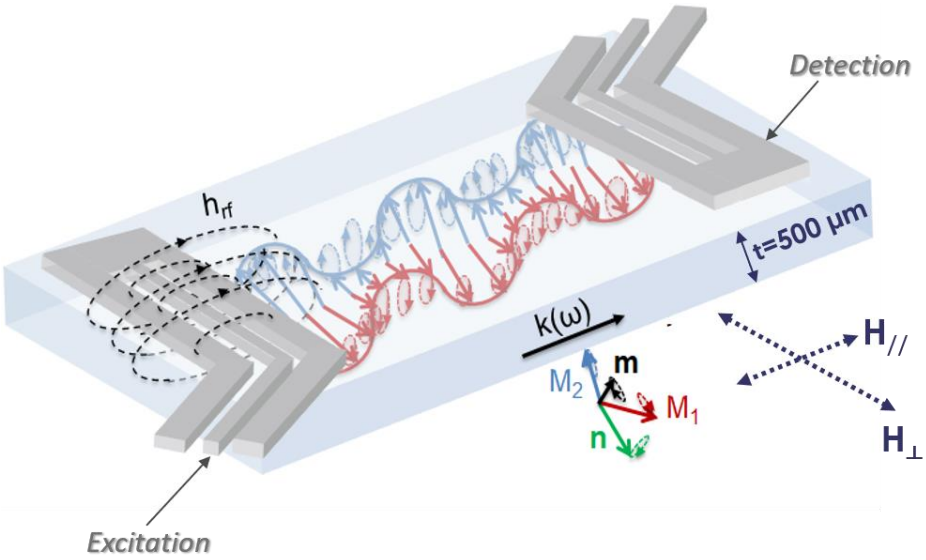

Figure 5-4: Propagating spinwave spectroscopy on α-Fe_2O_3: *Schematics of the setup. The net sub-lattice magnetization M_1 and M_2 have strongly elliptical trajectory, oscillating mainly in the sample plane (easy-plane) with only a small opening angle in the out-of-plane direction.* ***n*** *and* ***m*** *respectively correspond to the Néel vector and the canted moment dynamics.* ***n*** *is linearly polarized in the sample plane whilst* ***m*** *is elliptically polarized. The static net moment m is aligned along the applied field* ***H****, and the Néel vector* ***n*** *is perpendicular to it.*

To generate and detect spinwaves in the characterized sample of Hematite, we used the propagative spinwave spectroscopy. For this, we measure the reflected L_{11} and transmitted L_{21} parameters between the two inductive antennas. We will first show results that mainly

focus on the design 1 (see ***Table 5-2***), which primarily excite spinwaves with a wave vector of 0.6 rad/μm. Furthermore, we will show additional measurements conducted with design 2 and 3 to verify the observations with different k-values.

In our measurements, as illustrated in ***Figure 5-4***, the k-vector is oriented in plane and perpendicular to the antennas, specifically in the x-direction. The antiferromagnetic order vector, $\boldsymbol{n}$, lies in-plane and perpendicular to the propagation vector $\boldsymbol{k}$. Because of the small canted moment $\boldsymbol{m}$, the direction of $\boldsymbol{n}$ can be oriented perpendicular to the applied field H with fields as low as 50 mT (*23*). We recall that in this low-frequency mode of magnons, the sublattice magnetizations $\boldsymbol{M_1}$ and $\boldsymbol{M_2}$ undergo circularly polarized precession, following an elliptical trajectory and oscillating in the basal plane—the plane in which they lie. Due to the small canting, the oscillation is accompanied by a small opening angle in the out-of-plane direction. Consequently, $\boldsymbol{m}$ follows an elliptical polarization, while the Neel vector follows a linear polarization.

To explore the origin and characteristics of spin waves, we will be focusing on two configurations of the applied magnetic field. One orientation will be parallel to the propagation vector (equivalently, $\boldsymbol{H} \perp$ to $\boldsymbol{n}$ and $\boldsymbol{k}$), and the other orientation will be perpendicular to it (equivalently, $\boldsymbol{H}//\boldsymbol{n}$).

5.4 THE EXPERIMENTAL RESULTS

In this section, we will present the results obtained from the experiment, as described in ***5.3 5.3.2***. The organization of this section is as follows:

We will present the results by starting with the reflection spectrum as a starting point for our observations. Next we move to the transmission spectrum, and we focus on the investigation of bulk magnon modes in two different applied field configurations. Subsequently, in both configurations, we observe a rich spectrum of modes. Therefore, we conduct frequency-time gating measurements for both configurations to extract information about the group velocities. A significant non-degeneracy is evident when comparing the two cases, and this will be backed up by theoretical analysis. Finally, we highlight the existence of surface modes in the configuration where $\boldsymbol{H}$ is perpendicular to the propagation of SWs, supported by the application of time gating, enabling a comprehensive study of the non-reciprocal behavior of these modes.

5.4.1 The reflection spectrum: Observation of resonance

Since reflected signals are anticipated to be more sensitive to uniform magnetization dynamics (i.e., the case of the $k = 0$ mode), and to gain deeper insight into the system's response, we initially start our analysis of the reflected inductance parameter L_{11}.

We first put our sample with an applied field that is parallel to the k-vector. The results are shown in the panel **a)** of ***Figure 5-5***, where we were able successfully to detect a clear signal spanning from about 10 to 20 GHz for fields going from 0 to 155 mT.

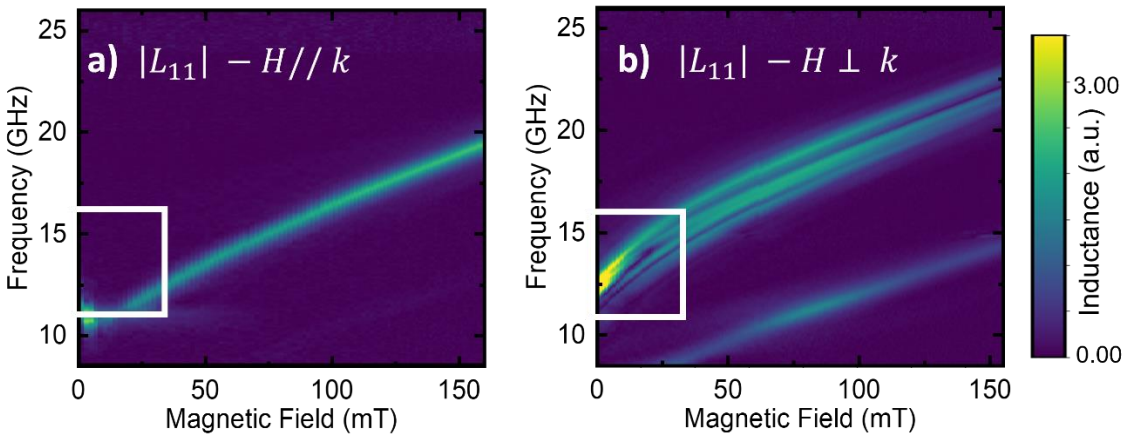

Figure 5-5: Reflection spectra in the different fields configurations: a) *Colormap showing $|L_{11}|$ parameter in function of the swept field and frequency for the* ***H*** *//****k*** *configuration (equiv.* ***k*** *⊥* ***n****),* ***b)*** *Colormap showing $|L_{11}|$ parameter in function of the swept field and frequency for the* ***H*** *⊥* ***k*** *configuration (equiv.* ***k*** *//* ***n****). The white square in both panels is to focus on the 0-field region.*

If we recall expression $\boldsymbol{f_{10}}$, representing the resonance frequency without accounting for dipolar effects, and consider it at $\mu_0 H = 0\ mT$, one will obtain a frequency value lower than

what is shown in panel **a)** (around 6.8 GHz versus 10 GHz for this case). Then, if we move to the other configuration where the field is perpendicular to the k-vector, a similar behavior would be expected in absence of dipolar interactions, as predicted by f_{10}. Yet, contrary to these expectations, as shown in panel **b)**, the spectrum is not as simple as in the previous case, as it is constituted of multiple branches at higher frequencies (see the white squares on the figure to highlight the differences between the two cases). Therefore, to make a complete study of these observations and to be able to make a link with the theoretical expectations, an analysis in the transmission spectrum is required.

5.4.2 Transmission spectrum: Checking the Cross-talk

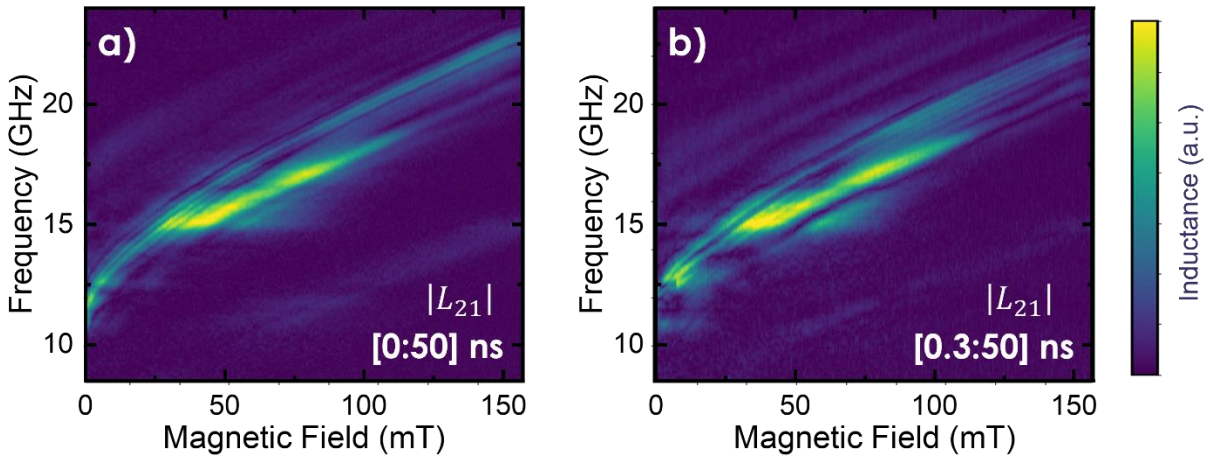

Figure 5-6 Spin wave transmission measurement showing the transmitted amplitude $|L_{21}|$ for k // n. *For a time gate of* ***a)*** *[0:50 ns] and* ***b)*** *[0.3:50 ns]*

Prior the measurements and analysis, we check the contribution provided from the cross talk between the antenna in the signal. We first performed a VNA calibration using a micro probe RF calibration kit. This is done at the pitch of the microwaves probes that will be connected later to the microwave antennas. Thereafter, to eliminate any potential cross-talk contributions, we executed time gate VNA measurements (refer to **Chapter 3**). We set an initial time gate set at 0.3 ns and we compare the results obtained without setting a gate i.e. from time 0. As shown in the ***Figure 5-6***, we can identify similar spin-wave signal in panel **a)** representing the measurement performed with a time gate from 0 to 50 ns and the gated measurement in panel **b)** performed with a time gate starting from 0.3 ns to 50 ns. This similarity between the two transmission signals thus verify our ability to exclude any potential contributions from direct cross-talk.

5.4.3 SW transport in canted α-Fe_2O_3: Case of $\boldsymbol{H}$ // $\boldsymbol{k}$.

In this first case, where the applied magnetic field $\boldsymbol{H}$ is parallel to the propagation direction $\boldsymbol{k}$, and perpendicular to the antiferromagnetic order vector $\boldsymbol{n}$ (i.e. $\boldsymbol{H}//\boldsymbol{k}$ and $\boldsymbol{k} \perp \boldsymbol{n}$) we observe, as shown in ***Figure 5-7***, two closely spaced spin wave branches. These branches have frequencies ranging from approximately 10 GHz to up to 22 GHz for magnetic fields

ranging from 0 to 175 mT.

In the figure, we show the fittings conducted using the theoretical expression ***(Eq. 5-4)*** for the bulk magnon modes in this field configuration, with the value of $k = 0.6\, rad/\mu m$. The fitting is done by firstly identifying the maxima in the spectrum and fitting each branch using the expression with the material parameters from the ***Table 5-1*** as initial values for the fit. The result of the fit is in a perfect match with the modes present in the spectrum. We however attribute the presence of the two modes to slight non-uniform anisotropies in the sample, as we show later from the obtained parameters of the fit.

Additionally, the inset exhibits fittings with the L_{11}. Notably, a slight down frequency shift is observed between the reflection with respect to transmission. As mentioned earlier, this discrepancy may be linked to the increased sensitivity to the $k = 0$ mode in reflection.

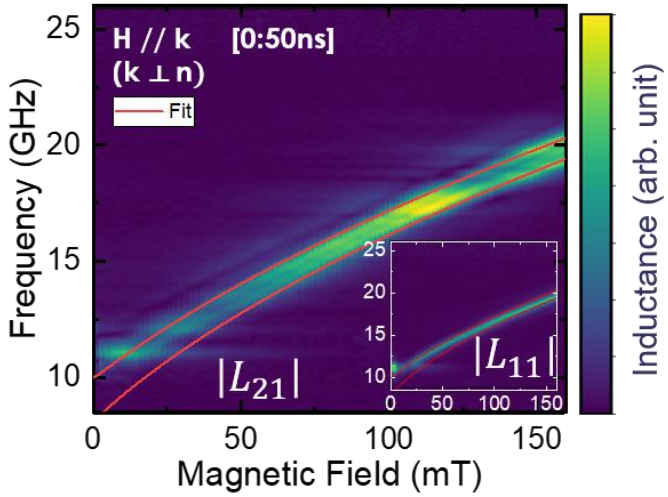

Figure 5-7: Transmission spectra in H // k configuration: *Colormap showing the transmitted L_{21} parameters for **H // k** configuration (equivalently **k⊥n**), showing two propagative mode that are in-line with the fits (red lines) using the theoretical bulk spin-wave equations for the case where **k ⊥ n** at k=0.6 rad/µm. Inset show the amplitude of the reflected signal $|L_{11}|$ as well as the theoretical fits.*

- **Time of flight SW spectroscopy:**

To access the properties of these propagating modes, one needs to examine the phase. Therefore, we will conduct an in-depth study of the phase profile using the imaginary part of L_{21}.

We restrict our analysis for magnetic fields above 50 mT to ensure that the Néel vector $\boldsymbol{n}$ is always strictly perpendicular to the $\boldsymbol{H}$. In ***Figure 5-8.*** **a)** we present the imaginary part of the transmitted spin-wave spectra L_{21} for $\boldsymbol{k} \perp \boldsymbol{n}$. As shown in ***Figure 5-8.*** **b)** we observe the expected oscillatory behavior of the phase delay($\varphi = kD_{ant}$, with D_{ant} being the distance between the two transducer antennae) accumulated by the spin wave during its propagation. From these oscillations, the spin-wave group velocity is given by:

$$v_g = \frac{\partial f}{\partial k} \sim D_{ant}.\Delta f$$

(Eq. 5-1)

can thus be extracted from the periodicity of phase oscillations Δf. As discussed, the imaginary part gives the direct access of the phase oscillations. Thus, from Im(L_{21}) one can extract delta f from the difference between two consecutive peaks.

However as shown in the black curve of ***Figure 5-8.*** **b)** the envelop of the signal shows the presence of ripples indicating the presence of more than one spin-wave packet. Those are due to both wide k-bandwidth of our antenna ($\partial k \approx 0.2 - 1\, rad/\mu m$), and potentially to propagating spin-waves with non-uniform thickness profile in our 500 µm thick film.

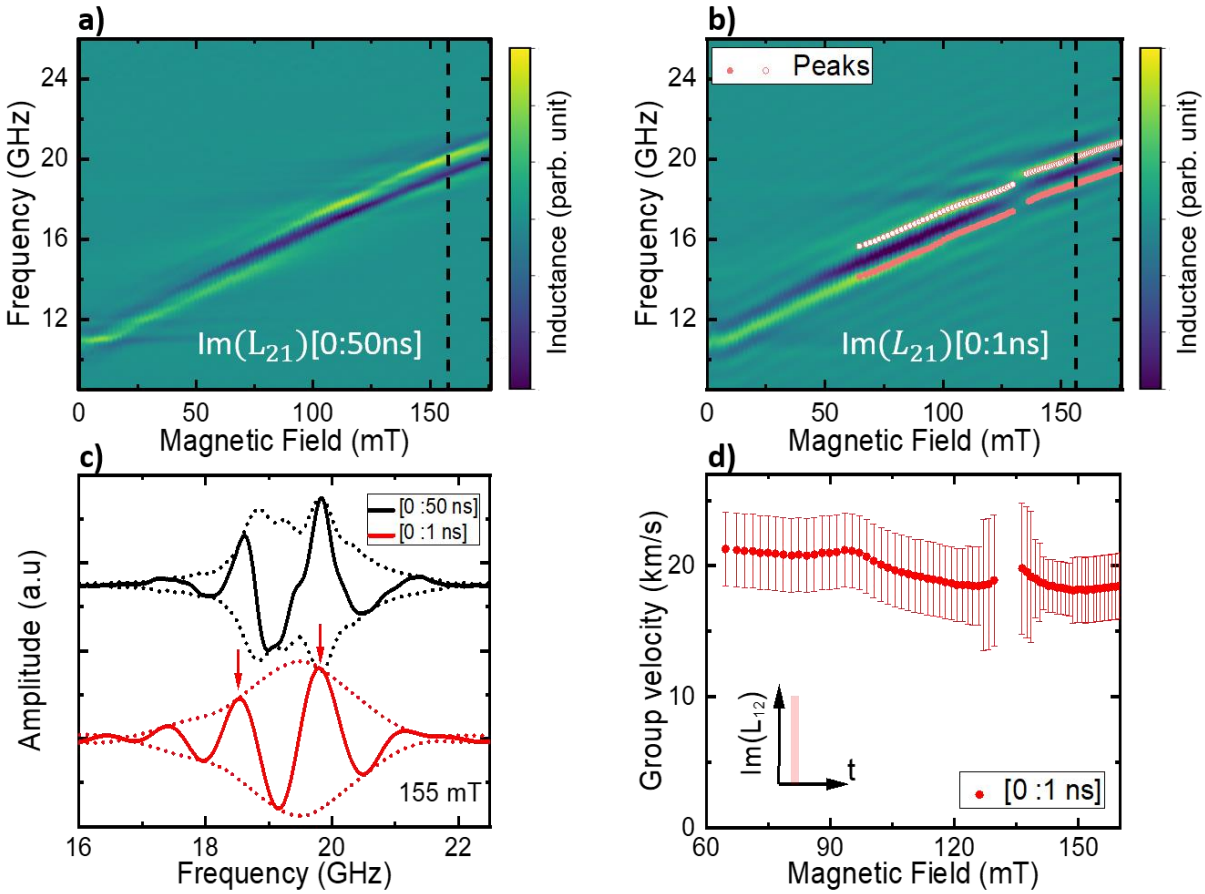

Figure 5-8: Ultra-fast antiferromagnetic spin-waves for H // k revealed by time gating*: a) Imaginary part of the transmitted spin-wave Im(L_{21}) as a function of field without time gating. b) Im(L_{21}) as a function of field with gating [0:1ns], the red dots are extracted peaks shown in c) and used to calculated the velocity in d). c) Example of Im(L_{21}) spectra of the full spin-wave signals (time gate of [0:50 ns], black) and of the main spin-wave packet (time gate of [0:1 ns], red) for $\mu_0 H = 155\, mT$ for an edge-to-edge antenna distance of 14 µm, oscillations (red) indicate a spin-wave group velocity > 14 km/s. Dotted lines correspond to the signal envelopes. d) Group velocity of the main spin-wave packet for a time gating of [0:1 ns]. Error bars are defined as the noise level from the Im(L_{21}).*

To access the group velocity of each spin-wave packets, we perform time gating VNA measurements(*29*) with different time intervals. We keep reducing the time gate until we

obtain a clean oscillatory profile indicating nearly single mode propagation. This is achieved when applying a gate of [0:1ns] whose parameters are shown in the spectra of ***Figure 5-8.*** **b)** and oscillations are represented by the red curve of ***Figure 5-8.*** **c)**

In fact, when applying a gate that starts from 0 ns and cuts the signal after 1 ns, we cut from the measured the signal the contribution of the slower modes and also all other measurement losses. Therefore, we observe cleared oscillations of the inductance L_{21} enabling to fit field-by-field the position in frequency of these peaks. This will give us the evolution of the phase oscillation Δf at all the swept field, for the spinwave packet propagating between the two antennae with an edge-to-edge antenna of 14 µm. Therefore, one can extract the group velocity of the associated to this spin-wave mode as shown in ***Figure 5-8.*** **d)**. We find a v_g lying in an average value of around 20 km/s over the measured field range. This value is in accordance with the theoretical formulation of the group velocity ***(section 2.2.8A)***. It must be noted that such values of group velocities represent a record velocity for spin-waves in a magnonics device.

5.4.4 SW transport in canted α-Fe_2O_3: Case of $\boldsymbol{H} \perp \boldsymbol{k}$

In this second case, the applied magnetic field $\boldsymbol{H}$ is now perpendicular to the propagation direction $\boldsymbol{k}$, and thus parallel to the antiferromagnetic order vector $\boldsymbol{n}$. Here, we observe as shown in the figure below, a richer transmission spectrum hosting many branches with respect to the previous configuration. We observe a main spin-wave mode (blue line) as shown in ***(Figure 5-9)*** along with several spin-wave branches at slightly higher frequencies (represented by orange and green lines).

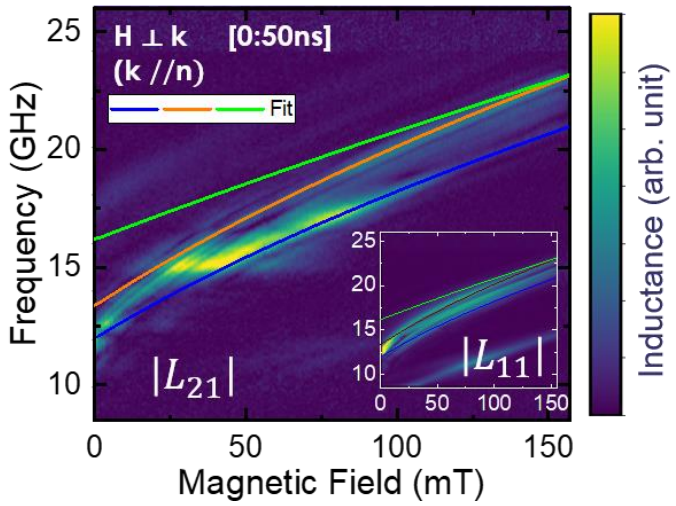

Figure 5-9: Transmission specta in H ⊥ k: *Spin wave transmission measurement showing the transmitted amplitude $|L_{21}|$ for* ***k // n*** *at k ≈ 0.6 rad/µm. The blue line corresponds to fits using the theoretical bulk spin-wave equations for* ***k // n (Eq. 5-1)****, orange and green lines respectively correspond to a modelling of the high-frequency spin-wave branch for* ***k // n*** *assuming a bulk or a surface mode (refer to* ***(Eq. 5-3)****, and Refs. (9, 10, 12) and more in details in the suppl mat. of ref. (22)). Inset show the amplitude of the reflected signal $|L_{11}|$.*

Regarding the theoretical fittings, as in the previous case, we have used here the theoretical

expression from ***(Eq. 5-1)***. We observe a match with the lower frequency branch of the spectra meaning that this mode corresponds to a bulk SW mode in this configuration; however, for the other branches present over higher frequencies, the used expression does not align.

These modes needs further investigation as their behavior is much complex than the bulk modes. For this a modeling on these observed modes have been done where an expression for surface SW modes have been developed based on *(9, 10, 12)* and is provided by ***(Eq. 5-3)***. The fitting of these modes is presented by the orange and green lines in ***Figure 5-9***. We therefore associate these different branches to the presence of magneto-static modes(*7*, *10*, *19*, *30*) and are further discussed in the following sections.

Knowing that the color-bar intensity scale is kept the same for all the figures , we notice that the intensity of the signal's amplitude in this configuration is higher than in the previous one ($\boldsymbol{H} \,//\, \boldsymbol{k}$). This is indeed linked to the excitation efficiency by the inductive antennae, i.e., the coupling with the dynamic components of the magnetic field. As stated and discussed in **Chapter 3**, in the case where $\boldsymbol{H} \perp \boldsymbol{k}$, the excitation is sensitive to both the z-component and x-component, whereas, for $\boldsymbol{H} \,//\, \boldsymbol{k}$, the excitation is affected only by the out-of-plane component of the dynamic field.

Regarding the signal amplitude at low fields, one should notice that it strongly varies below 50 mT, which is due to, the reorientation of the Néel vector $\boldsymbol{n}$ and canted moment $\boldsymbol{m}$(*19*, *31*) within this low field range.

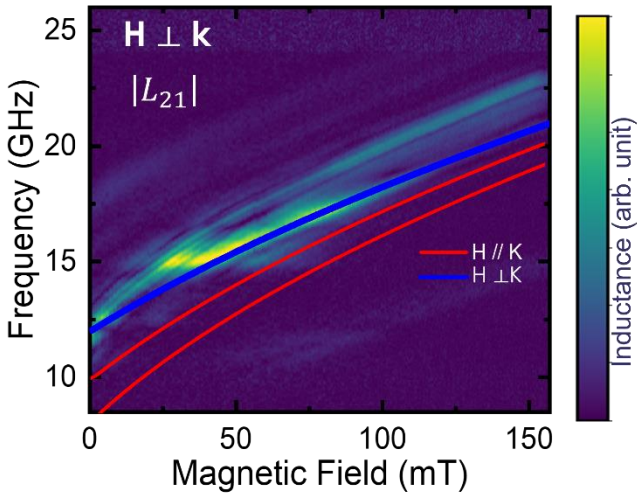

Figure 5-10: Comparison between bulk modes: H // k *(blue lines) bulk versus* ***H ⊥ k*** *modes(red lines).*

Now, let's compare the spectra obtained from both field configurations. We replot the bulk modes found in the $\boldsymbol{H} \,//\, \boldsymbol{k}$ configuration, represented by the red lines, on the spectrum of $\boldsymbol{H} \perp \boldsymbol{k}$ and compare them to the low frequency mode from this configuration (blue line) as shown in ***Figure 5-10***. From this, we notice that these two bulk modes vary in a similar

tendency, with an evident frequency shift. Hence, from these measurements, we were able to observe and demonstrate a lifted degeneracy of the SWs modes, with a frequency difference of around 1 GHz. This will be investigated more in details in the following sections.

❖ **Time of flight SW spectroscopy:**

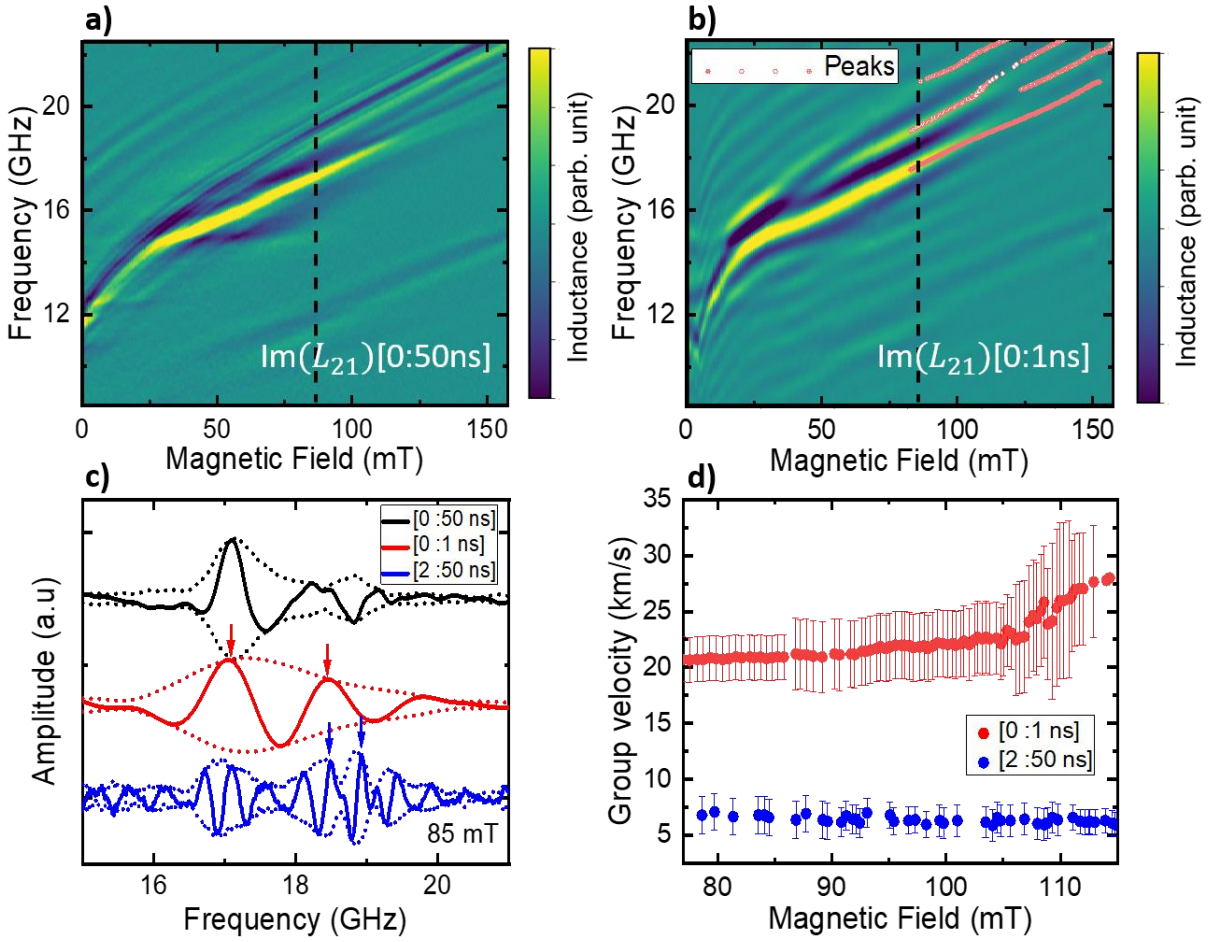

Figure 5-11: Ultra-fast antiferromagnetic spin-waves for H ⊥ k revealed by time gating*: Imaginary part of the transmitted spin-wave Im(L_{21}) a) with a large time gate from 0 to 50 ns .b) with a time gate from 0 to 1 ns.The red dots are the extracted data points representing the maxima of the Im(L_{21}) oscillations c) Exemplary spectra of Im(L_{21}) for $\mu_0 H$ = 85 mT for different time gating, [0:50 ns]: full spin-wave signals (black), [0:1 ns]: first spin-wave packet (red), [2:50 ns]: secondary spin-wave packets (blue). Dotted lines correspond to the signal envelops. c) Group velocity of the different spin-wave packets. Error bars are defined as the noise level from the imaginary part of the transmitted inductance L_{21}. Higher frequency modes propagate around 3 times slower with around 8 km/s than the bulk mode, with around 20 km/s.*

Focusing back on the case of $\boldsymbol{H} \perp \boldsymbol{k}$ where we have seen the existence of these multiple spin-wave branches separated by a few GHz, we employ time gating measurements to selectively access these distinct modes. Without applying a gate, the spectrum of Im(L_{21}) (as seen in ***Figure 5-11.*** **a)**) exhibits a multimodal profile, with many peaks overlapping and interfering with one another.

Conversely, as in the previous configuration ($\boldsymbol{H}$ // $\boldsymbol{k}$), by applying a time gate within the range

of [0:1 ns], we can isolate a single-mode oscillation profile (in ***Figure 5-11.* c),** in red, obtained at a field of 85 mT). The corresponding spectrum is presented in ***Figure 5-11.* b)**, on which we follow three neighboring peaks represented by the red dots and used to calculate the group velocity shown in panel **d)**. From this, we can admit that we have a spinwave travelling at about 20 km/s. Similarly to the previous case, this value is in accordance with the theoretical expression of v_g derived from the bulk magnon dispersion ***(section 2.2.8A)*** in the $\boldsymbol{k}//\boldsymbol{n}$ configuration.

One should however notice the SWs velocity slightly increases with field, leading to larger phase oscillations Δf that become difficult to extract above 120 mT. Surprisingly, the higher-frequency spin-wave modes were identified by applying a gate of [2:50 ns] (as seen in the blue curves in ***Figure 5-11.* c)**). This suggests that these modes propagate more slowly, yet they still travel in less than 10 ns. Since these modes are so close in frequency and have similar travel times, we can only determine an average group velocity of 6 km/s.

5.4.5 Non degenerate magnon modes: Redefining the SW dispersion relation

Here we come back to the observed frequency shift between the two configurations and the mode non degeneracy upon changing the field orientation.

For this aim and to gain a deeper understanding of the underlying reasons for this anisotropic magnon transport, we measure spin-wave dispersion measurements for $\boldsymbol{k}//\boldsymbol{n}$ (shown as black and blue data points) and $\boldsymbol{k}\perp\boldsymbol{n}$ (depicted as red data points) by using the different transducer design as described in ***Table 5-2***.

A. Spin-wave spectroscopy for k at different k-values:

In this section, we show the results of the measurements done on designs 2 and 3 (***Table 5-2***). We present here the measurements done for both directions of $\boldsymbol{k}$, while repeating the measurements with the exact parameters used as in the case of design 1, and with no time gating applied.

In ***Figure 5-12***, we show the colormaps of $\log|L_{21}|$ as a function of the swept frequency and of the applied field when $\boldsymbol{H}//\boldsymbol{k}$ (respectively, $\boldsymbol{k}\perp\boldsymbol{n}$). For $k=0.6$ and$k=2.3\,rad/\mu m$, we observe the dominance of one spin-wave mode while at $k=1.2\,rad/\mu m$ we observe an increase in frequency of about 1 GHz for the dominant mode. We also observe the presence of a secondary spin-wave branch lower in amplitude and in frequency for $k=1.2\,rad/\mu m$, which goes beyond standard analysis and would require further investigation using for example Brillouin Light Scattering.

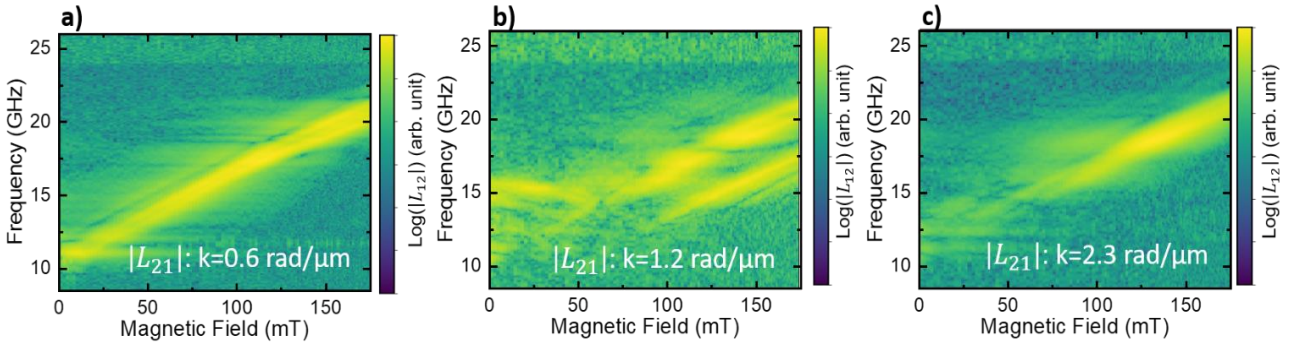

***Figure 5-12: Frequency transmission spectra of the three designs for H // k**: Colormaps showing of |L_{21}| (in log scale) for the design 1 having an excitation k at 0.6 rad/µm (panel **a)**) for the Design 2 having an excitation k at 1.2 rad/µm(panel (**b)**), Design 3 having an excitation k at 2.3 rad/µm (panel **c)**).*

In ***Figure 5-13***, we then show the results for $\boldsymbol{k} \,//\, \boldsymbol{n}$, we observe a clear increase in frequency between $k = 0.6\, rad/\mu m$ and $k = 2.3\, rad/\mu m$ for the main spin-wave peak, corresponding to the bulk spin-wave mode. One should however notice that more secondary spin-wave peaks can be observed for $k = 0.6\, rad/\mu m$, as the devices are larger and enable a more efficient detection. The frequency of the spin-wave mode with surface character has a smaller increase than expected for a surface mode. Also, in this case, the device with $k = 1.2\, rad/\mu m$ shows more pronounced secondary spin-wave peaks, which could indicate that the mode hybridization is maximum for this range of k-vectors.

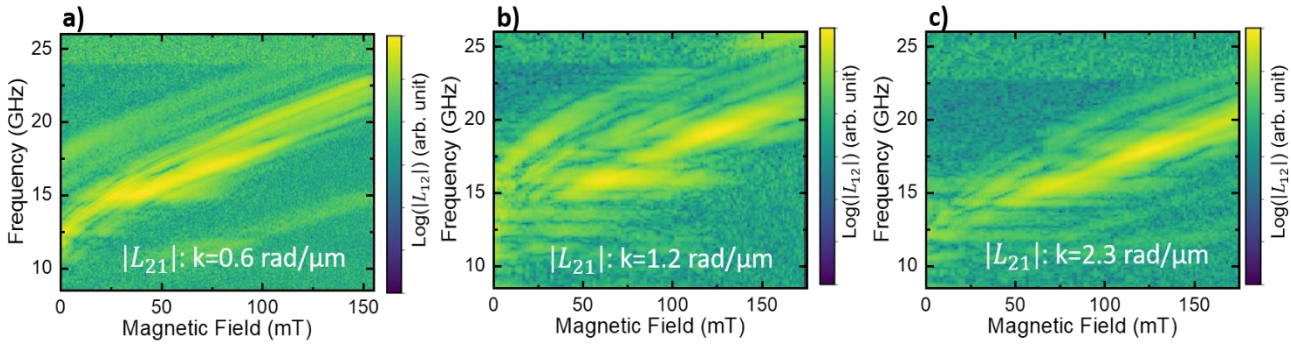

***Figure 5-13: Frequency transmission spectra of the three designs for H ⊥ k**: Colormaps showing of |L_{21}| (in log scale) for the design 1 having an excitation k at 0.6 rad/µm (panel a)) for the Design 2 having an excitation k at 1.2 rad/µm (panel b)), Design 3 having an excitation k at 2.3 rad/µm (panel c)).*

We clearly observe the persistence of well-separated magnon branches for the two configurations, with always higher frequencies for $\boldsymbol{H} \perp \boldsymbol{k}$ modes as we vary the wavelength value of the antenna.

By following these measurements and utilizing data from three distinct k-vectors corresponding to the respective devices, we constructed the dispersion relation. This enable a deeper understanding of the different modes present in the system as shown by their corresponding points in ***Figure 5-14*** (blue and black representing the perpendicular

configuration of field, red represents the parallel configuration of field).

Thereby, by using the adapted theoretical models, we have successfully fitted the dispersion relation representing the frequency of the bulk spin-wave modes as a function of the applied magnetic fields for both configurations, as shown in red and blue in ***Figure 5-14***.

This result highlights the importance of the presence of magneto-static interactions in shaping the spin-wave dynamics of canted antiferromagnets, particularly at small wavevectors ($k < 10\, rad/\mu m$). Nevertheless, it's important to note that these models fail to explain the presence of the higher-frequency spin-wave branches observed when we are in the perpendicular configuration of the field. This necessitates further investigations into these modes, which will enable us to gain a deeper understanding of their behavior and origin.

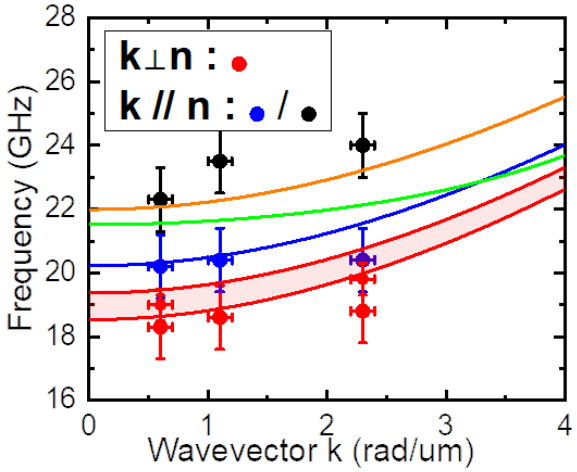

Figure 5-14: Magnon dispersion curves: *Magnon branch dispersion for* ***k // n*** *and* ***k ⊥ n*** *at a magnetic field of 140 mT. Blue and red lines correspond to the theoretical bulk spin-wave branches* ***k // n*** *and* ***k ⊥ n*** *respectively using the fitting in magnetic field.*

One should mention that this obtained behavior does not validate the expected degenerated linear dispersion typically reported for antiferromagnets. This is the reason why, other regimes should be considered, namely, the dipole-exchange regime of canted antiferromagnets, which, to our knowledge, has not been yet experimentally explored.

A refined expression of the bulk spin-wave bands in the dipole-exchange regime leads to a frequency difference expressed as:

$$\Delta f_{SW} = f_{\mathbf{k}\,//\,\mathbf{n}} - f_{\mathbf{k}\perp\mathbf{n}} = \sqrt{f_{10}^2 + \frac{4\pi M_s}{H_E}\left(\frac{\gamma}{2\pi}\right)^2 (H + H_{DMI})^2} - f_{10}\left(1 + \frac{4\pi M_s}{H_E}\right)$$

(Eq. 5-5)

with f_{10} the frequency gap for the lowest magnon mode(*32*, *33*), γ is gyromagnetic ratio, H_E is exchange field and H_{DMI} is the Dzyaloshinskii-Moriya field. By using the material parameters

of Hematite ***Table 5-1***, we estimate $\Delta f_{SW} \approx 0.5 - 1$ GHz for small k-vectors (10 rad/µm) which agrees with the observation that the spin-wave frequencies are higher for $\boldsymbol{k} // \boldsymbol{n}$ than for $\boldsymbol{k} \perp \boldsymbol{n}$.

A. Discussion:

	$\boldsymbol{k} \perp \boldsymbol{n}$	$\boldsymbol{k} // \boldsymbol{n}$
$\mu_0 H_{DMI}$ (T)	2 (blue) - 1.9(brown)	1.8
Freq, γH_{DMI} (GHz)	56 - 52	50
f_{10} (GHz)	10.3 (blue) – 12 (brown)	9.5 (lower red) – 1.5 (higher red)
f_{20} (GHz)	184	184
$\xi = 4\pi M_s / H_E$	0.013	0.013
c **(km/s)**	24.5	24.5

Table 5-3: Material parameters*: The obtained values from fitting the experimental frequency dispersions for $\boldsymbol{k} \perp \boldsymbol{n}$ and $\boldsymbol{k}//\boldsymbol{n}$, and as a function of k.*

In ***Table 5-3***, we present the various parameters obtained from fitting the experimental dispersion frequency as a function of k, by using the different designs, as previously explained, and for two configurations. These parameters are therefore utilized to fit the experimental spectra with respect to the applied field, as illustrated in ***Figure 5-7*** by the red lines and ***Figure 5-9*** by the blue, orange and green lines.
One should notice that the obtained value of ξ is larger than the standard value found for Hematite. This may indicates a potential divergence in the behavior between the crystal's surface and its bulk.

For the first configuration ($\boldsymbol{H} // \boldsymbol{k}$), the expression aligns well with the observed SW modes, indicating that these are indeed bulk modes in the ($\boldsymbol{k} \perp \boldsymbol{n}$) configuration. Similarly, for the case of the second configuration ($\boldsymbol{H} \perp \boldsymbol{k}$), the modeling fits well with the lowest frequency branch, suggesting that this branch represents a bulk mode for ($\boldsymbol{k} // \boldsymbol{n}$). However, this does not hold true for the higher frequency modes, which require further investigation to determine their origin, as discussed in the next section and specifically in **Chapter 6**, where an alternative mean of detection is used.

5.4.6 Non reciprocity: Time gating of k perp to n, and k parallel to n:

Non-reciprocity can be attributed for the existence of surface modes and it has been extensively studied in ferromagnetic materials, where the referred as Damon-Eschbach mode.

It is mainly described by a non-reciprocal spin wave amplitude, with opposite signs of wavevectors(*34*). This non reciprocity of SWs is a key property for many spin-wave analog devices (such as circulators) and up to our knowledge, it is only predicted in antiferromagnets(*25*, *26*).

In the following, we will check the non-reciprocity of the spin-wave packets for $\boldsymbol{H} // \boldsymbol{k}$ and examine deeper the high-frequency modes that do not align with the bulk magnon modes fit, as we observed in the case of $\boldsymbol{H} \perp \boldsymbol{k}$.

A. $\boldsymbol{H} // \boldsymbol{k}, (\boldsymbol{k} \perp \boldsymbol{n})$:

In ***Figure 5-15***, we present the absolute values of L_{12} and L_{21} of the same device for negative (panels **a)** and **c)** ,respectively) and positive fields (panels **b)** and **d)** respectively) with $\boldsymbol{H} // \boldsymbol{k}$ and all under the same experimental conditions.

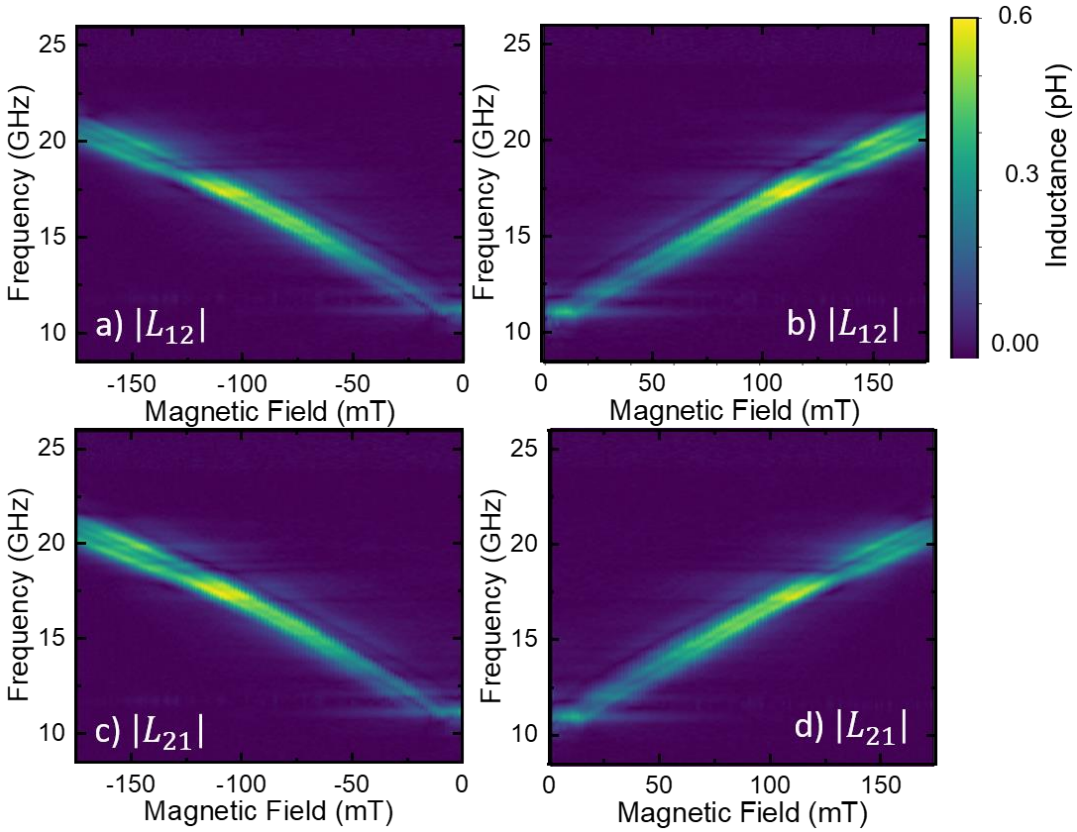

Figure 5-15: Transmission spectra for k⊥n without time gating: *(a-b) The $|\boldsymbol{L_{12}}|$ as a function of frequency and the negative magnetic field. In (c-d), we repeat the same measurements for $|\boldsymbol{L_{21}}|$ and observe similar results.*

In this case, we observe a slight difference for positive and negative fields at magnetic fields between 100-150 mT. However, we can associate this with the small hysteretic behaviour in the sample and not to a potential non-reciprocity as we measure the same signals for L_{12} and L_{21}. This latter feature also indicates that our devices have nearly symmetric antennas and that our setup has well calibrated radiofrequency properties. Hence, the absence of non-reciprocity in this configuration is in line with standard predictions for bulk antiferromagnetic

spin-waves(*8*, *25–27*).

B. $H \perp k, (k//n)$:

In ***Figure 5-16.*** **a)-b)**, we present the amplitude of the transmitted spin-wave packets $|L_{21}|$ for negative and positive fields respectively. When applying a gate of [2:50 ns], we were able to isolate the high frequency mode as shown in ***section 5.4.4*** and as clearly seen from the figure below.

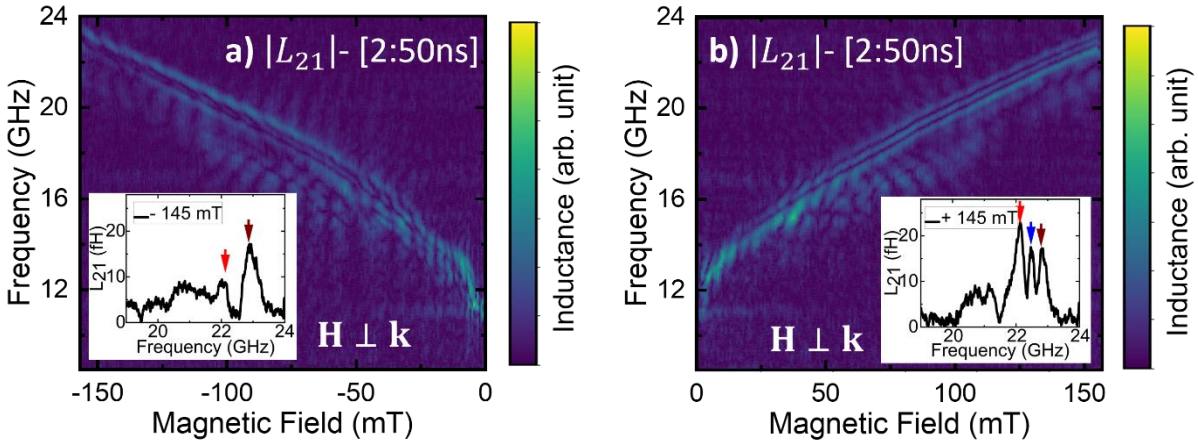

Figure 5-16: Non-reciprocal spin-wave for H ⊥ k. *Absolute value of the transmitted spin-wave spectra* $|L_{21}|$ *with a time gating of [2:50 ns], for positive fields in a) and negative in b). Insets shows exemplary spectra for magnetic fields of respectively +145 mT and –145 mT. Arrows indicates the position of the three different modes.*

In panel **b)**, with the positive field sweep, the spectrum consists of three distinct branches. The lowermost branch has the highest amplitude among the three, as clearly illustrated in the inset of panel **b)**, which shows the associated peaks at a field of +145 mT. Moving on to panel **a)** with the negative field sweeps, a noticeable change occurs: the low-frequency branch experiences a drastic drop in amplitude, and the middle branch completely disappears. This is evident in the inset showing the cut at -145 mT and confirming the described observation.

In ***Figure 5-17.*** **a),** we back up our observation by plotting the obtained peaks for both field polarity overlapping on the same graph; where for negative field sweep the data points are represented by empty dots and full dots for the positive field ones. Therefore we confirm by so that there is no noticeable shift in frequency when going from negative to positive fields.

However, as far as the spin-wave amplitude is concerned, as shown we find a clear non-reciprocity for two out of the three spin-wave modes. This amplitude non reciprocity is more evident in ***Figure 5-17.*** **b),** we represent the amplitudes of the peaks extracted from the spectra in ***Figure 5-16***, again the data points corresponding for the negative fields are represented by empty dots while the positive field with the full dots. We observe for the negative magnetic fields a reduction by about a factor 2 of the red mode (of lowest frequency) and even the absence of the blue mode (the middle frequency mode). Hence we verified this non-reciprocal behavior is by measuring different amplitudes for the $|L_{12}|$ parameters upon

reversing the field polarity.

Therefore, these results are indicates the presence of spin-wave mode with a surface like character for $\boldsymbol{H} \perp \boldsymbol{k}$ which are expected also in case of an antiferromagnet(*10*, *25*, *26*). This is in contrast to what we have seen in the previous case, for $\boldsymbol{H} \,//\, \boldsymbol{k}$, where a reciprocal behavior was found. To understand in more details the symmetry of these spin-waves and how they decay within the AFM requires further experimental and theoretical investigation but it remains beyond the observations performed in this thesis.

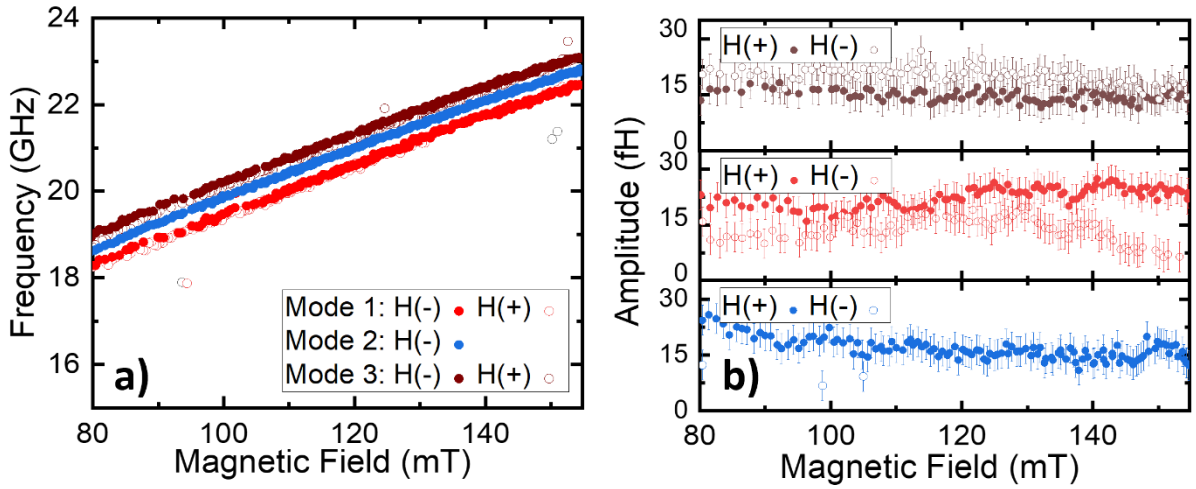

Figure 5-17: Non-reciprocal spin-wave for H ⊥ k. a) *Frequency and* ***b)*** *amplitude of the three main spin-wave modes for negative and positive fields. Error bars are defined as the noise level from the transmitted inductance L_{21}.*

- **Example of non-reciprocity spectra for $k = 2.3\, rad/\mu m$:**

In ***Figure 5-18***, we show the transmission spectra in both L_{21} and L_{12} for the sample design with $k = 2.3\, rad/\mu m$ for $\boldsymbol{k}//\boldsymbol{n}$. Here we also evidence a nonreciprocal behaviour with larger amplitude at high fields (above 100 mT) at one given field direction such as in panel a) with L_{12}, we see a at high negative fields an amplitude much higher than that of the positive fields, and vice versa in panel b) showing L_{21}. This evidences that the non-reciprocity is also present at larger k-value, in line with the theory. Add to that, one can also notice that this non-reciprocity is mainly present for the main spin-wave branch, indicating the presence of mode hybridization between the bulk spin-wave mode and the surface modes which has been reported in ferromagnets (*35*) and therefore goes beyond the standard theory developed.

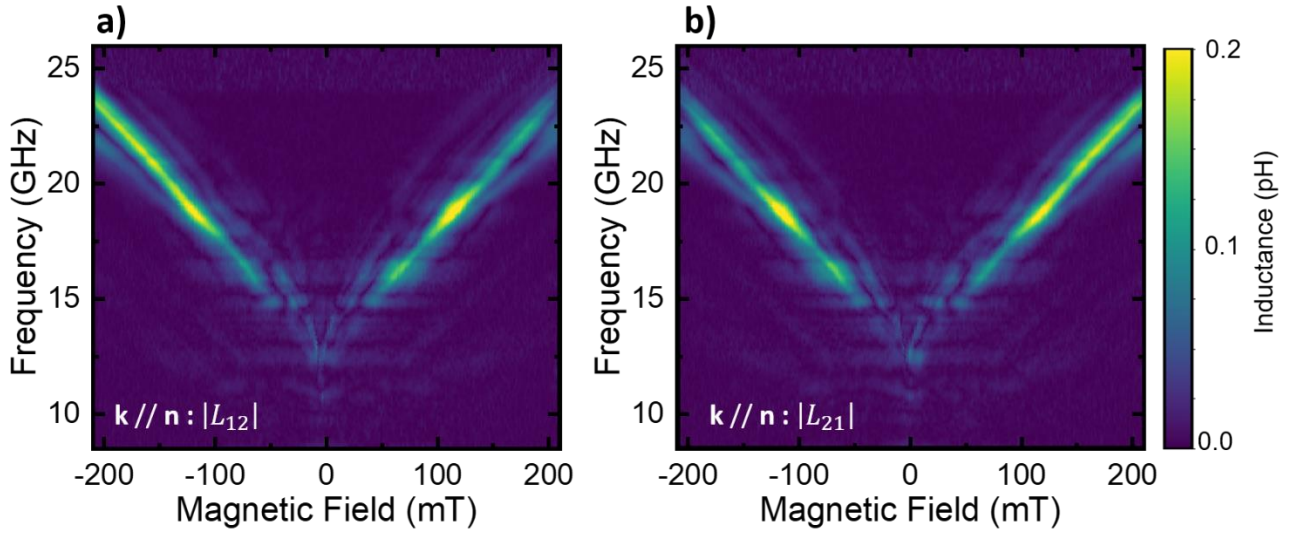

Figure 5-18: Case of other k-value in H⊥k, (k // n): *The transmission spectra of* $|\boldsymbol{L_{12}}|$ *and* $|\boldsymbol{L_{21}}|$ *for* ***k // n*** *in a) and b) respectively, as a function of magnetic field for design 2 with k = 2.3 rad/um: Clear difference in intensity from negative to positive fields, dominance of spin-waves in negative fields for* $|\boldsymbol{L_{12}}|$ *in a), and in positive fields for* $|\boldsymbol{L_{21}}|$ *in b).*

c. Discussion on surface mode stability :

From the theoretical expression of the surface waves ***(Eq. 5-1)*** the frequency of these AFM surface spin-wave mode was around 32 GHz at 100 mT for a wavevector of approximately 0.6 rad/µm and with using the material properties of hematite. However, from the experimental observations the surface modes are around 20 GHz for a same field value which could only be explained by introducing an unrealistic phenomenological effective DMI field, and will be explained in the following:

In the following we will provide a theoretical support developed by Prof. Olena Gomonay

In ***Figure 5-19,*** we present data for two sets of parameters, one derived from the experimental measurements (shown previously), and another using theoretical parameters with a smaller $\mu_0 H_{DMI} = 1.3\,T$. Surface mode exists only in a certain range of the k-vectors that is $k > k_{cr}$, at which spin-wave cannot propagate into the bulk. One can thus notice that surface modes are not supposed to be stable in the experimental accessible range of k-vectors with $\mu_0 H_{DMI} = 2\,T$, and also not stable above a critical $k_{cr} \approx 3$ rad/µm for a lower H_{DMI} and larger value of $\frac{M_S}{H_E}$. This could indicate that these surface modes should be more easily detectable in Brillouin Light Scattering experiments. The discrepancy between experiments and theory could indicate that the surface of hematite have slightly different parameters than the bulk as reported in some articles(*36*, *37*).

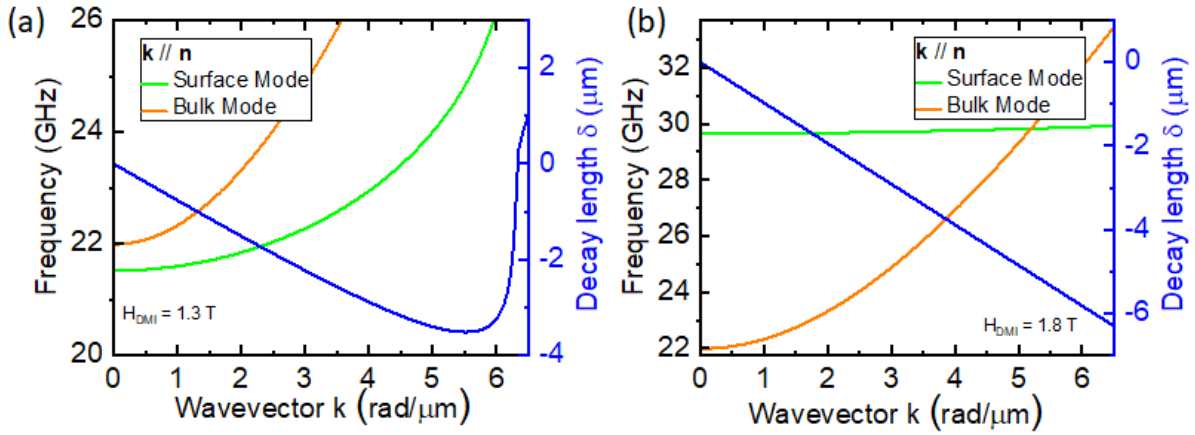

***Figure 5-19: Frequency and decay length of the surface spin-waves modes for k // n**: (a) The $\mu_0 H_{DMI} = 1.3\,T$ and ratio $\frac{M_S}{H_E}$ = 0.2 are fixed in this figure. Other parameters remain the same as in **Table 5-3**. (b) Case corresponding to the experimental parameters given in **Table 5-3**.*

These above conditions are related to the fact that surface modes are only stable when the permeability in the bulk of the material is negative, leading to the following condition on the decay length δ:

$$\delta = -\mathrm{k}\frac{(1+\chi_{\{zx\}})}{1+\chi_{\{zz\}}} > 0$$

(Eq. 5-6)

The diagonal component $\chi_{\{zz\}}$ corresponds to the dynamic magnetization $\boldsymbol{n} \times \dot{\boldsymbol{n}}$ out of the c-plane. It depends on the frequency of oscillations, anisotropy H_a, and $\frac{M_S}{H_E}$. The component $\chi_{\{zx\}}$ corresponding to the out-of-plane oscillations of the in-plane canted moment, being thus proportional to H_{DMI} (, to the surface frequency f_{sur} and to ($\frac{M_S}{H_E}$). Add to that, $1+\chi_{\{zx\}}$and $1+\chi_{\{zz\}}$ should have different signs. One should notice that if nondiagonal susceptibility is zero (i.e., no canted moment), no localised solution is possible.

Now, if the DMI is extremely large and anisotropy is small, the frequency is large and the factors have the same sign. Whereas, if DMI is zero, there is no canted magnetization and thus no coupling with the dynamic magnetization can occur. Here, due to the low magnetic anisotropy of hematite, the gap of the bulk spin-wave mode is particularly small so that one requires a small DMI field to lower the frequency of the surface mode (see ***(Eq. 5-3)*** for the surface mode) in order to fulfil this condition.

5.5 CONCLUSION AND PERSPECTIVES TO PERFORM ISHE MEASUREMENTS:

We thus electrically detect by inductive transducers the presence of non-degenerated and non-reciprocal spin-waves in the dipolar-exchange regime of a canted antiferromagnet, with record group velocities (of about 20 km/s) and micrometers propagation distances. We can well model the presence of a bulk spin-wave frequency band of a few GHz with lifted degeneracy for $\boldsymbol{k} \perp \boldsymbol{n}$ and $\boldsymbol{k} \,//\, \boldsymbol{n}$, which is anticipated to be a generic feature for canted antiferromagnets at low k-vectors.

Furthermore, for $\boldsymbol{k} \,//\, \boldsymbol{n}$, we observe the co-existence of non-reciprocal with reciprocal spin-wave modes. Moreover, we see that this non-reciprocal behavior is even enhanced at larger k-values.

The investigation of surface depth experimentally and the comparison with the theory revealed that stability conditions are not fulfilled the standard DMI field reported in literature, yet it suggests that the frequency of the observed stable surface modes at around 20 GHz can only be fitted with an unrealistic phenomenological effective DMI field ($\mu_0 H_{DMI} \approx 1.3\, T$)

Just like in the case of thick ferromagnets, a canted antiferromagnetic crystal also exhibits a strong hybridization of bulk and surface spin-waves within a single crystal. This can results in spin-wave modes that possess a combination of properties and may provide an explanation for the presence of spin-wave modes with frequencies that closely resemble either non-reciprocal or reciprocal behaviors.

Overall, it's important to note that our research findings are only partially consistent with the conventional theory of antiferromagnetic spin-waves. Therefore, further theoretical investigations are necessary to delve deeper into the interactions and hybridization of spin-wave modes, especially considering the system's geometry, as well as the unique magnetic characteristics of α-Fe_2O_3, as highlighted in references (*7*, *8*, *10*) and (*12*, *14*).

5.6 BIBLIOGRAPHY:

1. J. R. Hortensius, D. Afanasiev, M. Matthiesen, R. Leenders, R. Citro, A. V. Kimel, R. V. Mikhaylovskiy, B. A. Ivanov, A. D. Caviglia, Coherent spin-wave transport in an antiferromagnet. *Nat. Phys.* **17**, 1001–1006 (2021).
2. V. G. Bar'yakhtar, B. A. Ivanov, M. V. Chetkin, Dynamics of domain walls in weak ferromagnets. (1985).
3. R. E. Camley, Long-Wavelength Surface Spin Waves on Antiferromagnets. *Phys. Rev. Lett.* **45**, 283–286 (1980).
4. R. L. Stamps, R. E. Camley, Bulk and surface spin waves in thin-film antiferromagnets. *J. Appl. Phys.* **56**, 3497–3502 (1984).
5. T. Moriya, Anisotropic Superexchange Interaction and Weak Ferromagnetism. *Phys. Rev.* **120**, 91–98 (1960).
6. I. Dzyaloshinsky, A thermodynamic theory of "weak" ferromagnetism of antiferromagnetics. *J. Phys. Chem. Solids* **4**, 241–255 (1958).
7. W. Jantz, W. Wettling, Spin wave dispersion of FeBO3 at small wavevectors. *Appl. Phys.* **15**, 399–407 (1978).
8. V. I. Ozhogin, Nonlinear dynamics of antiferromagnets with anisotropy of easy-plane type. *JETP Lett.* **21**.
9. R. Orbach, Spin Wave Spectra for Canted Antiferromagnets and Ferromagnets. *Phys. Rev.* **115**, 1189–1193 (1959).
10. V. V. Tarasenko, V. D. Kharitonov, Surface magnetostatic waves in uniaxial antiferromagnets. *JETP Lett.* **33** (1971).
11. L. Šmejkal, J. Sinova, T. Jungwirth, Altermagnetism: spin-momentum locked phase protected by non-relativistic symmetries. *Phys. Rev. X* **12**, 031042 (2022).
12. L. Šmejkal, J. Sinova, T. Jungwirth, Altermagnetism: a third magnetic class delimited by spin symmetry groups. *ArXiv210505820 Cond-Mat* (2021).
13. L. Šmejkal, A. Marmodoro, K.-H. Ahn, R. Gonzalez-Hernandez, I. Turek, S. Mankovsky, H. Ebert, S. W. D'Souza, O. Šipr, J. Sinova, T. Jungwirth, Chiral magnons in altermagnetic RuO2. arXiv arXiv:2211.13806 [Preprint] (2022). https://doi.org/10.48550/arXiv.2211.13806.
14. L. Šmejkal, J. Sinova, T. Jungwirth, Emerging Research Landscape of Altermagnetism. *Phys. Rev. X* **12**, 040501 (2022).
15. M. Białek, A. Magrez, A. Murk, J.-Ph. Ansermet, Spin-wave resonances in bismuth orthoferrite at high temperatures. *Phys. Rev. B* **97**, 054410 (2018).
16. S. Das, A. Ross, X. X. Ma, S. Becker, C. Schmitt, F. van Duijn, E. F. Galindez-Ruales, F. Fuhrmann, M.-A. Syskaki, U. Ebels, V. Baltz, A.-L. Barra, H. Y. Chen, G. Jakob, S. X. Cao, J. Sinova, O. Gomonay, R. Lebrun, M. Kläui, Anisotropic long-range spin transport in canted antiferromagnetic orthoferrite YFeO3. *Nat. Commun.* **13**, 6140 (2022).
17. G. F. Herrmann, Magnetic Resonances and Susceptibility in Orthoferrites. *Phys. Rev.* **133**, A1334–A1344 (1964).
18. D. Treves, Magnetic Studies of Some Orthoferrites. *Phys. Rev.* **125**, 1843–1853 (1962).
19. R. Lebrun, A. Ross, O. Gomonay, V. Baltz, U. Ebels, A.-L. Barra, A. Qaiumzadeh, A. Brataas, J. Sinova, M. Kläui, Long-distance spin-transport across the Morin phase transition up to room temperature in ultra-low damping single crystals of the antiferromagnet α-Fe 2 O 3. *Nat. Commun.* **11**, 6332 (2020).
20. M. Białek, J. Zhang, H. Yu, J.-Ph. Ansermet, Antiferromagnetic resonance in α-Fe2O3 up to its Néel temperature. *Appl. Phys. Lett.* **121**, 032401 (2022).

21. F. J. Morin, Magnetic Susceptibility of α Fe 2 O 3 and α Fe 2 O 3 with Added Titanium. *Phys. Rev.* **78**, 819–820 (1950).
22. A. El Kanj, O. Gomonay, I. Boventer, P. Bortolotti, V. Cros, A. Anane, R. Lebrun, Antiferromagnetic magnon spintronic based on nonreciprocal and nondegenerated ultra-fast spin-waves in the canted antiferromagnet α-Fe $_2$ O $_3$. *Sci. Adv.* **9**, eadh1601 (2023).
23. A. H. Morrish, *Canted Antiferromagnetism: Hematite* (World Scientific, 1994).
24. R. Lebrun, A. Ross, S. A. Bender, A. Qaiumzadeh, L. Baldrati, J. Cramer, A. Brataas, R. A. Duine, M. Kläui, Tunable long-distance spin transport in a crystalline antiferromagnetic iron oxide. *Nature* **561**, 222 (2018).
25. B. Lüthi, D. L. Mills, R. E. Camley, Surface spin waves in antiferromagnets. *Phys. Rev. B* **28**, 1475–1479 (1983).
26. B. Lüthi, R. Hock, Dipolar surface spin waves in antiferromagnets. *J. Magn. Magn. Mater.* **38**, 264–268 (1983).
27. V. Veerakumar, R. E. Camley, Magnetostatic bulk and surface spin-wave focusing in antiferromagnetic thin films. *Phys. Rev. B* **81**, 174432 (2010).
28. V. Vlaminck, M. Bailleul, Spin-wave transduction at the submicrometer scale: Experiment and modeling. *Phys. Rev. B* **81**, 014425 (2010).
29. T. Devolder, G. Talmelli, S. M. Ngom, F. Ciubotaru, C. Adelmann, C. Chappert, Measuring the dispersion relations of spin wave bands using time-of-flight spectroscopy. *Phys. Rev. B* **103**, 214431 (2021).
30. D. E. Beeman, Magnetostatic Modes in Antiferromagnets and Canted Antiferromagnets. *J. Appl. Phys.* **37**, 1136–1137 (1966).
31. J. Han, P. Zhang, Z. Bi, Y. Fan, T. S. Safi, J. Xiang, J. Finley, L. Fu, R. Cheng, L. Liu, Birefringence-like spin transport via linearly polarized antiferromagnetic magnons. *Nat. Nanotechnol.* **15**, 563–568 (2020).
32. H. J. Fink, Resonance Line Shapes of Weak Ferromagnets of the α-Fe2O3 and NiF2 Type. *Phys. Rev.* **133**, 1322–1326 (1964).
33. I. Boventer, H. T. Simensen, A. Anane, M. Kläui, A. Brataas, R. Lebrun, Room-Temperature Antiferromagnetic Resonance and Inverse Spin-Hall Voltage in Canted Antiferromagnets. *Phys. Rev. Lett.* **126**, 187201 (2021).
34. M. Jamali, J. H. Kwon, S.-M. Seo, K.-J. Lee, H. Yang, Spin wave nonreciprocity for logic device applications. *Sci. Rep.* **3**, 3160 (2013).
35. I. V. Rojdestvenski, M. G. Cottam, A. N. Slavin, Dipole-exchange theory for Brillouin light scattering from hybridized spin waves in ferromagnetic thin films. *Phys. Rev. B* **48**, 12768–12777 (1993).
36. D. S. Ellis, E. Weschke, A. Kay, D. A. Grave, K. D. Malviya, H. Mor, F. M. F. de Groot, H. Dotan, A. Rothschild, Magnetic states at the surface of alpha-Fe2O3 thin films doped with Ti, Zn, or Sn. *Phys. Rev. B* **96**, 094426 (2017).
37. G. S. Krinchik, V. E. Zubov, Surface magnetism of hematite. *JETP Lett.* **42** (1975).

6 CHAPTER 6: MAGNON SPINTRONICS WITH HEMATITE:

So far, we have investigated magnetization dynamics in ferromagnets and in a canted antiferromagnet, whereby we have explored the propagation properties of spin-waves. Here, we will focus on the utilization of spin currents within transport mechanisms, while employing magnonic approaches.

Two aspects will be discussed and explored in this chapter on the canted α-Fe_2O_3. Firstly, we will present measurements of spin waves utilizing a non-local technique conducted by means of the inverse spin Hall effect. This method allows to give more insights on the previously discussed results on spinwaves in the material. Secondly, we will move into discussing experimental measurements showing the potential for realizing a spin diode effect.

6.1 NON-LOCAL SW DETECTION VIA ISHE

Over the past decade, spintronic research has introduced various strategies for detecting and manipulating antiferromagnetic spin-waves through spin-to-charge phenomena (*1–3*), such as spin pumping, SP, and inverse spin hall effects, ISHE.

Spin Hall effect, SHE, is the generation of a pure spin current transverse to a charge current applied through a material with high spin orbit coupling, SOC. However, it has been demonstrated (*4*) that a reverse mechanism of the spin Hall effect can take place in such materials, whereby the spin current $\boldsymbol{j}_s$ can be converted into a charge current, $\boldsymbol{j}_c$, which is known by the inverse spin hall effect. The spin and charge currents are therefore related by the following relationship (cf. **Chapter 2**):

$$\boldsymbol{j}_c = -\frac{2e}{\hbar}\,\theta_{SHE}(\boldsymbol{e}_p \times \boldsymbol{j}_s)$$

(Eq. 6-1)

where θ_{SHE} stands for the efficiency of the spin to charge conversion in the material with spin orbit coupling, and $\boldsymbol{e}_p$ for the spin polarization direction.

In fact, when placed on top of a magnetic material, and upon magnetization precession, spin pumping (*5*) can take place, which is the injection of spin currents into the non-magnetic material, in which consequently, ISHE can occur. As a result, a detection of a charge current is possible across the non-magnetic layer, NM.

In this sense, with SP and ISHE we can transform the magnons in an FM (or AFM) into a spin current carried by electrons and therefore to a charge current in the NM layer. Past experiments (*6* ,*7*), used this mechanism and proved its efficiency. By placing a platinum bar on top of a ferromagnet (such as YIG) away from a SW injector (an RF- antenna), a DC voltage is thus generated across the platinum from the propagating SWs excited by the antenna. This

means that traveling SWs are converted into spin currents, which can be useful for spintronic applications.

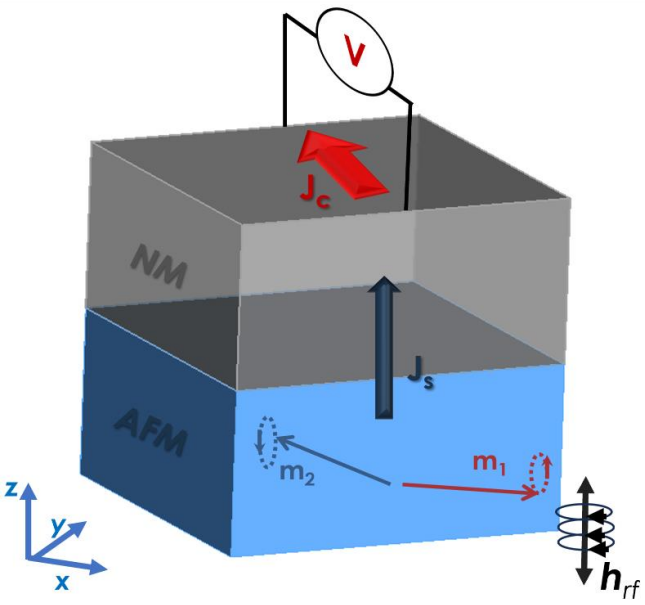

Figure 6-1: Illustration of Inverse Spin Hall Effect (ISHE): *The oscillating magnetic moments of the AFM, excited by the external rf-field, act as a pump for the normal metal, by a spin current that is directed normal to the interface. By ISHE, the spin current is converted into a charge current in the normal metal, which is measurable as an output DC voltage.*

Until now, this electrical detection based on inverse spin-Hall effect was achieved only for the uniform mode ($k = 0$) with generated voltage amplitudes as low as tens of nV in both colinear (*8*, *9*) and in canted antiferromagnets (*10*, *11*). In Ref.(*10*) , the antiferromagnetic resonance in the canted phase of hematite was experimentally and theoretically investigated via spin pumping and ISHE measurements, thereby opening up the possibility to generate and detect AFM SWs via these mechanisms.

A key challenge in magnonic devices is the amplitude of the output voltage generated by the propagating spin-waves and efficient alternatives to standard inductive transducers (*12*) are still lacking, where this challenge is even amplified in antiferromagnetic materials, given the reduced generated stray field.

In the previous chapter, we were able to detect non-reciprocal AFM spinwaves in α-Fe_2O_3 in the $\boldsymbol{k} \perp \boldsymbol{n}$ configuration by using inductive antennas. In this section, we will show the electrical detection of these AFM spinwaves, while using a platinum-based metallic transducer via the inverse spin hall effect, yielding an output voltage similar to what we get in ferromagnets like YIG (*13*, *14*). First, we will explain the experimental scheme and the mechanism at play. Then, we will move on to presenting the results, starting with power-dependent field sweep measurements, followed by angular-dependent measurements showing the efficiency of detection in relation to the angle of the applied field to conclude finally the best configuration for the detection via ISHE.

6.1.1 The experimental scheme and mechanism:

We excite spinwaves in the 500-micrometer-thick bulk hematite using an inductive antenna in which we inject a pulsed frequency AC signal using a lock-in amplifier. In fact, from ***Figure 6-2***, the antenna is connected to an RF probe, which is linked to the lock-in amplifier delivering the signal with a modulation frequency of 6.666 kHz. To detect the SWs this time, instead of using another antenna connected to the VNA, we replace both components with a 5 nm-thick Platinum layer placed a few micrometers away from the excitation antenna. The Platinum layer has gold DC-contacts, which are connected in turn to the lock-in and through which we measure a voltage.

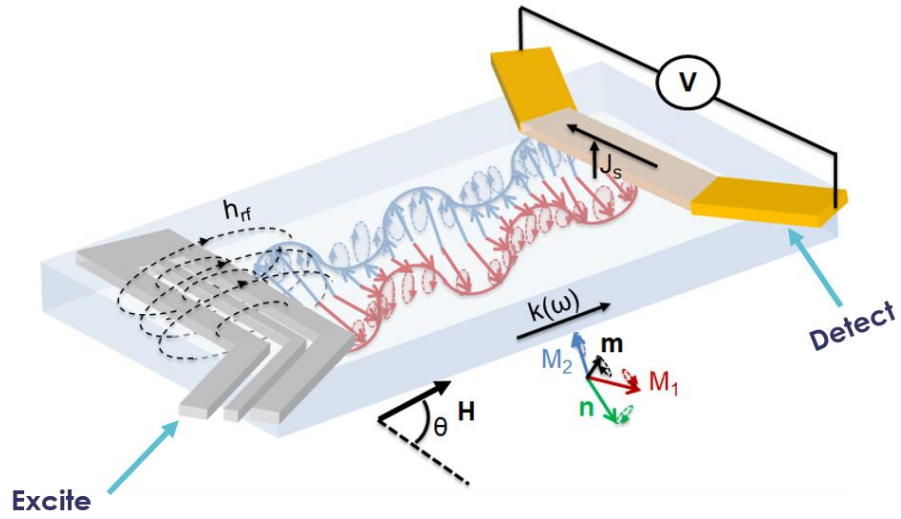

Figure 6-2: Schematic of the experiment: *Excitation of spinwaves with a GSG antenna of k=0.6rad/µm, leading to their propagation until beneath the platinum layer. This give rise to a spin current into the platinum that is converted into a charge current via ISHE allowing the detection of a* V_{ISHE} *across the Pt strip.*

Regarding the mechanisms coming into play in this measurement, we can describe them as follows:

Firstly, the magnetic moments in the bulk Hematite beneath the antenna are excited, which leads to the propagation of spin waves. Seocondly,these propagating spin waves reach underneath the non-magnetic layer, where the precessing magnetic moments now serves as a spin pump, leading to the transfer of spins from hematite into this adjacent layer and therefore the generation of a spin current. Due to the high spin-orbit coupling in platinum, the spin current is converted into a charge current via the inverse spin Hall effect, resulting in the detection of an inverse spin Hall voltage across the platinum stripe.

❖ On the angular dependency of the power absorbed in the antiferromagnet:

One important issue we need to address is the dependence of the angle at which we apply the magnetic field with respect to the antenna. In fact, one can calculate the amount of power absorbed by the magnetic volume from the applied rf-field. This can be calculated through Maxwell's equations and by applying the energy conservation law (Poynting theorem). Therefore, for a magnetic volume, the absorbed amount of the electromagnetic wave is given by:

$$P_{abs} = \omega \chi h^2$$

where χ is the magnetic susceptibility for the magnetic medium

For the case of a ferro- or an antiferromagnet, the amount of absorbed power in the material is therefore:

$$P_{abs} = \frac{\omega}{2}(\chi_{\perp}|h_{\perp}|^2 + \chi_{//}|h_{//}|^2)$$

(Eq. 6-2)

with $\chi_{\perp}$ and $\chi_{//}$ the susceptibilities elements of matrix χ .

For a magnetic field H applied in the sample with an angle θ from the transducer axis, we thus get the two components of the rf-excitation field (see ***Figure 6-3*** for orientations):

$$h_{\perp} = h_x \cos\theta \, e_{\perp} + h_z e_z \qquad \text{and} \qquad h_{//} = h_x \sin\theta \, e_{//}$$

(Eq. 6-3)

Therefore, we can obtain (*15*):

$$P_{abs} = A \cos\theta^2 + B$$

(Eq. 6-4)

with $A = \frac{\mu_0 \omega}{2}(\chi_{\perp}|h_x|^2 - \chi_{//}|h_x|^2)$ and $B = \frac{\mu_0 \omega}{2}(\chi_{\perp}|h_z|^2 - \chi_{//}|h_x|^2)$

The parallel susceptibility (cf. **Chapter 2**) is of negligible value with respect to $\chi_{\perp}$, therefore the terms containing $\chi_{//}$ can be neglected in our case. We highlight on the z component of the rf-magnetic field in term B. This component is non-zero in the regions outside of the antenna as shown in ***Figure 6-3***. For this out-of-plane term of the rf-field, the k-selectivity of the antenna (as discussed in the previous chapters) is different from what we have calculated, since the calculations takes into account only the in-plane field.

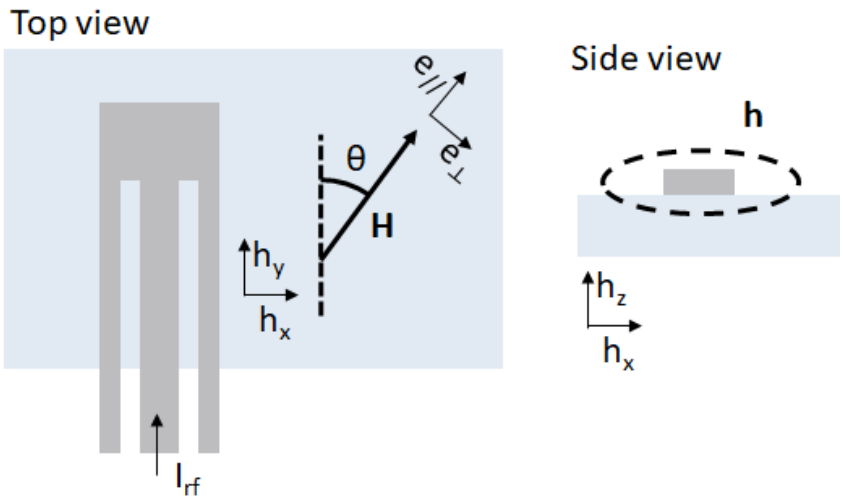

Figure 6-3: Sketch of the antenna with the rf excitation fields.

Therefore, one should expect that the excitation is mostly efficient for $\theta = 0$, applied field parallel to the antenna. However, one should take into consideration the spin hall effect symmetry, giving that the detected voltage should be proportional to sin θ, ($V_{ISHE} \propto \sin\theta$). Therefore, we expect the angular dependence of the inverse spin-Hall voltage to be proportional to the cross product of the absorbed power P_{abs} with the detection of the inverse spin-Hall effect (in $\sin\theta$), as represented in ***Figure 6-4*** and written as following:

$$P_{absorbed} = sin\,\theta\,(A\,cos\,\theta^2 + B)$$

(Eq. 6-5)

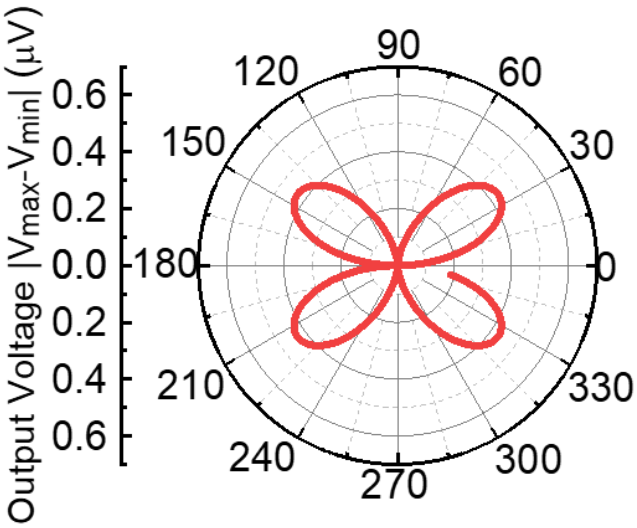

Figure 6-4: The expected $(A\,cos\,\theta^2 + B)|sin\,\theta|$ dependency shape.

6.1.2 Experimental results:

By fixing the frequency at 23 GHz, tilting the magnetic field with respect to the platinum stripe at an angle of 135°, and maintaining the input RF power at +16 dBm, we swept the magnetic field and measured the output DC voltage across the platinum stripe.

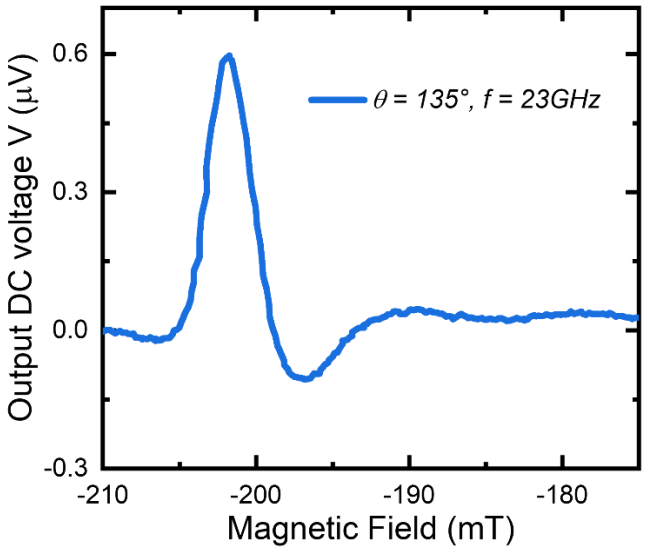

Figure 6-5: Output DC voltage in function of the magnetic field. *The angle **θ** represents the angle between the magnetic field and the platinum bar. The resonance peak occurs at $\mu_0 H_{res}$ = 200 mT, and its amplitude is approximately 0.7 μV.*

The result of the measurement is shown in ***Figure 6-5:***, showing the shape of the resonance peak with an amplitude on the order of a few microvolts (~ 0.7 μV) at a field value of 200mT. However, multiple factors can affect the amplitude and shape of the detected voltage, mainly the angle at which we tilt the magnetic field and the power level injected into the excitation antennas. The resonance shape might also change when varying the frequency.

All these factors will be studied in the following sections: we will begin with a frequency-dependent measurement, followed by an angular-dependent measurement, and conclude with a power-dependent measurement.

A. Frequency dependency:

We vary the frequency and measure the output voltage, and show the response at different frequencies. The input RF-power is held constant at 16 dBm, and the magnetic field is tilted at 45°, for which an optimized signal amplitude was obtained ad as expected from antenna detection efficiency and the ISHE as discussed in ***Figure 6-4***. This will be further discussed in the angular-dependent measurements.

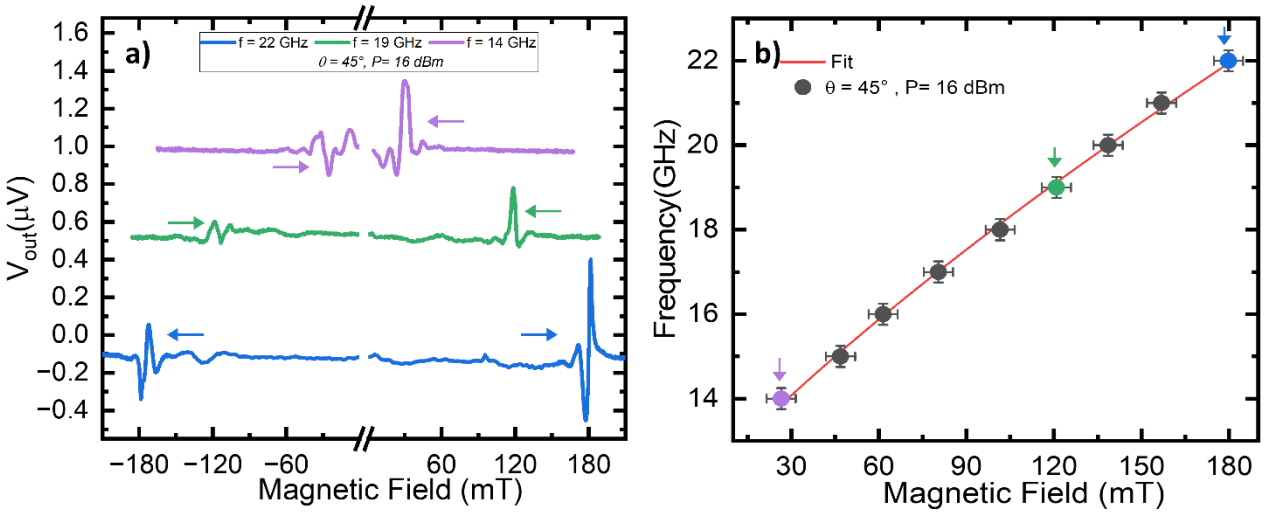

Figure 6-6: Frequency dependent measurement: *a) Output voltage in function of the magnetic field swept from negative to positive fields showing the shape and amplitude of the signal as changing the frequency. b) Plotting the frequency versus the resonance field by taking the middle field between the max and minimum peaks. The red curve is a fit. The highlighted points corresponding to the frequencies shown in (a).*

From ***Figure 6-6.*** **a)**, it is evident that the resonance field vary with frequency. The resonant fields as shown by the arrows, consistently align with our findings from inductive measurements (as shown in **Chapter 5**). Additionally, one can observe from the shape of the response the existence of some secondary peaks around the main peak, which are associated with different spinwave modes, as discussed in the inductive measurements. Another point to highlight, the pronounced non reciprocity of the signal's amplitude as we sweep from negative (low amplitude of the resonance peaks) to positive fields (high amplitude of the resonance peaks). On the other hand, the amplitude varies slightly in certain regions, particularly noticeable at a frequency of 19 GHz (represented by the green color). This variation is expected as we did not perform a calibration of the rf-source prior the measurements and can be linked as well to the presence of inhomogeneities in the system. In panel **b)** we show the resonance fields associated to each frequency. The resonance field is extracted as the middle point between the resonance at a maximal and a minimal peak (see panel **a)**).

B. Angular dependency: Amplitude:

In this experiment, we conducted a measurement where we swept the magnetic field from negative to positive values while keeping the angle and frequency constant, as illustrated in ***Figure 6-7.*** **a)**. Then, we repeated the same measurement while varying the angle θ between the magnetic field and the transducer, covering a range from 0 to 180 degrees. At each angle, we measured the peak-to-peak amplitude of the output DC voltage, and the resulting data points are collected in ***Figure 6-7.*** **b)** and represented by the blue dots. These data correspond to a device with a separation distance of 14 μm between the antenna and the Pt stripe.

Consequently, in panel **a)**, one can observe a change in sign of the generated DC voltage in response to positive and negative magnetic fields, indicating the spin-pumping nature of the effect. Another significant feature is the pronounced asymmetry, approximately 40%, in the output voltage, which suggests the non-reciprocal nature of the detected spinwaves. This aligns with the observations we have shown in ***Chapter 5*** and supports that these spin-waves are localized at the surface of the crystal.

Furthermore, in panel **b)**, the detected output voltage exhibits an asymmetric dependence on the angle θ, following ***(Eq. 6-5)***, with maxima occurring when the external magnetic field is at 45° and 135° relative to the transducer's direction. This behavior is consistent with both the excitation efficiency of the inductive transducers, $(A\,cos\,\theta^2 + B)$ as well the inverse spin-Hall detection, which adheres to a standard $sin\theta$ law (*10*, *14*).

One should also mention that the additional asymmetry arises from the spin-wave non-reciprocity as discussed in the previous chapter.

Accordingly, we note that the shape of the output voltage peak can change towards high power due to nonlinear effects coming into play, arising from the ultra-low damping of hematite, (as we have discussed in the power dependency measurements) and that would require further study.

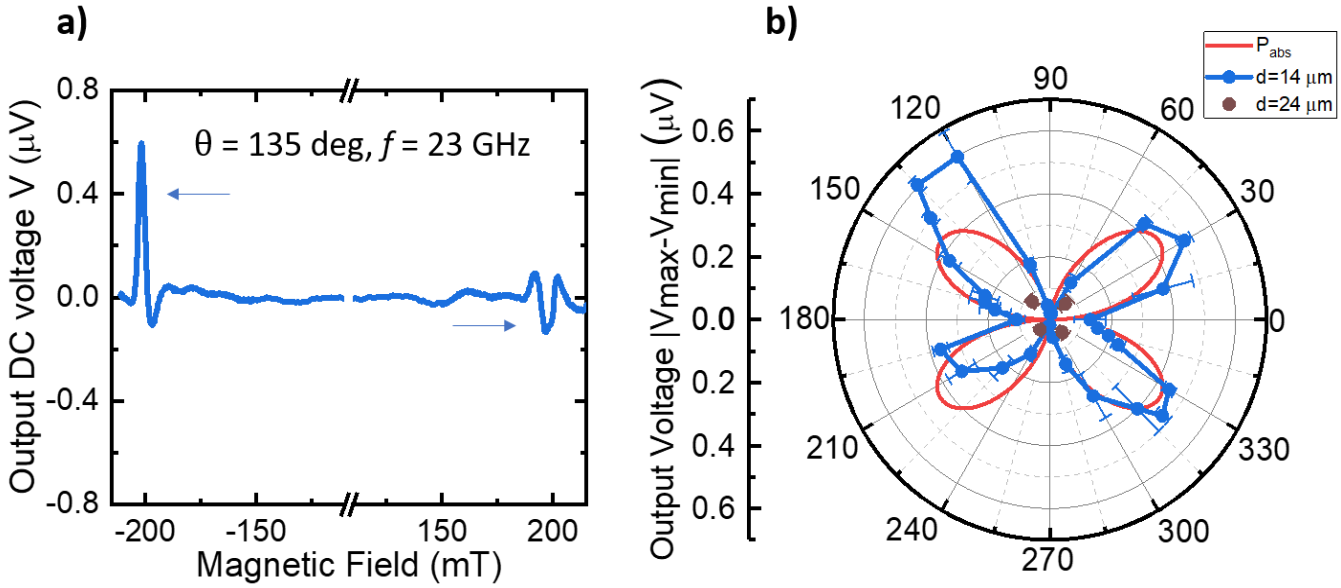

Figure 6-7: Amplitude angular dependency: *a) Example of inverse spin-Hall spectra for a magnetic field applied at θ = 135° from the inductive transducer (with an input power P_{rf} = +16 dBm. b) Angular dependency of the DC inverse spin-Hall voltage V_{pp} for a 14 μm distance between the injector and the detector for f = 17 GHz, for a 14 μm distance between the injector and the detector (blue dots), and for another device having a distance of 24 μm (brown dots). Red line corresponds to the fit with* $(A\,cos\,\theta^2 + B)|sin\,\theta|$

C. Angular dependency: Field

Here, we show at each angle the resonance field with respect to the angle of the applied field. The resulting data points are collected in ***Figure 6-7. a)*** and represented by the blue dots. These data correspond to the device with a separation distance of 14 µm between the antenna and the Pt strip. In the same figure in panels **b** to **d)** we show the represented data points output voltages with respect to the field to highlight on the shape of the resonance peak and the asymmetry that we have already discussed in the previous section for the main angles of 90, 45 and 0 degrees.

It's worth to mention that we can observe that for a frequency of 17 GHz, the resonance field at is larger for $\boldsymbol{\theta = 90°}$, $\boldsymbol{(H // k)}$ than for $\boldsymbol{\theta = 0°}$, $\boldsymbol{(H \perp k)}$, which is in line with the results shown and discussed in detail in the previous section on the non-degeneracy of SWs modes in Hematite.

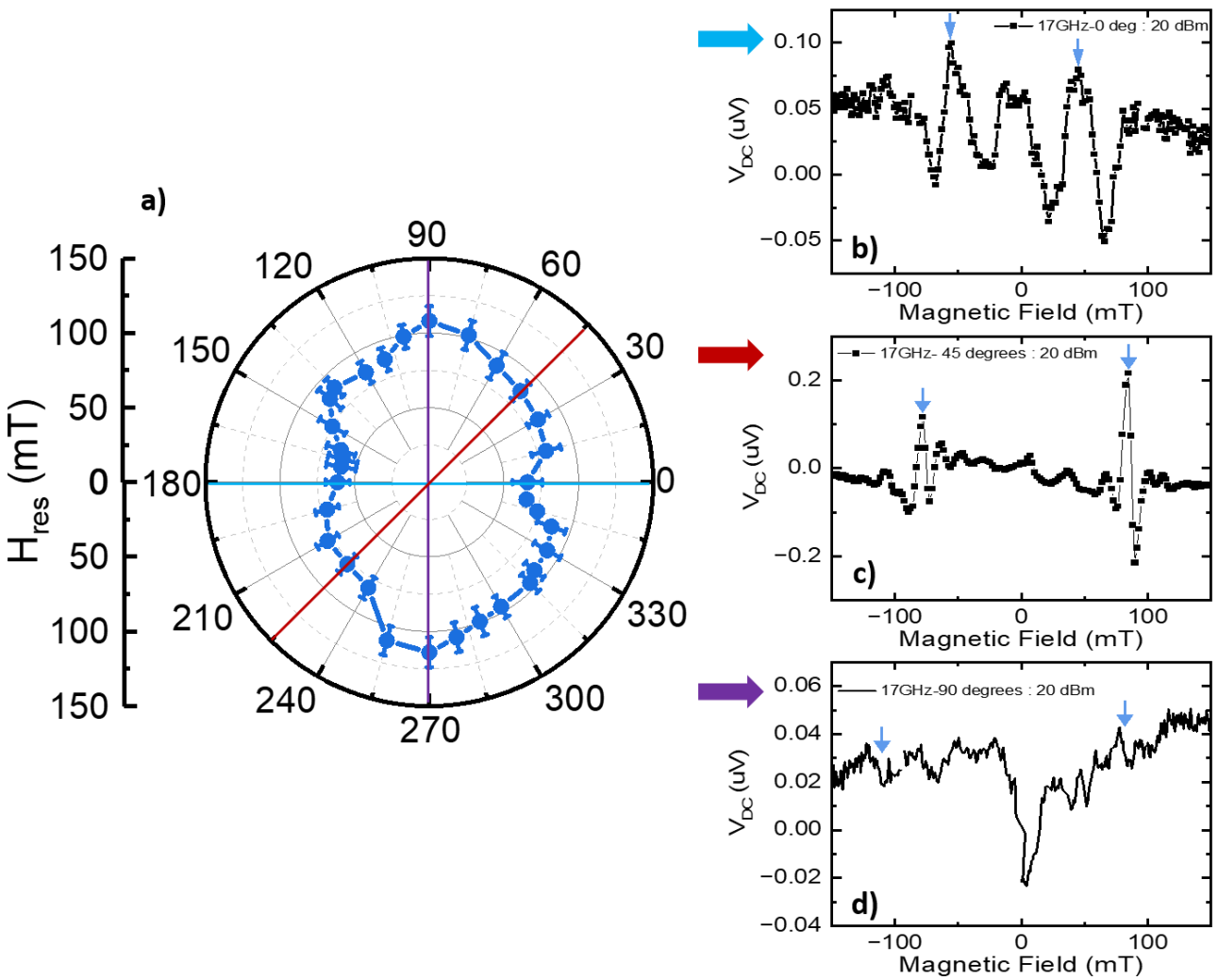

Figure 6-8: Resonance field angular dependency: *a) Angular dependency of the resonance field for f = 17 GHz. b)-d): Output voltage with respect to the field sweep from negative to positive values, for the main angles 0° in a), 45° in b) and 90° in c).*

It is important to observe the variation in the peak shape when the angle is changed. For instance, when the angle is set to 0 degrees, the primary peak host secondary peaks at adjacent fields (as highlighted by the arrows on ***Figure 6-8*. b)**, unlike the case at 45 degrees (panel **c)**). This indicates that we are detecting multiple propagating modes since at 0 degrees, where we are the most sensitive to surface waves, and therefore a multipeak shape can be explained. Further theoretical studies should be made to understand such a shape of the detected DC voltage and its dependence on the field orientation.

D. Power dependency:

When the magnetic system is excited with an RF signal, one must be careful about the input power level and ensure it does not exceed a threshold that would push the system into the non-linear regime. For this reason, we first conducted a power-dependent measurement, with a fixed frequency of 17 GHz and an angle of 45 degrees between the applied field and the antenna (as predicted for optimal power absorption, as discussed above). In this measurement, we sweep the power while measuring the amplitude of the signal from peak-to-peak.

The results are shown in the figure below, and where two linear fits are presented: one considering the data points (straight line) and the other the error bars (dashed lines). Both fits show that using an input power of 40 mW (i.e., around 16 dBm) is sufficient to maintain the system within the linear regime.

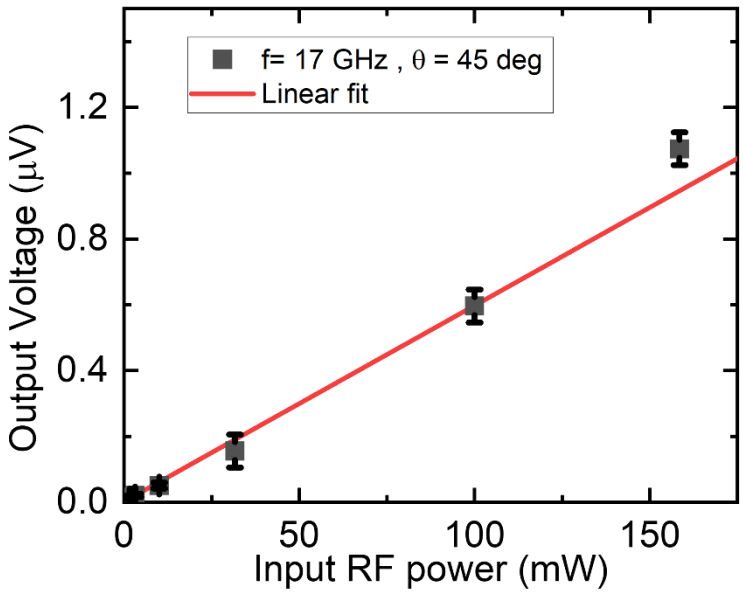

Figure 6-9: Output voltage versus the input RF-power: *Collected data points of the output voltage when varying the input RF power injected in the antenna. The red line shows a linear fit indicating the linear behavior of the output voltage upon the increase of power.*

6.1.3 Discussion:

By comparing the voltage amplitude ratio (estimated to be a factor of 6 to 7) for two distances between the injector and the detector (d= 14 and 24 µm) , we can extract an attenuation length as follows:

$$V = V_0 e^{-d/l_{att}}$$

(Eq. 6-6)

From this we obtain an attenuation length of about 3-4 µm.

An example of the measurement with a device, where the distance between the injector and the detector is 24 µm, is presented in the figure. The measurement conditions in this example include an angle of 135 degrees for the magnetic field, a power of 16 dBm, and a frequency of 22 GHz. One can observe a notable amplitude drop (in comparison to ***Figure 6-7.* a)**, the blue curve) and the absence of secondary peaks that were detected in the first case, which is normal and attributed to the increased detection distance.

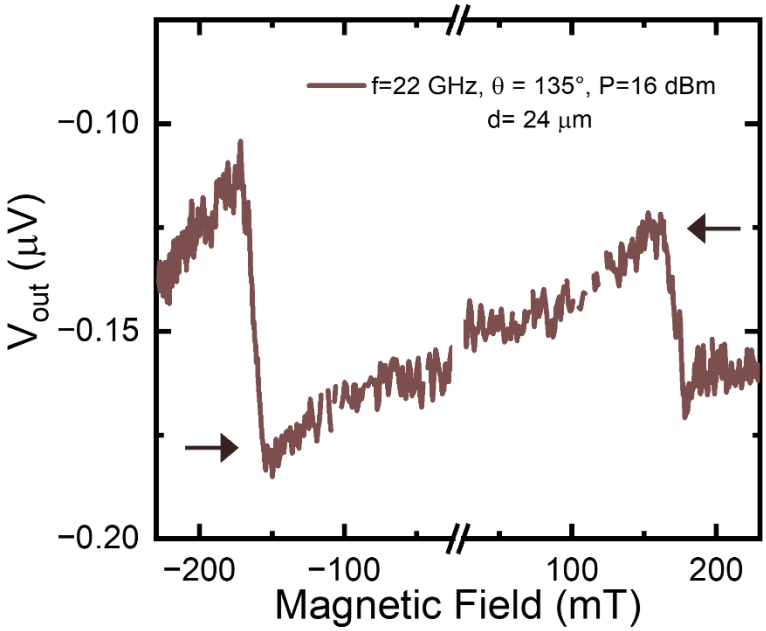

Figure 6-10: Measurement with different Injector-Detector distance: *The output voltage with respect to the magnetic field, detected at d = 24 µm from the injector. The arrow are to highlight the peaks of the signal.*

As also shown in ***Figure 6-6*** we measure output inverse spin-Hall voltages in the microvolt range, whilst the excitation frequency being one order of magnitude larger than in ferromagnets(*13*, *14*). This large inverse spin-Hall voltage can be explained by the reported amplitudes of the spin hall magnetoresistance in bilayers of Pt/Hematite(*16* ,*17*).

Therefore, we finally achieved efficient electrical detection of the propagating spin-waves through the surface sensitive inverse spin-Hall effect using a platinum based metallic

transducer. These mentioned features further evidence that spin-pumping effects represent a promising tool to detect the spin-wave dynamics in antiferromagnets, and favorize their integration in magnonic devices.

6.2 SPIN-DIODE EFFECT:

Diodes play an essential role in electronic circuits due to their ability to convert AC to DC and to control current flow by creating an asymmetric electrical conductance, enabling forward transport while blocking the reverse direction. This unique property is used in applications like rectification and signal clipping. Thus, allowing for applications for logic gates, where they control current flow for digital circuit operations. Traditionally, solid-state diodes were associated with semiconductor materials, but recent developments have expanded their possibilities to function in various materials and band structures, opening up new horizons for new electronic applications.

Over the past few decades, spin transfer torques have been widely investigated. This spintronic approach, when applied in magnetic tunnel junctions (MTJ), has paved the way for further research for developing spintronic devices such as spin torque nano-oscillators (18) and STT-diodes (19). Accordingly, by considering the interplay between magnetization dynamics (SWs / magnons) and spin-dependent transport phenomena, an unusual diode-like effect emerges. Numerous studies on ST-diodes have been conducted in ferromagnetic materials characterized by low damping, such as YIG (20). However, in these ferromagnets, the achievable frequency range is limited. To avoid this limitation, a promising approach involves the use of antiferromagnetic materials. The potential for an AFM spin diode was predicted in (21) and (22) for materials with biaxial anisotropy and specifically, NiO.

In this study, we demonstrate the feasibility of realizing spin diode rectification in hematite. First, we will present the experimental setup and the underlying mechanisms. Next, we will discuss our experimental results based on measurements obtained solely through the application of an AC signal and discuss the excitation mechanisms evidencing that as expected the Oersted field excitation dominates over spin-torque effects in the case of a signal crystal. We also evidence the presence of non-linear effects when pumping the system with high powers. To go further, we measure the output voltage from the device by simultaneously applying both AC and DC currents and examine the DC dependent characteristics of the system.

6.2.1 The experimental scheme and mechanism:

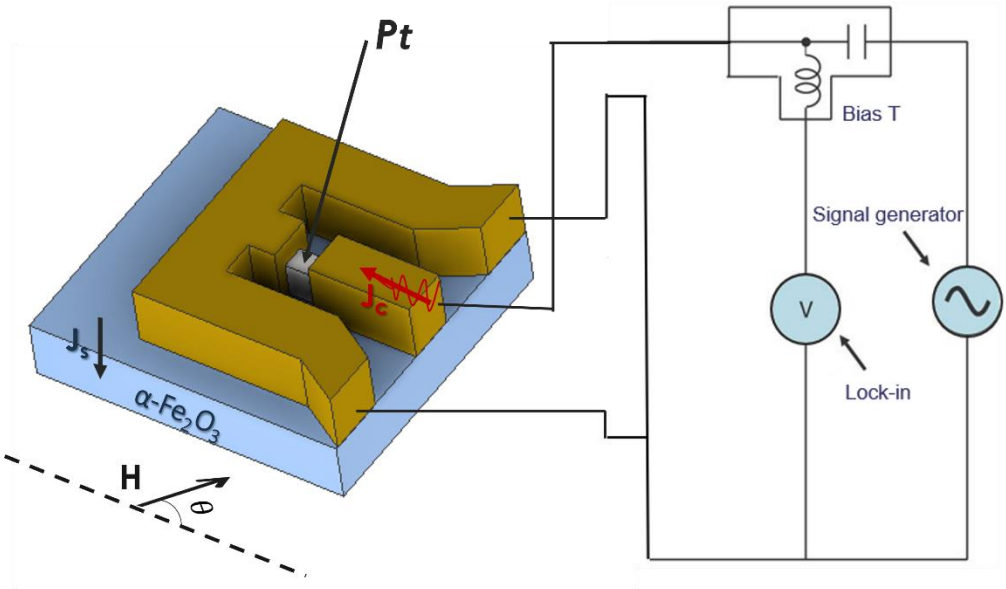

Figure 6-11: Schematic of the experiment: *The device under study consisting of a Ti/Au G-S-G antenna on top of a 500 µm α-Fe_2O_3, the signal line consists of contacting a platinum strip of 5 nm thickness.*

In this experiment, we use a device consisting of a 5 nm-thick Pt strip that is patterned on the 500 µm-thick hematite surface, then in a second lithography step we pattern a G-S-G antenna in a way to have the signal line contacting the platinum. The antenna is fabricated using optical lithography and it has ground lines of 35 µm and a single line of 15 µm wide and a separation of 20 µm. The antenna is metalized with a 20nm, 280 nm bilayer of titanium and gold respectively.

- ***Excitation mechanisms:***

An RF current provided by a signal generator, operating at a fixed frequency, is injected into the GSG antenna using microwave probes. As a result, the oscillating current in the platinum (x-direction) is converted into an oscillating spin current via the spin hall effect directed along a direction normal to the interface (z-direction). This leads to spin accumulation at the interface and therefore to an oscillating spin transfer torque acting on the magnetization precession in Hematite. Therefore, two mechanisms are mainly responsible in driving the antiferromagnetic layer to resonance, and their contributions are added as torques acting on the magnetization dynamics:

1. The Oersted field torque from the field generated by the antenna from the injected rf-current.

2. The spin transfer torque resulting from the SHE in the Pt layer.

Therefore, one can write the LLG equation as:

$$\frac{d\boldsymbol{m_{1,2}}}{dt} = -\gamma \boldsymbol{m_{1,2}} \times \boldsymbol{H}_{eff} + \alpha \boldsymbol{m_{1,2}} \frac{d\boldsymbol{m_{1,2}}}{dt} + \gamma \frac{\hbar}{2eM_s t_{AF}} \boldsymbol{J}_s - \gamma \boldsymbol{m_{1,2}} \times \boldsymbol{h}_{rf}$$

(Eq. 6-7)

We recall α the gilbert damping factor, $\boldsymbol{H}_{eff}$ is the effective field, $\boldsymbol{h}_{rf}$ the rf-field, $\boldsymbol{m_{1,2}}$ is the magnetic moment for sublattice 1 and 2, respectively. t_{AF}, is the thickness of the antiferromagnet, M_s is the saturation magnetization of each sublattice, and $\boldsymbol{J}_s$ is the spin current generated by the SHE in the Pt layer. It should be noted that the last two terms of this equation are dependent on the rf-current, as $\boldsymbol{J}_s$ is related to the SHE created upon the injection of $I_{rf,}$ and as $\boldsymbol{h}_{rf}$ is generated upon the injection of I_{rf}.

The spin current expression was adapted for the case of antiferromagnets and was shown by Manchon (*23*) as:

$$\boldsymbol{J}_s = \frac{Re(G_m)}{e} \boldsymbol{m_{1,2}} \times \boldsymbol{\mu}_s + \frac{Im(G_m)}{e} \boldsymbol{m_{1,2}} \times \boldsymbol{\mu}_s + \frac{G_n}{e} \boldsymbol{n} \times \boldsymbol{\mu}_s$$

(Eq. 6-8)

with $\boldsymbol{\mu}_s$ being the spin accumulation at the pt/hematite interface, G_m and G_n represent the magnetic and the Néel spin mixing conductances, respectively.

- ***Detection mechanisms:***

Two mechanisms (*4*) can contribute to a DC voltage when exciting the antiferromagnet at resonance by spin-torque or Oersted field excitations. First, one can detect a spin-pumping signal as described and reported previously. Secondly, it was shown that in bilayers of HM/FM insulators (*24* ,*25*) that the electrical resistivity in the heavy metal depends on the angle between the magnetization direction and the spin-accumulation direction in the normal metal. This effect is called the Spin Hall Magnetoresistance (SMR), and it arises from the interplay between the SHE and its inverse the ISHE. At resonance, the electrical resistance in the heavy metal can thus oscillates and its cross product with the oscillations of current can also generate a DC current.

One should notice that SMR effects have been largely studied in the case of AFMs as in (*26* ,*27*), and proven to be valuable tools to detect the static magnetization of an antiferromagnets in both single crystals and in thin films. The reported SMR ratio have also been reported to be as large as for ferromagnetic insulators in some systems as in Ref. (*28*). One should notice an interesting difference in the experimental observation of spin-pumping and SMR effects in hematite. The spin-pumping signals detected at the resonance of hematite has been reported to be due to the dynamics of the canted moment, and to be relatively smaller than in ferromagnets, whilst the SMR signal is determined by the direction of the antiferromagnetic order (and not by the canted moment) and is as large as in ferromagnets. One can thus anticipate that SMR effects could be more efficient to detect spin-diode effects in the case of hematite/heavy metal bilayers. This will be discussed further from detected

output voltage line shape and by symmetry interpretations.

Experimentally, to measure the output signal, we use a bias tee, allowing to simultaneously apply the microwave current and measure the DC voltage across the sample using a lock-in amplifier. The amplitude of the rf-current is modulated at 6.66 kHz,. During our experiments, we sweep the magnetic field within the sample plane, where θ represents the angle between the magnetic field and the platinum layer axis, as indicated in ***Figure 6-11***.

In a subsequent measurement, we investigate the changing in the resonance line shape and amplitudes as a result of injecting a DC current generated by a Keithley current source, in parallel to the driving radio-frequency current. Importantly, throughout this measurement, we maintain the input power within ranges in which the system remains within the small angle precessions regime.

6.2.2 Experimental results:

In this section we will present an analysis of the results obtained from the measurements organized as follows; First with the results obtained from the AC measurements and second with the results obtained from AC-DC measurements.

A. AC measurements:

In the following section, we will discuss the dependencies of different factors influencing the output voltage, including the frequency, angle, and power.

- ***Frequency Sweep:***

Firstly, we want to investigate the frequency dependency of the spin-diode voltage. For this we drive the system by applying solely an RF current from a signal generator, at a constant frequency. We sweep the magnetic field, from negative to positive values, while simultaneously collecting the output DC voltage at the lock-in amplifier. To ensure that we remain within a linear regime, the power is initially set to 0 dBm. The measurement is then repeated for a set of frequencies from 12 to 21 GHz with a step of 1 GHz.

The output voltage is shown in ***Figure 6-12.*** **a)** as function of the magnetic field for different frequencies ($f = 12, 15, 18$ and 21 GHz in black, green, purple and yellow, respectively). As can be seen from the plot, the signal's response has an antisymmetric tendency with a peak and an anti-peak that increase in field as the frequency increases, indicating the magnetic resonance. In panel **b)** we follow the evolution of the maximum peak of the resonance as indicated by the arrows in panel **a)**, as function of the frequency. We can see a slight decrease of the peak voltage as we go higher in frequency, which is roughly about 0.5 μV. In panel **c)** we show the frequency in function of the resonance fields. We fit the collected data (red curve in panel **c)**) with the expression of the AFMR (dispersion at $k = 0$) given by:

$$f = \sqrt{f_0 + \gamma H_{ext}(H_{ext} + H_{DMI})}$$

(Eq. 6-9)

where f_0, H_{DMI} are used as initial parameters to set before the fit. We find therefore a value of $\mu_0 H_{DMI}$ that is of 2 T aligning with the value expected for Hematite.

We note that a convenient value of frequency to take for the following measurements is 17 GHz since the resonance field falls within the middle of the accessible range of the magnetic field (therefore, we make sure that the resonance peaks are far away from the switching peak at 0 mT and nearby fields, as well as to have all the necessary information of the signal).

Going back to the lineshape of the response, we observe that the resonance peaks exhibit a combination of symmetric and antisymmetric Lorentzian shapes, consistent with the expectations from ST-driven FMR measurements (*29* , *30* , *31*). As introduced above, it was shown in these studies that the detected output DC voltage results from the contribution of both SMR and spin pumping, and that the excitation can come from the Oersted field or from spin-torque effect. One should notice here that the excitation is likely dominated by the Oersted field as we used bulk single crystal. This is confirmed by the fact that the peak is largely an anti-symmetric Lorentzian which is not expected for a spin-torque excitation in the model developed by. Chiba *et al.* (*32*, *33*) for a ferromagnet. Here we will use this model in first approximation for two main reasons. Firstly, the spin-pumping voltage was reported to be proportional to the direction of the canted moment, thus with a symmetry similar to a ferromagnet. Secondly, when we excite the system at 45° from the platinum stripe, the excitation and the detection are similarly at half their efficiencies for a FM and for an AFM.

Nevertheless, as a remark, a more complete model taking into account both the effect of SOT on the canted and the compensated AFM will be developed in collaboration with O. Gomonay, beyond the frame of this thesis.

Coming back to the shape of the spindiode voltage, following the model developed by Chiba, the Oersted field excitation can lead to a symmetric shape for the spin pumping voltage contribution (Lorentzian lineshape), while it generate a mix of symmetric and a antisymmetric terms for the SMR contribution. For a thick magnetic layer, we thus expect an anti-Lorentzian lineshape for a dominated Oersted field excitation and SMR detection.

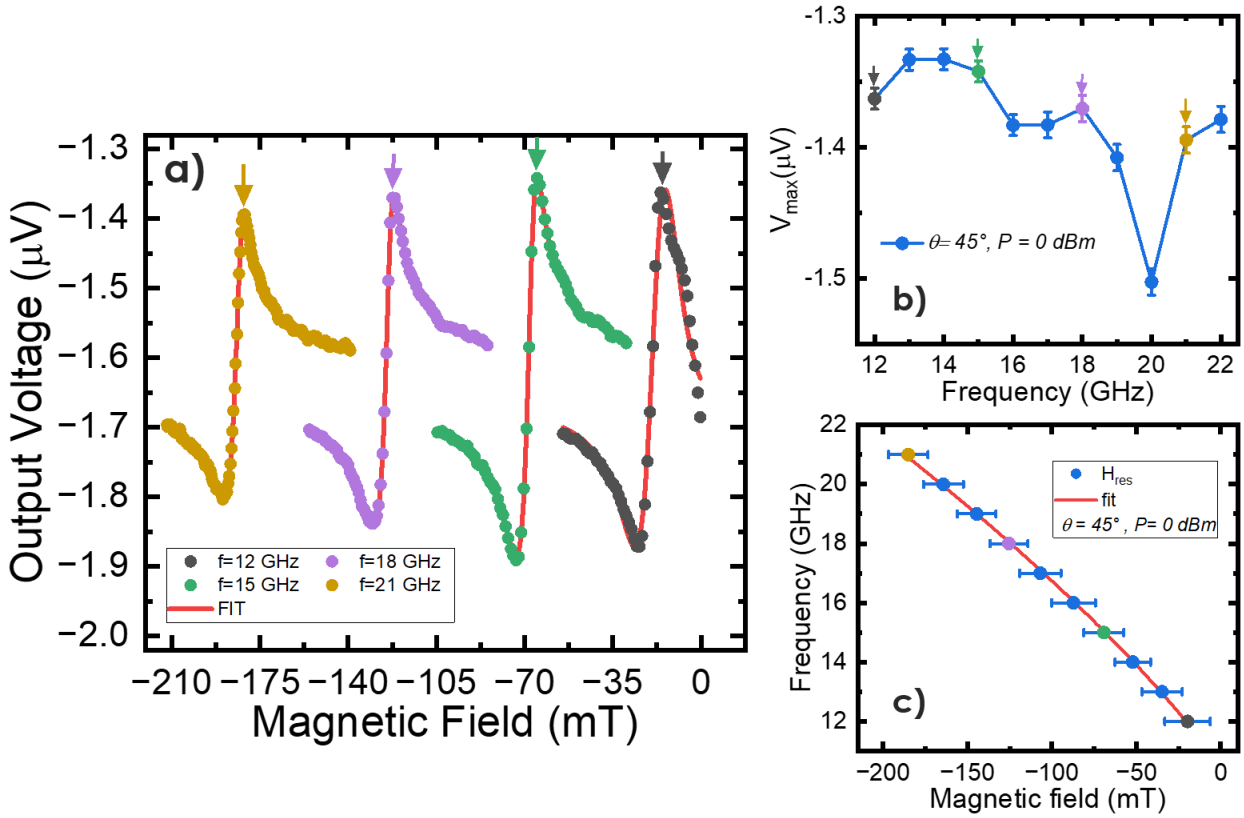

Figure 6-12: Frequency sweep measurements: *a) Output DC voltage, measured in microvolts using the lock-in amplifier, as a function of the magnetic field oriented with θ =45° relative to the platinum and an input power of 0 dBm. The resonance spectra are shown at f=12(black), 15(green), 18(purple) and 21(yellow) GHz. b) The evolution of the maximum peak voltage (highlighted by arrows in a)) with respect to the frequency. c) Frequency versus resonance fields data points, fitted by the red curve using the dispersion relation at k=0 for canted AFM.*

In ***Figure 6-13***, we present the DC output voltage in function of the magnetic field, applied at an angle θ = 45° with respect to the Pt stripe, and at a fixed frequency of 17 GHz with an input power of 0 dBm. The empty blue circles are the collected data points, while the blue curve represents a fit of the data points using the following analytical expression:

$$V_{out} = d_{offset} + A\frac{dH^2}{(H - H_{res})^2 + dH^2} - B\frac{dH.(H - H_{res})}{(H - H_{res})^2 + dH^2}$$

(Eq. 6-10)

with dH is the FWHM of the resonance peak, H_{res} the resonance field, d_{offset} is the offset voltage and A, B are the amplitude of the symmetric and anti-symmetric contributions.

The expression is composed of a combination of symmetric and antisymmetric terms and are shown in the figure by the red and green curves, respectively. Clearly, the antisymmetric response dominates the output voltage lineshape over the symmetric response. Therefore, by following the theory of Chiba *et al.* this would indicate a dominated spin hall magnetoresistance detection in our system.

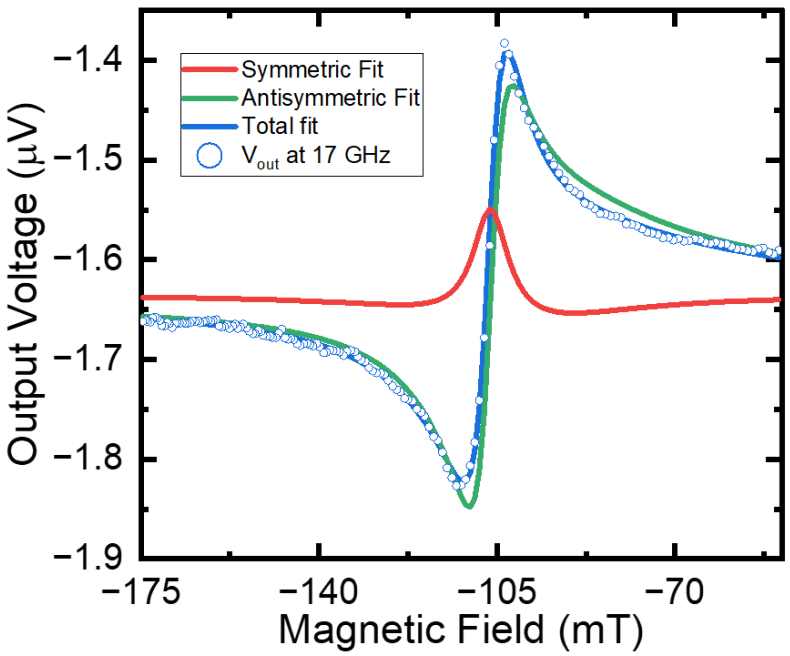

Figure 6-13: Resonance line shape*: Output voltage versus magnetic field at 17 GHz with axis* $\boldsymbol{\theta}$*=45° and an input power of 0 dBm. The empty blue circles denote the collected data points, while the blue curve represents a fit using*

(Eq. 6-10)*. The green and red components represent the symmetric and antisymmetric terms in*

(Eq. 6-10)*, respectively.*

One should note the output voltage amplitude, that is here approximately 0.5 μV at 0 dBm. This value is comparable and even higher than results reported for YIG(*31*) , where similar magnitudes were achieved of few microvolts and with significantly higher power inputs.

- ***Angular dependency:***

We performed an angular sweep of the in-plane applied magnetic field at a constant frequency of 17 GHz. In ***Figure 6-14.*** **a)** we illustrate the three primary directions of the magnetic field at θ = 45°, 0°, and 90° shown by blue, red and brown respectively. By comparing the amplitude of the resonance peak of each angle, we observe a strong dependence of signal amplitude on the field direction with respect to the platinum, where we see a clear decrease of the amplitude by about a factor of 10 when going from 45 ° to the two other directions.

In ***Figure 6-14.*** **b)**, the plot shows the peak-to-peak amplitude voltages (black dots) as a function of the different angles. The data points show a strong agreement with the theoretical model (red curve), which suggests a dependency proportional to $cos(\boldsymbol{\theta}).sin(2\boldsymbol{\theta})$, for both voltages of SMR and SP. We add to that, the discussed efficiency of detection rising from the transducer, which as we have shown in the previous section with the non-local measurements via ISHE, that it follows a $\cos^2\theta$ trend, and therefore aligning well with what we have here.

By so, this explains the maximal voltages obtained at angles of $\boldsymbol{\theta = 45 + 90n}$ (where n=0,1, 2…), and the vanishing voltages at 90. Regardless of the low detected voltage at 0°, it is however higher than that detected at 90°. The reason behind this is still unknown but can be linked to the excitation or the coupling with propagating spin-waves modes and not only uniform mode excitaiton.

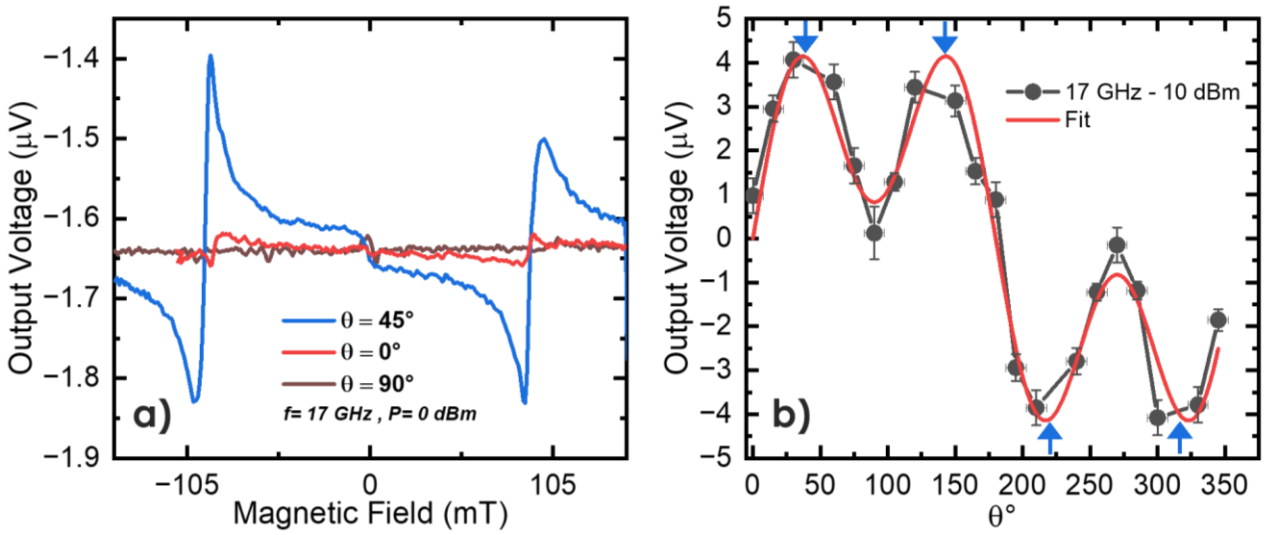

Figure 6-14: Angular Dependency on the output voltage: *a) output voltage with respect to the magnetic field from negative to positive values showing the resonance at the main three angles of orientation of the field with respect to the platinum layer, θ= 0° in red ,45° in blue and 90° in brown. b)The black points represent the experimental data measured at a frequency of 17 GHz and a power level of 10 dBm. The red curve represents a fit using the expected dependency on the voltages of* $(\cos\theta \cdot \sin 2\theta) * \cos^2\theta$ *from Chiba et al. and the transducer efficiency. The blue arrows mark the angles of 45°+90°.n at which we have the highest amplitudes.*

- ***Power dependency:***

Here, we investigate the power dependence of the output voltage. In the linear regime, the output voltage increases as we increase the input power without distorting the lineshape of resonance. However, as we pump the system harder, the damping tends to increase i.e. the magnetization precession angle increases. As a result, the lineshape of the resonance peak will start to change and distort, indicating the onset of the nonlinear regime.

For this, we conduct a power sweep measurement, while keeping the frequency fixed at 17 GHz and simultaneously sweeping the magnetic field from negative to positive values. We repeat this measurement for the three principal field directions. The results from these sweeps are shown in ***Figure 6-15***.

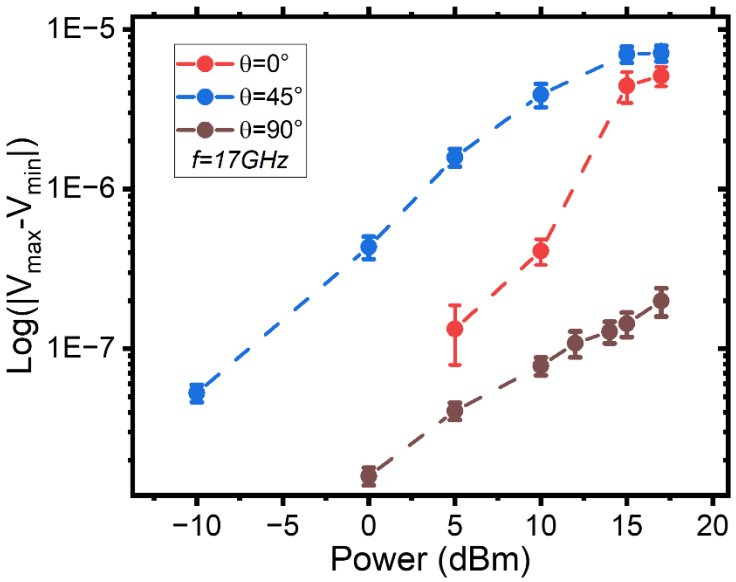

Figure 6-15: Power dependency at main angles: *Amplitude of the output voltage with respect to the input power (dBm) represented in a logarithmic scale. The results measurements conducted at angles of* $\boldsymbol{\theta} = 0°$ *in red ,45° in blue and 90° in brown.*

From the plot, we observe a linear increase in the amplitude as the power increases. Notably, the amplitude remains higher at an angle of 45 degrees as discussed previously. Specifically for this case, we remark that the linear increase persists until a threshold power of 10 dBm, after this value the amplitude shows saturation. Conversely, for the 90 degrees angle, the linear trend seems to hold for higher power levels than 10 dBm and therefore requires powers exceeding this value before reaching saturation. In contrast, for the case of 0 degrees saturation is also observed for powers higher than 10 dBm. We however must note missing data points between the 10 to 15 dBm that can help in explaining the sudden jump of amplitude for this case.

In ***Figure 6-16.*** **a-i)**, we show the evolution of the output voltage resonance shape changing with power levels at +5 dBm, + 15 dBm and to +17 dBm (left to right) at a given angle.

For the 45-degree angle orientation, at +5 dBm, at one field polarity we observe a resonance characterized by a minimum and a maximum peak voltage. As expected, on the negative field side the peak at $\mu_0 H = -105\, mT$ is a minimum whereas at the same field but in the positive direction, the peak is a minimum, meaning that we have a polarization switching by switching the field polarity.

Moving to the nonlinear region, the shape of these peaks gets distorted as shown in **b)**. where we highlight by arrows, the formation of secondary peaks at slightly higher fields than these shown in **a)**. Significantly, the number of these secondary peaks multiplies as we increase to 17 dBm in panel **c)** while the amplitude remains similar to that with 15 dBm. This behavior can be linked to a non-equilibrium in the magnon modes leading to the transfer of energy from the initially excited AFMR mode to other magnon modes.

At 0°, similar analysis applies, yet here the secondary resonances are more pronounced as

shown in panel **e)**. We observe at 10 dBm the formation of two well separated peaks at lower fields this time than the main one at 105 mT. The lineshape gets more distorted while the main gets lower in amplitude as we progress to an input of + 17 dBm as depicted in **f)**.

At 90°, the amplitude of the resonance decreases further, reaching levels on the order of nanovolts. Once again, a notable non-reciprocity of the resonance voltage amplitude is observed (panel **g)**), accompanied by the formation of a secondary peak (indicated by brown arrows) and a distinct broadening of the lineshape. This broadening becomes more pronounced as we increase the input power (panels **h-i**).

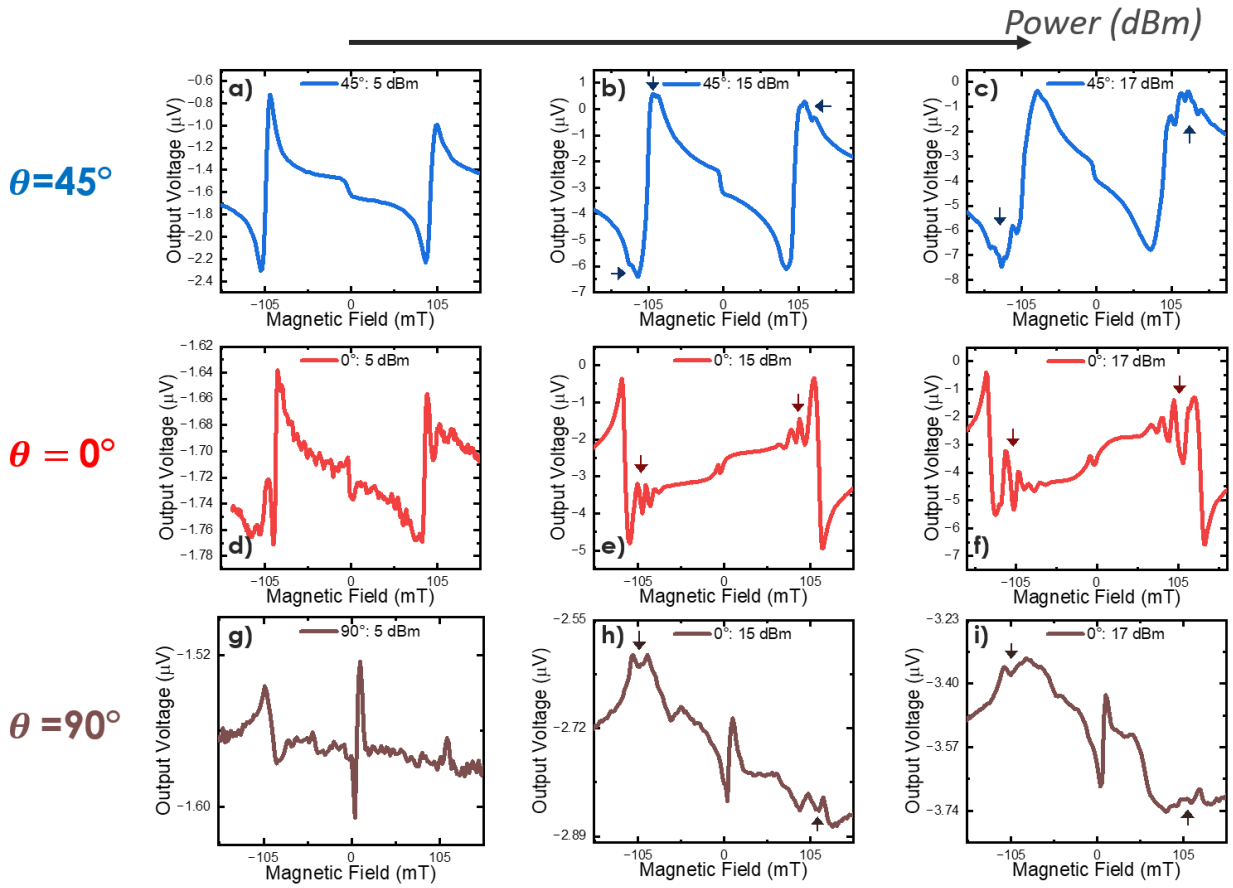

Figure 6-16: Power dependency on output voltage: *(a-c), (d-f),(g-i): output voltage in function of the swept field for a 45-degree (red) , 0 degree (blue) and 90 degree (brown) angles orientation, respectively, at three different power levels from 5 dBm , +15 dBm and +17 dBm.*

One should note that, for the three shown angles at +5 dBm, the resonance field (of the main peak) consistently maintains a value near 105 mT as shown in the figure. This observation suggests that, indeed, in the linear regime, we are exciting and detecting the antiferromagnetic resonance mode of Hematite.

Another aspect to consider is the offset present in all the figures at 0 mT and nearby low fields. This can be attributed to the Spin Seebeck effect, SSE which changes sign when we reverse the direction of the small canted moment. The SSE is generally explained by the thermal nonequilibrium between the magnons in the antiferromagnetic layer and the conduction electrons in the Pt layer. This effect could also contribute at resonance, but the

change in magnon population due to the rf excitation is expected to be much lower than the total magnon population due to k_bT at room temperature.

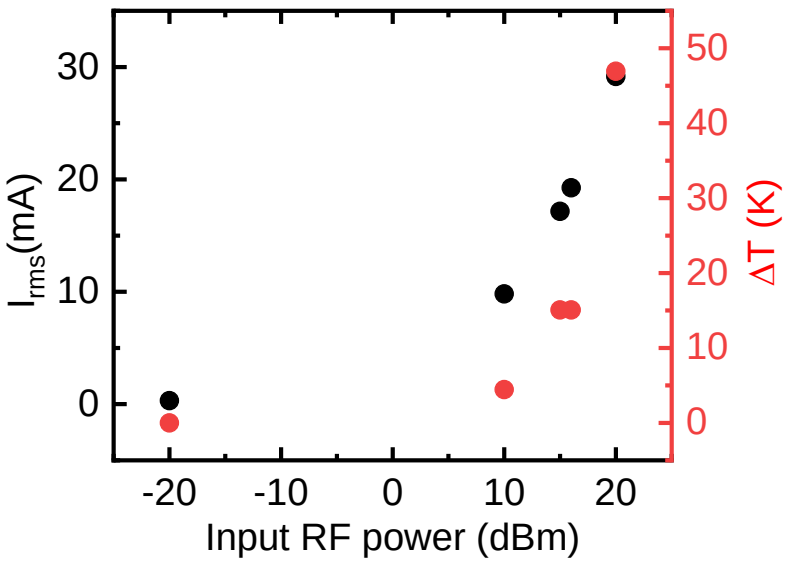

Figure 6-17 : Power dependency of the temperature in the spindiode devices

One should notice that the onset of a nonlinear regime can arise directly from nonlinear spin-wave dynamics as mentioned above or from thermal effects that could modify the magnon spectra. To evaluate the amplitude of thermal effects, we thus determine the increase in temperature due to the input RF current. We thus recorded the increase in temperature in the platinum wire as a function of the input power using:

$$R = R(300K)\big(1 + a(T - 300K)\big)$$

(Eq. 6-11)

with the temperature coefficient of platinum $a = 3.9.10^{-3}$. We thus extracted the increase in temperature of about 50K at 20 dBm as shown in ***Figure 6-17***. The maximum temperature is thus far below the Néel temperature of hematite (T_N = 685K), enabling us to discard a domination of the thermal effects in the change of the spin diode spectra.

B. AC – DC measurements:

Now, in parallel to the RF-current, we inject a DC current in the platinum layer, this can add a spin-transfer torque to the magnetization dynamics at the interface, which could therefore be detected by means of SP, but also generate thermal gradient at the interface between platinum and hematite and generate SSE.

We present the results with a fixed frequency of 20 GHz, in the configuration where we had the best signal amplitude at 45°, and with an input power of 8 dBm which ensures remaining in the linear regime before introducing the DC contribution. From ***Figure 6-18.*** **a)**, we can see the evolution of the resonance peak as we increase the injected current value. Here, we notice that the lineshape becomes quickly symmetric and not anymore anti-symmetric as in

absence of DC current. This effect could be associated to a spin-torque effect. However, we observe the same behavior for both negative and positive current.

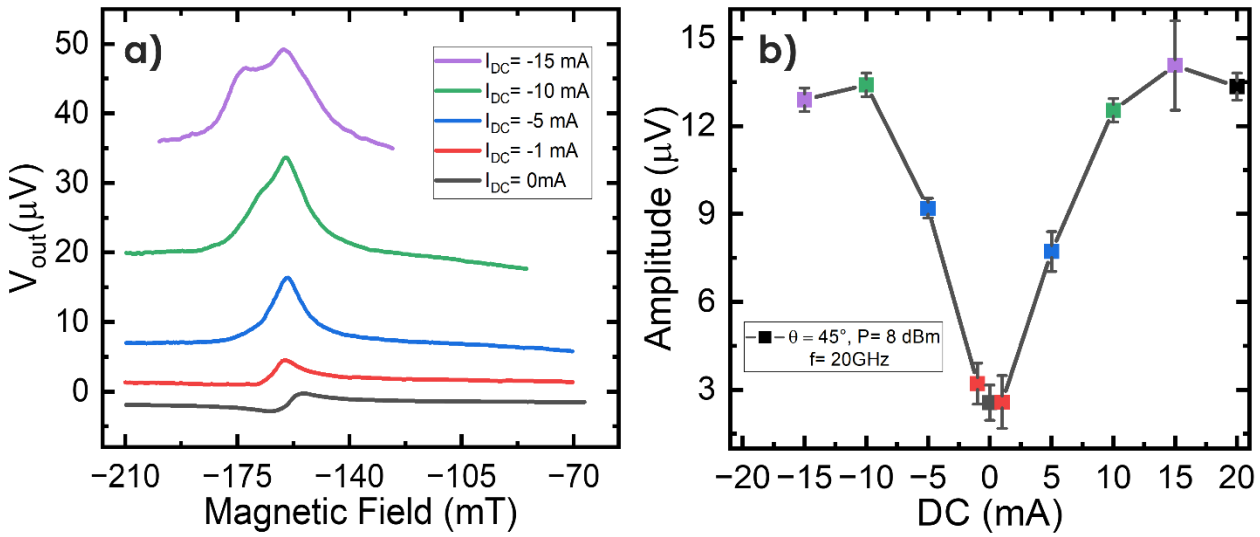

Figure 6-18: AC-DC measurements: *a) Evolution of the output voltage versus the magnetic field upon injection of I_{DC} = 0mA (black), -1mA (red), -5mA (blue), -10mA (green), -15mA (purple), at f= 20 GHz, P=8 dBm and θ=45°. b) The amplitude of the output voltage obtained at different DC currents; the highlighted points mark the currents shown in a) with the same color code.*

In **b)** we show the evolution of the amplitude of the detected voltage with respect to the injected DC current, with positive and negative values. A slight asymmetry in the amplitude is observed when moving from one polarization of current to the other but the curve is largely symmetric in current. Then the amplitude increases as we increase the DC and appears to saturate and fluctuate after values of 10 mA. We thus observe the appearance of the secondary peak, as shown in panel **a)** with the curve at -15 mA (green). This behavior may indicate a change of the magnetic properties below the platinum stripes due to the application of a DC current. The DC current could thus modify and artificially separate the properties close to the surface and within the bulk of the material. Such a surface behavior would be inline with the transition from an anti-symmetric to a symmetric curve when we start applying a DC current as the SMR term is anticipated to be symmetric for small thicknesses.

To further disentangle between a potential Oersted field and spin-torque excitations for this surface like behavior, we perform measurements for both positive and negative DC currents and observed no differences. This indicates that the spin-torque excitation remains negligible here and would likely require to perform measurements in antiferromagnetic thin films which go beyond the frame of this PhD manuscript.

6.2.3 Discussion with VNA measurments:

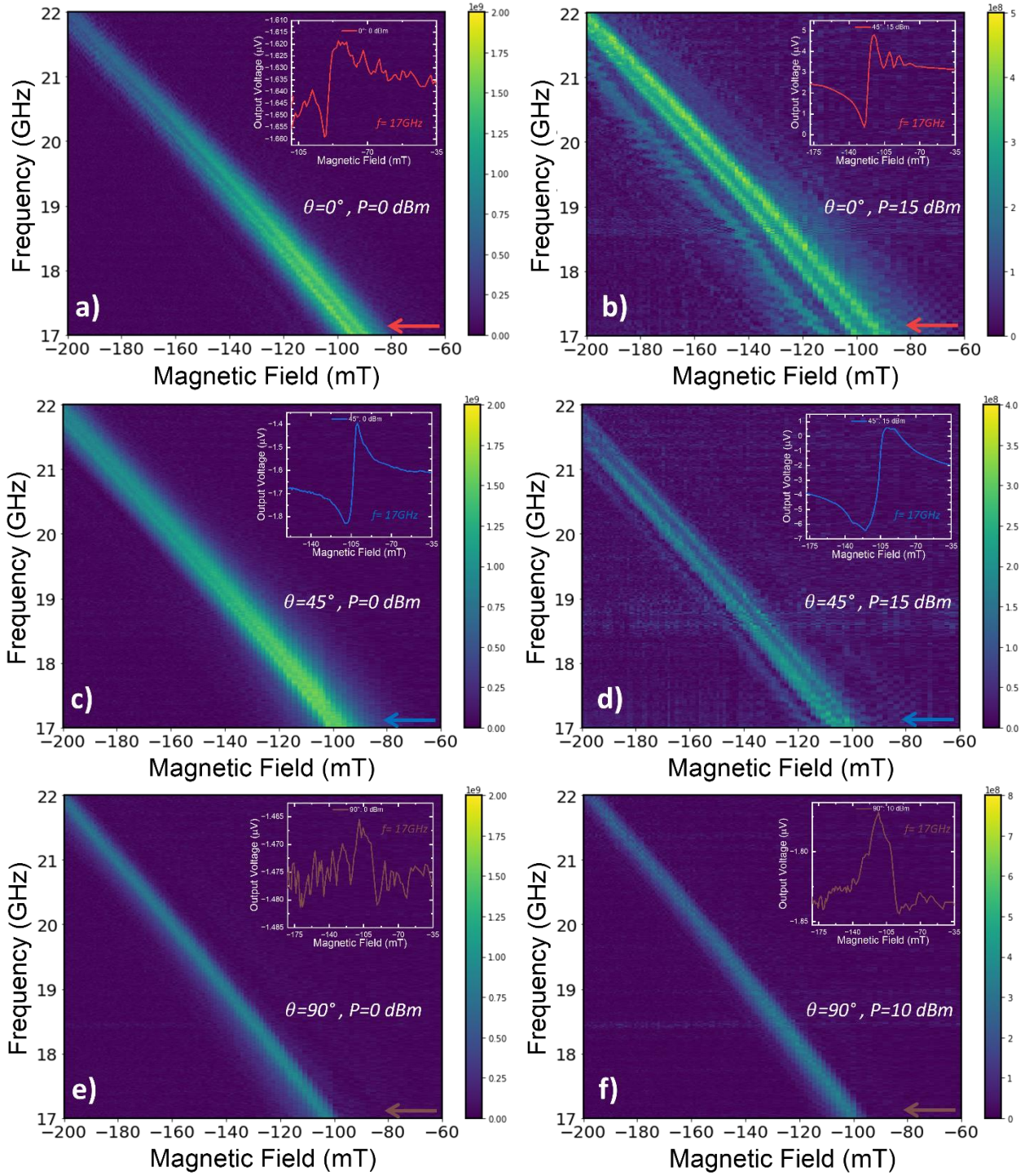

Figure 6-19: Frequency sweep measurements with VNA: *Frequency versus magnetic field at different field orientations ; θ = 0° (a-b), 45° (c-d), and 90° (e-f), showing the dispersion in Hematite. We illustrate the broadening effect of the resonance maxima in the spectrum by moving from a power of 0 dBm (a, c, e) to 15 dBm (b, d) and 10 dBm f).*

We also performed measurements while connecting the microprobes to a VNA and performed frequency sweep measurements while collecting the reflected S-parameters and varying injected input power in the antenna. The measurements were repeated for the main

angles of the magnetic field orientation. The frequency sweep ranges from 12 to 25 GHz, with a total of 12001 points, sweeping from negative to positive fields. Our primary focus will be on comparing the S_{11} spectrum at 0 dBm, representing the linear regime, with the S_{11} in the nonlinear regime at 15 dBm. We show the spectra, with zooming on frequencies from 17 GHz to 22 GHz. It is important to note that the amplitudes of the S-parameters data have been treated in a way to eliminate background noise and offset. As a result, the colormap scale used does not facilitate direct comparison of amplitudes between different orientations and power levels.

In ***Figure 6-19***, we present the case where the field is applied parallel to the platinum bar, and consequently, perpendicular to the k-vector- the vector at which the spinwaves are excited by the antenna. At an input power of 0 dBm, we observe a resonance composed of two closely spaced branches in frequency, similar to what we observed in the previous spin-diode voltage measurements (depicted in the inset of panel **a)**). As we increase the power, multiple peaks emerge along with a broadening of the lineshape, as evident in the spectrum shown panel **b)** at a power level of 15 dBm, where a clear additional peak appears at a lower frequency along with other less clear at even lower frequencies.

This still holds true when we move for the intermediate field orientation of 45°, as we see the separation of the main branch in **c)** to multiple ones in **d)**, consistent with voltage measurements as recalled from the insets of both panels **c)** and **d)** .

Finally, in the orientation where the magnetic field is perpendicular to the platinum bar (i.e., $\boldsymbol{H} \,//\, \boldsymbol{k}$ at a 90° angle), the results reveal no notable difference between the cases of 0 dBm and 10 dBm (refer to panels **e)** and **f)**). As discussed previously, we have shown that for this field orientation it requires more input power before reaching saturation of the detected signal, and consistent with what we obtain here.

Through these additional measurements, we have retrieved the same results as our earlier measurements and clarified the emergence of the new resonance peaks upon entering the nonlinear regime. These nonlinear effects can be attributed to the energy transfer between magnon modes and therefore exciting magnon modes at nearby frequencies as seen from the shown spectra. The effect of the orientation of the field is related to the efficiency of the detection from the antenna mainly, as discussed throughout this chapter, making the signal relatively high at intermediate angles, and therefore easier to reach the nonlinear regime upon pumping the system.

6.3 BIBLIOGRAPHY:

1. R. Cheng, M. W. Daniels, J.-G. Zhu, D. Xiao, Antiferromagnetic Spin Wave Field-Effect Transistor. *Scientific Reports* **6**, 24223 (2016).
2. I. Proskurin, R. L. Stamps, A. S. Ovchinnikov, J. Kishine, Spin-wave chirality and its manifestations in antiferromagnets. *Physical Review Letters* **119** (2017).
3. R. Cheng, D. Xiao, A. Brataas, Terahertz Antiferromagnetic Spin Hall Nano-Oscillator. *Phys. Rev. Lett.* **116**, 207603 (2016).
4. E. Saitoh, M. Ueda, H. Miyajima, G. Tatara, Conversion of spin current into charge current at room temperature: Inverse spin-Hall effect. *Applied Physics Letters* **88**, 182509 (2006).
5. Y. Tserkovnyak, A. Brataas, G. E. W. Bauer, Spin pumping and magnetization dynamics in metallic multilayers. *Phys. Rev. B* **66**, 224403 (2002).
6. A. V. Chumak, A. A. Serga, M. B. Jungfleisch, R. Neb, D. A. Bozhko, V. S. Tiberkevich, B. Hillebrands, Direct detection of magnon spin transport by the inverse spin Hall effect. *Applied Physics Letters* **100**, 082405 (2012).
7. O. d'Allivy Kelly, A. Anane, R. Bernard, J. Ben Youssef, C. Hahn, A. H. Molpeceres, C. Carrétéro, E. Jacquet, C. Deranlot, P. Bortolotti, R. Lebourgeois, J.-C. Mage, G. De Loubens, O. Klein, V. Cros, A. Fert, Inverse spin Hall effect in nanometer-thick yttrium iron garnet/Pt system. *Appl. Phys. Lett.* **103**, 082408 (2013).
8. J. Li, C. B. Wilson, R. Cheng, M. Lohmann, M. Kavand, W. Yuan, M. Aldosary, N. Agladze, P. Wei, M. S. Sherwin, J. Shi, Spin current from sub-terahertz-generated antiferromagnetic magnons. *Nature*, 1–5 (2020).
9. P. Vaidya, S. A. Morley, J. van Tol, Y. Liu, R. Cheng, A. Brataas, D. Lederman, E. del Barco, Subterahertz spin pumping from an insulating antiferromagnet. *Science* **368**, 160–165 (2020).
10. I. Boventer, H. T. Simensen, A. Anane, M. Kläui, A. Brataas, R. Lebrun, Room-Temperature Antiferromagnetic Resonance and Inverse Spin-Hall Voltage in Canted Antiferromagnets. *Phys. Rev. Lett.* **126**, 187201 (2021).
11. H. Wang, Y. Xiao, M. Guo, E. Lee-Wong, G. Q. Yan, R. Cheng, C. R. Du, Spin Pumping of an Easy-Plane Antiferromagnet Enhanced by Dzyaloshinskii--Moriya Interaction. *Phys. Rev. Lett.* **127**, 117202 (2021).
12. A. V. Chumak, P. Kabos, M. Wu, C. Abert, C. Adelmann, A. O. Adeyeye, J. Åkerman, F. G. Aliev, A. Anane, A. Awad, C. H. Back, A. Barman, G. E. W. Bauer, M. Becherer, E. N. Beginin, V. A. S. V. Bittencourt, Y. M. Blanter, P. Bortolotti, I. Boventer, D. A. Bozhko, S. A. Bunyaev, J. J. Carmiggelt, R. R. Cheenikundil, F. Ciubotaru, S. Cotofana, G. Csaba, O. V. Dobrovolskiy, C. Dubs, M. Elyasi, K. G. Fripp, H. Fulara, I. A. Golovchanskiy, C. Gonzalez-Ballestero, P. Graczyk, D. Grundler, P. Gruszecki, G. Gubbiotti, K. Guslienko, A. Haldar, S. Hamdioui, R. Hertel, B. Hillebrands, T. Hioki, A. Houshang, C.-M. Hu, H. Huebl, M. Huth, E. Iacocca, M. B. Jungfleisch, G. N. Kakazei, A. Khitun, R. Khymyn, T. Kikkawa, M. Kläui, O. Klein, J. W. Kłos, S. Knauer, S. Koraltan, M. Kostylev, M. Krawczyk, I. N. Krivorotov, V. V. Kruglyak, D. Lachance-Quirion, S. Ladak, R. Lebrun, Y. Li, M. Lindner, R. Macêdo, S. Mayr, G. A. Melkov, S. Mieszczak, Y. Nakamura, H. T. Nembach, A. A. Nikitin, S. A. Nikitov, V. Novosad, J. A. Otálora, Y. Otani, A. Papp, B. Pigeau, P. Pirro, W. Porod, F. Porrati, H. Qin, B. Rana, T. Reimann, F. Riente, O. Romero-Isart, A. Ross, A. V. Sadovnikov, A. R. Safin, E. Saitoh, G. Schmidt, H. Schultheiss, K. Schultheiss, A. A. Serga, S. Sharma, J. M. Shaw, D. Suess, O. Surzhenko, K. Szulc, T. Taniguchi, M. Urbánek, K. Usami, A. B. Ustinov, T. van der Sar, S. van Dijken, V. I. Vasyuchka, R. Verba, S. V. Kusminskiy, Q. Wang, M. Weides, M. Weiler, S. Wintz, S. P. Wolski, X. Zhang, Advances in Magnetics Roadmap on Spin-Wave Computing. *IEEE Transactions on Magnetics* **58**, 1–72 (2022).
13. A. V. Chumak, A. A. Serga, M. B. Jungfleisch, R. Neb, D. A. Bozhko, V. S. Tiberkevich, B.

Hillebrands, Direct detection of magnon spin transport by the inverse spin Hall effect. *Appl. Phys. Lett.* **100**, 082405 (2012).
14. O. d'Allivy Kelly, A. Anane, R. Bernard, J. B. Youssef, C. Hahn, A. H. Molpeceres, C. Carrétéro, E. Jacquet, C. Deranlot, P. Bortolotti, R. Lebourgeois, J.-C. Mage, G. de Loubens, O. Klein, V. Cros, A. Fert, Inverse spin Hall effect in nanometer-thick yttrium iron garnet/Pt system. *Applied Physics Letters* **103**, 082408 (2013).
15. O. D'Allivy Kelly, Détection et excitation d'ondes de spin dans des microstructures de couches ultraminces $Y_3Fe_5O_{12}$/métal à fort couplage spin orbite. *PhD thesis* (2015).
16. R. Lebrun, A. Ross, O. Gomonay, S. A. Bender, L. Baldrati, F. Kronast, A. Qaiumzadeh, J. Sinova, A. Brataas, R. A. Duine, M. Kläui, Anisotropies and magnetic phase transitions in insulating antiferromagnets determined by a Spin-Hall magnetoresistance probe. *Commun Phys* **2**, 50 (2019).
17. J. Fischer, M. Althammer, N. Vlietstra, H. Huebl, S. T. B. Goennenwein, R. Gross, S. Geprägs, M. Opel, Large Spin Hall Magnetoresistance in Antiferromagnetic α − Fe 2 O 3 / Pt Heterostructures. *Phys. Rev. Applied* **13**, 014019 (2020).
18. A. S. Jenkins, R. Lebrun, E. Grimaldi, S. Tsunegi, P. Bortolotti, H. Kubota, K. Yakushiji, A. Fukushima, G. De Loubens, O. Klein, S. Yuasa, V. Cros, Spin-torque resonant expulsion of the vortex core for an efficient radiofrequency detection scheme. *Nature Nanotech* **11**, 360–364 (2016).
19. P. N. Skirdkov, K. A. Zvezdin, Spin-Torque Diodes: From Fundamental Research to Applications. *Annalen der Physik* **532**, 1900460 (2020).
20. R. Kohno, K. An, E. Clot, V. V. Naletov, N. Thiery, L. Vila, R. Schlitz, N. Beaulieu, J. B. Youssef, M. Anane, V. Cros, H. Merbouche, T. Hauet, V. E. Demidov, S. O. Demokritov, G. de Loubens, O. Klein, Non-local magnon transconductance in extended magnetic insulating films.\\ Part I: spin diode effect. arXiv arXiv:2210.08304 [Preprint] (2023). http://arxiv.org/abs/2210.08304.
21. A. Safin, V. Puliafito, M. Carpentieri, G. Finocchio, S. Nikitov, P. Stremoukhov, A. Kirilyuk, V. Tyberkevych, A. Slavin, Electrically tunable detector of THz-frequency signals based on an antiferromagnet. *Applied Physics Letters* **117**, 222411 (2020).
22. R. Khymyn, V. Tiberkevich, A. Slavin, Antiferromagnetic spin current rectifier. *AIP Advances* **7**, 055931 (2017).
23. A. Manchon, Spin Hall magnetoresistance in antiferromagnet/normal metal bilayers. *Physica Rapid Research Ltrs* **11**, 1600409 (2017).
24. H. Nakayama, M. Althammer, Y.-T. Chen, K. Uchida, Y. Kajiwara, D. Kikuchi, T. Ohtani, S. Geprägs, M. Opel, S. Takahashi, R. Gross, G. E. W. Bauer, S. T. B. Goennenwein, E. Saitoh, Spin Hall Magnetoresistance Induced by a Nonequilibrium Proximity Effect. *Phys. Rev. Lett.* **110**, 206601 (2013).
25. K. Ganzhorn, J. Barker, R. Schlitz, B. A. Piot, K. Ollefs, F. Guillou, F. Wilhelm, A. Rogalev, M. Opel, M. Althammer, S. Geprägs, H. Huebl, R. Gross, G. E. W. Bauer, S. T. B. Goennenwein, Spin Hall magnetoresistance in a canted ferrimagnet. *Phys. Rev. B* **94**, 094401 (2016).
26. J. H. Han, C. Song, F. Li, Y. Y. Wang, G. Y. Wang, Q. H. Yang, F. Pan, Antiferromagnet-controlled spin current transport in SrMnO 3 / Pt hybrids. *Phys. Rev. B* **90**, 144431 (2014).
27. D. Hou, Z. Qiu, J. Barker, K. Sato, K. Yamamoto, S. Vélez, J. M. Gomez-Perez, L. E. Hueso, F. Casanova, E. Saitoh, Tunable Sign Change of Spin Hall Magnetoresistance in Pt / NiO / YIG Structures. *Phys. Rev. Lett.* **118**, 147202 (2017).
28. A. Ross, R. Lebrun, C. Ulloa, D. A. Grave, A. Kay, L. Baldrati, F. Kronast, S. Valencia, A. Rothschild, M. Kläui, Structural sensitivity of the spin Hall magnetoresistance in antiferromagnetic thin films. *Phys. Rev. B* **102**, 094415 (2020).
29. L. Liu, T. Moriyama, D. C. Ralph, R. A. Buhrman, Spin-Torque Ferromagnetic Resonance Induced by the Spin Hall Effect. *Phys. Rev. Lett.* **106**, 036601 (2011).
30. S. Karimeddiny, J. A. Mittelstaedt, R. A. Buhrman, D. C. Ralph, Transverse and Longitudinal Spin-

Torque Ferromagnetic Resonance for Improved Measurement of Spin-Orbit Torque. *Phys. Rev. Applied* **14**, 024024 (2020).
31. M. B. Jungfleisch, W. Zhang, J. Sklenar, J. Ding, W. Jiang, H. Chang, F. Y. Fradin, J. E. Pearson, J. B. Ketterson, V. Novosad, M. Wu, A. Hoffmann, Large spin-wave bullet in a ferrimagnetic insulator driven by spin Hall effect. *Phys. Rev. Lett.* **116**, 057601 (2016).
32. T. Chiba, G. E. W. Bauer, S. Takahashi, Current-Induced Spin-Torque Resonance of Magnetic Insulators. *Phys. Rev. Applied* **2**, 034003 (2014).
33. T. Chiba, M. Schreier, G. E. W. Bauer, S. Takahashi, Current-induced spin torque resonance of magnetic insulators affected by field-like spin-orbit torques and out-of-plane magnetizations. *Journal of Applied Physics* **117**, 17C715 (2015).

7 CONCLUSION AND PERSPECTIVES

As we conclude this manuscript, it is essential to summarize the results that have been presented throughout this thesis and explored in earlier chapters. Then in this final section we highlight on the perspectives and motivations that can push this field forward.

7.1 CONCLUSION:

As highlighted, discussed, and thoroughly explored, this thesis primarily focused on investigating the dynamics of spin waves starting from a well-known ferromagnetic to another promising candidate material for magnonics, namely, the canted antiferromagnet Hematite. This profound understanding of spin waves in diverse materials provides us with a perspective on the potential applications achievable through magnonics, especially in the development of rapid and energy-efficient RF-devices.

Firstly, we have successfully constructed the time-domain dispersion relation of spin waves in a thick film of YIG, by using the two injecting and detecting RF antennas. This was achieved through propagating spin-wave spectroscopy in both time and frequency domain measurements. We validated our results by converting the time-domain data back to the frequency domain and comparing it with the frequency domain measurements, thus confirming the consistency with expected theoretical results. The k-selectivity of antennas on exciting the spin waves, and depending on the design, can yield in multiple modes in the spectrum of a given material. When investigating a thick film, the presence of thickness modes can further complicate the analysis of spin wave properties in the frequency domain, primarily due to mode hybridization. Bu using this approach we were able to distinguish and isolate the signals of individual spin wave-packets within a complex spectrum. Consequently, we gained a deeper understanding of properties such as group velocity and the delay time. This therefore contribute to enhance and tailor the antenna designs for future applications, such as a YIG delay lines.

Secondly, we were successfully able to investigate experimentally the propagation of spinwaves in a canted antiferromagnet, which was lacking for SWs in antiferromagnets. Due to the presence of Dzyaloshinskii-Moriya interaction in such a material, a canting of the magnetic moments occur, which anticipates in the presence of magnetostatic spinwaves. For this aim, we conducted the study of the propagation in two configurations, the propagation vector $\boldsymbol{k}$ perpendicular to the Néel vector $\boldsymbol{n}$ $(\boldsymbol{k}\perp\boldsymbol{n})$ and the propagation vector $\boldsymbol{k}$ parallel to the Néel vector $\boldsymbol{n}$ $(\boldsymbol{k}//\boldsymbol{n})$, where we find a lifted non-degeneracy between the two magnon dispersion modes of up to 1 GHz. Then, by using time-of-flight spin-wave spectroscopy and time gating measurements, we find that the magnon wave packets can propagate as fast as 20 km/s for the reciprocal the bulk spin-wave in both $\boldsymbol{k}\perp\boldsymbol{n}$ and $\boldsymbol{k}//\boldsymbol{n}$ modes while up to 6 Km/s for other spin-waves modes propagating in the $\boldsymbol{k}//\boldsymbol{n}$ configuration. Non-reciprocity is a common feature observed for surfaces spin-waves in the case of ferromagnets. Therefore, by investigating in depth the $\boldsymbol{k}//\boldsymbol{n}$ configuration, and when comparing the transmission

signals in negative and positive fields, a difference of amplitudes was clearly evidenced for certain modes. This translate into a signature of presence of surface spin wave modes propagating with opposite directions at the two surfaces of the sample for $\boldsymbol{k}//\boldsymbol{n}$, which had been predicted without been observed until now in antiferromagnets. In parallel, for $\boldsymbol{k}\perp\boldsymbol{n}$, similar measurements show reciprocity of the SWs modes which are in line with theoretical modelling.

Another aspect that was covered in the course of this thesis, is the spintronic aspect with magnonics, known as magnon spintronics, and was done on hematite. We therefore detected in an alternative way to the inductive measurements, now by using the spin transport mechanisms, with an eltelctical detection of the AFM spinwaves. This is achieved via the ISHE upon using a platinum based metallic reciever in place of the detecting antenna. The obtained output voltage in our system, is conmparable as obtained in ferromagnets like YIG, which marks an efficient electrical detection of propagating spinwave through a surface sensitive technique, and thereby also validate and backup our observations made with the inductive measurements to understand the surface spinwaves in such a material.

A further spintronic aspect has also been achieved, that is the realization of spin diode rectification in Hematite. In this work we evidence that as expected the Oersted field excitation dominates over spin-torque effects in the case of a single crystal, and we compare our results with what was obtained on ferromagnetic models. We also observe the presence of non-linear effects when pumping the system with high powers. To validate further our observations, we measure the output voltage from the device by simultaneously applying both AC and DC currents and examine the DC dependent characteristics of the system. Henceforth we were able upon resonance conditions to detect a DC voltage in a magnetic insulator/ platinum bilayers, consistent with theoretical predictions (done on ferromagnets) and attributed to a spin-torque diode effect mediated by the SMR. These mentioned features further demonstrate that spin-pumping effects represent a promising tool to detect the spin-wave dynamics in antiferromagnets, and favorize their integration in magnonic devices.

In summary, both fundamental and applicative objectives of this thesis have been achieved. Basic understandings for microwave devices in thick YIG films were realized and characterized. The utility of the time domain function in vector network analyzers was demonstrated and have been used in many measurements to reveal the material's properties. An important demonstration of propagating SWs in hematite have been realized marking all the potentials of such antiferromagnets for establishing a new research field in magnonic based on canted antiferromagnets, which can also possess altermagnet behavior, and holds a lot of opportunities for high frequency magnonics.

These promising obtained results encourage further experimental studies to continue this research work.

7.2 PERSPECTIVES:

During this thesis, I focused on exploring RF-applications in magnonics, utilizing a vector network analyzer to detect the spinwave signals. To enhance the response of low signal devices, I employed time gating and I employed the time domain spectroscopy implemented within the VNAs, that is based on based on continuous wave (CW) excitation and can not provide information about the transient regime of SWs. To access this regime, we aim at real-time domain data representation, while implementing pulsed rf- VNA measurements. Towards the end of my thesis, we initiated testing this method, and promising results are currently underway. This method hold potential to significantly enhance the designs of RF magnonic devices, namely delay lines.

Following this, we were able to uncover interesting properties of SW in a single crystal like Hematite. This fundamental study on a bulk material can open up the possibilities of different types of investigations, addressing the same physical aspects as those found in Ferromagnets. Hence, as perspective of these initial steps toward AFM magnonics many investigation paths can be envisioned :

1. Accessing thin films

Towards the end of the thesis, we initiated the fabrication of devices with thin films of Hematite to explore the behavior of spin waves while reducing the film thickness and unraveling the physics underlying in this complex material. Currently, we are conducting tests with thicknesses ranging from 500 nm to 20 nm, and resonance has been observed in most of the fabricated devices, while ongoing transport experiments are in progress. Additionally, our objective is to explore the higher-frequency modes that should be accessible through Brillouin light scattering measurements. If successful, numerous interesting applications in the field of ultrafast magnonics are expected.

2. Auto-oscillation and Amplification of SWs:

In thin films of YIG, it has been demonstrated that injecting a DC current through a platinum layer, specifically via spin-orbit torques, can lead to the onset of auto-oscillation regime at a certain threshold current(*1*). However, a significant challenge persists in achieving the amplification of spin waves beyond this threshold, primarily due to non-linear interactions that originate mostly from dipolar interactions. Interestingly, it has been shown that Bi-doped YIG, with an engineered perpendicular magnetic anisotropy(*2*, *3*), can overcome these magnon-magnon scatterings. In this context, amplification of SWs amplitude has been observed very recently through μ-BLS experiments(*4*). Now, with spin waves in Hematite, the opportunity arises to explore the effects of spin-orbit torques in antiferromagnets. By taking the advantage of the high frequencies associated with Hematite, this therefore opens up promising avenues for complex magnonic computing and logic gates.

3. Bose-Einstein condensation:

Magnons can undergo Bose-Einstein condensation at room temperatures. This have been extensively been studied in YIG films. More recently, the Bose-Einstein condensation (BEC) have been evidenced in thin films of BiYIG where it was induced by spin-orbit torque and therefore permit an electronic control of the magnonic BEC (*5*). An opening to this finding can be to pursue the study of the interaction between the spinwaves and the magnonic BEC. This pushes to investigate the possibility to unravel this rich physics of magnon condensation in the antiferromagnetic Hematite. This can pave the way towards promising researches in the field of neuromorphic and quantum magnonics.

4. Topological spin texture ; AFM half-skyrmions

It has been demonstrated that in thin films of hematite, it is feasible to stabilize topological antiferromagnetic spin-textures of half-skyrmion type, recognized as merons and bimerons (*6*, *7*). Through manipulation of anisotropy and exchange bias, the reported size of these magnetic textures is within the range of a few hundred nanometres, making from Hematite a promising material for the logic and memory applications.

With these promising opportunities, remaining challenges and open questions are still under investigation. One of the challenges lies in the device integration of such materials. This can be overcome by shifting our focus towards the exploration of polycrystalline materials, offering an increased flexibility in growth conditions, and thereby reducing limitations on the integration and application side.

7.3 BIBLIOGRAPHY:

1. M. Evelt, V. E. Demidov, V. Bessonov, S. O. Demokritov, J. L. Prieto, M. Muñoz, J. Ben Youssef, V. V. Naletov, G. De Loubens, O. Klein, M. Collet, K. Garcia-Hernandez, P. Bortolotti, V. Cros, A. Anane, High-efficiency control of spin-wave propagation in ultra-thin yttrium iron garnet by the spin-orbit torque. *Applied Physics Letters* **108**, 172406 (2016).
2. L. Soumah, N. Beaulieu, L. Qassym, C. Carrétéro, E. Jacquet, R. Lebourgeois, J. Ben Youssef, P. Bortolotti, V. Cros, A. Anane, Ultra-low damping insulating magnetic thin films get perpendicular. *Nature Communications* **9**, 3355 (2018).
3. D. Gouéré, H. Merbouche, A. El Kanj, F. Kohl, C. Carrétéro, I. Boventer, R. Lebrun, P. Bortolotti, V. Cros, J. Ben Youssef, A. Anane, Temperature-independent ferromagnetic resonance shift in Bi-doped YIG garnets through magnetic anisotropy tuning. *Phys. Rev. Mater.* **6**, 114402 (2022).
4. H. Merbouche, B. Divinskiy, D. Gouéré, R. Lebrun, A. El-Kanj, V. Cros, P. Bortolotti, A. Anane, S. O. Demokritov, V. E. Demidov, True amplification of spin waves in magnonic nano-waveguides.
5. B. Divinskiy, H. Merbouche, V. E. Demidov, K. O. Nikolaev, L. Soumah, D. Gouéré, R. Lebrun, V. Cros, J. B. Youssef, P. Bortolotti, A. Anane, S. O. Demokritov, Evidence for spin current driven Bose-Einstein condensation of magnons. *Nat Commun* **12**, 6541 (2021).
6. H. Jani, J.-C. Lin, J. Chen, J. Harrison, F. Maccherozzi, J. Schad, S. Prakash, C.-B. Eom, A. Ariando, T. Venkatesan, P. G. Radaelli, Antiferromagnetic half-skyrmions and bimerons at room temperature. *Nature* **590**, 74–79 (2021).
7. A. K. C. Tan, H. Jani, M. Högen, L. Stefan, C. Castelnovo, D. Braund, A. Geim, A. Mechnich, M. S. G. Feuer, H. S. Knowles, A. Ariando, P. G. Radaelli, M. Atatüre, Revealing emergent magnetic charge in an antiferromagnet with diamond quantum magnetometry. *Nature Materials*, doi: 10.1038/s41563-023-01737-4 (2023).

F. RÉSUMÉ EN FRANÇAIS

Le magnétisme est un sujet étudié depuis environ trois mille ans. Après la découverte des ondes électromagnétiques et des principes de la relativité, plusieurs avancements ont eu lieu dans ce domaine au cours des deux derniers siècles. Avec la découverte du spin de l'électron en 1925 et de son moment magnétique associé, l'exploitation des propriétés magnétiques des matériaux a suscité un grand intérêt.

Avec l'augmentation de demande des appareils électroniques à forte consommation d'énergie, plusieurs défis sont apparus dans l'utilisation de l'électronique conventionnelle, notamment en ce qui concerne les problèmes de chauffage par effet Joule. De plus, les contraintes de la technologie CMOS, telles que les limitations de miniaturisation, contribuent à une déclin de la validité de la loi de Moore, qui prédit le taux d'augmentation du nombre de transistors dans les circuits. En conséquence, il y a eu un passage notable vers l'exploration d'alternatives au-delà du CMOS, qui ont gagné un intérêt significatif au cours des dix dernières anneés cherchant à trouver des composants performants et évolutifs tout en surmontant le chauffage par effet Joule.

Les matériaux magnétiques ont connu une croissance mondiale remarquable au fil des années, ce qui a stimulé le développement de découvertes scientifiques dans ce domaine. Les avancées dans le magnétisme permanent, l'enregistrement magnétique et les matériaux haute fréquence sont en train d'accélérer les progrès dans les secteurs de l'informatique, des télécommunications et du stockage des données, essentiels pour la vie quotidienne.

La spintronique, découverte pour la première fois en 1936 par Mott, a lié le spin de l'électron à sa charge. Notamment, dans les matériaux magnétiques, l'orientation du spin peut être manipulée par l'utilisation de champs magnétiques externes. La différence de mobilité et de population entre les électrons de spin up et spin down dans ces matériaux induit un flux net de courant polarisé en spin. Par conséquent, ce domaine étudie le transfert, le traitement et le stockage de l'information via le spin de l'électron au lieu de sa charge, surmontant ainsi les limitations de l'électronique.

Quand les moments magnétiques sont alignés spontanément, le matériau est appelé ferromagnétique, ce qui entraîne une aimantation spontanée finie. Ce comportement ferromagnétique persiste tant que la température est inférieure à une température critique appelée température de Curie T_c. Ainsi, l'application de champs faibles peut produire une aimantation très forte dans ces matériaux. Au-dessus de T_c, l'aimantation disparaît et le matériau devient paramagnétique. Un autre cas peut exister, où les moments magnétiques sont alignés de manière antiparallèle, résultant en une aimantation spontanée nulle ; dans ce cas, le matériau est appelé antiferromagnétique, avec une température critique appelée température de Néel.

Pendant des décennies, les ferromagnétiques à haute température de Curie et grande

aimantation ont été largement utilisés dans l'industrie du stockage magnétique, comme les disques durs magnétiques. En 1988, la découverte de la magnétorésistance géante (GMR) par Albert Fert et Peter Grünberg dans des couches alternées ferromagnétiques et conductrices non magnétiques a suscité un immense intérêt pour la recherche fondamentale et appliquée. Cela a rapidement favorisé le développement d'un nouveau type de capteur magnétique, désormais largement utilisé dans les têtes de lecture de disque dur, et a conduit à un prix Nobel de physique en 2007. Peu après la GMR, il a été démontré que les courants polarisés en spin pouvaient être utilisés pour manipuler les états magnétiques, via un effet appelé transfert de spin, actuellement implémenté dans les mémoires magnétiques. Avec ces découvertes, la spintronique a marqué un tournant dans le développement de l'informatique moderne il y a trois décennies. Pourtant, malgré son application prometteuse, les courants polarisés en spin sont générés par des courants électriques et n'évitent donc pas les pertes dues au chauffage par effet Joule.

Lorsqu'un système de moments magnétiques ordonnés est soumis à une perturbation, entraînant une déviation de leur position d'équilibre, ces moments magnétiques tendent à revenir à l'équilibre par un mouvement de précession amortie. Cette perturbation localisée se propage dans le matériau, formant une onde magnétique appelée « onde de spin » (Spin waves, SWs), reconnue par Bloch en 1929. Les ondes de spin possèdent des longueurs d'onde allant du micromètre jusqu'à l'échelle nanométrique, avec des vitesses atteignant quelques km/s et des fréquences allant du gigahertz au térahertz. La relation entre leur fréquence et leur vecteur d'onde, connue sous le nom de relation de dispersion, caractérise ces ondes et différencie leurs propriétés variées. Ces ondes peuvent ainsi se propager dans le milieu magnétique sans interagir avec la charge de l'électron, évitant ainsi les effets de chauffage. Le domaine qui étudie les ondes de spin de leur excitation, propagation, manipulation et détection est appelé « magnonique », en reconnaissance des quanta d'ondes de spin, les magnons. Grâce à leurs caractéristiques uniques, les nanodispositifs magnoniques sont perçus comme des candidats prometteurs pour les technologies de traitement de l'information par micro-ondes.

Le domaine de la magnonique a vu des avancées significatives avec l'introduction des cristaux photoniques. L'exploration des cristaux magnoniques a commencé avec leur première introduction en 2001, marquant le début d'une recherche approfondie sur le concept. Des cristaux magnoniques, des investigations approfondies sur la propagation des ondes de spin ont été menées, exploitant la riche physique des matériaux magnétiques. Cette recherche a conduit au développement de prototypes de dispositifs pour les circuits magnoniques, y compris des transistors, des portes logiques magnoniques et des composants micro-ondes tels que des filtres, des amplificateurs, des diodes et des circulateurs. À ce jour, le domaine de la magnonique couvre désormais une gamme diversifiée de sujets de pointe, tous visant à réaliser des dispositifs magnoniques fonctionnels. Les sujets couverts par la magnonique sont tous combinés dans le dernier papier de la «roadmap» de la magnonique publiée en 2021.

Pour détecter les ondes de spin, les techniques les plus couramment utilisées peuvent être

des techniques électriques, telles que les antennes inductives ou les cavités résonantes, des techniques optiques comme la spectroscopie de diffusion de la lumière Brillouin micro-focalisée (μ-BLS) ou l'effet Kerr magnéto-optique résolu en temps (TR-MOKE), ou même des techniques de diffraction des rayons X telles que la dichroïsme circulaire magnétique des rayons X (XMCD). Dans cette thèse, nous avons utilisé une technique entièrement électrique pour détecter les ondes de spin appelée spectroscopie de propagation des ondes de spin, basée sur le couplage inductif entre les antennes RF et le matériau magnétique. Ces mesures sont effectuées à l'aide d'un analyseur de réseau vectoriel (VNA), où deux types de mesures peuvent être réalisées: dans les domaines fréquentiel et temporel. Ce dernier est rarement utilisé en magnonique jusqu'à présent. Cependant, dans cette thèse, nous avons largement appliqué cette méthode pour distinguer les différents modes présents dans un système magnétique, permettant ainsi une compréhension approfondie du comportement des ondes de spin dans le matériau étudié et l'amélioration des conceptions d'antennes RF adaptées à des applications spécifiques.

Lors de la précession, et en raison de la présence d'un amortissement magnétique dans le matériau, l'aimantation est soumise à des oscillations amorties et à une propagation limitée. Pour cette raison, dans les dispositifs magnoniques, un défi clé est de surmonter l'amortissement magnétique dans le matériau pour atteindre de longues distances de propagation des ondes de spin. Cela nécessite l'utilisation de matériaux avec un faible amortissement magnétique. La grenat d'yttrium de fer (YIG), un matériau ferrimagnétique, possède de loin le plus faible amortissement magnétique, permettant la propagation des ondes de spin sur des distances de plusieurs centimètres. Cependant, dans le cadre des approximations micromagnétiques, le YIG est traité comme un ferromagnétique (FM). Pour ces raisons, le YIG a été considéré comme un matériau de référence pour des études approfondies sur la dynamique des ondes de spin au fil des ans. Cela a positionné le YIG comme un candidat prometteur pour le développement de dispositifs pour les applications micro-ondes, tels que les filtres et les lignes à retard, ainsi que les dispositifs magnéto-optiques tels que les déflecteurs, grâce à l'effet Faraday important dans ce matériau. Il est intéressant de noter que selon l'application, divers substrats peuvent être utilisés pour la croissance de YIG. Par exemple, pour obtenir un faible amortissement et une largeur de raie étroite, le GGG est couramment utilisé. Cependant, des substrats alternatifs prometteurs incluent l'utilisation de silicium ou d'arséniure de gallium, qui sont particulièrement favorisés dans les applications CMOS en raison de leur excellente mobilité des porteurs de charge et de leur large bande interdite. Par conséquent, la croissance sur de tels substrats ouvre la possibilité d'intégration future de dispositifs magnoniques. En outre, le YIG reste un sujet de recherche majeur, dans lequel la physique fondamentale de la magnonique est encore en cours d'investigation, y compris la condensation de Bose-Einstein et l'exploration de la manipulation des ondes de spin par les couples spin-orbite.

Dans certaines applications, l'utilisation de ferromagnétiques ne répond pas à certaines exigences en raison de limitations telles que l'atteinte de fréquences plus élevées au-delà de la région GHz, la présence de champs parasites et la dépendance des propriétés des ondes de spin à l'aimantation. Par conséquent, il est intéressant d'explorer des matériaux alternatifs

qui peuvent répondre à ces besoins tout en découvrant la même physique observée dans les ferromagnétiques.

Les matériaux antiferromagnétiques (AFM) peuvent atteindre des fréquences de résonance facilement dans les échelles THz, offrant ainsi des avantages par rapport à leurs homologues ferromagnétiques, car ils ont une aimantation nette nulle et une robustesse aux champs extérieurs. Cependant, l'intérêt pour les isolants antiferromagnétiques a considérablement augmenté ces derniers temps en raison de leur potentiel à réduire le chauffage par effet Joule, ouvrant ainsi la voie au transport du moment angulaire de spin avec l'onde de spin propagée, où émerge la magnonique antiferromagnétique.

Des recherches théoriques approfondies sur la dynamique des ondes de spin antiferromagnétiques propagées, pour des longueurs d'onde longues et courtes, ont été menées au cours des dernières décennies. Cependant, en raison des défis des techniques expérimentales et de l'intégration dans des dispositifs magnoniques, les preuves expérimentales manquent encore dans ce domaine.

Dans certains orthoferrites, des effets magnétostatiques peuvent survenir en raison du possible canting des moments magnétiques. Cela est observé dans des matériaux tels que $YFeO_3$, $TmFeO_3$, $ErFeO_3$ et α-Fe_2O_3. Notamment, des travaux de Boventer et al. ont montré théoriquement et expérimentalement qu'un antiferromagnétique canted à température ambiante, comme α-Fe_2O_3, peut avoir deux modes de magnons, où ils ont pu accéder au mode de magnons de basse fréquence et détecter des résonances via ISHE et le pompage de spin, avec des fréquences situées dans la gamme GHz (30 GHz pour un champ de 0.5 T). Cela suggère la possibilité de détecter des ondes de spin antiferromagnétiques propagées dans la phase canté de l'hématite en sondant son mode de basse fréquence. L'utilisation d'une technique inductive telle que la spectroscopie des ondes de spin, comme détaillé dans notre article récemment publié, fournit une preuve expérimentale pour l'observation d'ondes de spin ultrarapides propagées à quelques km/s, en raison de la présence d'effets magnétostatiques. Ces résultats ont également été soutenus par des modèles théoriques développés par nos collaborateurs.

Ces dernières années cependant, des progrès substantiels ont été réalisés dans le domaine de la spintronique antiferromagnétique, en particulier avec les isolants antiferromagnétiques. Ce domaine de recherche s'est concentré sur la manipulation de l'ordre antiferromagnétique par des mécanismes de spin à charge. Actuellement, la détection électrique réussie utilisant l'effet Hall inverse du spin a été limitée au mode uniforme ($k = 0$), résultant en des amplitudes de tension générées dans la gamme de quelques dizaines de nanovolts pour les antiferromagnétiques colinéaires et canted. De plus, des travaux de Lebrun et al. ont démontré un potentiel pour le transport de magnons à longue distance et ont validé expérimentalement le transport sans dissipation du spin dans l'hématite à température ambiante. Notamment, notre travail récent a fourni des preuves pour la détection des ondes de spin propagées via ISHE. Cette réalisation fusionne non seulement les mécanismes de spintronique avec les ondes de spin ultrarapides, mais ouvre également la voie à l'intégration

future de dispositifs magnoniques avec des antiferromagnétiques cantés.

Dans ce manuscrit, nous allons étudier l'excitation, la propagation et la détection des ondes de spin dans deux matériaux distincts : le grenat d'yttrium de fer (YIG) ferromagnétique et l'Hématite antiferromagnétique.

Le chapitre 2 fournit un aperçu théorique complet essentiel pour comprendre les concepts fondamentaux explorés tout au long de la thèse. Il commence par décrire les principaux concepts cruciaux pour distinguer les différents modes d'ondes de spin dans les ferromagnétiques. Ensuite, il introduit les matériaux antiferromagnétiques, en expliquant leurs équations énergétiques et en se concentrant sur les spécificités des antiferromagnétiques canté, exemplifiés par l'Hématite. Le chapitre se termine en introduisant les mécanismes de transport du spin et en établissant des concepts clés qui forment un lien crucial avec les résultats présentés dans les chapitres suivants.

Le chapitre 3 est une description des techniques expérimentales utilisées tout au long de la thèse. Il contient des méthodes de fabrication, de caractérisation et de détection des ondes de spin.

Le chapitre 4 couvre les résultats du développement d'une technique expérimentale via la spectroscopie des ondes de spin propagées. En mettant en œuvre l'option du domaine temporel de l'analyseur de réseau vectoriel (VNA), les mesures sont présentées dans le domaine temporel après transformation de Fourier inverse, plutôt que dans le domaine fréquentiel. Le chapitre met en évidence une complexité dans le spectre du YIG, révélant sa nature multimodale et où nous menons une étude pour distinguer ces modes entremêlés.

Dans le chapitre 5, l'accent est mis sur les antiferromagnétiques, en particulier la phase canté de l'Hématite. Nous présentons une observation expérimentale de la propagation cohérente des ondes de spin dans l'Hématite bulk. Ces ondes de spin présentent un mode non dégénéré avec des vitesses allant jusqu'à 20 km/s ainsi qu'un caractère non réciproque. Ces résultats expérimentaux sont soutenus par des modèles théoriques développés et fournis par nos collaborateurs pour le cas spécifique de l'Hématite.

Le chapitre 6 continue l'exploration de l'hématite, cette fois en intégrant les phénomènes magnoniques et spintroniques. L'investigation de la spintronique magnétique sur l'hématite implique la détection des ondes de spin en utilisant l'effet Hall inverse du spin, où l'excitation est initiée par une antenne inductive et la détection via un transducteur en platine. Le chapitre démontre ensuite un effet de rectification basé sur un effet de diode spin dans l'Hématite.

Le chapitre 7 sert à conclure et à résumer des résultats présentés dans les chapitres précédents. Enfin, nous concluons la thèse avec quelques perspectives et motivations qui peuvent servir à faire progresser le domaine de la magnonique ultrarapide.

Les résultats sont résumés comme suit:

F.1 CHAPITRE 4: SPECTROSCOPIE DE TEMPS DE VOL SUR LE YIG :

Nous introduisons une méthode d'extraction d'informations temporelles sur les paquets de SWs propagatifs à l'aide du VNA. L'approche implique la transformée de Fourier inverse des données de domaine fréquentiel, montrant son utilité dans les VNA disponibles commercialement. Nous réalisons donc des mesures sur un film de YIG, ayant un spectre complexe de mode. On arrive alors à identifier les modes ainsi que d'isoler leur contribution afin de pouvoir étudier les propriétés de chaue mode. À partir de ces résultats, nous avons pu mieux comprendre le comportement des SWs dans une ligne de retard de YIG et ainsi adapter la conception des antennes selon l'application souhaitée.

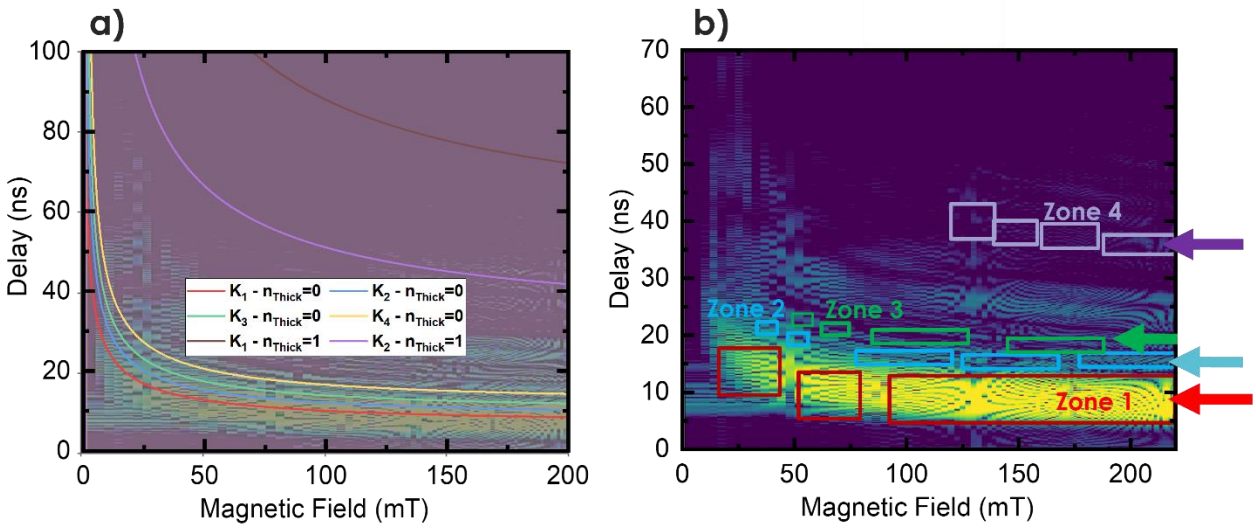

Figure F-1: Zones-BW pour FT : *a) Le délai attendu des modes potentiellement disponibles dans le système. b) Carte de couleur montrant la décomposition du spectre de domaine temporel en zones sur lesquelles la transformée de Fourier est effectué*

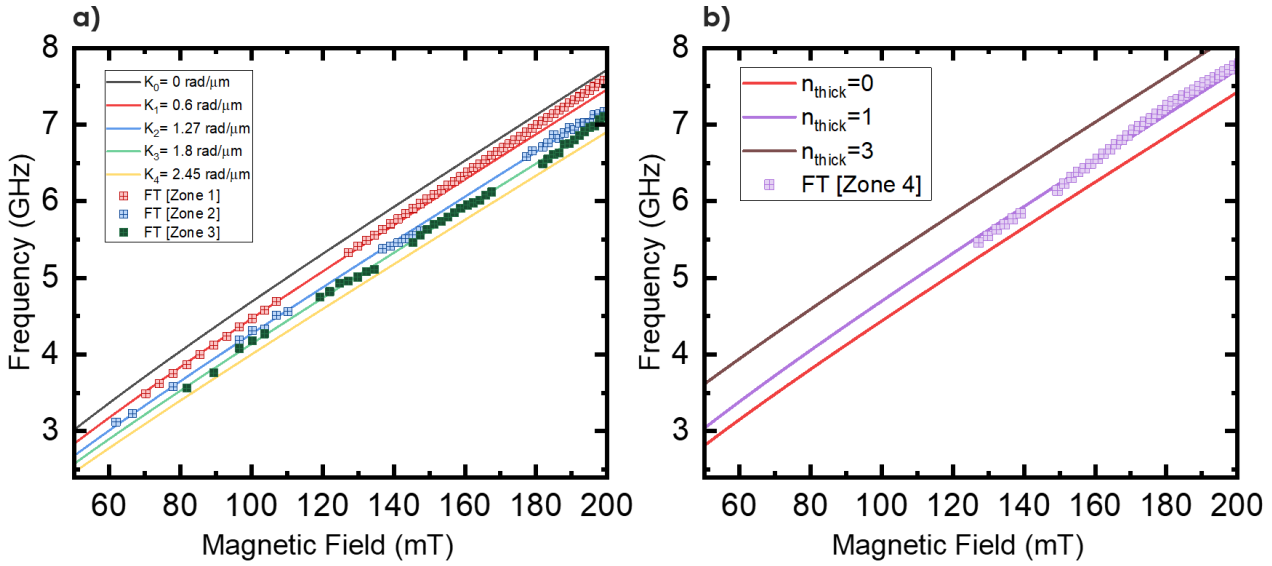

Figure F-2: BW- Theorie versus Experience: *a) Modes d'antenne : Les modes attendus selon la théorie (lignes pleines) par rapport au résultat de la transformée de Fourier des zones dans* ***Figure 4-19****.* ***a)*** *La*

transformée de Fourier sur la zone 1 contenant la branche la plus intense dans le spectre (points rouges) correspond à la courbe théorique (ligne rouge) pour k=K1. Le même résultat est obtenu pour les branches étroites plus lentes ; zone 2 en bleu et zone 3 en vert correspondant aux courbes théoriques de k=K2 et k=K3, courbes bleue et verte, respectivement. b) Modes d'épaisseur : la relation de dispersion attendue des modes d'épaisseur avec k=K1 dans le système, avec nthick=0 représentant la même courbe k=K1 dans le panneau a). La transformée de Fourier de la zone 4 pour la branche la plus lente dans les spectres chevauchant le premier mode d'épaisseur avec k=K1.

F.2 CHAPITRE 5: ONDES DE SPIN DANS L'HEMATITE :

Les ondes de spin dans les AFM sont également étudiés depuis des anées, mais leurs observation en expérimentale font toujours défaut. Les AFM cantés tel que l'hématite avec la présence des interactions Dzyaloshinskii-Moriya et sous l'influence d'un champs magnétique appliqué, permettent un régime d'échange dipolaire de SWs. Nous avons réussi donc à détecter et démontrer la présence de tels SWs ayant un caractère non réciproques ultra-rapides et non dégénérés, en utilisant des moyens de détection inductifs sur l'Hématite épais. En utilisant la spectroscopie de temps de vol, nous constatons que les paquets d'ondes de magnons peuvent se propager aussi rapidement que 20 km/s pour les modes de bulk réciproques et jusqu'à 6 km/s pour les ondes de spin de surface se propageant parallèlement au vecteur Néel. Ces résultats peuvent faire avancer le domaine de la magnonique antiferromagnétique et dévoiler la physique riche des SWs cohérents.

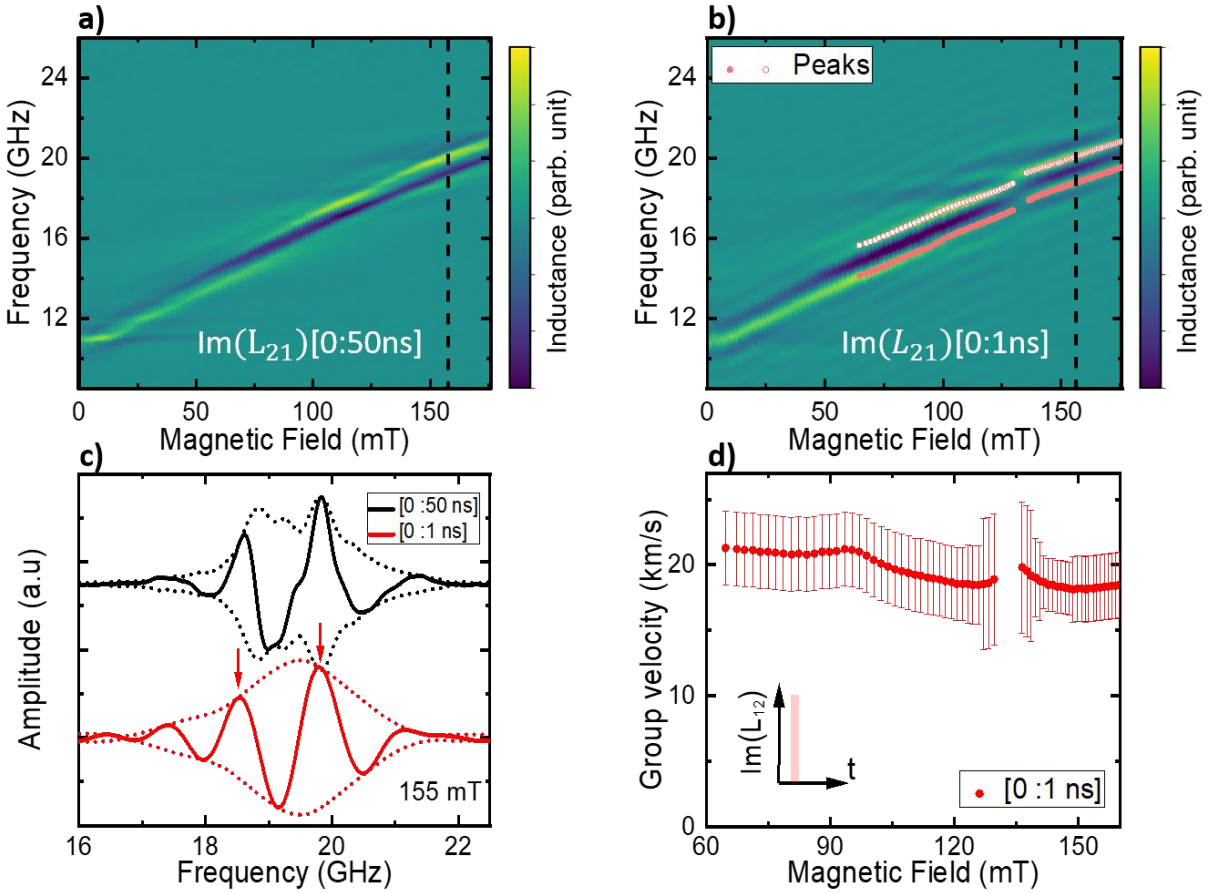

Figure F-3: Ondes de spin antiferromagnétiques ultra-rapides pour H // k révélées par la porte temporelle: *a) Partie imaginaire de l'onde de spin transmise Im(L21) en fonction du champ sans porte temporelle. b) Im(L21) en fonction du champ avec porte temporelle [0:1 ns], les points rouges sont les pics extraits montrés en c) et utilisés pour calculer la vitesse en d). c) Exemple de spectres de l'Im(L21) des signaux d'onde de spin complets (porte temporelle de [0:50 ns], noir) et du paquet principal d'onde de spin (porte temporelle de [0:1 ns], rouge) pour H = 155 mT pour une distance d'antenne à antenne de 14 µm, les oscillations (rouge) indiquent une vitesse de groupe de l'onde de spin > 14 km/s. Les lignes pointillées correspondent aux enveloppes du signal. d) Vitesse de groupe du paquet principal d'onde de spin pour une porte temporelle de [0:1 ns]. Les barres d'erreur sont définies comme le niveau de bruit de l'Im(L21).*

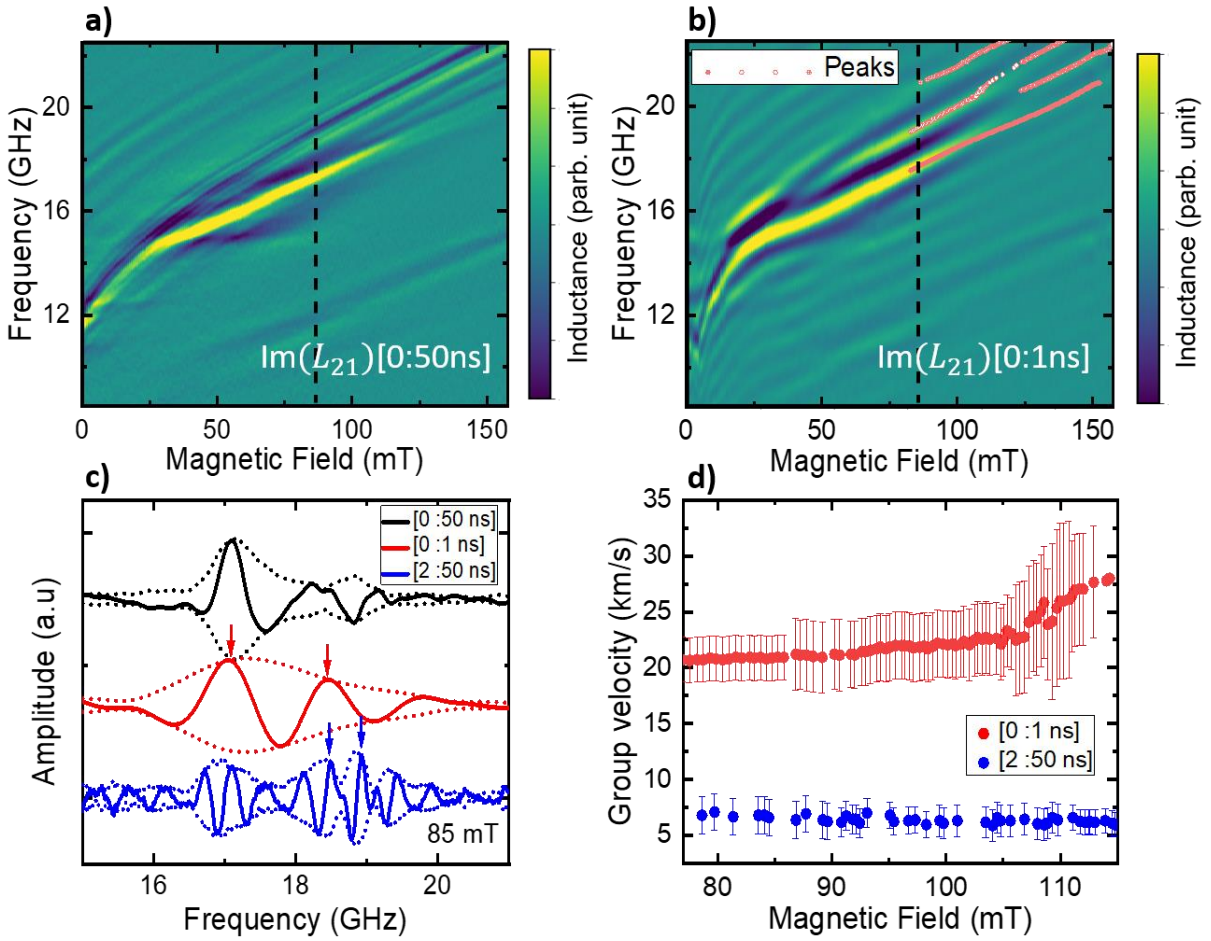

Figure F-4: Ondes de spin antiferromagnétiques ultra-rapides pour H ⊥ k révélées par la porte temporelle : *Partie imaginaire de l'onde de spin transmise Im(L21) a) avec une large fenêtre temporelle de 0 à 50 ns. b) avec une fenêtre temporelle de 0 à 1 ns. Les points rouges sont les données extraites représentant les maxima des oscillations de l'Im(L21). c) Spectres exemplaires de l'Im(L21) pour H = 85 mT pour différentes fenêtres temporelles, [0:50 ns] : signaux d'onde de spin complets (noir), [0:1 ns] : premier paquet d'onde de spin (rouge), [2:50 ns] : paquets d'onde de spin secondaires (bleu). Les lignes pointillées correspondent aux enveloppes du signal. d) Vitesse de groupe des différents paquets d'onde de spin. Les barres d'erreur sont définies comme le niveau de bruit à partir de la partie imaginaire de l'inductance transmise L21. Les modes de fréquence plus élevée se propagent environ 3 fois plus lentement à environ 8 km/s que le mode de volume, à environ 20 km/s.*

F.3 CHAPITRE 6: MAGNON SPINTRONICS SUR HEMATITE:

Une technique alternative aux mesures inductives pour détecter les SWs peut être réalisée en utilisant une détection électrique. Cela est accompli en utilisant un transducteur métallique à base de platine via l'effet Hall de spin inverse (ISHE). Nous obtenons une tension de sortie sur l'hématite comparable à celle obtenue dans un FM comme le YIG, marquant une détection électrique efficace des SWs propagatifs à travers ISHE sensible à la surface. Un autre effet a également été obtenu dans cette thèse ; la réalisation de la rectification de diode de spin dans l'hématite. Grace a ces etudes on a pu démontrer que les effets de spin-pumping représentent un outil prometteur pour détecter la dynamique de SW dans les AFM.

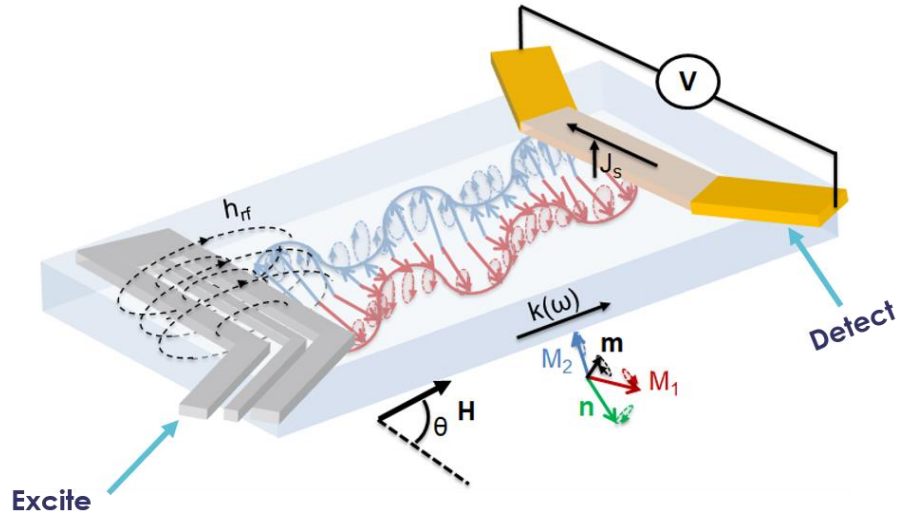

Figure F-5: Schéma de l'expérience *Excitation des ondes de spin avec une antenne GSG de k=0.6rad/µm, conduisant à leur propagation jusqu'à sous la couche de platine. Cela donne lieu à un courant de spin dans le platine qui est converti en courant de charge via l'ISHE, permettant la détection d'un VISHE à travers la bande de Pt.*

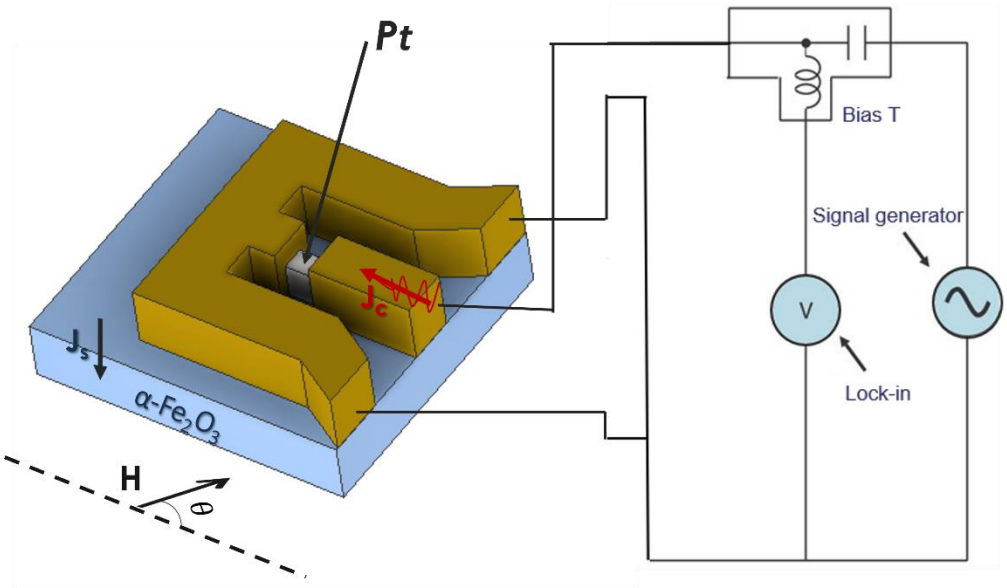

Figure F-6: Schéma de l'expérience : *Le dispositif étudié consiste en une antenne G-S-G en Ti/Au sur un α-Fe2O3 de 500 µm d'épaisseur. La ligne de signal consiste en une bande de platine de 5 nm d'épaisseur.*

F.4 CONCLUSION:

La thèse a atteint à la fois des objectifs fondamentaux et applicatifs. Elle a avancé la compréhension des dispositifs micro-ondes dans les films épais de YIG, démontré l'utilité de la spectroscopie en domaine temporel, et fourni une démonstration significative des ondes de spin propagantes dans l'Hématite. Ces résultats soulignent le potentiel des antiferromagnétiques canted pour la magnonique haute fréquence et encouragent de nouvelles études expérimentales.

F.5 PERSPECTIVES

1. Représentation des Données en Temps Réel :

- Améliorer les dispositifs à faible signal en passant de l'excitation en onde continue (CW) à des mesures RF-VNA pulsées pour accéder aux régimes transitoires des ondes de spin.

2. Investigations sur les Films Minces :

- Explorer les ondes de spin dans des films minces d'Hématite pour comprendre leur comportement avec une épaisseur réduite, en visant des applications dans la magnonique ultra-rapide.

- Tests actuels sur des films de 500 nm à 20 nm, avec résonance observée dans la plupart des dispositifs et expériences de transport en cours.

3. Auto-Oscillation et Amplification des Ondes de Spin :

- Investiguer le potentiel des couples de spin-orbite dans les antiferromagnétiques pour atteindre l'auto-oscillation et amplifier les ondes de spin, en s'inspirant des résultats récents dans le YIG dopé au bismuth.

4. Condensation de Bose-Einstein :

- Étudier l'interaction entre les ondes de spin et la condensation magnétique de Bose-Einstein (BEC) dans l'Hématite antiferromagnétique, inspirée par des recherches récentes dans les films de YIG.

5. Textures de Spin Topologiques :

- Explorer la stabilisation et la manipulation des textures de spin antiferromagnétiques comme les demi-skyrmions (merons et bimerons) dans des films minces d'Hématite pour des applications logiques et de mémoire.

Défis et Questions Ouvertes :

- L'intégration de tels matériaux dans des dispositifs reste un défi, potentiellement abordé en

explorant des matériaux polycristallins pour améliorer la flexibilité des conditions de croissance et réduire les limitations d'intégration.

En résumé, cette thèse a fourni des insights significatifs sur les dynamiques des ondes de spin et a ouvert de multiples voies de recherche future dans la magnonique et la spintronique, notamment avec les propriétés prometteuses de l'Hématite et ses applications potentielles dans des dispositifs haute fréquence et économes en énergie.